DEPARTMENT OF PHYSICS AND ASTRONOMY
UNIVERSITY OF HEIDELBERG

Master Thesis in Physics
submitted by

Friederike Bock

born in Gardelegen (Germany)

2012

Neutral Pion and Eta Meson Production in pp and Pb–Pb Collisions at the LHC with the ALICE Detector

This Master Thesis has been carried out by Friederike Bock at the

Physikalisches Institut at the University of Heidelberg

under the supervision of

Prof. Dr. Johanna Stachel

Abstract

In this thesis the differential invariant cross-section of the inclusive π^0 and η meson for pp collisions at $\sqrt{s} = 0.9$, 2.76 and 7 TeV is presented. Additionally, the first measurement of the differential invariant yield of π^0 and η mesons in several centrality classes for Pb–Pb collisions at $\sqrt{s_{\mathrm{NN}}} = 2.76$ TeV will be shown and the nuclear suppresion factor R_{AA} will be calculated for the neutral pion in these centrality bins. The mesons have been measured by reconstructing the converted photons from the electron-positron pairs, which were detected in the Inner Tracking System and the Time Projection Chamber. It allows the extraction of the π^0 (η) signal down to 0.3 (0.4) GeV/c in pp collisions and 0.4 (1.5) GeV/c in Pb–Pb collisions. For all collision systems the spectra obtained with the photon conversion method (PCM) are compared to the spectra measured via the PHOton Spectrometer (PHOS). Afterwards, the measurements are combined using the weighted average. The combined π^0 and η meson transverse momentum spectra agree with NLO perturbative QCD predictions at $\sqrt{s} = 0.9$ TeV, however, the calculations fail to reproduce the measured spectra at higher center-of-mass energies. Also m_{T} scaling has been tested for Pb–Pb at $\sqrt{s_{\mathrm{NN}}} = 2.76$ TeV and pp collisions at $\sqrt{s} = 2.76$ TeV. While for Pb–Pb collisions the measured η meson transverse momentum spectra agree with the m_{T} scaled spectra, they do not seem to match in pp collisions. Finally ,the neutral pion R_{AA} has been compared to measurements from different particle species, lower center-of-mass energies and theory calculations. The neutral pion suppression for central Pb–Pb collisions at $\sqrt{s_{\mathrm{NN}}} = 2.76$ TeV agrees with the charged pion and unidentified charged hadron measurement at high transverse momenta and is twice as large as the suppression measured in Au–Au collisions at $\sqrt{s_{\mathrm{NN}}} = 200$ GeV. Moreover, none of the presented theory calculations, is capable of simultaneously describing the transverse momentum and centrality dependence of the nuclear suppression factor, seen in the data.

Zusammenfassung

In der vorliegenden Arbeit werden die invarianten Wirkungsquerschnitte für π^0 und η Mesonen in Abhängigkeit vom transversalen Impuls für Proton-Proton Kollisionen bei Schwerpunktsenergien von $\sqrt{s} = 0.9$, 2.76 und 7 TeV präsentiert werden. Darüber hinaus wird die erste Messung der Transversalimpulsspektren für π^0 und η Mesonen in Pb–Pb Kollisionen bei $\sqrt{s_{\mathrm{NN}}} = 2.76$ TeV in mehreren Zentralitätsklassen vorgestellt werden. Für das neutrale Pion berechnen wir desweiteren den nukleare Formveränderungsfaktor R_{AA} in den entsprechenden Zentralitätsklassen. Die Mesonen-Messung erfolgte durch die Rekonstruktion konvertierter Photonen über deren Zerfallsprodukte, welche im Inner Tracking System und der Time Projection Chamber gemessen werden können. Darüber hinaus erlaubt die Photon Konversions Methode (PCM) die Extraktion des π^0 (η) Signals bis hin zu sehr kleinen Impulsen, beginnend bei 0.3 (0.4) GeV/c in pp Kollisionen und 0.4 (1.5) GeV/c in Pb–Pb Kollisionen, mit einer exzellenten Auflösung (rund 3 MeV/c^2). Die auf diese Weise bestimmten Spektren werden mit den Spektren, die im PHOton Spectrometer (PHOS) gemessen werden konnten, verglichen und im Anschluss mit diesen über das gewichtete Mittel kombiniert. Der Vergleich der so für das π^0 und η Meson erhaltenen Transversalimpulsspektren mit störungtheoretischen QCD-NLO-Rechnungen zeigt, dass während die Rechungen bei $\sqrt{s} = 0.9$ TeV mit den Daten übereinstimmen, die Transversalimpulsspektren bei höheren Schwerpunktsenergien nicht reproduziert werden können. Darüber hinaus wurde die m_{T}-scaling Hypothese in Pb–Pb und Proton-Proton Kollisionen bei $\sqrt{s} = 2.76$ TeV getestet. Es zeigt sich, dass für Pb–Pb Kollisionen die gemessenen und die mit m_{T}-scaling berechneten Spektren für das η Meson innerhalb ihrer Fehler übereinstimmen, während für Proton-Proton Kollisionen dies nicht gegeben ist. Abschließend wurde der nukleare Formveränderungsfaktor für neutrale Pionen mit den Ergebnissen für andere Teilchenarten, andere Schwerpunktsenergien und theoretischen Berechnungen verglichen. Es zeigt sich, dass die Unterdrückung von neutralen Pionen in zentralen Pb–Pb Kollisionen bei $\sqrt{s_{\mathrm{NN}}} = 2.76$ TeV mit den Ergebnissen für geladene Pionen und unbestimmte geladene Hadronen bei der gleichen Schwerpunktsenergie übereinstimmt, während im Vergleich zu den Messungen in Au–Au Kollisionen bei $\sqrt{s_{\mathrm{NN}}} = 200$ GeV eine zweifach stärkere Unterdrückung gemessen werden konnte. Darüber hinaus wurde festgestellt, dass keine, der in Betracht gezogenen theoretischen Berechnungen, gleichzeitig die Abgängigkeit des nukleare Formveränderungsfaktors vom transversalen Impuls und der Zentralität beschreiben kann.

Contents

1. Introduction

"A scientist in his laboratory is not a mere technician:
he is also a child confronting natural phenomena that impress him
as though they were fairy tales."

<div align="right">Marie Curie (1867 - 1934)</div>

As a child we see the world with different eyes, everything is fascinating and new. Every day new phenomena can be studied and although they might be well known to the adults, for a child they are exciting and it tries to explain them. While growing older most of these children stop asking questions and accept the world around them as it is and as it is told to be. Some of them, however, remain curious and some of these even become scientists, trying to unravel the mysteries and fairy tales of nature. Today our understanding of the world is rather good, we know the main mechanisms how the earth and universe developed over the last 14 billion years. Nevertheless, there are still white spots remaining and scientists from the different disciplines try to fill these.

The Large Hadron Collider (LHC), currently the most powerful particle accelerator ever built, was designed to study two of the most important questions for particle physicists:

- *How did the universe evolve after its creation?*

- *What are the smallest building parts of nature?*

Although these questions are located at opposite ends of the observation horizon, both can be studied at the LHC. In the accelerator protons can be collided with a center-of-mass energy of up to $\sqrt{s} = 14$ TeV and heavy ions up to a $\sqrt{s_{\mathrm{NN}}} = 5.5$ TeV per nucleon-nucleon pair. Such conditions were never reached before in a laboratory and, therefore, offer a new possibility to test current theories. Highly energetic pp collisions not only allow to search for the Higgs boson but also to study the known particles to a new level of precision. In heavy-ion collisions, on the other hand, a state of strongly coupled matter is created, the quark-gluon plasma, which only existed shortly after the creation of the universe. Therefore, the evolution of matter shortly after the Big Bang can be investigated by several of the LHC experiments.

One of these experiments is the ALICE (A Large Ion Collider Experiment) detector system, in which context this thesis has been carried out. It has been designed to handle large charged-particle densities, while at the same time being able to identify these particle down to very low momenta. Thus it allows to study a variety of aspects of the produced strongly coupled medium. One of these aspects, the suppression of high-momentum particles due to the interactions in the medium will be studied in this thesis. It is quantified using the nuclear suppression factor R_{AA}, which is the ratio of the yield measured in Pb–Pb collisions scaled by the number of binary collisions to the yield measured in pp collisions.

This thesis describes the measurement of the neutral pion and eta meson production in pp at $\sqrt{s} = 0.9$, 2.76 and 7 TeV and Pb–Pb collisions at $\sqrt{s_{\mathrm{NN}}} = 2.76$ TeV. Both mesons are detected

in their two-photon decay channel and the photons are reconstructed using the photon conversion method. While the measured invariant cross sections in pp collisions allow insights to the neutral pion and eta particle production, the measurement in Pb–Pb collisions allows to distinguish between different energy loss scenarios in the created medium.

The structure of the thesis is as follows: After this short introduction, a theoretical overview together with the current state of knowledge from the experimental point of view will be presented (Chapter 2). Then an overview of the experimental setup (Chapter 3) is given and the photon reconstruction via the photon conversion method is explained (Chapter 4). Chapter 5 is dedicated to the calculation of the error of the material budget in ALICE. The results on the neutral pion and eta meson measurements in pp and Pb–Pb collisions are presented in Chapter 6. The thesis concludes with a summary and outlook.

2. Theoretical Background and Current Status of Knowledge

2.1. The Standard Model and Quantum Chromodynamics

The Standard Model (SM) of particle physics is a gauge Quantum Field Theory (QFT) combining the quantum field theories of the electro-weak interaction and Quantum Chromodynamics (QCD). It was conceived by S. L. Glashow [1], A. Salam [2,3] and S. Weinberg [4] in 1967/8. Their work was awarded with the Nobel Prize in Physics in 1979. The model describes the constituents of matter as well as their interactions. Its fundamental particles, quarks and leptons, each organized in three generations, and the four gauge bosons mediating the fundamental forces, are shown in Figure 2.1.

The electroweak theory is the unified description of two interactions: QED[1] and weak interaction. While the theory of weak interaction explains how a quark can change into another quark or a lepton into another lepton (flavor changes), QCD is the theory that characterizes the properties

---

[1] Quantum Electrodynamics (QED)

Figure 2.1.: Schematic overview of the particles contained in the Standard Model of particle physics. The leptons and quarks together with their anti-particles represent the constituents of the matter, while the gauge bosons mediate the different forces between these constituents. Adapted from [5]

of the strong interaction, the fundamental force describing the interaction between quarks and gluons. According to QCD, the quantum number of color plays the role that the charge plays in the electromagnetic interaction. The gauge bosons mediating the strong interaction are called gluons, they carry color charge themselves. As such they can interact with each other. All bound states of quarks and gluons have to be colorless. The combinations, which have been observed in experiments are: 3 quarks with different colors (baryons), 3 anti-quarks with different anti-colors (anti-baryons) or one quark and one anti-quark carrying color and anti-color (mesons). The Lagrange density of QCD is given by

$$\mathcal{L} = \sum_q \overline{\psi}_q \gamma^\mu (i\partial^\mu - g_s A_q^\mu \frac{\lambda_a}{2})\psi_q - \sum_q m_q \overline{\psi}_q \psi_q - \frac{1}{4}\sum_a F_a^{\mu\nu} F_{\mu\nu,a}. \tag{2.1}$$

The ψ_q represents the quark field, g_s is the effective strong charge and A_q^μ is a gluon field, while the λ_a are the Gell-Mann matrices. The gluon field strength tensor $F_a^{\mu\nu}$ can be expressed as:

$$F_a^{\mu\nu} = \partial^\mu A_a^\nu - \partial^\nu A_a^\mu + ig_s f_{abc} A_\mu^b A_\nu^c \tag{2.2}$$

The last term represents the gluon self interaction. For massless particles the QCD Lagrangian is invariant under the exchange of left- and right-handed components of the quark spinor, which is called *chiral symmetry*. As the quarks have masses, this symmetry is explicitly broken. However, even for massless quarks, the strong force would give rise to a so-called *chiral condensate*, which is not invariant under exchange of right- and left-handed fermions. Thus, the chiral symmetry of the QCD Lagrangian is spontaneously broken. This leads to the existence of massless *Goldstone bosons*, which can be identified with the octet of the lightest mesons (π^0, $\pi^\pm$, $K^\pm$, K^0, $\overline{K}^0$, η), which again acquire mass due to the explicit breaking of chiral symmetry.

The coupling strength g_s of QCD can be expressed as $\alpha_s = g_s^2/4\pi$. The value of α_s cannot be predicted by QCD but needs to be determined from experiments. It is much larger than the coupling constant in QED ($\alpha_{em} \simeq \frac{1}{137}$) and varies as a function of momentum transfer. Therefore, it is often referred to as the running coupling constant of QCD. The dependence of α_s on Q in leading order can be expressed by

$$\alpha_s(Q^2) \approx \frac{12\pi}{(33 - 2N_f)\ln\frac{Q^2}{\Lambda^2}}. \tag{2.3}$$

where N_f is the number of quark flavors and Λ is the QCD scaling parameter, which was experimentally determined to be about 200 MeV. Equation 2.3 does not hold if $Q^2 \simeq \Lambda^2$.

The phenomenological potential between a $q\bar{q}$ pair is given approximately by:

$$V_s = -\frac{4}{3}\frac{\alpha_s}{r} + kr, \tag{2.4}$$

where r is the radial distance between the quarks. For smaller r the first term dominates, and it is equivalent to a Coulomb-like interaction. As r increases, the potential grows linearly, and consequently the energy to take out a quark from a hadron should be infinite. At some point it becomes energetically more favorable to create a new quark-anti-quark pair (a meson) from the vacuum. This behavior at long-distances is called *confinement* and is the reason why single quarks are never observed in nature. For high momentum transfer, on the other hand, the coupling strength decreases and the particles behave like free particles, which was later called the *asymptotic freedom* of QCD at short distances and high energies.

High-energy hadron collisions can be divided in two basic collision classes: (i) elastic collisions, where the initial- and final-state particle are of the same type, and (ii) inelastic collisions, where the hadrons are exited or even break up. The latter can be further divided into soft, low momentum transfer, and hard, high momentum transfer, interactions. Hard processes can be described

with perturbative QCD (pQCD) calculations and form, together with the *intial-* and *final-state radiation*, the hard part of the hadron collision. Currently most of the calculations include the Leading Order (LO) terms and the corrections due to single gluon emission, Next-to-Leading Order (NLO). However, some groups already go to higher-order corrections, Next-to-Next-to Leading Order (NNLO), increasing the accuracy of the predictions. The rest of the initial hadrons can produce low-momentum particles, which build the so-called *underlying event*. Regardless of the scattering process, all final-state partons undergo a non-perturbative hadronization process to form the colorless particles observed in nature. The high-momentum partons hadronize in a spray of lower momentum particles, so-called *jets*. This process is called fragmentation and includes final-state radiation of the parton as well as the hadronization process itself.

Although the Standard Model is a renormalizable theory and the predictions extracted from this theory are self-consistent and well reproduced by experimental data, it still leaves some unexplained phenomena. These are mainly related to energies and distances, where the gravitational force, which can be described by general relativity, plays a role and gravitons should emerge. Therefore, it is seen as an effective field theory in the context of modern field theories. For high-energy physics, however, these gravitational effects are rather small and therefore they can be neglected in the calculations. Not all particles included in the Standard Model were known when it was invented, the big successes for the predictions made by the model were:

1973: the observation of neutral currents [6]

1974: the observation of the J/ψ [7,8]

1983: the discovery of the W$^\pm$ and Z^0 bosons [9]

1994: the observation of the top quark [10,11]

2000: the observation of the τ neutrino [12]

The last missing piece, the mechanism [13–18] that breaks electroweak symmetry in the SM and gives mass to massive elementary particles, has not yet been fully verified experimentally. The search for the manifestation of this mechanism, a scalar particle called Standard Model Higgs boson, is one of the highlights of the physics program at LHC[2]. During the past two centuries limits on the Higgs boson mass have been set indirectly by global fits to electroweak results [19] and directly by searches at the LEP[3] [20], the Tevatron [21–24] and the LHC [25], leaving a very narrow mass window for a low-mass Higgs between 116 GeV/c^2 and 127 GeV/c^2. During the first week of July 2012 ATLAS[4] [26] and CMS[5] [27] finally announced the discovery of a new neutral boson with a mass of 126 GeV/c^2, which is consistent with a Standard Model Higgs boson.

2.2. The Quark-Gluon Plasma

The idea of asymptotic freedom in QCD has the interesting consequence that at very high energies as well as high energy and baryon densities hadronic matter dissolves into its constituents. This state of deconfined matter with free quarks and gluons is referred to as Quark-Gluon Plasma (QGP). It is expected to have existed from about 10 picoseconds to 10 microseconds after the Big Bang.

---

[2]Large Hadron Collider (LHC)
[3]Large Electron Positron Collider (LEP)
[4]A Toroidal LHC Apparatus (ATLAS)
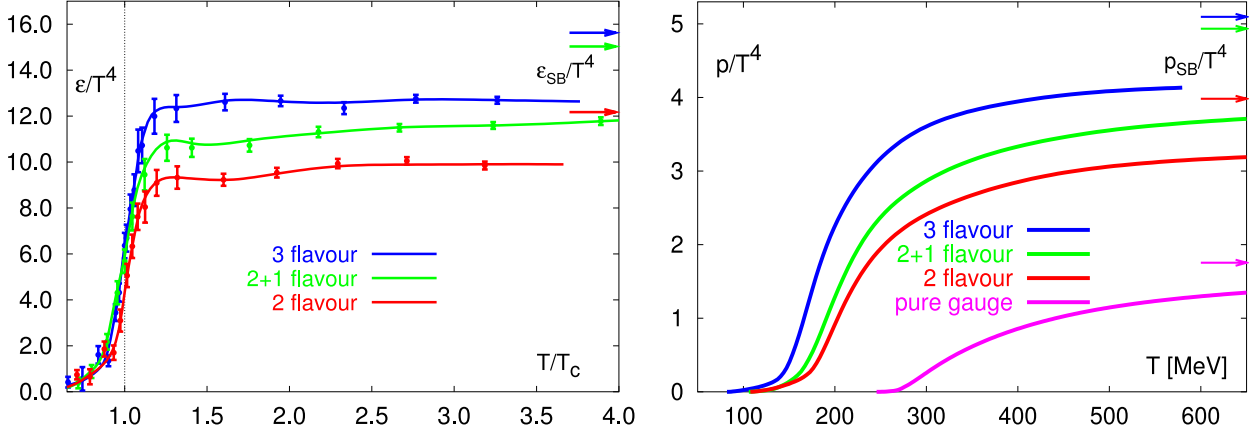[5]Compact Muon Solenoid experiment (CMS)

Figure 2.2.: Left: Energy density as a function of the temperature calculated with lattice QCD for different compositions of quark flavors. The critical temperature is around 174 MeV. Right: The pressure in QCD with different number of degrees of freedom as a function of temperature calculated with LQCD. The curves labeled $(2+1)$-flavor corresponds to a calculation with two light and a four times heavier strange quark mass. Taken from [30].

2.2.1. Characteristics of the Quark-Gluon Plasma

The critical temperature T_c at which normal matter undergoes a phase transition into a QGP has been estimated by different groups over the last decades to be of the order 100-250 MeV. Already in the 1960s, Rolf Hagedorn discovered, by detailed investigations of hadronic matter, that there is a limiting temperature of 140 MeV for hadronic systems. The advances in Lattice QCD (LQCD) calculations, which are non-perturbative calculations of QCD on a space-time lattice allowing to calculate the interactions in the region of low momentum transfer, lead to more precise values of $T_c \sim 150-160$ MeV at vanishing baryon chemical potential $\mu_B \approx 0$ [28, 29]. Depending on the number of included quarks in LQCD calculations the critical temperature varies. The results of one group [30] for the energy density and the pressure divided by T^4 for several quarks compositions as a function of the temperature are shown in Figure 2.2. However, the pion mass in all these calculations is still unphysical. Both variables rise at T_c, indicating a significant change of the number of degrees of freedom above T_c, and a possible formation of the QGP. For 2-flavor QCD the expected critical temperature is found to be $T_c = 173 \pm 8$ MeV and in the 3-flavor case it is $T_c = 154 \pm 8$ MeV. Taking two light quarks and one heavier one delivers nearly the same value [31], but it increases slower as in the 3 flavor case. However, to be able to talk about temperatures and phases the system needs to consist of a large number of particles. Moreover, it has to reach local equilibrium, so that variables like pressure, temperature, energy and entropy density can be defined and their relations be studied. A consequence of these requirements is that the lifetime of the system has to be significantly larger than the inverse rate of interactions, so that at least some interactions occur for each variable, driving the system towards equilibrium [32, 33]. A schematic view of the QCD phase diagram of hadronic matter including the QGP can be seen in Figure 2.3. It is believed that collisions of protons or electrons do not produce high enough particles densities to create a quark-gluon plasma. Heavy-ion collisions, on the other hand, seem to be a good candidate for the production of a QGP state, at least if the energy of the colliding nuclei is large enough.

Since 1986, high-energy heavy-ion collisions have been produced in different laboratories, starting with the AGS[6] at BNL[7] and the SPS[8] at CERN[9]. These experiments started with rather low

---

[6] Alternating Gradient Synchrotron (AGS)
[7] Brockhaven National Laboratory (BNL), Brookhaven, United States
[8] Super Proton Synchrotron (SPS)
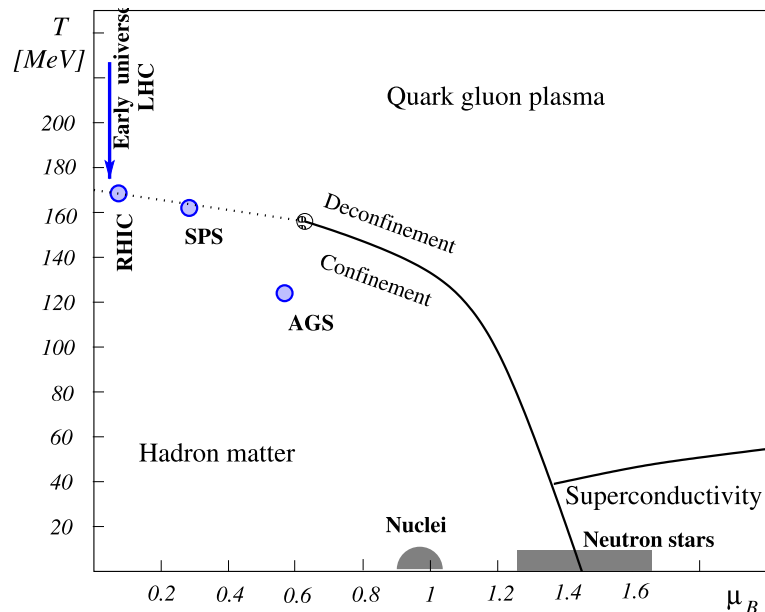[9] European Organization for Nuclear Research (CERN), Geneva, Switzerland

Figure 2.3.: Schematic QCD phase diagram in the $T - \mu_B$ plane, taken from [34]. At low T and μ_B nuclear matter shows confinement and hadrons determine the number of degrees of freedom. On the other hand, at higher T a phase transition to a deconfined quark-gluon plasma with restored chiral symmetry is predicted by lattice QCD. The phase diagram might exhibit a critical point at about $\mu_B \sim 700$ MeV. At higher densities more exotic phases can be reached, e.g. states in very dense neutron stars. In this figure the chemical freeze-out conditions for RHIC, SPS and AGS are indicated as well. The LHC will contribute to measurements at low μ_B, but very high temperatures. The blue arrow illustrates how matter is supposed to have evolved after the Big Bang and before chemical freeze-out at LHC.

energies of $\sqrt{s_{\mathrm{NN}}} = 4.6$ and 17.2 GeV per colliding nucleon pair. Figure 2.3 shows that at the SPS at least an intermediate state between the hadron gas and the quark-gluon plasma had been reached already. Continuing with this research, the Relativistic Heavy Ion Collider (RHIC) was built at BNL, which reached $\sqrt{s_{\mathrm{NN}}} = 200$ GeV per nucleon pair. The results from RHIC give very clear indications for the creation of a quark-gluon plasma. The LHC at CERN provides energies that are up to a factor 30 larger than RHIC energies. The fireball is then expected to contain tens of thousands of gluons and quarks and should exceed the critical temperature for the phase transition several times.

To measure signatures of the QGP, one first has to define event classes for heavy-ion collisions. One of the criteria to define such classes is the collision *centrality*: an event selection related to the *impact parameter b* (the distance between the colliding nuclei perpendicular to the beam axis). However, this parameter is not directly measurable, but it can be determined via multiplicity measurements and model fits to these distributions. In very central events (e.g. $0-5\%$ of the nuclear inelastic cross-section) two ions collide head-on and the QGP is expected to be formed. Peripheral events (e.g. $> 70\%$ centrality), on the other hand, should behave like a superposition of pp collisions. Quantitative estimates of the collision centrality are given by the number of participating nucleons N_{part}, binary nucleon-nucleon collisions N_{coll} or spectators $N_{spec} = 2A - N_{part}$ (where A is the mass number of the initial nuclei). These quantities can be related to the impact parameter via Glauber Model calculations [35] . For instance, the mean number of collisions $\langle N_{coll} \rangle$ can be derived from the nuclear overlap function T_{AA} and the inelastic cross section of nucleon nucleon collisions σ_{NN}^{inel}:

$$\langle N_{coll} \rangle = \langle T_{AA} \rangle \, \sigma_{NN}^{inel} \tag{2.5}$$

2.2.2. Signatures of the Quark-Gluon Plasma

The equilibrium state of the QGP cannot be observed directly in heavy-ion collisions, as it has a lifetime of the order of 10^{-23}s [32]. However, several distinctive signatures can be observed in the experiment, a selection of these is given here [32, 34, 36, 37].

Global Event Properties

By investigating the characteristics of the majority of the particles at low momentum (p_T below a few GeV/c), often referred to as "soft particles", we can access the global event properties, which allow insights into the state and dynamical evolution of the bulk matter created in heavy-ion collisions. These global event properties include multiplicity distributions, yields and transverse-momentum spectra of unidentified and identified particles.

Multiplicity Distributions
The basic global observable, which can be measured within days after the first collision as it needs just a small amount of statistics, is the average multiplicity of charged particles per unit (pseudo)rapidity dN_{ch}/dy ($dN_{ch}/d\eta$). During the design phase of the LHC the predictions for the particle density ranged from 1000 to above 8000 particles per unit in rapidity, due to the large extrapolation which was necessary from Sulphur beams at $\sqrt{s} = 20$ GeV to Pb–Pb beams at $\sqrt{s_{NN}} = 5.5$ TeV at the LHC. The uncertainties of the predictions were reduced by including the measured data from RHIC to $dN_{ch}/d\eta = 1500\text{-}4000$ [38]. The final value, measured by the three LHC experiments taking part in the heavy-ion program, in very central Pb–Pb collisions (0-5%) is $dN_{ch}/d\eta \approx 1600$ [37, 39–41]. The evolution of $dN_{ch}/d\eta$ [10] versus the center-of-mass energy is shown in Figure 2.4.
The average particle density can be related to a rough estimate of the initial energy density ϵ by the Bjorken formula [42]

$$\epsilon \geq \frac{dE_T/d\eta}{\tau_0 \pi R^2} = 3/2\langle E_T/N\rangle \frac{dN_{ch}/d\eta}{\tau_0 \pi R^2} \tag{2.8}$$

where τ_0 is the formation time of the system, R is the nuclear radius and $E_T/N \approx 1$ GeV is the transverse energy per emitted particle. The value for $dN_{ch}/d\eta$ measured by the LHC experiments therefore leads (at $\tau_0 = 1$ fm/c) to an initial energy density of about 15 GeV/fm^3 [43], which is roughly three times higher than at top RHIC energy [44–47].

Identified Particle Spectra
The production of particles is a non-perturbative process, which cannot be calculated directly from first principles in QCD, therefore the particle spectra and ratios in event generators are adjusted to the data of pp and e$^+$e$^-$ collisions using a large number of parameters. The low-momentum spectra in heavy-ion collisions, on the other hand, can be described by statistical/thermal [48–50] and hydrodynamical models [38, 51, 52]. In these models the particle composition is determined during the hadronization or close to the QGP phase boundary

---

[10]The rapidity y of a particle is defined as

$$y = \frac{1}{2}\ln\left(\frac{E + p_z}{E - p_z}\right), \tag{2.6}$$

where E is the energy of the particle and p_z the longitudinal momentum relative to the beam axis. In high energy collisions the rapidity is often replaced by the pseudo-rapidity η in the limit, where $p \gg m$:

$$\eta = -\ln\left[\tan\left(\frac{\theta}{2}\right)\right] = \frac{1}{2}\ln\left(\frac{|\vec{p}| + p_z}{\vec{p} - p_z}\right) \approx y, \tag{2.7}$$

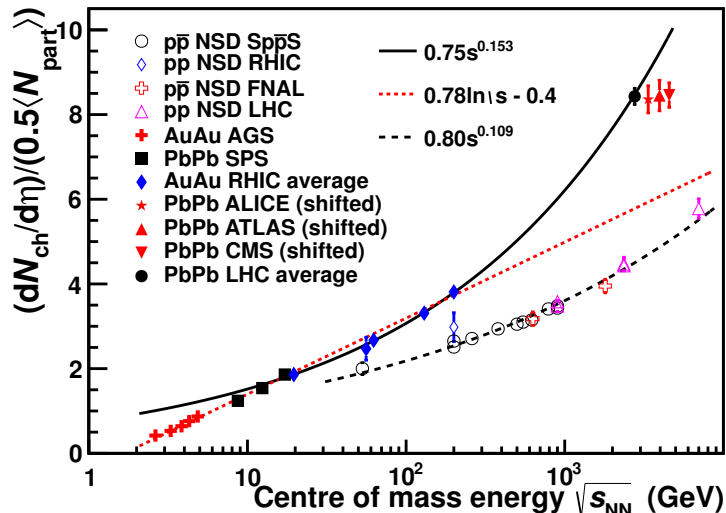where θ is the polar angle relative to the beam axis.

Figure 2.4.: Charged particle pseudo-rapidity density per participant pair as a function of $\sqrt{s_{NN}}$ for central A+A and pp collisions [37].

("chemical freeze-out"), whereas the measured spectra reflect the conditions later in the collision, during the "kinematic freeze-out" [37].

In pp collisions the particle production at low p_T can be described by an exponentially decreasing function ($p_T <$ few GeV/c), while at high p_T it follows a power-law, reflecting the hard QCD scattering and fragmentation. In heavy-ion collisions, on the other hand, there seems to be an ordered motion amongst the emitted hadrons in the soft part of the momentum spectrum [53, 54], which is referred to as collective flow. In contrast to pp collisions the particles do not follow a random thermal motion anymore but a strong correlation between the position of a particle and its transverse momentum can be observed. This flow arises in a strongly interacting medium in the presence of local pressure gradients [37]. As the flow pattern depends on the initial conditions of the collisions, it is classified in terms of the azimuthal angle φ with respect to the reaction plane. The uniform (i.e. φ-independent) component is called *radial flow*. The radial flow can be extracted by fitting the transverse-momentum spectra with a "blastwave" fit [55]; however, the fit values need to be taken with caution as they highly depend on the particle types which have been included as well as the momentum range in which they have been fitted.

Preliminary transverse-momentum spectra for identified π^+, K^+, p, Ξ and Ω for central Pb–Pb collisions can be seen in Figure 2.5 [37, 56] compared to a boost-invariant hydrodynamic model with and without rescattering in the hadronic phase [51]. The published results for pions, protons and kaons can be found in [57]. The spectral shape differs significantly from the pp results. For protons, the characteristic mass-dependent blue-shift, generated by the radial flow, leads to a flattening of the spectrum between 0.5 and 1.5 GeV/c and to a harder spectrum at high p_T, leading to p/$\pi \approx 1$ at 3 GeV/c. The hydrodynamical calculations are each normalized to the particle species, to be able to compare the shapes, as the absolute particle yields and ratios are an external input to the hydrodynamical models discussed here. The pure hydrodynamical model (full line) can be improved by the inclusion of final-state rescattering (dashed line), calculated by the URQMD [58, 59] transport code, coming closer to the data due to the higher radial flow. Both models, however, fail to describe the spectral shape above 2 GeV/c for pions, kaons, and protons indicating a progressive decoupling of high-momentum particles from the thermalized bulk [37].

The results of a simultaneous blastwave fit to the available identified-particle transverse-momentum spectra for different centralities are shown in Figure 2.5. It can be seen that the two parameters T_{f_0} (kinetic freeze-out temperature) and $\langle\beta\rangle$ (average radial flow velocity)
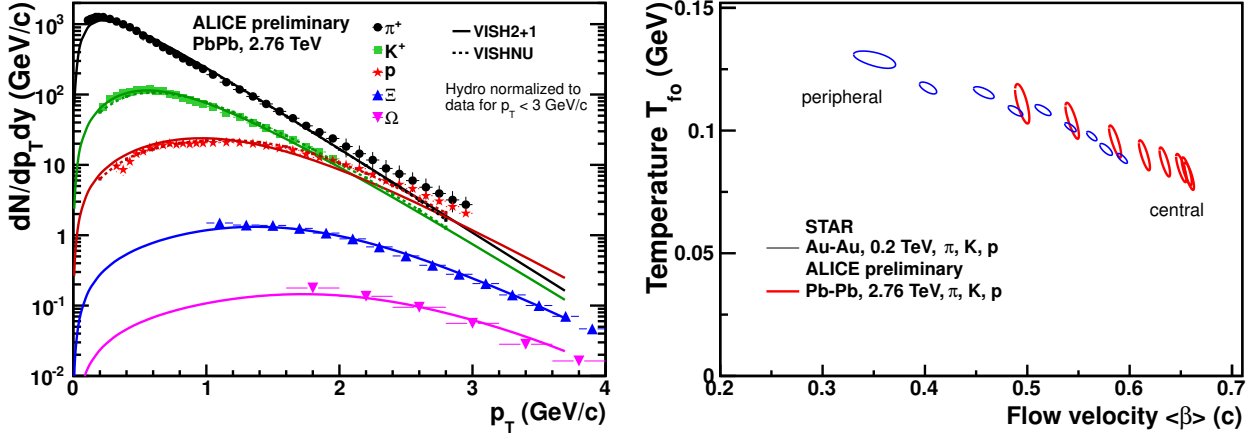
Figure 2.5.: Left: Comparison of the preliminary results on identified transverse-momentum spectra for central Pb–Pb collision at $\sqrt{s_{NN}} = 2.76$ TeV measured by the ALICE collaboration and scaled results from a boost-invariant hydrodynamic model with (VISHNU, dashed lines) and without (VISH2+1, full lines) rescattering in the hadronic phase. Right: Results from a simultaneous "blastwave"-fit to the identified spectra (π K, p) at LHC (Pb–Pb) and RHIC (Au–Au) for different centralities.

are strongly correlated. Moreover, the comparison to a similar fit on the RHIC data [47] shows that the average flow velocity increases ($0.65c$ for central collisions), while the kinetic freeze-out temperature drops below the one extracted from the RHIC results.

Identified Particle Yields

While the transverse-momentum spectra of identified particles contain the information about the collective expansion of the fireball, the integrated yields carry the information about the process of hadron production itself. The particle production in heavy-ion collisions from $\sqrt{s_{NN}} = 2$ GeV to $\sqrt{s_{NN}} = 200$ GeV is well described by the thermal (statistical) hadronization model [48, 49]. This model assumes that all particle species are created in thermal equilibrium. The only free parameters in this model are: the chemical freeze-out temperature T_{ch}, the baryon potential μ_B and the volume V. By including another free parameter, the strangeness suppression factor γ_s to account for the difference to the grand-canonical thermal expression, lighter collision systems can be described as well [60]. In order to extract the four free parameters a thermal fit to the integrated yield at midrapidty dN/dy in central Pb–Pb or pp collisions has been performed, the results are shown in Figure 2.6. While the fit to lower energy data yielded a temperature between $160 - 170$ MeV, with a value of 164 MeV predicted for LHC, the best fit to the data for central Pb–Pb collisions gives a temperature of 152 ± 3 MeV. However, none of the two predictions can describe all particle ratios simultaneously, as the fit (152 MeV) misses the multi-strange ratios and the prediction (164 MeV) fails do describe the p/π and Λ/π. A possible explanation for the significant deviation might be the interactions in the hadronic phase with a particularly large cross-section for antibaryon-baryon annihilation. While γ_s decreases from $0.9 - 1$ in A–A to $0.5 - 0.6$ in pp collisions the temperature range stays constant, ranging from 154 MeV to 170 MeV [61,62]. Again the model cannot reproduce the p/π ratio with 170 MeV regardsless of the volume, while for 154 MeV the multi-strange ratios are underestimated.

Anisotropic Flow

When nuclei collide with non-zero impact parameter the resulting overlap region is not isotropic perpendicular to the beam axis but rather has an almond shape, which changes depending on the centrality. This spatial asymmetry translates into anisotropic pressure gradients in the created medium, leading to an anisotropic expansion of the medium, called *flow* [63]. The flow pattern
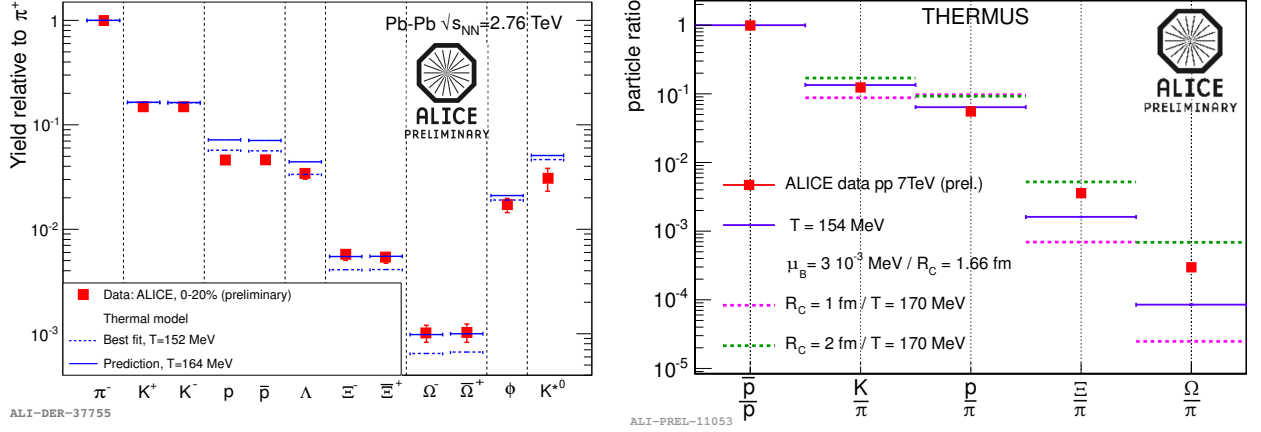
Figure 2.6.: Left: Particle ratios in 0-20% central Pb–Pb collisions at $\sqrt{s_{NN}} = 2.76$ TeV measured by ALICE together with a thermal model prediction [48] (solid line) and the fit to the data (dashed line). Right: Particle Ratios in pp collisions at $\sqrt{s} = 7$ TeV together with THERMUS model predictions (dashed lines) for different R_c [60] and a thermal model fit to the data (solid line).

can be quantified by analyzing the particle production in the transverse plane with respect to the reaction plane, which is defined by the shorter axis of the almond. The asymmetry in this distribution can be decomposed into Fourier components of the density distribution [64]

$$E\frac{\mathrm{d}^3 N}{\mathrm{d}^3 p} = \frac{1}{2\pi}\frac{\mathrm{d}^2 N}{p_{\mathrm{T}} dp_{\mathrm{T}} dy}\left(1 + 2\sum_{n=1}^{\infty}\left(\nu_n \cos\left[n(\varphi - \Psi_n)\right]\right)\right), \qquad (2.9)$$

where E is the energy of the particle, $p_{(T)}$ its (transverse) momentum, y the rapidity, φ the azimuthal angle of the particle and Ψ_n the azimuthal orientation of the reaction plane which does not need to be the same for all ν_n. The Fourier (or flow) coefficients ν_n are p_{T}, y and centrality dependent. The can be calculated using Equation 2.10. Moreover, the reaction plane can be different for each Fourier components.

$$\nu_n(p_{\mathrm{T}}) = \langle\cos\left[n(\varphi - \Psi_n)\right]\rangle. \qquad (2.10)$$

The ν_n provide insights into the hydrodynamic evolution of the plasma and allow estimates on the shear viscosity η/s of the produced medium. The first harmonic ν_1 is called directed flow, which is largest close to beam rapidity [65], but will here not be discussed any further. In the past mainly the largest remaining component ν_2, referred to as elliptic flow, was considered, as it can be directly linked to the almond shape of the initial spatial geometry. However, lately it was realized that initial fluctuations in the distribution of the nucleons in the nuclei lead to a deformation of the almond, inducing higher harmonic flow patterns. Several experimental methods are available for the measurement of the ν_n as well as the symmetry plane angles, a detailed discussion can be found in [53, 54, 66, 67].

Bounds on the shear viscosity can be extracted either by comparing the momentum dependent flow parameters to results of viscous hydrodynamical calculations with different η/s or by fitting the centrality dependence of the p_{T}-integrated value of these flow coefficients. The accuracy of this can be improved by taking into account as many Fourier coefficients as possible. Results from SPS and RHIC [53, 54] showed that the ν_2 increases with increasing $\sqrt{s_{NN}}$, reaching at top RHIC energy a value, which is compatible with the prediction by hydrodynamics for a "perfect fluid" [44–47, 69]. The latest results on the harmonic decomposition of two-particle correlations measured by the ALICE collaboration [68] can be seen in Figure 2.7, similar results where obtained by the other LHC [67, 80–82] and RHIC experiments [83]. The elliptic flow as a function of p_{T} is very similar to the one measured at RHIC; however, the momentum-integrated flow increases by 30%, supporting
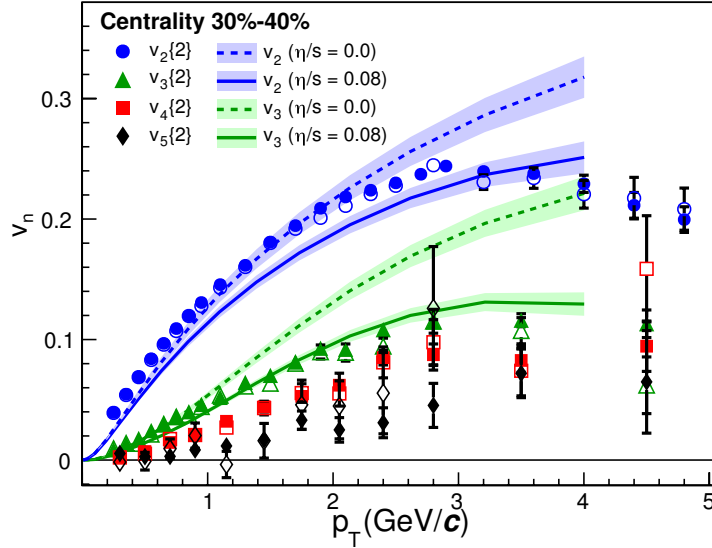
Figure 2.7.: ν_2, ν_3, ν_4, ν_5 as a function of transverse momentum for 30-40% central Pb–Pb events at LHC measured by ALICE compared to hydrodynamical calculations with different shear viscosities (η/s) [68]. The full and open symbols are for $\Delta\eta > 0.2$ and $\Delta\eta > 1.0$, respectively.

the hydrodynamical prediction that the transport properties do not change significantly between RHIC and LHC energies. Moreover, the access to higher harmonics allows to constrain the shear viscosity to $4\pi\eta/s \leq 2$ [52], regardless of the initial conditions. Nevertheless, none of the currently used initial-state models can describe all experimental flow observations simultaneously. Similar conclusions have been drawn from the latest RHIC results [84, 85].

The measurement of identified-particle flow is a most stringent test of the collective-flow interpretation of the azimuthal anisotropies, as the characteristic mass splitting needs to be reproduced. The latest results from ALICE[11] are shown in Figure 2.8 for light particles [70, 71] and in Figure 2.9 for D-mesons [73] together with different hydrodynamical calculations. The mass splitting, which is also seen in ν_3, can be understood taking into account that the collective radial flow does not equalize the particle momenta, but their velocities. Therefore, the azimuthal flow asymmetry for higher-mass particles manifests itself at higher momenta. This effect can be well reproduced by hydrodynamic models up to intermediate transverse momenta. For p_T above 1.5 GeV/c the pion and kaon predictions deviate from the data, while the hydrodynamical curves follow the data for baryons up to 3 GeV/c. This different behavior for mesons and baryons, also seen at RHIC [44–47, 69], has been attributed to quark recombination or coalescence [86–90]. While the RHIC data can be explained by quark scaling, it does not seem to hold at LHC for low momenta. The result of ν_2 for prompt D-mesons is consistent with the unidentified charged particle ν_2 at high p_T, this can be explained by both elliptic flow and the path length dependence of heavy-quark energy loss, however, the latter is the most probable scenario at high p_T.

Suppression of Particle Production and Nuclear Suppression factor (R_{AA})

A key observable for the QGP is the nuclear suppression factor R_{AA}, which quantifies the modification of particle yields due to medium effects. If heavy-ion collisions could be interpreted as a superposition of many binary collisions of the individual nucleons the value for R_{AA} would be equal to unity at high p_T ($p_T \geq 2$ GeV/c). This is called binary scaling. The R_{AA} is defined as

---

[11]A Large Ion Collider Experiment (ALICE)
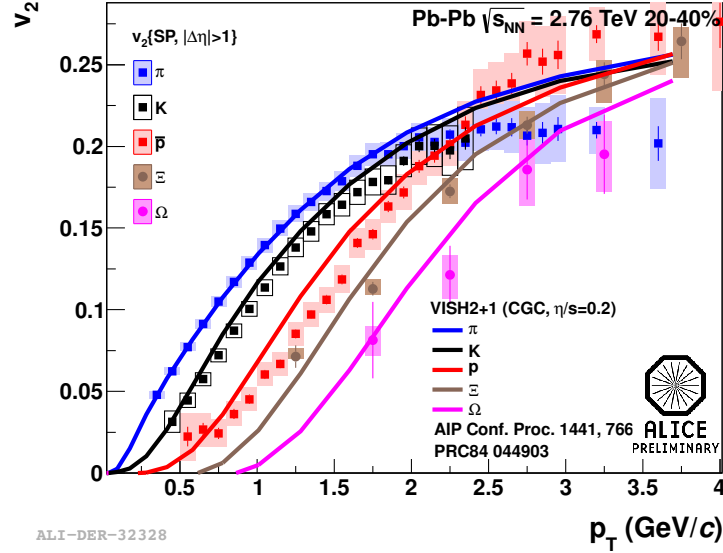
Figure 2.8.: ν_2 as a function of transverse momentum for low-momentum π, K, $\bar{p}$, Ξ and Ω together with the corresponding hydrodynamical calculation [70–72].
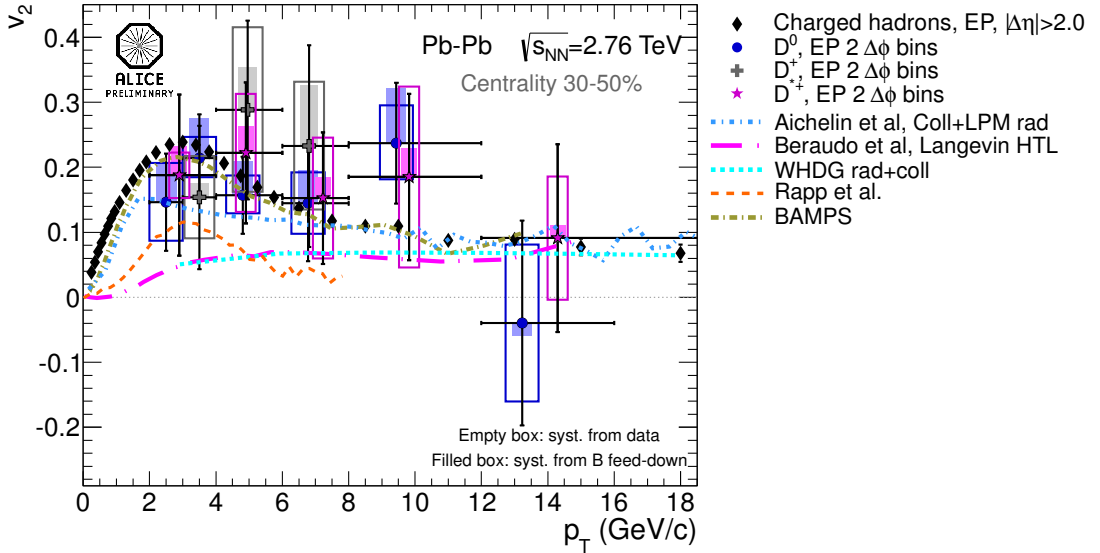
Figure 2.9.: ν_2 as a function of transverse momentum for various D-mesons [73] together with the charged particle ν_2 [68] and theoretical calculations [74–79].

$$R_{AA} = \frac{\frac{1}{N_{evt}^{AA}} d^2 N^{AA}/\mathrm{d}\eta dp_{\mathrm{T}}}{\langle N_{coll}\rangle \frac{1}{N_{evt}^{pp}} d^2 N^{pp}/\mathrm{d}\eta dp_{\mathrm{T}}}, \tag{2.11}$$

where N_{evt}^{xx}, with $xx = AA$ or pp, is the number of events and $\mathrm{d}^2 N^{xx}/\mathrm{d}\eta dp_{\mathrm{T}}$ is the double differential yield of a certain particle type in heavy-ion and pp collisions respectively. $\langle N_{coll}\rangle = \langle T_{AA}\rangle \sigma_{\mathrm{NN}}^{inel}$ was defined in Equation 2.5.

Binary scaling is not only broken due to final state effects occurring in Åcollisions which are related to collisional or radiative energy loss of partons. It can be broken by initial-state effects as well, for instance the Cronin effect or the modification of the nuclear parton density functionss (PDFs) with respect to nucleon PDFs. These effects would be seen both in p–A and Åcollisions and can therefore be probed by p–A collisions, to distinguish them from final state effects.

The Cronin effect [91] is the transverse momentum (k_{T}) increase of the incident partons due to multiple scattering in their path through the nucleus A. The projectile partons acquire an extra

transverse momentum (k_T), which contributes to an increase of the transverse momentum of the produced hadron. This leads to an increase of the R_{pA}, the nuclear suppression factor for proton-nucleus collisions, at low momenta. At high p_T this extra k_T broadening becomes a negligible fraction of the measured p_T and therefore R_{pA} will be unity again.

An additional initial effect is the strong modification of the parton density distributions in nuclei with respect to those in the free nucleon. These nuclear modifications depend on the fraction x of the hadron momentum carried by the parton, the momentum scale Q^2, and the mass number of the nucleus. The PDFs of heavy nuclei can be related to the ones for the proton via:

$$f_i^A(x, Q^2) = R_i(A, x, Q^2) f_i^p(x, Q^2) \tag{2.12}$$

where R_i is a functional representation of the modification with respect to the parton distribution for the proton f_i^p. These functions vary for valence quarks, sea quarks and gluons [92]. Depending on the collision energy, a different region of x and Q^2 is probed and one speaks of shadowing or anti-shadowing, a depletion or enhancement respectively of the parton densities with respect to the free parton. These effects lead to a different shape of the R_{pA} as well as of the R_{AA} at different energies, not necessarily allowing any statement on the existence of final state effects.

The final state effects, seen in heavy-ion collisions, can be described by two main contributions: the energy loss due to scattering on other partons, proportional to s^{-2} (center-of-mass energy), and the radiation of gluons. The first one is called collisional energy loss and dominates at low energies, whereas the latter represents gluon bremsstrahlung, dominating at high energies. In both cases the reduction of the parton energy translates into a reduction in the average momentum of the produced hadron and therefore into a reduction of the yield at high p_T with respect to pp-collisions. Owing to the power-law shape of the initial p_T spectrum for $p_T > 3$ GeV/c, a modest reduction in the parton energy leads to a significant decrease in the hadron yield. A popular model for describing the radiative energy loss due to gluon radiation is the BDMPS approach [93, 94]. In this model the mean energy loss depends on the Casimir factor C_R, the length L of the particle traveling through the medium and the transport coefficient $\hat{q}$ in the following way:

$$\langle \Delta E \rangle \propto \alpha_s\, C_r\, \hat{q}\, L^2 \tag{2.13}$$

The dependence on L^2 takes into account the probability of emitting a bremsstrahlung gluon and the fact that this might interact with the medium as well, however, the power of L might vary between different models. The Casimir factor introduces different weightings for the interaction vertices: 3 for a gluon-gluon interaction and 4/3 for a quark-gluon interaction. Finally, the transport coefficient is related to the medium properties and the gluon density and it allows an indirect measurement of the medium energy density.

In order to be able to quantify the influence of the QGP on the measured particles, the disentanglement of the contribution from the mentioned initial-state effects to the final state effects is required. This might be realized by a measurement of p–A collisions at the same energy as the A–A collisions in order to measure the initial-state effects directly. The first results on the charged hadron R_{pA} from the LHC for p–Pb collisions at $\sqrt{s_{NN}} = 5.02$ TeV are shown in the left plot of Figure 2.10. They were obtained using the data collected during a short p–A test run in 2012. A longer p–A run is planned at the beginning of 2013, which allow to measure the R_{pA} for identified particles as well. The R_{pA} of unidentified charged hadrons shows no suppression for high momenta ($p_T > 2$ GeV/c) can be seen in the data, which indicates that the strong suppression in Pb–Pb collisions at the LHC is not due to intial-state effects.

The nuclear suppression factor is a general quantity and can be built for all particle types, giving access to different properties of the medium. The fastest measurement which will be available for new collision energies is the charged hadron R_{AA} since it does not require particle ID and only the p_T reach is statistics limited. The ALICE collaboration was the first of the LHC experiments to publish this measurement after only few weeks of data taking in 2010 for Pb–Pb collisions at
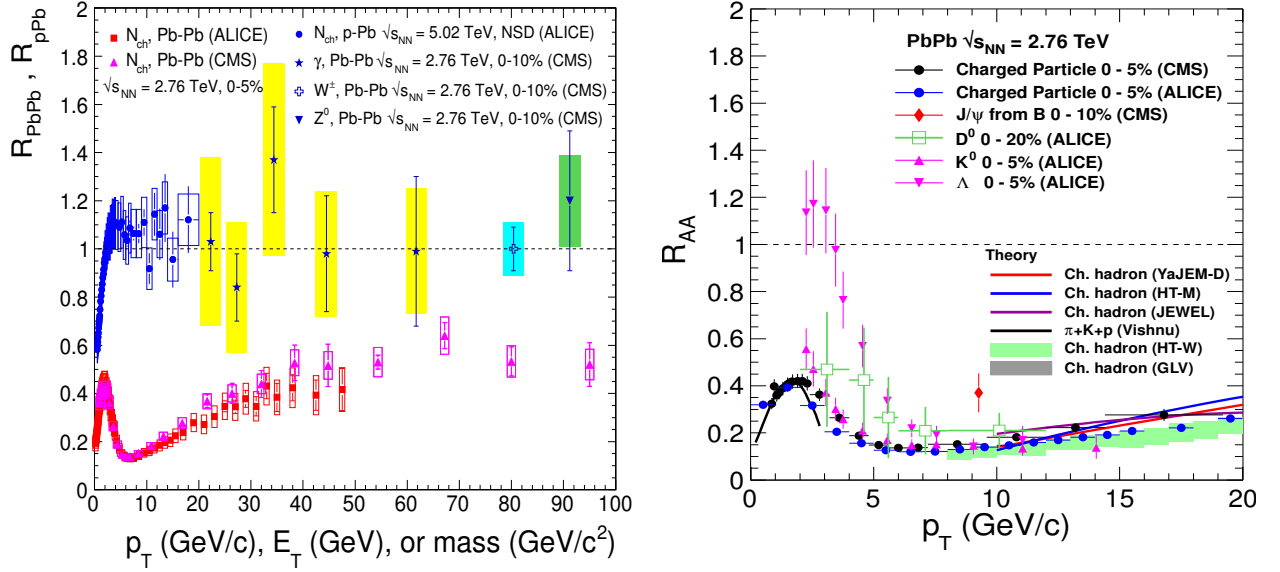
Figure 2.10.: Left: Comparison of the charged hadron nuclear modification factor R_{AA} (R_{pA}) for Pb–Pb collisions at $\sqrt{s_{NN}} = 2.76$ TeV [95, 96] and p–Pb collisions at $\sqrt{s_{NN}} = 5.02$ TeV [97]. In addition the nuclear modification factors for isolated photons [98, 99], the Z^0 [100] and the $W^\pm$ [101, 102] are shown. Plot taken from [103]. Right: Nuclear modification factor R_{AA} as a function of p_T for a variety of particle species together with theoretical predictions [104–107]. The error bars of the experimental points correspond to the total error (systematic and statistical errors added in quadrature). a) Low momentum ($p_T < 20$ GeV) R_{AA} for unidentified charged particles (blue and black points), J/Ψ from B (red points), D^0-mesons (green rectangles) and strange particles (blue triangles). Plot taken from [37].

$\sqrt{s_{NN}} = 2.76$ TeV [108]. A complication for this measurement was the at that point not measured pp-reference spectrum. Thus the pp-reference was built with an interpolated spectrum based on the measured spectra of ALICE at 0.9 and 7 TeV and the assumption that the scaling follows a power-law. Since then the pp reference spectrum at $\sqrt{s} = 2.76$ TeV has been measured and an updated result can be found in [95]. The rise in the R_{AA} for most central collisions for $p_T > 7$ GeV/c was never observed in such a significant way, although there were indications from the π^0 data measured by PHENIX [109]. A compilation of the R_{AA} and R_{pA} results from LHC is shown in the left plot of Figure 2.10. The results from the two LHC experiments agree within the statistical and systematic errors up to 50 GeV/c. The CMS measurement extends the p_T reach up to 100 GeV/c with charged hadrons and 300 GeV/c with jets, giving a better chance to discriminate between the different theoretical predictions. The R_{AA} is lower by a factor 2 for $\sqrt{s_{NN}} = 2.76$ TeV than for the measured charged-particle spectrum at RHIC, though the shape agrees.

In the QGP the strong force dominates over the electro-weak interaction, due to the smaller coupling strength of the electo-weak interaction. Therefore, any particle traversing it will mainly experience the strong force. Direct photons or the gauge bosons, however, will not be influenced by the plasma at first order, therefore their yields should scale with the number of collisions. These particles provide an ideal control probe and should show an R_{AA} of unity at high p_T. This measurement was performed at RHIC and yielded the expected result [110], although latest results show a slight deviation from unity [111] for the highest p_T bins. The first attempt to measure the control probes at LHC was presented by the CMS collaboration [98–100] and is shown in the left plot of Figure 2.10. The measurement agrees with unity within the error bars. This has been the first measurement of the Z^0 in Pb–Pb collisions and its suppression factor [100]. Additional measurements exist for the W-boson R_{AA} [101, 102], which are in agreement with the other control probes. Lately an even more differential study of the Z boson production in heavy-ion collisions has been presented by the ATLAS collaboration [112].

Although the charged-particle spectra allow to distinguish between different models, identified par-

ticles and jets need to be measured in addition as they probe different properties of the medium. They give access to the energy density and the quark content or the quark multiplicity. Measurements exist for identified π, K^0, Λ [113, 114], D-mesons [114], jets [115], J/Ψ [116] and Υ [117]. Some of the first measurements on identified particle R_{AA} are shown in right plot of Figure 2.10. Surprisingly, even the heavier quarks, as shown by the R_{AA} of prompt D mesons and non prompt J/Ψ, are almost as strongly suppressed as the inclusive charged particles. This seems contrary to the prediction that gluons, which are the main source of inclusive charged particles at LHC, should suffer twice as much energy loss as light quarks. Moreover, their energy loss should be less due to the mass dependence of radiation ("dead-cone" effect [118]). From the data it seems that the mass dependence is weaker than expected from radiative energy loss, and above $p_T \approx 8$ GeV/c the suppression is universal for all particles. However, more precise data on identified particles are needed to confirm this observation.

Photon Signals

The main advantage of photons as probes for the quark-gluon plasma is, that they carry the information about the conditions of their production outside of the plasma as they can only interact electromagnetically. Therefore, they will be affected much less by the quark-gluon plasma and the following stages of the collision than hadronic probes. That is why especially direct-photons can be used as probes for the PDF and for measurements of jet quenching. In some cases the other jet arising from the collision will be a hadronic jet losing energy in the medium, whereas the γ energy will remain unchanged. This might lead to better understanding of the properties of the medium. This has already been discussed in [119].

Photon production in heavy-ion collisions occurs at different stages after the collision. Photons originating from nucleon-nucleon collision can be separated into 3 categories: Direct photons, fragmentation photons and photons, which are produced by decays subsequent to the collision. In typical $2 \rightarrow 2$ processes ($q + g \rightarrow q + \gamma$, $\bar{q} + q \rightarrow g + \gamma$) direct and fragmentation photons are summarized under the name prompt photons. For A–A collisions, however, there are additional sources of photons: the medium contributions which are discussed in detail in [120]. These contributions include:

- **Jet-Photon Conversion**
  These photons are produced when a jet crossing the hot medium undergoes annihilation or QCD Compton scattering. Here the p_T distribution is similar to the hard processes. But the jet-photon conversions will be dominated by the gluon-channel (Compton scattering), as the gluon density should be higher than the quark density in the plasma. Moreover, high-p_T photons are emitted preferentially early during the QGP phase, when the temperature is largest.

- **Bremsstrahlung Photons**
  Hard partons in the medium produce photons by bremsstrahlung while scattering in the medium. Whereas the rate of the production of these photons is larger than the one from jet-conversions, they normally carry only a fraction of the initial jet energy. Therefore, the jet conversions turned out to dominate over the bremsstrahlung photons if one folds them with the steeply falling jet spectrum.

- **Thermal Photons**
  They are emitted from a thermally equilibrated phase. In heavy-ion collision they come from the QGP phase and from the hot hadron phase following the QGP. The photon production rate and the shape of the transverse momentum distribution depend on the temperature at which the photon was emitted. Therefore, photons produced in the quark-gluon plasma carry information on the thermodynamical state of the medium at the moment of their production.
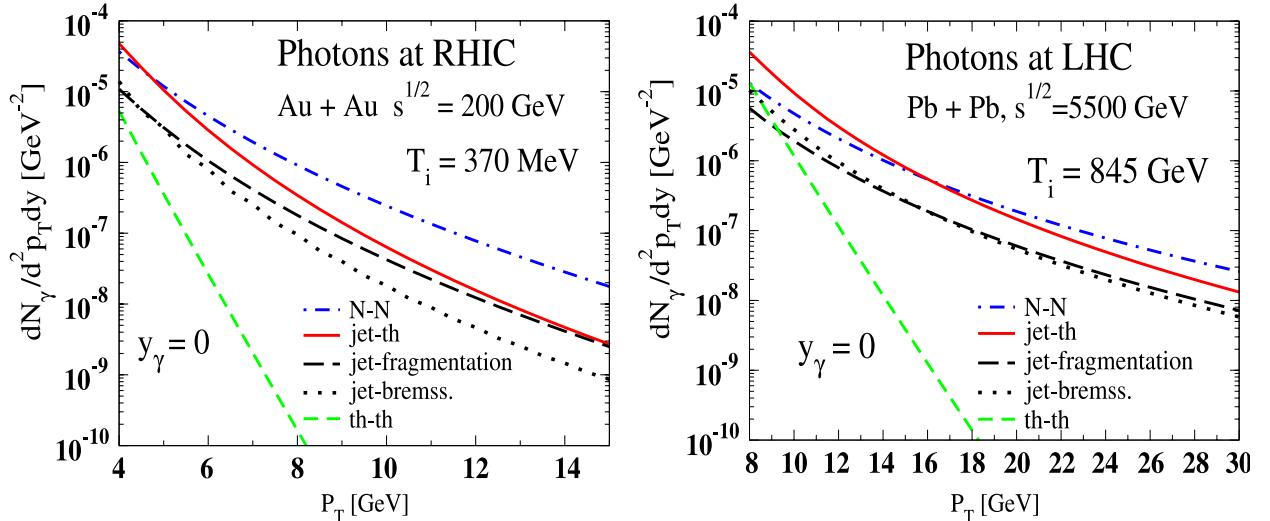
Figure 2.11.: Sources of high p_T photons at midrapidity in central Au-Au collisions at RHIC (left) and for Pb-Pb collisions at LHC (right). The different contributions are (red solid line) Jet-photon conversions in the plasma, (black dotted line) bremsstrahlung from jets in the plasma; (green dashed line) thermal induced production of photons, (black dashed line) fragmentation of jets outside the plasma, (blue dot-dashed line) direct contribution from primordial hard scattering [120].

All these sources and their particular contributions for different transverse momenta are shown in Figure 2.11 for RHIC energies and for LHC energies. It can be clearly seen, that at the LHC the jet-photon conversion will dominate the direct-photon spectrum for p_T larger than 4 GeV/c up to around 16 GeV and afterwards the direct contribution from the primordial hard scattering is dominant. Furthermore, it is shown that at RHIC nearly everywhere (for $p_T > 4$ GeV/c) the hard direct-photon component is the leading part. Photon production via jet bremsstrahlung in the plasma turns out to be weak, it is approximately a factor 3 below the jet-photon conversion contribution. As well as thermal induced production is far beyond all other contribution in intensity. However, this contribution is important at low p_T, see figure 10 from ref [34].

Particularly interesting are the low-momentum thermal and jet photons, as these could give a hint about the temperatures in the plasma. However, in order to obtain the direct-photon spectrum the background from meson decays needs to be subtracted. One of the most promising methods for measuring the thermal photons is the measurement of the direct-photons via the subtraction method in combination with the double ratio method [121]. The direct-photon signal (γ_{direct}) is extracted by subtracting the meson-decay photon spectrum (γ_{decay}), which is dominated by the photons originating from π^0 and η decays, from the inclusive photon spectrum (γ_{inc}), Equation 2.14.

$$\gamma_{\text{direct}} \quad = \quad \gamma_{\text{inc}} - \gamma_{\text{decay}} = \left(1 - \frac{\gamma_{\text{decay}}}{\gamma_{\text{inc}}}\right) \times \gamma_{\text{inc}} \tag{2.14}$$

The photon decay spectrum is obtained by a cocktail simulation, which is based on a yield parametrization of mesons with photon decay branches, with the dominating sources the π^0 ($\sim 80\%$) and the η ($\sim 18\%$). As input for the calculation all available measured neutral meson spectra are used and the unknown meson yields are obtained by m_T-scaling [122]. To reduce the systematic uncertainties, the ratio $\frac{\gamma_{\text{decay}}}{\gamma_{\text{inc}}}$ is calculated as:

$$\frac{\gamma_{\text{inc}}}{\gamma_{\text{decay}}} \quad = \quad \frac{\gamma_{\text{inc}}/\pi^0}{\gamma_{\text{decay}}/\pi^0_{param}} \tag{2.15}$$

By using the same sample of photon candidates to create the meson spectra and the inclusive photon spectra further uncertainties cancel out [121, 123]. The first measurement of the direct-photons at low p_T in Pb–Pb collisions at LHC was presented at Quark Matter 2012 [124] and
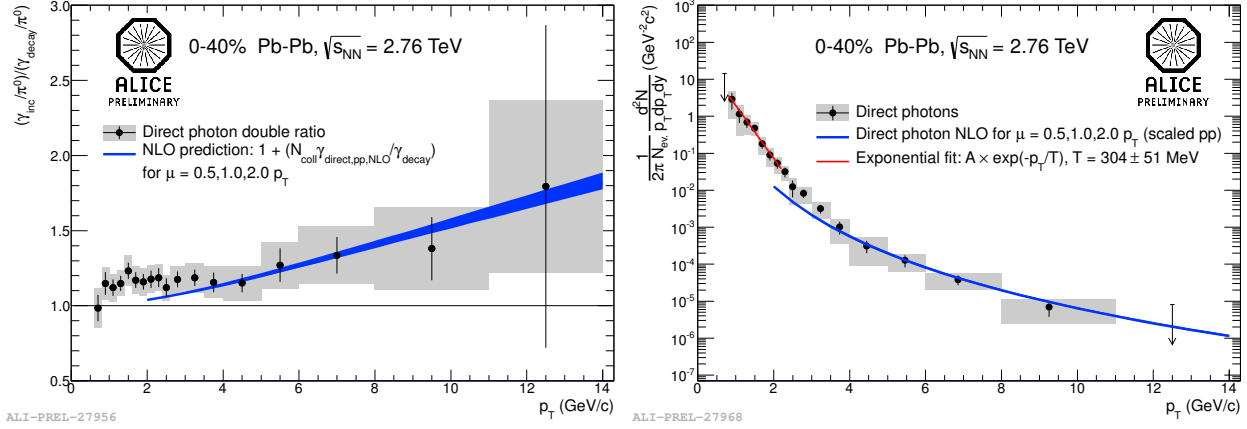
Figure 2.12.: The left plot shows the direct-photon double ratio and the right plot the direct-photon invariant yield in Pb–Pb collisions at $\sqrt{s_{\mathrm{NN}}} = 2.76$ TeV for 0-40% centrality with NLO pQCD predictions, the latter contains an additional exponential fit ($p_{\mathrm{T}} < 2$ GeV/c) to the data [124].

is shown in Fig. Figure 2.12. The result is based on the same photon-reconstruction framework and relies partially on the π^0 transverse-momentum spectra obtained in the analysis, which will be presented in this thesis, and the preceding analysis [125, 126]. In the double ratio for 0-40% central Pb–Pb events a clear excess above unity is seen for low momenta ($p_{\mathrm{T}} < 2$ GeV/c), at high momentum the ratio follows the expectations from pQCD NLO predictions [127]. The resulting direct-photon spectrum was fitted with an exponential function ($f(p_{\mathrm{T}}) = A\exp(-p_{\mathrm{T}}/T)$) from 0.8 GeV/$c$ to 2.2 GeV/c. The inverse slope parameter is extracted as $T_{LHC} = 304 \pm 51^{\mathrm{syst+stat}}$ MeV. A similar analysis at RHIC yielded $T_{RHIC} = 221 \pm 19^{\mathrm{stat}} \pm 19^{\mathrm{syst}}$ MeV for 0-20% central Au-Au-collisions at $\sqrt{s_{\mathrm{NN}}} = 200$ GeV [128, 129], which indicated by comparison to a hydrodynamic calculation an initial temperature of the QGP that exceeds the critical temperature T_c.

2.3. Interactions of Photons with Matter

Photons can be described as electromagnetic radiation with zero mass, zero charge and a velocity that is always c, the speed of light. As they are electrically neutral, they do not steadily lose energy via Coulombic interactions with atomic electrons. Instead, they travel a considerable distance before undergoing an interaction, they are far more penetrating than charged particles. All interactions of photons with matter lead at least to partial if not total transfer of the photon energy to an electron. Therefore, photons either suddenly disappear or scatter by a significant angle with high energy loss. The three mechanisms of photon interactions with matter are the *photoelectric effect*, *Compton scattering* and *pair production*. The relative strength of the different processes in Carbon and Lead are shown in Figure 2.13. The analysis presented in this thesis concentrates on photons with a transverse momentum larger than 100 MeV/c, therefore the photoelectric effect and Compton scattering will not be discussed any further; a detailed discussion can be found in [119, 130–132].

Pair creation
If an energetic photon enters matter and its energy is higher than 1.02 MeV it may interact with the matter via pair creation, also-called photon conversion. In this process, an electron-positron pair is created from the energy of the incoming photon in the electromagnetic field of a nucleus, hence the threshold energy for pair creation. Momentum and energy could not be conserved without the nucleus carrying away a part of the momentum and the energy. As just a small fraction of the kinetic energy will be transferred to the nucleus, its state will remain the same and it has a rather
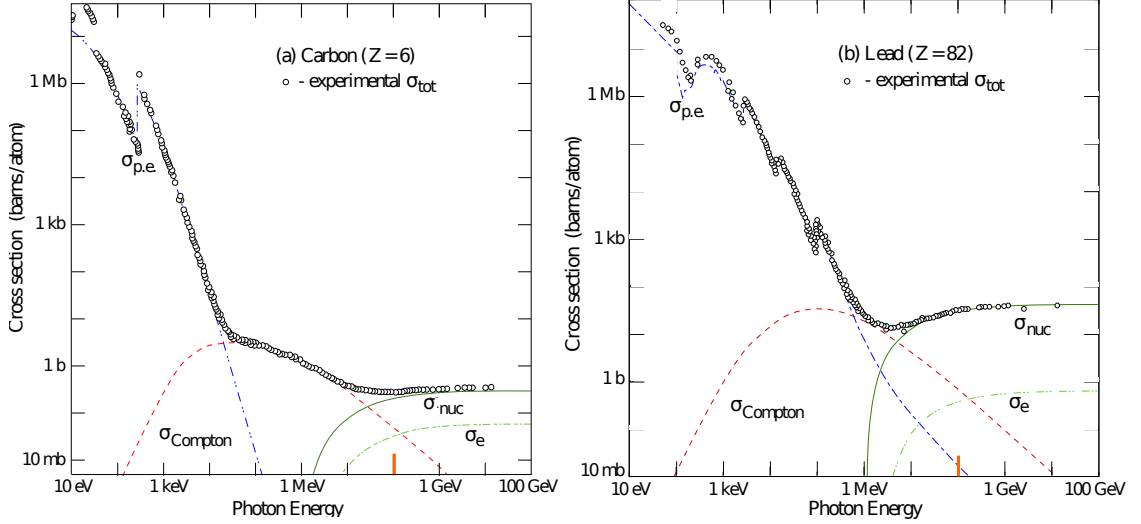
Figure 2.13.: Photon cross section as a function of energy in a) carbon and b) lead. The different cross sections shown are:

$\sigma_{p.e.}$ = Photoelectric effect (blue dashed-dotted line)

$\sigma_{Compton}$ = Compton scattering of an electron (red dashed line)

σ_{nuc} = Pair production in nuclear field (green solid)

σ_e = Pair production in electron field (green dashed-dotted line)

The approximate starting point for the analysis presented in this analysis is marked with an orange vertical line at 100 MeV. Plot adapted from [130].

passive role. The angle between the conversion electron and positron for high-momentum photons is very small due to momentum conservation.

As the pair creation dominates with increasing energy, an approximation for the differential cross section can be introduced in the complete screening limit, which is valid for high energies. The differential cross section is then given by:

$$\frac{\mathrm{d}\sigma}{\mathrm{d}x} = \frac{A}{X_0 N_A}\left[1 - \frac{4}{3}x(1-x)\right] \tag{2.16}$$

where A is the atomic number of the material the photon is transversing, N_A the Avogadro constant and X_0 the total radiation length. In addition, $x = E/k$ is the fractional energy transfer to the pair-produced electron (or positron), with k the total energy of the incident photon. Taking this into account the cross section has to be symmetric between x and $1 - x$.

Integrating the differential cross section (Equation 2.16) leads to the high-energy limit for the total e^+e^- pair-production cross section:

$$\sigma_{pair} = \frac{7}{9}\frac{AN_A}{X_0} \tag{2.17}$$

The radiation length is the mean distance over which a high-energetic electron loses all but $1/e$ of its energy due to bremsstrahlung, and $7/9$ of the mean free path for pair production by a high energy photon. The radiation length can be approximated by:

$$X_0 = \frac{716.4 \text{ g cm}^2 \ A}{Z(Z+1)\ln 287/\sqrt{Z}} \tag{2.18}$$

where Z is the atomic number and A is the mass number. The radiation length in mixtures or compounds may be approximated by:

$$\frac{1}{X_0} = \sum_{j=1}^{n} w_j/X_j \tag{2.19}$$

21

here w_j and x_j are the fraction by weight and radiation length of the jth element. The probability that a photon converts after traversing a material of thickness x in the high momentum limit is given by:

$$P_{\text{conv}} = 1 - \exp\left(-\frac{7}{9}\frac{x}{X_0}\right) \qquad (2.20)$$

Moreover, this probability can be calculated in detector simulations like GEANT [133] by the ratio:

$$P_{\text{conv}} = \frac{N_{\text{conv}\gamma}}{N_{\text{all}\gamma}} \qquad (2.21)$$

The description of the detector in GEANT simulations has to be accurate in terms of the geometry, and of the chemical composition of the different materials used, in order to obtain results that are compatible with those of data.

3. Experimental Setup

This chapter will give an overview of the experimental setup used for in this analysis. The first section is dedicated to the accelerator system. Afterwards, the ALICE (A Large Ion Collider Experiment) detector system and its sub-detectors will be discussed in detail, including triggering, track and vertex reconstruction.

3.1. The Large Hadron Collider

The LHC is located at the CERN, near Geneva, Switzerland. At present it is the largest and most powerful man-made particle accelerator with a circumference of 27 km. It is designed to collide protons up to a center-of-mass energy of $\sqrt{s} = 14$ TeV or heavy ions (eg. Pb, Ar, Si) up to an energy of $\sqrt{s_{\mathrm{NN}}} = 5.5$ TeV per nucleon-nucleon pair, respectively. The design luminosity of the LHC is $\mathcal{L} = 10^{34}$ cm^{-2}s^{-1} for colliding protons and $\mathcal{L} = 10^{27}$ cm^{-2}s^{-1} for lead ions [134]. These high center-of-mass energies and luminosities allow new insights into the structure of matter. In particular, the LHC will help to extend the knowledge about the generation of mass through spontaneous symmetry breaking in the electroweak and strong interaction and its manifestation, the Higgs boson, which is the last missing piece of the standard model. Furthermore, the experiments at the LHC search for new physics beyond the standard model, as the standard model neither allows the desired unification of the four fundamental forces nor explains the three-folded structure of lepton and quark families or the existence of dark matter in the universe.

The LHC has been constructed in the existing tunnel of the LEP which was operating until 2000. In order to reach such high beam energies in the LHC it is necessary to accelerate the particles in several steps, therefore the previous accelerators at CERN are used as preaccelerators for the LHC. A schematic overview of the CERN accelerator complex is given in Figure 3.1.

The LHC consists of 4 major components: (i) dipole magnets bending the beam on its orbit, (ii) quadrupole magnets focusing the beams, (iii) acceleration cavities increasing the beam energy and (iv) two beam pipes with an ultra-high vacuum containing the two beams. In order to keep the beam on its track at the maximum energy a magnetic field of 8.3 T is needed. This field is provided by superconducting magnets which are filled with liquid helium ($T = 4.5$ K) and then cooled to 1.9 K to reach the super-fluid state of helium. To reduce the number of interactions of the beam with the environment, an ultra-high vacuum is kept in the beam pipes reaching a quality of $\sim 10^{-17}$ bar on a total volume of 150 m^3 [134]. The start of the LHC in 2008 was followed by a major incident, destroying the magnets of one sector. Therefore, these magnets had to be exchanged and the full system needed to be reevaluated. During this process the LHC crew discovered that some of the connections within the magnets had developed resistance leading to a localized heating resulting in a quenching of the magnet. Therefore, they decided not to ramp up the LHC to its full energy before the long shut down in 2013/2014 during which the magnets will be modified. Since the restart of the LHC in 2009 no major incident happened and the machine keeps breaking one record after another. In 2009 LHC started delivering collisions at a center-of-mass energy of $\sqrt{s} = 0.9$ TeV, corresponding to the injection energy. After the winter shutdown in 2009 the first collisions at $\sqrt{s} = 7$ TeV were recorded in March 2010.The LHC has eight possible interactions points, four of them are equipped with large detector systems as shown in Figure 3.1. ALICE is the only dedicated heavy-ion experiment, it will be described in the
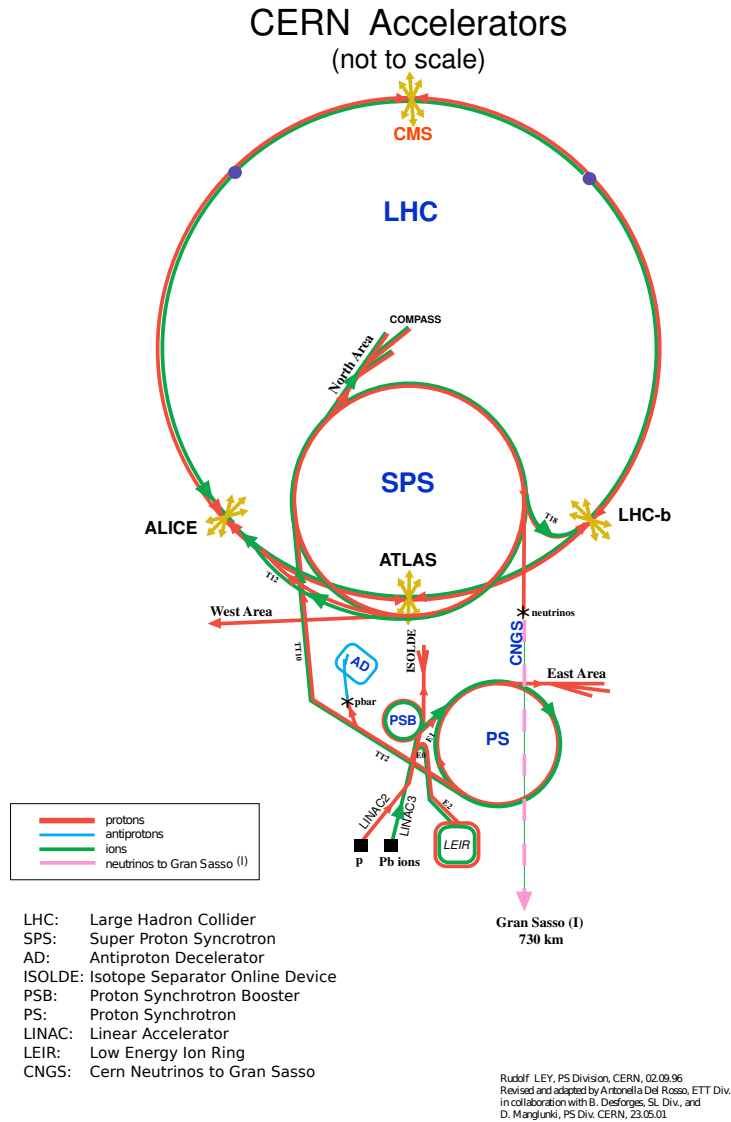
Figure 3.1.: Overview of the CERN accelerator complex [135].

next section. The detectors systems of ATLAS (A Toroidal LHC Apparatus) and CMS (Compact Muon Solenoid experiment) where designed primarily for pp collisions as complementary high-energy general-purpose detectors. Both collaborations focused on the detection of particles with large momenta with the a variety of detector techniques and the detection of all possible particles originating in the primary collision. Therefore, they installed silicon detectors, transition radiation detectors, large electromagnetic and hadronic calorimeters, as well as large muon detection arrays, covering the full azimuth and nearly the full pseudo-rapidity range. Their physics programs in proton-proton collisions are focused on finding and exploring the properties of the Higgs boson. First results on a possible Higgs candidate have been presented on the July, 4th 2012 by both collaborations. Furthermore, their proton-proton program includes precision measurements of the Standard Model particles as well as a search for physics beyond the Standard Model, e.g. extra dimensions or super-symmetric (SUSY) particles. Although both detectors have not been optimized for heavy-ion collisions, they contribute extensively to the high transverse momentum (p_T) analysis in Pb–Pb collisions profiting from their large pseudo-rapidity coverage as well as their excellent high-rate capabilities.

The LHC beauty experiment (LHCb) was dedicated to the search for CP-violation in the B-meson system and to carry out precision measurements in the charm and beauty sector. These measure-

THE ALICE DETECTOR

1. ITS
2. FMD, T0, V0
3. TPC
4. TRD
5. TOF
6. HMPID
7. EMCAL
8. PHOS CPV
9. MAGNET
10. ACORDE
11. ABSORBER
12. MUON TRACKING
13. MUON WALL
14. MUON TRIGGER
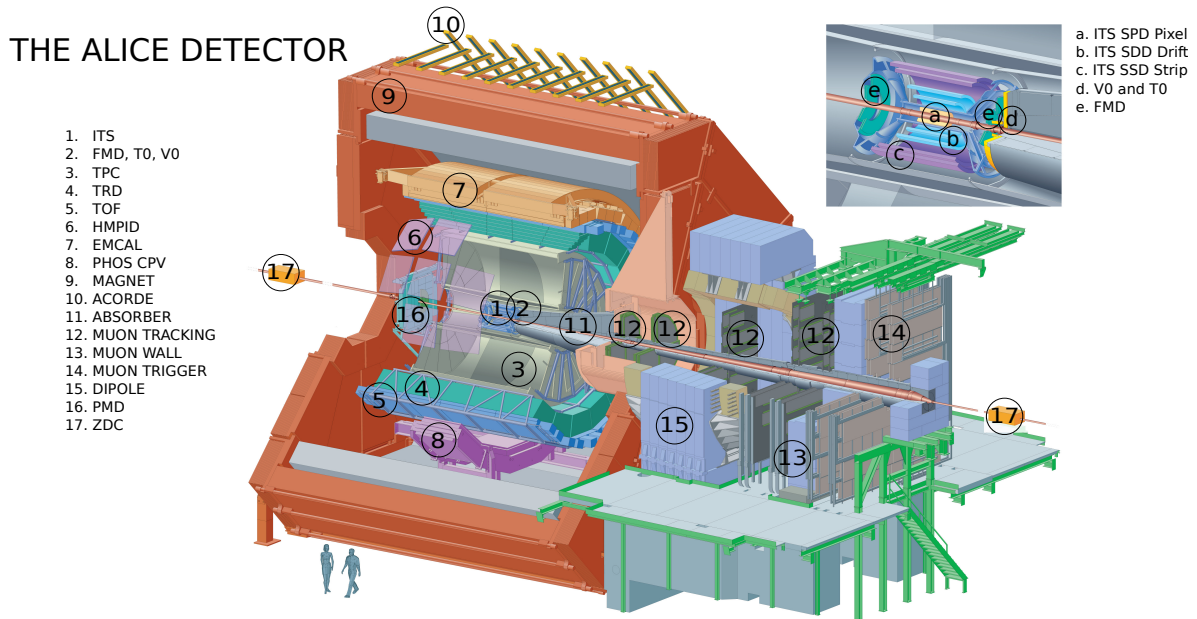15. DIPOLE
16. PMD
17. ZDC

a. ITS SPD Pixel
b. ITS SDD Drift
c. ITS SSD Strip
d. V0 and T0
e. FMD

Figure 3.2.: Layout of the ALICE detector system with an insert zooming into the detectors closest to the beam pipe [136].

ments will help in the understanding of the asymmetric distribution of matter and antimatter in our universe. As the mesons with open and hidden charm and beauty are highly boosted, the detector has been designed as a one-sided forward detector with an excellent primary vertex resolution, to separate the primary vertex from the decay vertex of the B/D-meson, excellent particle identification with Ring Imaging Cherenkov detectors (RICHs), electromagnetic and hadronic calorimeters and tracking in the silicon detectors and muon system. Due to the high occupancy in the detectors the LHCb experiment is not taking part in Pb–Pb runs, however it will participate in the p–A runs.

3.2. A Large Ion Collider Experiment

The ALICE detector system [137] is the general-purpose heavy-ion experiment at the LHC. Therefore, the detectors were designed to handle charged-particle densities up to $\mathrm{d}N/\mathrm{d}y \approx 8000$. We distinguish two main detector regions: the central barrel, measuring hadrons, electrons, positrons and photons, and the forward muon spectrometer. In addition ALICE is equipped with a cosmic ray detector (ALICE cosmic ray detector (ACORDE)) mounted on top of the central barrel. As this thesis deals with photon and light neutral meson physics the muon spectrometer and ACORDE will not be discussed any further.

3.2.1. The Detectors

The ALICE physics program focuses on particle identification down to very low-p_{T} making it unique among the four LHC experiments. Therefore, the central barrel is equipped with tracking and particle identification (PID) detectors capable of reconstructing charged primary particles over a large transverse-momentum range from 100 MeV/c up to 100 GeV/c and at the same time identifying the particle species with all known detector techniques. The central barrel detectors are embedded in a large solenoid magnet inherited from the L3 experiment at LEP, providing
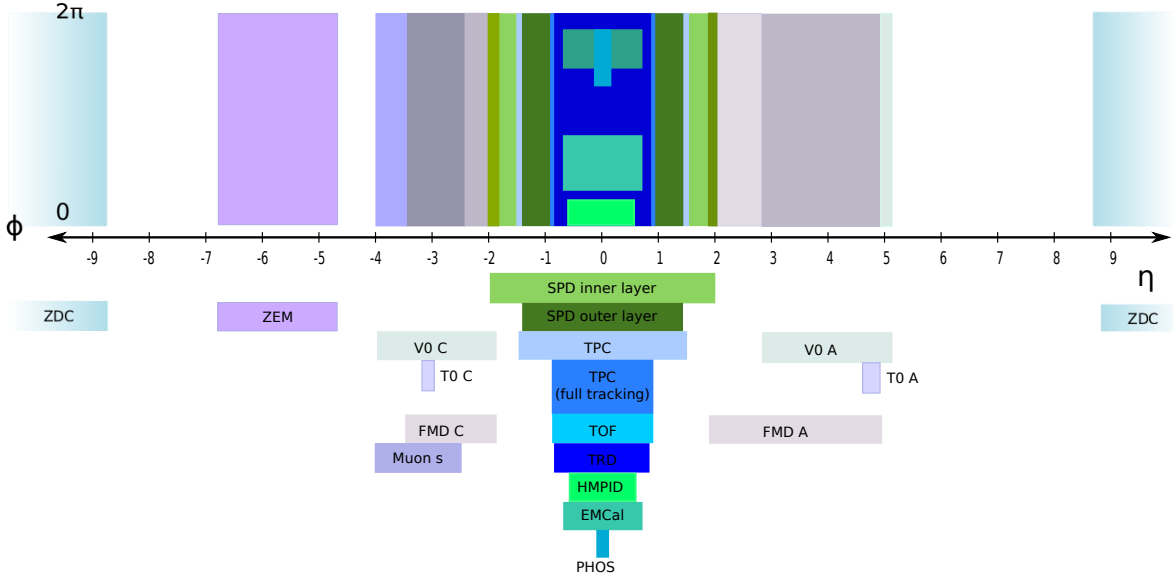
Figure 3.3.: Pseudo-rapidity and azimuthal coverage of the ALICE detector system.

a magnetic field of up to 0.5 T. From inside out it contains an Inner Tracking System (ITS), a cylindrical Time Projection Chamber (TPC), three particle identification detectors: a Transition Radiation Detector (TRD), a Time-Of-Flight detector (TOF) and a High Momentum Particle Identification Detector (HMPID), as shown in figure Figure 3.2. Moreover, two electromagnetic calorimeters are embedded in the magnetic field of the L3 magnet, Photon Spectrometer (PHOS) and Electromagnetic Calorimeter (EMCal). A brief description of the performance and the detector techniques is given in the following.

Detector	$\pm\eta$	φ	$\sigma_{r\varphi}$ [μm]	σ_z [μm]	Specific Resolution
ITS					
SPD 1(2)	± 2 (± 1.4)	$0° < \varphi < 360°$	12	100	
SDD	± 0.9	$0° < \varphi < 360°$	35	25	
SSD	± 0.97	$0° < \varphi < 360°$	20	830	$\sigma_{\mathrm{d}E/\mathrm{d}x} = 2.0\%$ at low p_{T}
TPC					
$r \simeq 1.4$ m	± 1.5	$0° < \varphi < 360°$	1100	1250	$\sigma_{\mathrm{d}E/\mathrm{d}x} = 5.0\%$ (for 160 clusters)
$r \simeq 2.8$ m	± 0.9	$0° < \varphi < 360°$	800	1100	
TRD	± 0.84	$0° < \varphi < 360°$	400	2	$\sigma_p/p = 2.5\% \oplus \frac{0.5\%p}{[\mathrm{GeV/c}]}$
TOF	± 0.9	$0° < \varphi < 360°$			$\sigma_t < 70$ ps
HMPID	± 0.6	$1.2° < \varphi < 58.8°$			
PHOS	± 0.12	$220° < \varphi < 320°$			$\sigma_E = 1.12\% \oplus \frac{3.6\%}{\sqrt{E}}$
					$\sigma_{x,y}[\mathrm{mm}] = \sqrt{\left(\frac{3.26}{\sqrt{E[\mathrm{GeV}]}}\right)^2 + 0.44^2}$
EMCal	± 0.7	$80° < \varphi < 187°$			$\sigma_E = 1.5\% \oplus \frac{7\%}{\sqrt{E}}$

Table 3.1.: Resolution and detector coverage for the central barrel detectors [137].

Inner Tracking System (ITS)

The ITS [138, 139] consists of six cylindrical layers of silicon detectors using three different techniques: silicon pixel (SPD), silicon drift (SDD) and silicon double-sided micro strip (SSD) with two layers each. It was designed to localize the primary vertex of the interaction and to separate it from secondary vertices, coming from the decay of short lived particles such as B and D mesons, in the region of high track density close to the primary interaction. The number of channels, the position of the layers as well as their segmentation are optimized for efficient track finding and high resolution. Therefore, the innermost radius is determined
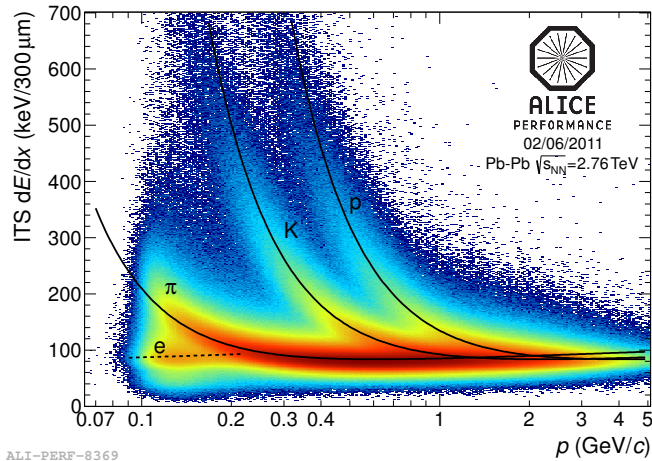
ALI-PERF-8369

Figure 3.4.: Performance plot (ALI-PERF-8369) of the energy loss measurement (dE/dx) performed in the outer layers of the ALICE ITS versus momentum measured by the combined tracking of ITS and TPC. The separation of the different particles species (electrons, pions, kaons, protons) can be clearly seen, the black line indicates the theoretical Bethe-Bloch-curves Equation 3.1.

by the radius of the beam pipe ($R_{BP} = 2.94$ cm) and the outermost radius was optimized to have the best possible track matching with the TPC. Moreover, the four outer layers have analogue readout, with a dynamic range large enough to provide a dE/dx measurement for low-momentum particles. The separation power of the ITS-standalone dE/dx can be seen in Figure 3.4. The track reconstruction in the central barrel is a combined ITS and TPC tracking. In addition to the vertex reconstruction and PID, the ITS can be used for standalone tracking, offering the possibility to fill the dead areas of the TPC and allowing to track charged particles down to $p_T \approx 100$ MeV/c. The coverage in η and φ is visualized in Figure 3.3 and detailed information about it, as well as the resolution in $r\varphi$ and z, are given in Table 3.1.

Time Projection Chamber (TPC)

The TPC [140, 141] is the main tracking detector in the central barrel. It consists of two main components: the field cage and the read-out chambers located at the end-plates.

The cylindrical field cage provides a uniform electrostatic field in the gas volume, consisting of a mixture of neon, nitrogen and carbon-dioxide with a total volume of approximately 90 m^3. Its active volume subtends a radial distance from $R =$84.8 cm up to 246.6 cm and covers the full azimuthal angle in a pseudo-rapidity range of $|\eta| < 0.9$ for full radial track length and $|\eta| < 1.5$ requiring 1/3 of radial track length. The initial gas admixture during data-taking was 85.7% Ne/ 9.5% CO$_2$ / 4.8% N$_2$, which was kept until end of 2010. Afterwards, the nitrogen was removed from the gas mixture and a gas mixture of 90% Ne/10% CO$_2$ was used. The gas mixture has been optimized concerning radiation length (low multiple scattering), low electron diffusion and high drift speed. To the central electrode, located at $Z = 0$, a high voltage of 100 kV is applied, leading to an electron drift time of about 90 μs.

For the signal readout multi-wire proportional chambers at the end plates are used. The TPC readout is segmented in 18 sectors in φ and 2 chambers per φ-sector in R. These chambers are then split again into small pads, where the size is tuned to the expected maximum track density depending on the radial position, reaching from 4×7.5 mm^2 up to 6×15 mm^2. For the reconstruction of 3D-track points the measured drift time (z-direction) (up to $t \sim 90$ μs) and the position on the cathode pads (x-,y-direction) of the induced signal are used.

From these 3D-dimensional track points the path of a particle through the detector can be reconstructed and the transverse momentum can be determined based on the curvature of the track. In the TPC, primary tracks with a p_T of 100 MeV/c up to 100 GeV/c can be
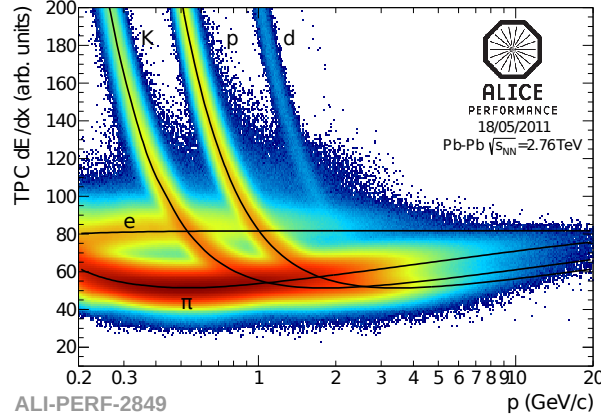
Figure 3.5.: The plot shows the dE/dx measurement versus momentum for data taken in Pb–Pb collisions in November 2010 (ALI-PERF-2849), and the theoretical Bethe-Bloch-Curves according to Equation 3.1 (black lines) for positrons, pions, kaons and protons.

reconstructed, where the low-momentum reach is limited by the probability of the particles reaching the TPC, due to their curvature in the magnetic field, and traversing more than $1/3$ of the radial length of the TPC. Secondary particles, on the other hand, can be produced at larger radial position and, therefore, the low-momentum reach is limited by the accuracy of the tracking algorithm, currently extending the low-momentum reach down to 50 MeV/c for secondary electrons.

The second main task of the TPC is the particle identification (PID) through energy loss measurements in the gas. Whenever a particle traverses matter it looses energy due to inelastic collisions with the atomic electrons of the material. Normally, this energy loss is rather small compared to the total energy of the particle. One distinguishes two different classes of energy loss: the soft collision, in which the atoms of the target material are only excited, and the hard collisions, in which ionization occurs. The products of hard collisions can be referred to as δ-electrons, if they are energetic enough to cause ionization themselves. The other energy loss mechanisms, like Cherenkov radiation, nuclear interactions, bremsstrahlung or transition radiation, are negligible compared to the previously mentioned processes in homogeneous materials. The mean energy loss per path length for elastic scattering and is described by the *Bethe-Bloch-formula*:

$$-\frac{dE}{dx} = 4\pi N_A r_e^2 m_e c^2 \rho z^2 \frac{Z}{A}\frac{1}{\beta^2}\left[\frac{1}{2}\ln\left(\frac{2m_e c^2\beta^2\gamma^2 T_{max}}{I^2}\right) - \beta^2 - \frac{\delta}{2}\right]. \tag{3.1}$$

The path length x in the medium is usually given in g cm^{-2} or kg m^{-2} and corresponds to the amount of matter transversed. In this formula z and v are the charge and the velocity of the transversing particle, N_A is the Avogadro number and I is an effective ionization potential of the atom species of the medium (roughly $I = 10Z$ eV). Furthermore, Z and A are the atomic mass numbers of the atoms in the medium.

Figure 3.5 shows the dE/dx measurement in the TPC for Pb–Pb collisions versus momentum. Electrons, pions, kaons and protons can be nicely separated and the black lines show the expected Bethe-Bloch curves. The dE/dx resolution of the TPC for tracks with 160 clusters (dE/dx measurements) is $\approx 5\%$ [141]. Detailed information on the coverage of the TPC as well as the resolution parameters can be found in Table 3.1 and further information on the reconstruction procedure and the calibration of the TPC can be found in [142].

Transition Radiation Detector (TRD)
The TRD [143] is situated outside of the TPC. It consists of 6 layers of radiators and multiwire-proportional chambers (MWPCs). It was designed to improve the tracking at high
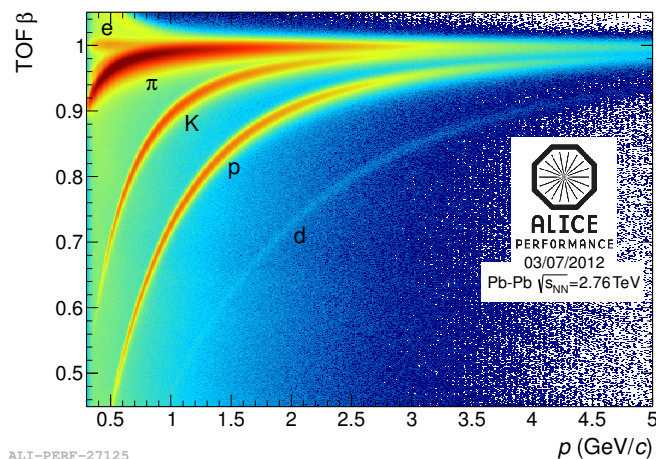
Figure 3.6.: Performance plot (ALI-PERF-27125) of the measured $\beta = \frac{v}{c}$ in the ALICE TOF detector versus momentum for data taken in Pb–Pb collisions in 2011. This measurement can provide an e/π separation between 0.3 GeV/c and 0.5 GeV/c as well as separation of pions and kaon up to ~ 3 GeV/c and kaons and proton up to ~ 4 GeV/c. Even deuterons can be seen and separated by this measurement from 1 GeV/c up to 5 GeV/c.

p_{T} and to provide electron identification in the transverse-momentum range of 1 GeV/c to 100 GeV/c. If a charged particle with $\gamma > 1000$ travels through the complex structure of hundreds of surfaces with different dielectrical constants in the radiator, transition radiation (TR) is emitted with some probability in form of X-rays. As the electron is much lighter than any other particle it is more likely to produce a TR-signal, which can then be observed in the high-Z-gas mixture (85% Xe, 15% CO_2) of the MWPCs. The signal observed in the MWPC is a sum of the energy loss of the particle and the signal of the absorbed TR-photons. Therefore, the TRD is not only capable of separating high-p_{T} pions from electrons but in addition can provide six additional dE/dx-measurements for the tracks. Moreover, the TRD is used as trigger detector for high-momentum particles as well as jets: the Global Tracking Unit (GTU) evaluates online the tracklets from the TRD and returns an L1-trigger signal.

Time of Flight Detetector (TOF)
The TOF [144] allows the separation of pions and kaons in the momentum range of $0.5 - 3.0$ GeV/c, proton identification for $0.5-4.0$ GeV/c and electron identification in pp-collisions from $0.3 - 0.5$ GeV/c, by measuring the time a particle needs to fly from the primary interaction point to the detector. For this Multigap Resistive Plate Chambers (MRPCs) are used. This techniques allows a time resolution up to 70 ps in the test setup. The TOF covers the full azimuthal angle like the other inner barrel detectors, but to reduce the amount of material in front of PHOS it does not cover the pseudo-rapidity range of $|\eta| < 0.9$ in that area. This also holds for the TRD. In Figure 3.6 the time of flight versus momentum can be seen for particles in heavy-ion collisions. The plot shows nicely the separation power of the TOF for light particles at low momentum and the separation power for heavier particles in the full momentum range.

High Momentum Particle Identification Detector (HMPID) The HMPID [145] is a Ring Imaging Cherenkov detector (RICH) consisting of 7 modules. Each of these is equipped with a chamber filled with a liquid radiator (C_6F_{14}), an MWPC filled with CH_4 and pad cathodes covered with a thin photo-sensitive CsI film. The detector is dedicated to inclusive measurements of identified hadrons at $p_{\mathrm{T}} > 1$ GeV/c enhancing the PID capabilities of ALICE beyond the ITS, TPC and TOF measurements. It covers only a small pseudo rapidity area ($|\eta| < 0.6$) and only reaches from 1.2° to 58.8° in φ (see Table 3.1). In this area the detector extends the useful range for π/K and K/p discrimination, on a track-by-track basis, up to 3 GeV/c and 5 GeV/c.
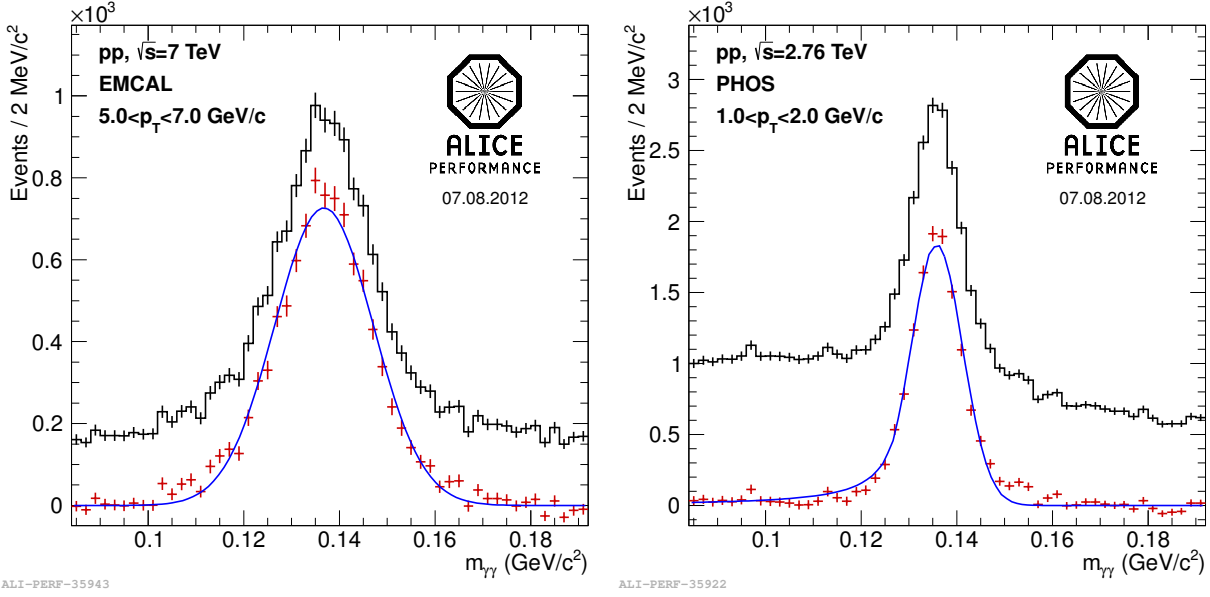
Figure 3.7.: Invariant two-photon mass measured with EMCal (left, ALI-PERF-35943) and the PHOS (right, ALI-PERF-35922). These invariant-mass plots are shown for data taken in pp collisions at $\sqrt{s} = 7$ TeV in one transverse-momentum bin (EMCal $5.0 < p_{\mathrm{T}} < 7.0$ GeV/c and PHOS $1.0 < p_{\mathrm{T}} < 2.0$ GeV/c). The black histograms represent the measured signal and background distributions, the red data point are obtained by subtracting the combinatorial background, calculated using mixed events. The red line represents a Gaussian fit to the signal distribution.

The Electromagnetic Calorimeters

ALICE is equipped with two calorimeters in the central barrel: PHOS and EMCal. They will try to observe the thermal and dynamical properties of the initial phase of a heavy-ion collision through measuring low-p_{T} direct photons as well as the jet quenching through the measurement of jets, high-p_{T} π^0 and γ-jet correlations.

PHOS [146, 147] is as a high-resolution electromagnetic spectrometer covering a limited rapidity and azimuthal area (see Table 3.1 and Figure 3.3). Measuring low-p_{T} thermal photons requires a fast response as well as very good position and energy resolution. For this purpose the material budget in front of the detector needs to be kept to a minimum. The Photon Spectrometer was planned to comprise five modules each equipped with 3584 lead-tungsten crystals (PbWO$_4$) of 20 X_0 with a granularity of the order of the Moliére radius; currently only three of the five modules are installed. The required timing resolution is achieved by using fast scintillators and preamplifiers. With this setup, a 2 ns time resolution is reached.

EMCal [148] was designed in 2008 to extend the capabilities of ALICE for full jet reconstruction. It is a large Pb-scintillator (Shashlik) sampling calorimeter located about 4.5 m from the interaction point. EMCal can provide a fast and efficient trigger for hard jets, photons and electrons. It provides full jet reconstruction as it can measure the neutral component of the jet as well. Due to the emphasis on high-p_{T} particles and the larger coverage in η and φ the intrinsic energy resolution is worse than the one of PHOS.

Figure 3.7 demonstrates the resolution showing the π^0 invariant-mass peaks measured by EMCal (left) and PHOS (right).

Forward Detectors

In addition to the already described detectors, there are the forward detectors providing information on the centrality of a Pb–Pb collision as well as the charged and neutral particle multiplicity in an η range beyond the coverage of the central barrel detectors. Furthermore, they can provide a fast level-0 trigger signal for the other detectors based on multiplicity or centrality. These detectors are :

The **V0 detector (VZERO)** [137], which is built out of two arrays of scintillation counters covering large pseudo-rapidity ranges ($-3.7 < \eta < -1.7$ and $2.8 < \eta < 5.1$). This detector can provide an interaction trigger, as well as a very fast multiplicity measurement. Therefore, it is used for the generation of the minimum bias trigger as well as a centrality trigger. Moreover, they are used for the luminosity measurement in pp collisions and the determination of the reaction plane in Pb–Pb collisions.

Additionally, the **Timing and Trigger detector at ALICE (TZERO)** [137] can provide a detailed measurement of the vertex position with the option to give a trigger signal. Therefore, the TZERO can generate a wake-up signal for the TRD as well as a start time for the TOF. It consists of 24 Cherenkov counters in two arrays and placed 73 cm away from the interaction point on the C-side and at 375 cm in the A-side.

In addition to the VZERO detectors, the charged-particle multiplicity can also be measured by the **Forward Multiplicity Detector (FMD)** [137], which is a silicon strip detector. It provides a charged-particle multiplicity measurement in a pseudo-rapidity range from $-3.4 < \eta < -1.7$ and $1.7 < \eta < 5$.

The **Photon Multiplicity Detector (PMD)** [137] was designed to measure the multiplicity and spatial distribution of photons in the forward pseudo-rapidity region of $2.3 \geq \eta \geq 3.7$. Moreover, this detector can provide an estimate on the transverse electromagnetic energy and the reaction plane on an event-by-event basis. The **Zero Degree Calorimeter (ZDC)** [137], which is designed to measure the centrality of heavy-ion collisions by measuring the number of spectators, consist of three detectors: the Zero Degree Neutron Calorimeter (ZN) for neutrons, the Zero Degree Proton Calorimeter (ZP) for protons and the Zero Degree Electromagnetic Calorimeter (ZEM) for measuring the energy of particles emitted at forward rapidity $4.8 < \eta < 6.7$.

3.2.2. The Trigger System

In the ALICE detector the interaction rate is approximately a factor 1000 smaller than in CMS and ATLAS. Additionally the readout of some of the detectors is relatively "slow", therefore the ALICE Trigger System (TRG) consists of three trigger levels, the Level 0 (L0) after 1.2 μs after the collision, the Level 1 (L1) after 6.5 μs and the Level 2 (L2) after 88 μs. This structure allows an optimal usage of the available luminosity based on a trigger decision after a short inspection of the event.

To create the trigger signals, the logical signals provided by the fast detectors (i.e VZERO, TZERO) concerning a specific measurement (e.g. multiplicity), are sent to the Central Trigger Processor (CTP), where they are combined by logical operations inside a Field Programmable Gate Array (FPGA) to form different physics triggers (e.g. minimum bias, centrality). The calculated output is sent to the Local Trigger Units (LTUs) of the different subdetectors, where they are processed and then forwarded to the Front End Electronics (FEE). Due to the relatively long readout time, some of the detectors expect a L0-trigger signal (1.2 μs) to initiate the readout of the detector, if this doesn't arrive the data in the detector are not processed any further. Not all detectors can process their data within the 1.2μs, therefore a second level is introduced, where additional information can be provided and processed. The third step is the L2 decision, which waits for the end of the TPC drift time. The read-out of the detector electronics into the optical data link is only initiated if a positive L2 signals was received. In addition, ALICE uses a very fast interaction "pretrigger", which can be derived from the interactions masks given by the LHC or from the multiplicity in the TZERO or VZERO. This pretrigger is needed within ≤ 100 ns to activate the TRD.

After having received an L2-accepted the FEE is read out and the data are sent in parallel to the Data Acquisition (DAQ) and to the High Level Trigger (HLT). The software-based HLT
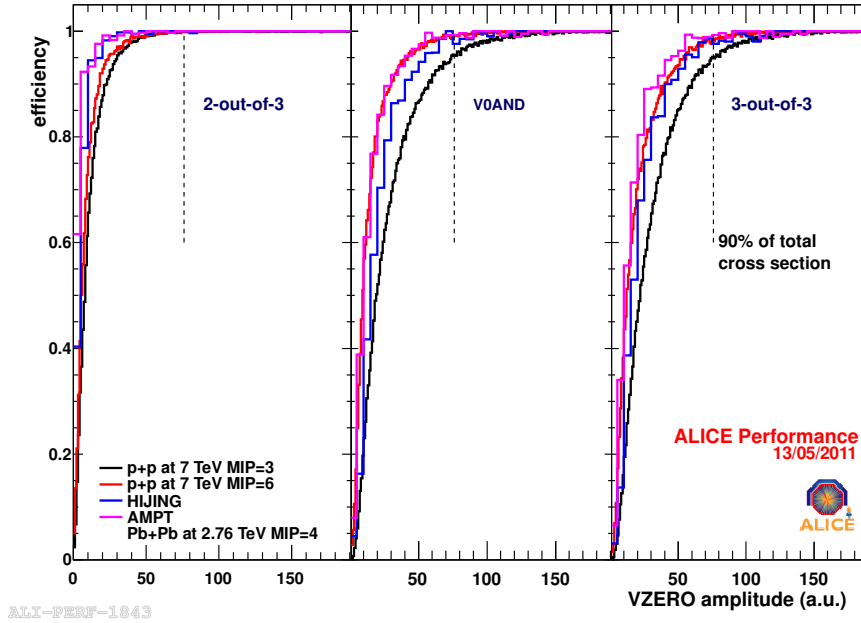
Figure 3.8.: Trigger efficiency for pp and Pb–Pb collisions under the detector conditions for data taken in 2010 (ALI-PERF-1843). The three different triggers use the VZERO and the SPD as inputs. For the left figure a coincidence of 2 out of the 3 detectors has to be present. This trigger measures the largest fraction of the total cross section. The central plot is a coincidence of V0-A and V0-C (MB$_{\text{AND}}$.), which comes closest to the having NSD events. The last class is the coincidence of all 3 detectors this measures the smallest fraction of the total cross section. All of these classes have very similar efficiencies for heavy-ion collisions and pp collisions as seen by different histograms shown in the figures.

is a farm of up to 1000 multiprocessor computer systems performing an on-line analysis of the events. Furthermore, it can reduce the data volume, either by choosing just a fraction of the data recorded according to an additional trigger condition or by compressing the complete or partial event information of the detectors. Since 2011 the HLT data compression for the TPC clusters is used by default to reduce the data volume of the raw events.

There are a number of physics triggers which can be implemented on the different levels. The simple triggers are based on multiplicity and coincidence of signals in more than one detector (e.g. minimum bias, centrality trigger). The more complex triggers are normally L1-trigger, which could be based on the charge, track or energy density (e.g. jet triggers in EMCAL, PHOS or TRD) or on identified particles (e.g. γ-jet trigger, di-muon or di-electron trigger). The trigger efficiency for the minimum bias triggers is shown in Figure 3.8 for Pb–Pb and pp collisions. The three different trigger classes represent different physics, while the MB$_{\text{OR}}$ is closest to having Inelastic (INEL) events, the MB$_{\text{AND}}$ measures mainly Non Single Diffractive Events (NSD) events.

3.2.3. The AliRoot Framework

In an experiment like ALICE not only the detectors need to be designed but also a software package which can deal with the output of these detectors. In ALICE this is provided by the AliRoot software framework [149], with the necessary tools for simulation, reconstruction and physics analysis of the events collected by the ALICE detectors. The framework is based on ROOT [150], a C++ based object-oriented programming tool for physics analysis, maintained and developed at CERN. As both frameworks are continuously under development they can adapt to the challenges provided by the physics analysis or detectors.

Within the AliRoot framework a number of Monte Carlo (MC) generators, i.e PYTHIA [151–153], PHOJET [154], HIJING [155] or AMPT [156] can be used for full-event or single-particle genera-

tion. These generators create the so called primary-particles with the corresponding full kinematic information as well as information about their heritage (mother-daughter relationship). These primary particles are then transported through the detector and their interactions are simulated using GEANT3 [133], GEANT4 [157] or FLUKA [158]. Each interaction point of a particle is stored with its particular time and position as a so-called hit. These hits are later processed into digits for each sub-detector, which correspond to the actual detector response.

The raw data reconstruction follows the same steps, regardless whether it is simulated data or real data. The first step is the generation of so-called clusters from neighboring digits assuming that the digits are caused by the same particle traversing the detector. Afterwards, the tracking combines these clusters to the most probable path of the particle through the detectors. The tracking is described in detail in section 3.2.4. The output of the reconstruction is stored in Event Summary Data (ESD) or the more compact Analysis Object Data (AOD) for further analysis.

3.2.4. Track and Vertex Reconstruction

Primary Vertex Reconstruction

The primary vertex reconstruction [137] is based on information provided by the SPD. In the first step, pairs of reconstructed points, which are required to be close in azimuthal and transverse direction, are selected in the 2 layers of the SPD. From their z-coordinates a first estimate of the primary vertex z-position is calculated by linear extrapolation. Afterwards, the same procedure is performed in the transverse plane, which can only give a rough estimate because of the bending of the track in the transverse plain due to the magnetic field. However, considering the small distance from the interaction point, the x and y coordinates can be determined with an adequate precision. With these coordinates, a correction of the z-coordinate can be performed. If the beam is well focused one determines the transverse position by averaging over several events.

The precision of this measurement highly depends on the multiplicity and therefore the charged-particle density. The functional dependence of the resolution in z can be expressed by

$$\sigma_z = \frac{A}{\sqrt{dN_{ch}/d\eta}} + B, \tag{3.2}$$

where typically $A = 290$ μm and B is a few micro meters, representing the residual misalignment of the silicon pixel layers [137]. In pp collisions a z-vertex resolution of 150 μm can be reached, while in Pb–Pb collisions down to 10 μm are feasible. The first calculation is improved after the track reconstruction using the measured track parameters. Therefore, for pp collisions the transverse resolution can be improved to 70 μm and the z-resolution down to 110 μm. In addition, the reconstruction of the primary vertex is performed on the level of the tracking, reaching a very good precision as well.

Track Reconstruction

The track reconstruction is done in several steps by finding and fitting the track using Kalman filtering [137, 160]. The seeding algorithm of the Kalman filter in ALICE uses space points close to the end of the TPC as input. For low multiplicities these space points are calculated by the center-of-gravity method in the directions of the pad row as well as the time direction; in a high-multiplicity environment, cluster unfolding is used. The seeding is done twice, once under the assumption that the track originates in the primary vertex and once that it originates somewhere else. The next step is combining these seeds in the outermost pad-rows of the TPC with the nearby clusters going inwards to a track under the constraint that the particle originates in the primary
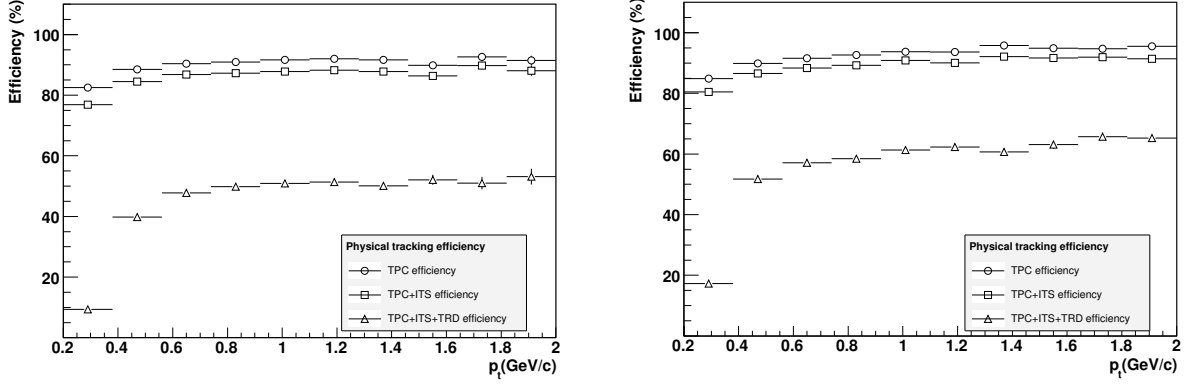
Figure 3.9.: Track finding efficiency for different combinations of tracking detector for central Pb–Pb collisions at $dN_{ch}/d\eta = 6000$ and pp collisions (right) [159].
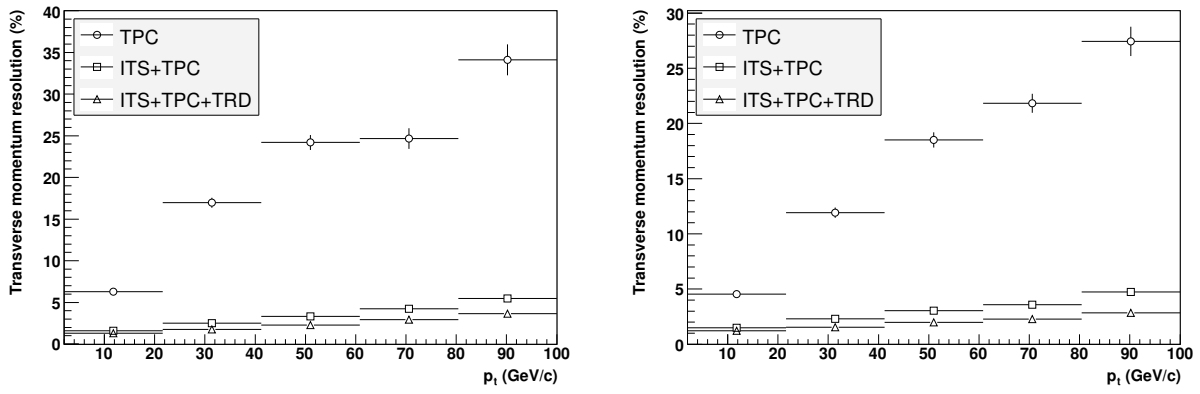

Figure 3.10.: Transverse momentum resolution for different combinations of tracking detectors for central Pb–Pb collisions at $dN_{ch}/d\eta = 6000$ and pp collision (right) [159].

vertex. This procedure is repeated several times, each time choosing in addition pad rows closer to the primary vertex. If a space point is close to the trajectory it is added to the track and the covariance matrix is recalculated. The procedure continues until the innermost pad row of the TPC is reached and is in parallel repeated under the condition that the track does not originate in the primary vertex.

After having finished the initial tracking in the TPC, the tracks are propagated to the outermost ITS layer with both parameter sets. The track matching starts with the highest momentum particles, as these are the easiest to propagate due to their smaller curvature. The tracks are then reconstructed following the same procedure as in the TPC for the six layers of the ITS going inwards to the primary vertex. As it is possible to assign more than one space point in the ITS to a track coming from the TPC each possibility is calculated separately and then the most probable track is selected based on the summed χ^2 values along the track.

After the combined ITS and TPC fit the Kalman filtering is reversed and proceeds outwards, using the already reconstructed tracks as seeds and recalculating the path through the TPC removing improperly assigned points. Then the tracking follows the track beyond the TPC and assigns space points in the TRD, TOF, HMPID and calorimeter towers in the EMCal or PHOS. The outer detectors except the TRD do not contribute to the momentum fit and the TRD is only included if it improves the momentum resolution. Finally, a last inversion of the Kalman filter is performed and the final track parameters are calculated twice, once assuming the track originating from the primary vertex and the other time without. This additional set of parameters is stored in order to allow subsequent studies of short-lived particle decays and photon conversions. An optional last step is the removal of all already assigned points from the ITS and fitting the remaining space
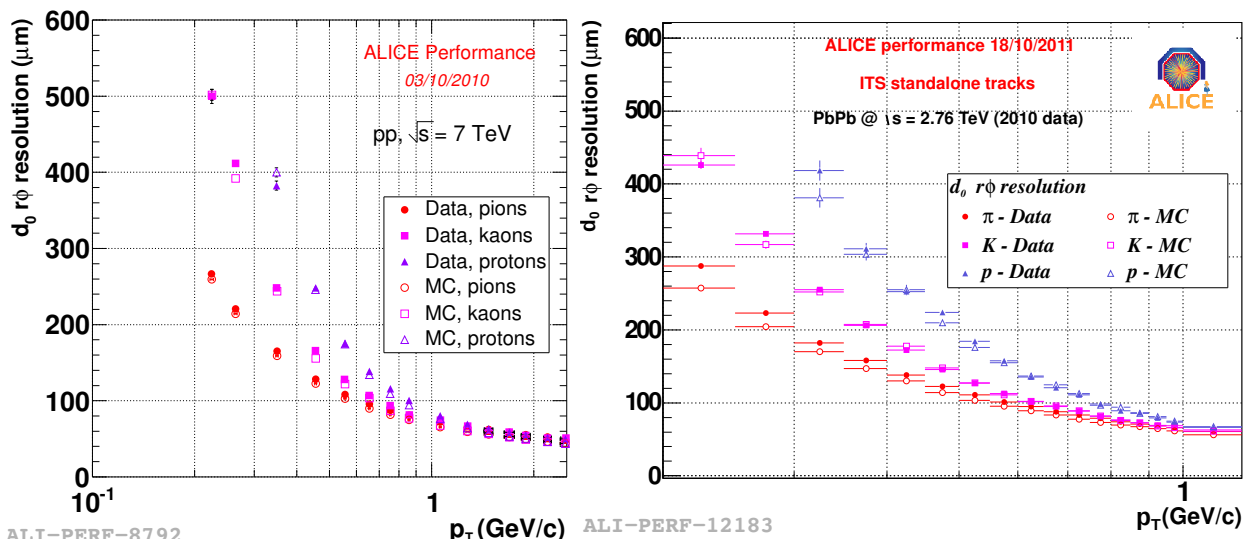
Figure 3.11.: Impact parameter resolution in pp (left, ALI-PERF-8792) and Pb–Pb collisions (right, ALI-PERF-12183) for different particle species as a function of p_T. For pp combined tracking of ITS and TPC is used, while in the Pb–Pb case the parameters are shown for ITS standalone tracking.

points of the ITS again to recover tracks which went through dead areas of the TPC.

The track finding efficiency (see Figure 3.9) is larger than 80% for TPC and TPC + ITS, it drops significantly after including the TRD into the fit, due to the additional interactions with the detector and additional dead regions. On the other hand, the p_T resolution improves significantly, as seen in Figure 3.10. Therefore, the TRD information is only used if it improves the resolution. The main performance parameter of such track finding algorithms is the resolution of the impact parameter (distance between the primary vertex and the track prolongation to the point of closest approach to the primary vertex), which depends on both the accuracy in the primary vertex position as well as the track parameters. This resolution was determined with Monte Carlo simulations and measured in data, the results can be found in Figure 3.11. As it can be seen in Figure 3.11 the impact parameter resolution depends on the particle species as well as the transverse momentum. The impact parameter resolution above 1 GeV, however, is better than 80 μm, regardless of the particle species or collision system.

Secondary Vertex Finding

The reconstruction of the V^0s, pairs of tracks with V-topology from a secondary vertex, is based on the combination of so called secondary tracks, which are the tracks with the parameter set obtained by not assuming the primary vertex as their origin. These secondary tracks usually have large impact parameters. The V^0 reconstruction method can be used to reconstruct the decay of a strange particle or a photon conversion, a sketch of the reconstruction method is shown in Figure 3.12.

The algorithm starts with the selection of two oppositely charged secondary tracks. Afterwards, the impact parameter of the track (b, $b+$) with respect to the primary vertex is calculated. If one of the tracks has a too small impact parameter it is removed from the secondary track sample and the procedure is restarted. For pairs with an impact parameter above some chosen limit the distance of closest approach (DCA) of the two tracks is calculated. If the DCA value is above a certain threshold, depending on the distance to the primary vertex and its resolution, the track pair is rejected. The largest allowed DCA is 1 cm. The remaining track pairs form accepted V^0s, with their point of closest approach being the secondary vertex. Only the vertices within a certain fiducial zone (given by the dotted line in Figure 3.12), reaching from a minimum radial distance
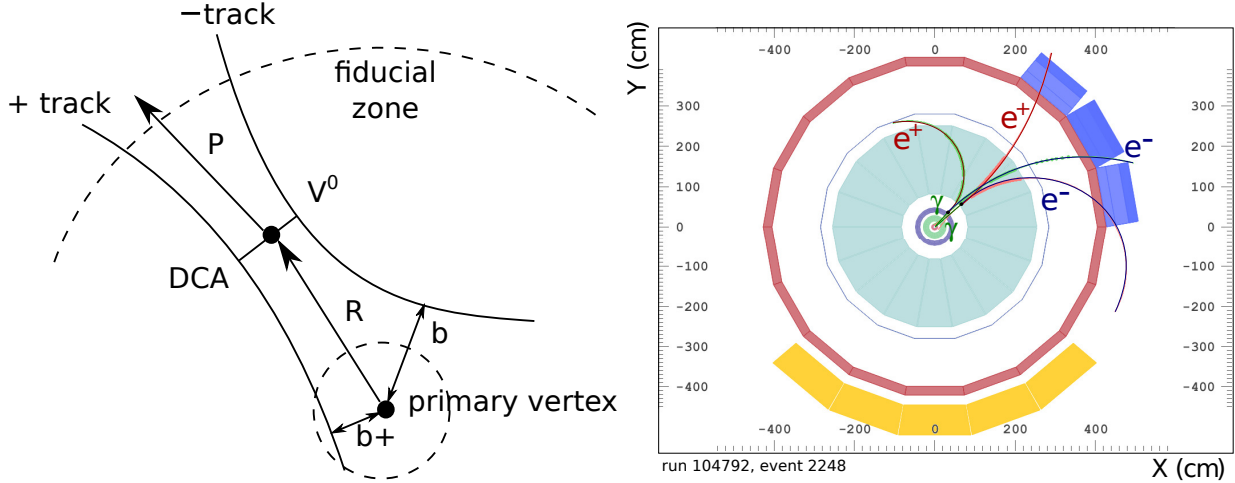
Figure 3.12.: Sketch of the reconstruction of a generic secondary vertex (left) [159] and a reconstructed π^0 candidate from 2009 data taking campaign at $\sqrt{s} = 900$ GeV (right). The reconstructed event shows a π^0 meson candidate from 2 reconstructed photon conversions using the V^0 method.
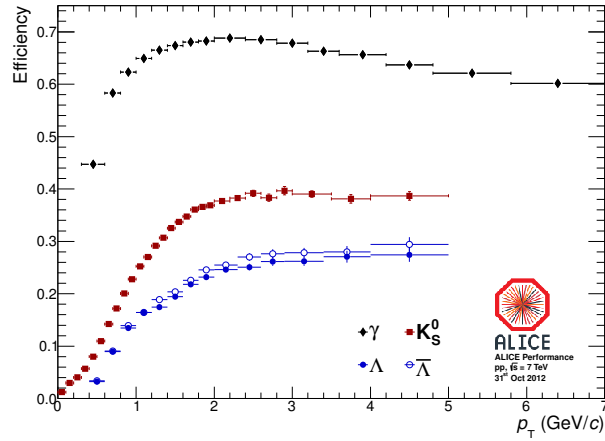
Figure 3.13.: Reconstruction efficiency of the On-the-flight V0 finder for all reconstructible V^0s versus p_T.

of 0.5 cm to the primary vertex to an outer limit of 220 cm, are kept. Next, the momentum of the V^0 is reconstructed by extrapolating the momenta of both tracks to the extrapolated DCA and calculating their sum in this point. Then it is checked whether the resulting momentum vector points to the primary vertex. Particles which do not match the condition that the cosine of the angle between the V^0 momentum vector (P) and the vector between the primary vertex and the V^0 position (R) is smaller than 0.85 are rejected.

In ALICE, two different V^0-finding algorithms are available, the **On-the-fly** and the **Offline V^0** finder. The On-the-fly V^0 finder is applied during the reconstruction and therefore the tracks can be refitted and the track parameters can be recalculated. These parameters can be recalculated, due to the fact that the full cluster information of the TPC and ITS, as well as the covariance matrix are still available. This allows to improve the position and momentum resolution compared to the Offline V^0 finder, which does the vertex finding after the full tracking is finished. The Offline V^0 finder, however, allows to redo the secondary vertex finding without a new reconstruction pass of the full data set.

The reconstruction efficiency of the On-the-flight V^0 finder for photons, K_s^0, Λ and $\overline{\Lambda}$ can be seen in Figure 3.13. For the photon, this plot shows the product of the PID efficiency of the lepton tracks and the actual efficiency of finding a photon.

4. Photon Detection in ALICE via Photon Conversions

This chapter is dedicated to the description of the Photon Conversion Method (PCM) from a general point of view. Therefore, the first section will give an overview over the data samples and Monte Carlo simulations, which will be used for the calculation of the systematic error of the material budget as well as for the neutral meson analysis. The second section will illustrate photon reconstruction and selection in general. Moreover, the standard selection cuts for the photons entering the three different analysis will be explained and motivated.

4.1. Data Sets and Monte Carlo Simulations

ALICE started collecting data from proton-proton (pp) collisions in November 2009. Since then pp collisions have been recorded at four different center-of-mass energies ($\sqrt{s} = 0.9$, 2.76, 7 and 8 TeV). Moreover, ALICE recorded Pb–Pb data at $\sqrt{s_{\mathrm{NN}}} = 2.76$ TeV and p–Pb data at $\sqrt{s_{\mathrm{NN}}} = 5.02$ TeV. However, this analysis will only cover pp data at $\sqrt{s} = 0.9$, 2.76 and 7 TeV and Pb–Pb data at $\sqrt{s_{\mathrm{NN}}} = 2.76$ TeV. The data taking is split into so called periods, which each corresponds to approximately a month of data taking. In this thesis only data taken in 2010 and early 2011 will be presented. An offline event selection was applied to reject events, which do not fulfill the central barrel trigger conditions or which are not of physics type (e.g. calibrations events). Furthermore, events assigned to noise or beam-gas interactions were rejected. This selection is called *Physics Selection* (PS). Only events which are consistent with the minimum bias trigger (MB_{OR}) are taken into account. This trigger requires a hit in either SPD or one of the two VZERO detectors.

4.1.1. Event Selection in pp Collisions

In addition to the criteria mentioned above, the events selected in our analysis have to have a reconstructed primary vertex with $|z_{vtx}| < 10$ cm to the center of ALICE. This vertex can be reconstructed either with global tracks or only SPD tracklets. However, it has to have at least one contributing track or tracklet to the vertex. Table 4.2 shows the data samples used for the pp analysis including the total number of events and the fraction of events being lost due to the different vertex conditions. We normalize our spectra with the following number of events:

$$N_{\mathrm{norm,evt}} = N_{\mathrm{MB_{OR},Vtx},|z_{Vtx}|<10\mathrm{cm}} + \frac{N_{\mathrm{MB_{OR},Vtx},|z_{vtx}|<10\mathrm{cm}}}{N_{\mathrm{MB_{OR},Vtx},|z_{vtx}|<10\ \mathrm{cm}} + N_{\mathrm{MB_{OR}},Vtx,|z_{vtx}|>10\mathrm{cm}}} N_{\mathrm{MB_{OR},no\ Vtx}}. \quad (4.1)$$

Since the start of the LHC in 2009 the machine has been constantly increasing the delivered instantaneous luminosity for all experiments. ALICE can only take data at a limited rate, as already discussed in Section 3.2.2. Therefore, to avoid overlapping events in ALICE in the TPC, both beams at the ALICE interaction point were displaced to stay at a lower interaction rate. However, this condition is not enough to guarantee that we only see one event at a time in our detectors, therefore a pile-up rejection, based on the number of reconstructed vertices in the SPD, was included in the analysis. This pile-up rejection removes events, which have more than one vertex

$\sqrt{s}$ (TeV)	$\sigma_{\mathrm{MB_{AND}}}$ (mb)	MB$_{\mathrm{AND}}$/MB$_{\mathrm{OR}}$		$\sigma_{\mathrm{MB_{OR}}}$ (mb)	$\sigma_{\mathrm{MB_{INEL}}}$ (mb)
		measured	simulated		
0.9	40.06	0.8401 ± 0.0004	$0.839^{+0.006}_{-0.008}$	47.78	$52.5^{+2.0}_{-3.3}$
2.76	47.73	0.8613 ± 0.0006	$0.863^{+0.02}_{-0.03}$	55.26	$62.8^{+2.4}_{-4.0}$(model) ± 1.2(lumi)
7	54.31	0.8727 ± 0.0001	0.871 ± 0.007	62.37	$73.2^{+2.0}_{-4.6}$(model) ± 2.6(lumi)

Table 4.1.: Cross sections for the different triggers and the ratio of the trigger efficiencies for MB$_{\mathrm{OR}}$ and MB$_{\mathrm{AND}}$ [163].

reconstructed based on SPD tracklets from our analysis.

For the data collected at $\sqrt{s} = 2.76$ TeV, part of the data was read out without the signals in the SDD. Therefore, if one wants to analyse the full data sample with homogenous reconstruction conditions, the full reconstruction has to be performed without taking into account the SDD signals. The same has to be done for the simulation. For the analysis presented in this thesis the reconstruction pass without the SDD signals has been selected, however, it has been checked that the results for the corresponding sample with the SDD signal used in the reconstruction agree within the statistical errors.

To convert the invariant yield to an invariant cross-section, the invariant yield needs to be multiplied with the cross-section for our trigger condition (MB$_{\mathrm{OR}}$). The cross-section for the MB$_{\mathrm{OR}}$ cannot be measured directly. First, the total inelastic cross-section and hence the luminosity needs to be measured. Therefore, several van der Meer scans [161] were performed to study the geometry of the beam interaction region in ALICE. The trigger condition for the van der Meer scans was a coincidence of the two VZERO detector, requiring at least one hit in each of the two VZERO arrays (MB$_{\mathrm{AND}}$) [162, 163]. The rate $\frac{dN}{dt}$ can then be determined by

$$\frac{dN}{dt} = A \times \sigma_{\mathrm{INEL}} \times \mathcal{L}, \tag{4.2}$$

where A is the acceptance and efficiency for the trigger condition, σ_{INEL} the inelastic cross-section for pp collisions and $\mathcal{L}$ the luminosity. The luminosity for a single proton bunch pair colliding with zero crossing angle can be determined from the beam-profile using

$$\mathcal{L} = f N_1 N_2 / h_x h_y, \tag{4.3}$$

where f is the revolution frequency for the accelerator (11245.5 Hz for the LHC), N_1, N_2 the number of protons in each bunch, and h_x, h_y the effective transverse width of the beam in the interaction region.

Combining this measurement with the trigger efficiency for the MB$_{\mathrm{AND}}$, which can be obtained from Monte Carlo simulations, we arrive at the final inelastic cross section in pp collisions at $\sqrt{s} = 2.76$ and 7 TeV. For 900 GeV the total inelastic cross section has been measured by UA5 [164] and therefore only the trigger efficiencies needed to be measured. To derive the cross-section for the MB$_{\mathrm{OR}}$, we need to simulate or measure in addition the ratio of the different triggers to each other. The resulting cross-sections and ratios are shown in Table 4.1.

4.1.2. Monte Carlo Simulations for pp Collisions

For the efficiency and acceptance corrections in pp collisions we use different Monte Carlo event generators as input for our full detector simulation: **Phojet** [154,165], **Pythia 6.4** (tune Perugia 0) [151] and **Pythia 8.1** [152,153]. All three generators are general purpose event generators.

Pythia
In ALICE we use two different versions of the Pythia library. While Pythia 6.4 is still written in Fortran 77, Pythia 8 is implemented in C++. As Pythia 8.1 was supposed to be used for

comparisons with the first LHC data, γp and $\gamma\gamma$ physics are not yet addressed in this version and some intended processes still remain to be implement.

The event generation in Pythia starts with the simulation of the hard scattering process, taking by default the description of the initial states from the CTEQ 5L PDFs [166]. The event generator is optimized for leading order $2 \longrightarrow 1$ and $2 \longrightarrow 2$ processes. However, in order to reproduce the measured data, also diffractive processes based on Regge Field Theory [167] were implemented. Within the last decades advances in automatic matrix-element code generation and phase space sampling were made. Additionally the possibility to import process level event via the Les Houches Accord (LHA) and Les Houches Event Files (LHEF) has been implemented, thus the need to implement an extensive process library in Pythia itself has decreased. Therefore, the focus for Pythia 8 has shifted to a good description of the subsequent steps, such as initial- and final state parton showers, multiple parton-parton interaction, string fragmentation and decay. The initial- and final-state algorithms are based on a $p_\perp$-ordered evolution, which was introduced in Pythia 6.3. The hadronization simulations are based on the LUND String Model [168]. Due to the fact that the produced hadrons are not necessarily stable particles, the decay properties of the all hadrons as summarized in [130] are stored in decay tables and the hadrons are decayed accordingly. As Pythia combines a lot of different processes, it has many tunable parameters with significant influence on the generated distributions, reflected especially in the low momentum transfer processes. One of these parameters is the connection between low and high momentum processes, which is given by a minimum momentum transfer ($p_{T,\text{cut-off}}$) of 2 GeV/c.

Phojet

This Monte Carlo event generator uses ideas of the Dual Parton Model (DPM) [169], dominant in the soft scattering regime, combined with perturbative QCD, dominant in the hard scattering regime, to give an almost complete picture of hadron-hadron, photon-hadron and photon-photon interactions at high energies [165]. The Dual Parton Model allows to simultaneously calculate the elastic (i.e cross sections) and inelastic processes (i.e. multiparticle productions) within a single event. Thus the model directly relates the free parameters necessary to describe the cross sections to the multiparticle production. Similar to Pythia the parton showers are initiated following the DGLAP evolution equations [170] and the hadronization is based on the LUND fragmentation model. The soft and hard part of the interaction are separated by a $p_{T,\text{cut-off}}$ of 3 GeV/c. However, within the two-component DPM the connection of the soft and hard subprocesses is given by an unitarization scheme, chosen in a way that the sum of the hard and soft cross sections is nearly independent of the $p_{T,\text{cut-off}}$. Therefore, the tune parameters, unlike for Pythia, are connected to each other.

As both Monte Carlo event generators are based on different models and in addition fail to simultaneously describe the low and high momentum part of the photon spectrum with a sufficient accuracy, the average of both Monte Carlo generators is taken for the efficiency and acceptance corrections. The remaining discrepancy between the Monte Carlo generators is taken as a systematic error source, however, this discrepancy for pp collisions at $\sqrt{s} = 7$ TeV is smaller than 2.5% for the photons and therefore negligible compared to the other systematic uncertainties. The Monte Carlo simulations used for the analysis at the different center-of-mass energies can be found in Table 4.2.

Figure 4.1 shows the measured mean number of primary track candidates in the TPC ($\eta < 0.8$) and Figure 4.2 the measured fraction of photon candidates per event as a function of the run number compared to the corresponding Monte Carlo simulations. The simulations were performed adapting the detector conditions to reproduce correctly the calibration of the individual detectors and dead detector layers (so called anchored Monte Carlo simulations). Both Monte Carlo generators fail to reproduce the mean number of TPC tracks and the fraction of photon candidates per event measured in data, except for Phojet at $\sqrt{s} = 900$ GeV to which the generator was tuned
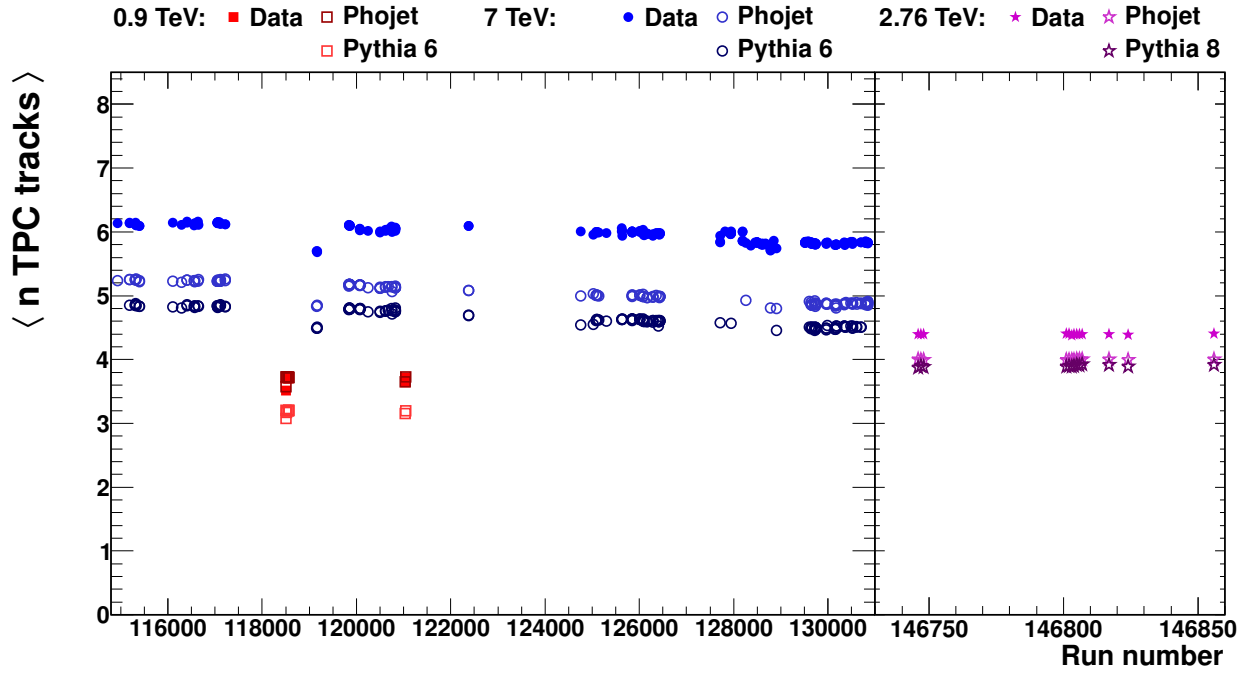
Figure 4.1.: Mean number of primary tracks reaching the TPC versus run number for the different pp data samples and the corresponding Monte Carlo simulations.
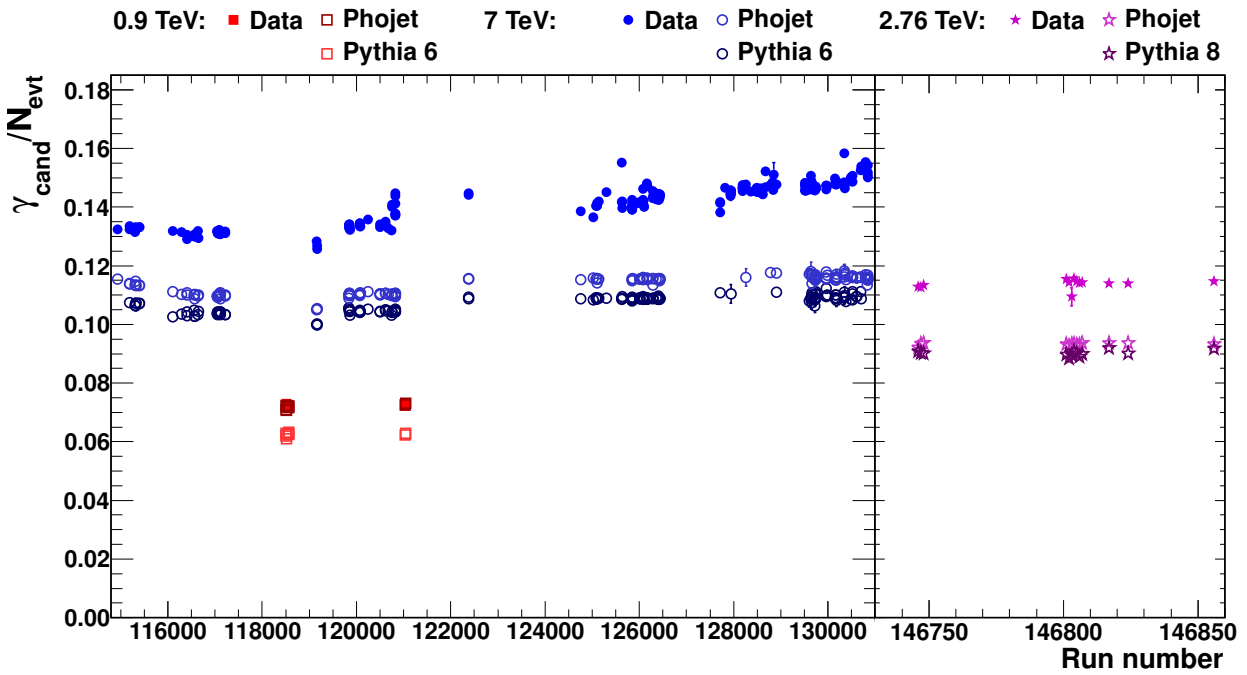
Figure 4.2.: Fraction of photon candidates in pp events normalized to the number of events, which fulfill our event selection criteria (full symbols). The points with open symbols represent the same quantity for the corresponding Monte Carlo simulations.

at previous experiments. However, in pp collisions it is not critical for efficiency and acceptance corrections to fully reproduce the total amount of particles seen in the detector, as the multiplicity is low and therefore the reconstruction efficiency is rather stable versus multiplicity. It is more important that the Monte Carlo simulations do not miss the total number of particles by an order of magnitude and reproduce the detector response correctly, taking into account the different data taking conditions for each run. As both event generators seem to reproduce the relative changes seen in data they can be used for the efficiencies extraction.

$\sqrt{s}$ (TeV)	Data Set		Events for normalization N_{evt}	Min. Bias. Events (MB) N_{MB}	$\frac{MB+Vtx+|z_{vtx}|<10}{MB}$	$\frac{MB+Vtx+|z_{vtx}|>10}{MB}$	$\frac{MB+\ no\ Vtx}{MB}$	$\frac{MB+Pile\text{-}up}{MB}$
0.9	Data	LHC10c, Pass3	6.01e+06	6.87e+06	0.76	0.106	0.13	0.002
	MC, Pythia 6	LHC10e13	5.89e+06	6.61e+06	0.76	0.093	0.15	0
	MC, Phojet	LHC10e12	5.63e+06	6.31e+06	0.81	0.098	0.09	0
2.76	Data	LHC11a, Pass4	4.53e+07	5.21e+07	0.78	0.111	0.11	0.006
	MC, Pythia 6	LHC12e6, Pass2	1.63e+06	1.65e+06	0.90	0.002	0.10	0
	MC, Pythia 8	LHC12f1a, Pass4	1.63e+06	1.65e+06	0.90	0.002	0.10	0
	MC, Phojet	LHC12f1b, Pass4	1.99e+07	2.00e+07	0.90	0.002	0.10	0
7	Data	LHC10b, Pass2	2.56e+07	2.61e+07	0.90	0.004	0.09	0.003
		LHC10c, Pass2	6.79e+07	6.96e+07	0.89	0.009	0.09	0.014
		LHC10d, Pass2	1.39e+08	1.58e+08	0.79	0.104	0.09	0.010
		LHC10e, Pass2	1.14e+08	1.31e+08	0.79	0.112	0.09	0.008
	MC, Pythia 6	LHC10d1, (b)	1.83e+07	1.84e+07	0.92	0.005	0.08	0
		LHC10d4, (c)	4.91e+07	4.97e+07	0.95	0.010	0.04	0
		LHC10f6a, (d)	1.18e+08	1.31e+08	0.81	0.093	0.10	0
		LHC10e20, (e)	6.60e+06	7.30e+06	0.82	0.087	0.10	0
	MC, Phojet	LHC10d2, (b)	1.44e+07	1.45e+07	0.95	0.004	0.05	0
		LHC10d4a, (c)	6.14e+07	6.20e+07	0.97	0.004	0.02	0
		LHC10f6, (d)	6.73e+07	7.49e+07	0.85	0.096	0.06	0
		LHC10e21, (e)	9.26e+06	1.02e+07	0.86	0.090	0.06	0

Table 4.2.: Number of events used in our analysis for the normalization for each data taking period and the corresponding Monte Carlo simulations. In addition the number of Minimum Bias triggers (MB) and the fractions for $\frac{MB+Vtx+|z_{vtx}|<10}{MB}$, $\frac{MB+Vtx+|z_{vtx}|>10}{MB}$, $\frac{MB+\ no\ Vtx}{MB}$ and $\frac{MB+Pile\text{-}up}{MB}$ are given.

4.1.3. Event Selection in Pb–Pb Collisions

The Pb–Pb data sample consisting of $\sim 19.2\times 10^{6}$ minimum bias events was collected by ALICE in November and December 2010. For the event selection the same conditions, except the pile-up rejection, were applied as in pp collisions. Up to a centrality of 80% the fraction of events without a vertex is negligible in Pb–Pb collisions. For the full sample 0.13% of the events are rejected due to this selection criterium. The cut on the vertex position in z_{vtx} removes approximately 15% of the statistics. This cut is necessary, as the efficiency and acceptance for the track and vertex reconstruction changes if the primary vertex is outside of $|z_{vtx}| < 10$ cm.

For the normalization of the neutral pion spectra the number of events fulfilling the conditions mentioned above is used. However, each centrality class is normalized to the individual number of events in the specific centrality class. The final number of events for each centrality class can be found in Table 4.4.

ALICE is capable of measuring the centrality with four different techniques: via the energy deposition in the ZDC or via the multiplicities measured with the SPD, VZERO or TPC detectors. The correlation of two of these measurements is shown in Figure 4.3 in the upper panel, in the lower panel the distributions of the uncorrected TPC track multiplicity is shown for minimum bias events.

In our analysis we rely on the centrality determination based on the Glauber fit to the VZERO amplitude to avoid correlations between the centrality determination and the measured particles. We divide our data sample in six centrality classes: 0-5%, 5-10%, 10-20%, 20-40%, 40-60% and 60-80%. The number of participating nucleons, $N_{\mathrm{part}}^{\mathrm{geo}}$, and the number of binary nucleon-nucleon collisions, $N_{\mathrm{coll}}^{\mathrm{geo}}$, are derived from the Glauber Monte Carlo simulations [35, 171], the final values
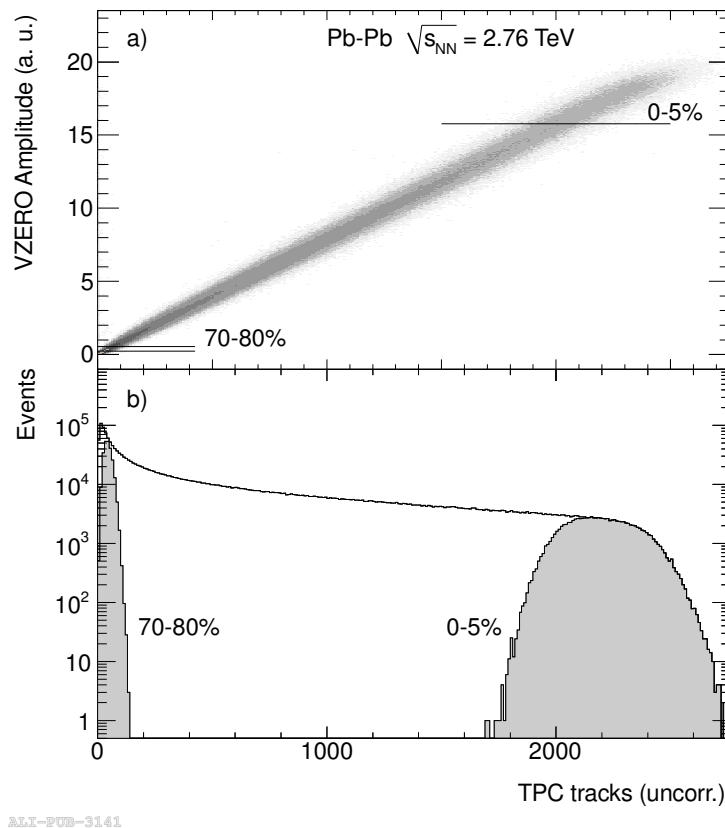

Figure 4.3.: a) Correlation between VZERO amplitude and the Time Projection Chamber (TPC) track multiplicity measured by the ALICE collaboration. b) Minimum bias distribution of the TPC track multiplicity with indicated bins for 70-80% and 0-5% centrality of the Pb-Pb collision at $\sqrt{s_{\mathrm{NN}}} = 2.76$ TeV. [?]

used in this analysis can be found in Table 4.3.

Centrality	$b_{\min}$ (fm)	$b_{\max}$ (fm)	$N_{\mathrm{part}}^{\mathrm{geo}}$ (syst %)	$N_{\mathrm{coll}}^{\mathrm{geo}}$ (syst %)	$T_{\mathrm{AB}}^{\mathrm{geo}}$ (syst %)
0-5%	0.00	3.48	382.7 (0.6)	1684.4 (8.2)	26.20 (3.2)
5-10%	3.48	4.91	329.4 (1.1)	1316.0 (8.2)	20.56 (3.3)
10-20%	4.91	6.95	260.1 (1.5)	921.2 (10.0)	14.39 (3.1)
20-40%	6.95	9.81	157.2 (2.0)	438.4 (9.7)	6.85 (3.3)
40-60%	9.81	12.03	68.56 (2.9)	127.7 (8.8)	1.996 (4.9)
60-80%	12.03	13.89	22.52 (3.4)	26.71 (7.3)	0.4174 (6.3)

Table 4.3.: Geometric properties ($N_{\mathrm{part}}^{\mathrm{geo}}$, $N_{\mathrm{coll}}^{\mathrm{geo}}$, $T_{\mathrm{AB}}^{\mathrm{geo}}$) of Pb–Pb collisions defined by sharp cuts in the impact parameter b including their systematic errors.

4.1.4. Monte Carlo Simulations for Pb–Pb Collisions

For heavy-ion collisions currently only one event generator is used in ALICE to obtain acceptance and efficiency corrections:

> **HIJING** [155]
> HIJING combines pQCD inspired models for multiple jet production with low p_{T} multistring phenomenology implemented along the lines of the LUND FRITIOF [172, 173] model and the Dual Parton Model [169], thus allowing to study multiparticle production in pp, p–A and A–A collisions. Moreover, the model includes descriptions for multiple minijet production with initial and final state radiation using the Pythia routines and nuclear shadowing of parton distribution functions. To simulate multiple collisions in p–A and A–A collisions Glauber geometry is used. Furthermore, the generator contains implementations of simple jet quenching models to study the energy loss in the hot and dense medium produced in heavy-ion collisions.
> Similar to Pythia, this generator has many tune parameters, which need to be adjusted for every new collisions system. Especially the total charged-particle multiplicity needs to be tuned to the measured quantity to correctly reproduce the data. The Monte Carlo samples used in our analysis were tuned to reproduce within reasonable errors the charged-particle multiplicity measured by the ALICE collaboration at $\sqrt{s_{\mathrm{NN}}} = 2.76$ TeV [171].

In our analysis four different HIJING Monte Carlo samples are used for the acceptance and efficiency corrections: LHC11a10a, LHC11a10a_bis, LHC11a10b_bis and LHC11a10b_plus. However, some of them were modified to enhance the signal for certain physics channels. These added signals have not been used in this analysis as to many different signals have been added and they could not be fully separated on the analysis level, introducing unphysical jumps in the efficiency. Moreover, even the signals added specifically for the π^0 and η analysis had been added with a discontinuous spectrum, which lead to even larger jumps in the efficiencies. Therefore, we decided to remove all added signals from our analysis and just select the underlying minimum bias event. The simulations do not have the same statistics in all centrality bins, like the data, therefore the statistical errors in the most central bin in our analysis are driven by the error of the efficiency corrections. Table 4.4 shows the available statistics in data and Monte Carlo for the different centrality classes and Monte Carlo samples. For each centrality class all four Monte Carlo samples are merged to obtain the final efficiencies.

Figure 4.4 shows the mean number of primary tracks measured by the TPC together with the result of the LHC11a10a_bis simulation for different centrality classes. The mean number of tracks is slightly higher in Monte Carlo simulations than in data. However, the general trend is quite

well reproduced. In heavy-ion collisions it is more important that the Monte Carlo simulations reproduces the multiplicities seen in the data, as the tracking in such high multiplicity environments is challenging and needs to be well understood. However, the discrepancies between data and Monte Carlo seen in the mean number of primary tracks are not worrisome as they just differ by a few percent ($< 5\%$ for central collisions). The fraction of photon candidates per event is shown in Figure 4.5 for the six centrality classes. It is stable with respect to time and reasonably well reproduced by the Monte Carlo. Small changes in the most central event class can be attributed to small changes in the centrality selection with respect to time, leading to a slightly lower number of photons per event for the second half of the data taking period.

	Sample	$\sqrt{s_{NN}}$	Centrality	Events with (PS+Vtx+$|z_{vtx}|$ <10)
Data	LHC10h, Pass2	2.76 TeV	0- 5%	8.43e+05
			5-10%	8.44e+05
			10-20%	1.68e+06
			20-40%	3.37e+06
			40-60%	3.37e+06
			60-80%	3.37e+06
MC	LHC11a10a *Minimum Bias*	2.76 TeV	0- 5%	8.46e+03
			5-10%	1.04e+04
			10-20%	2.31e+04
			20-40%	5.45e+04
			40-60%	6.15e+04
			60-80%	6.81e+04
	LHC11a10a_bis *Minimum Bias*	2.76 TeV	0- 5%	4.61e+04
			5-10%	5.43e+04
			10-20%	1.21e+05
			20-40%	2.87e+05
			40-60%	3.30e+05
			60-80%	3.66e+05
	LHC11a10b_bis *Minimum Bias + flat p_T $\Lambda, \Omega, K_s^0, \pi^\pm, K$ … + π^0 in p_T hard bins*	2.76 TeV	0- 5%	3.40e+04
			5-10%	3.76e+04
			10-20%	8.36e+04
			20-40%	2.00e+05
			40-60%	2.37e+05
			60-80%	3.04e+05
	LHC11a10b_plus *Minimum Bias + heavy resonances + flat p_T $\Lambda, \Omega, K_s^0, \pi^\pm, K$ … + π^0 in p_T hard bins*	2.76 TeV	0- 5%	4.68e+04
			5-10%	5.03e+04
			10-20%	1.08e+05
			20-40%	2.50e+05
			40-60%	2.94e+05
			60-80%	3.75e+05

Table 4.4.: Number of events passing our event selection in Pb–Pb for data and Monte Carlo simulations.
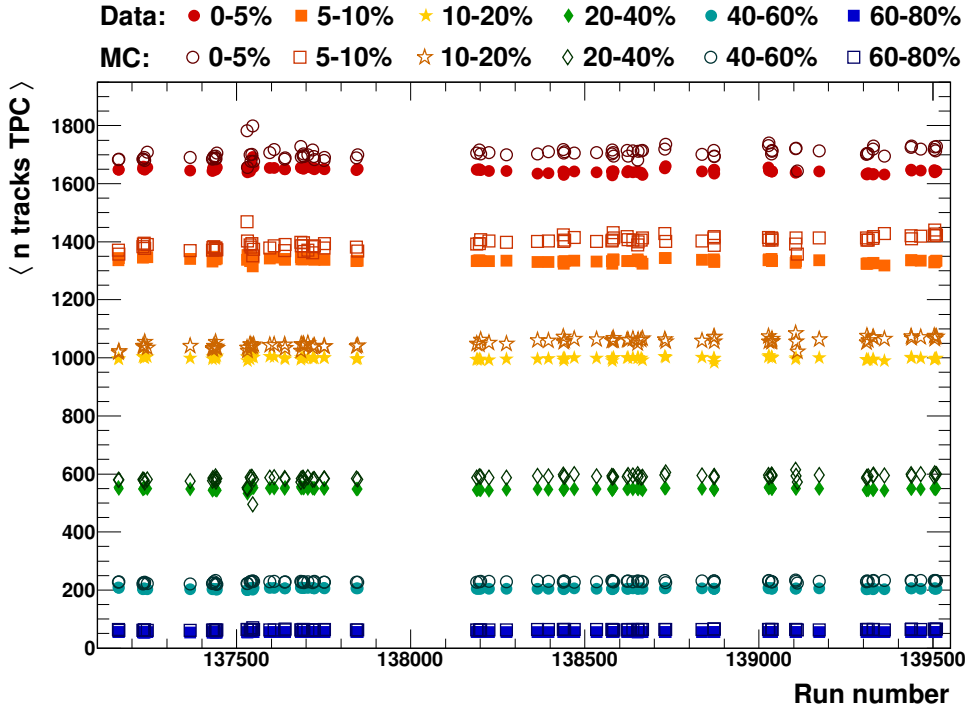
Figure 4.4.: Mean number of primary tracks measured in the TPC ($|\eta| < 0.8$) compared to minimum bias Monte Carlo simulations (LHC11a10a_bis) for the different centrality classes.
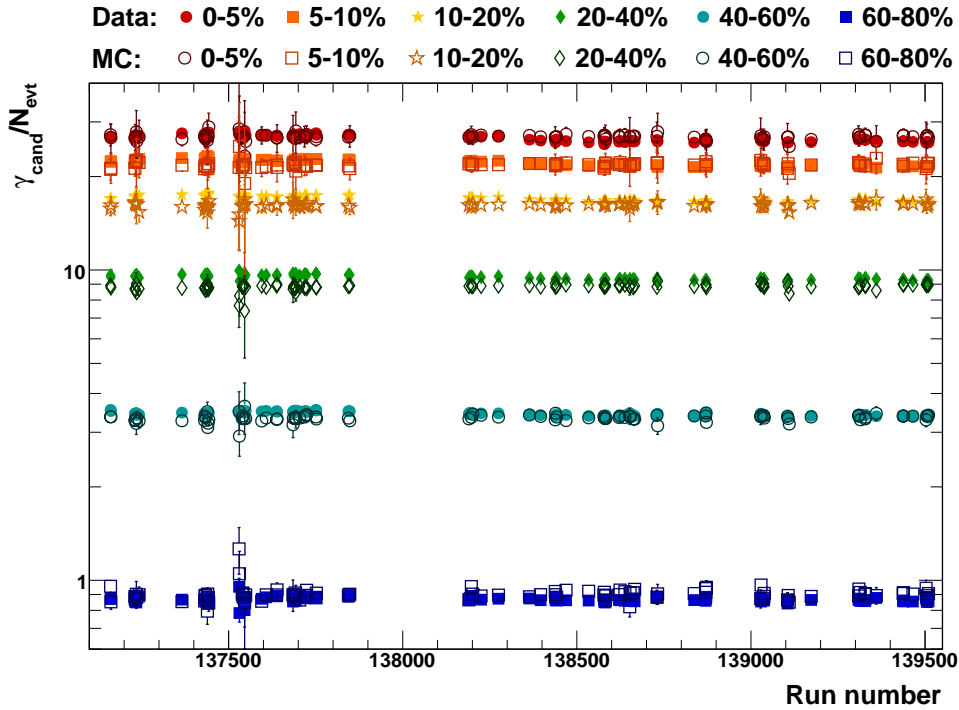

Figure 4.5.: Fraction of photons candidates in Pb–Pb events normalized to the number of events in the corresponding centrality class.

4.2. Photon Reconstruction and Selection

Photons, which have converted in the detector material, can be reconstructed via their conversion products using a secondary vertex finder, as already described in Section 3.2.4. The precision of the reconstructed conversion point can be improved by recalculating the position of the secondary vertex under the assumption that the momenta of the decay products are parallel at the point of their creation. This recalculation is described in detail in [119, 174] and the resulting spatial resolution of the photons in R, X, Y, Z and φ will be discussed in Section 5.1.2. The criteria for selection of photon candidates for the material budget and the neutral meson analysis can be split in three categories: track and V^0 selection, electron identification cuts and photon selection cuts.

4.2.1. Track and V^0 selection

Track & V0 cuts	Material Budget	Meson Analysis pp	Meson Analysis Pb–Pb
V0-finder	On-the-Fly/ Offline	On-the-Fly	On-the-Fly
minimum track p_T cut	$p_{T,track} > 0.05$ GeV/c	$p_{T,track} > 0.05$ GeV/c	$p_{T,track} > 0.05$ GeV/c
Cut on $\frac{N_{cluster\ TPC}}{N_{findable\ clusters}}$	$> 60\%$	$> 30\%$ (0.9, 7 TeV) $> 60\%$ (2.76 TeV)	$> 60\%$
η-cut for tracks & V^0s	$\|\eta_{track,\ V0}\| < 0.9$ $\|\eta_{track,\ V0}\| < 1.4$ $0.9 < \|\eta_{track,\ V0}\| < 1.4$	$\|\eta_{track,\ V0}\| < 0.9$	$\|\eta_{track,\ V0}\| < 0.9$
Cut on R_{conv}	0 cm $< R_{conv} <$180 cm	5 cm $< R_{conv} <$180 cm	5 cm $< R_{conv} <$180 cm
Cut on Z_{conv}	$\|Z_{conv}\| < 240$ cm	$\|Z_{conv}\| < 240$ cm	$\|Z_{conv}\| < 240$ cm.

Table 4.5.: Standard cuts for the track and V^0 selection for the different analysis.

The first category reflects the basic track and V^0 selection criteria. The standard cuts for the different analysis can be found in Table 4.5.

In this analysis the On-the-Fly V^0-finder is taken as the default one. However, for the systematic error estimate on the material budget we use the Offline V^0-finder as a systematic error source. One of the reasons for choosing the On-the-Fly V^0-finder as the standard method is the better conversion point resolution in pp and Pb–Pb collisions. In pp collisions both V^0 finders have been carefully optimized to give approximately the same efficiency and raw yields. For Pb–Pb collisions on the other hand the Offline V^0-finder has very tight cuts for all secondary tracks, while for the On-the-Fly V^0-finder they were relaxed for electron candidates. The tight cuts for the Offline V^0-finder are necessary to reduce the combinatorial background and the computing time during the reconstruction. However, they reduce the raw photon signal by $\approx 50\%$ (30%) in central (peripheral) collisions. To be able to recover this loss the tight cuts need to be well reproduced in the Monte Carlo simulation and therefore the Offline V^0-finder is bound to be more sensitive to differences between simulation and recorded data.

After having selected the V^0-candidates, we require that the secondary tracks originating in these V^0s have no kink-topology, fulfill the TPC refit condition and have opposite charges. Moreover, the secondary particles have to have a minimum momentum of 50 MeV/c. The last cut based on the track quality requires that the tracks have a minimum fraction of the TPC clusters which would theoretically be possible, taking into account their point of origin and their inclination.

Furthermore, the tracks and V^0 candidates have to pass the respective η-cuts given in Table 4.5. The η of the particle is determined based on the angle between the beam-axis and the orientation of

the 3-momentum vector of the particle in the ZR-plane alone. As the starting point of the track is not taken into account, some photon candidates will pass this cut although they are not contained in the geometrical η region defined by the center of the detector and the corresponding angles in the ZR-plane. Therefore, an additional condition has to be satisfied for the V^0 candidates:

$$R_{\text{conv}} < |Z_{\text{conv}}| \times ZR_{\text{Slope}} - Z_0, \tag{4.4}$$

where $ZR_{\text{Slope}} = \tan(2 \times \arctan(\exp(-\eta_{\text{cut}})))$, $Z_0 = 7$ cm and the coordinates of the secondary vertices (i.e. $R_{\text{conv}}, Z_{\text{conv}}$) are determined with respect to the nominal center of the detector $(X,Y,Z) = (0,0,0)$ and do not depend on the primary vertex position. This cut is often referred to as *line-cut* and is similar to a cut on the geometrical η distribution of the conversion points with (0,0,0) as point of their origin. If we want to have a gap in the η distribution we need to apply a similar cut on the inner border of the η distribution. To ensure the reconstruction of the secondary tracks in the TPC, secondary vertices with $R_{\text{conv}} > 180$ cm and $Z_{\text{conv}} > 240$ cm are rejected. Furthermore, we reject all V^0s with $R_{\text{conv}} < 5$ cm in the neutral meson analysis to reduce the contamination from π^0 and η Dalitz decays.

4.2.2. Electron Identification Cuts

PID cuts	Material Budget	Meson Analysis pp	Meson Analysis Pb–Pb
$n\sigma_e$ TPC dE/dx	$-3 < n\sigma_e < 5$	$-4 < n\sigma_e < 5$	$-3 < n\sigma_e < 5$
$n\sigma_\pi$ TPC dE/dx	0.25 GeV/c $< p <$ 3.5 GeV/c: $n\sigma_\pi > 2$ $p > 3.5$ GeV/c: $n\sigma_\pi > 0.5$	0.25 GeV/c $< p <$ 3.5 GeV/c: $n\sigma_\pi > 2$ $p > 3.5$ GeV/c: $n\sigma_\pi > 0.5$	0.4 GeV/c $< p <$ 100 GeV/c: $n\sigma_\pi > 3$
$n\sigma_e$ TOF	none	none	$-5 < n\sigma_e < 5$

Table 4.6.: Standard electron identification cuts for the different analysis. The cuts are applied in the order given in the table. The values stated here show which part of the distributions is kept.

In order to select the photons among the remaining V^0s (γ, K_S^0, Λ and $\overline{\Lambda}$), electron selection and pion rejection cuts are applied. The identification of electrons in ALICE can be done using five different techniques (see Section 3.2.1) :

- dE/dx in the ITS
- dE/dx in the TPC
- time-of-flight measurement with the TOF
- transition radiation or dE/dx measurement in the TRD
- energy deposit in the calorimeters

In this analysis we rely mainly on the dE/dx measurement in the TPC. The other techniques have not been used as they either were not ready at the time of the analysis (TRD) or just a very small fraction of the secondary tracks has the corresponding signal and, therefore, the statistics would be significantly reduced (TOF, ITS, TRD, calorimeters). Moreover, as we do not need the electron sample to be 100% pure we can afford to have some contamination. In Table 4.6 the PID selection criteria for the different analysis presented in this thesis are shown.

The main cut for the electron identification is a cut around the expected electron energy loss hypothesis in the TPC dE/dx in terms of number of sigmas ($n\sigma_e$) around this hypothesis. Even a selection of $|n\sigma_{e,\text{TPC}}| < 5$ removes 35% (10%) of the electron candidates from the secondary
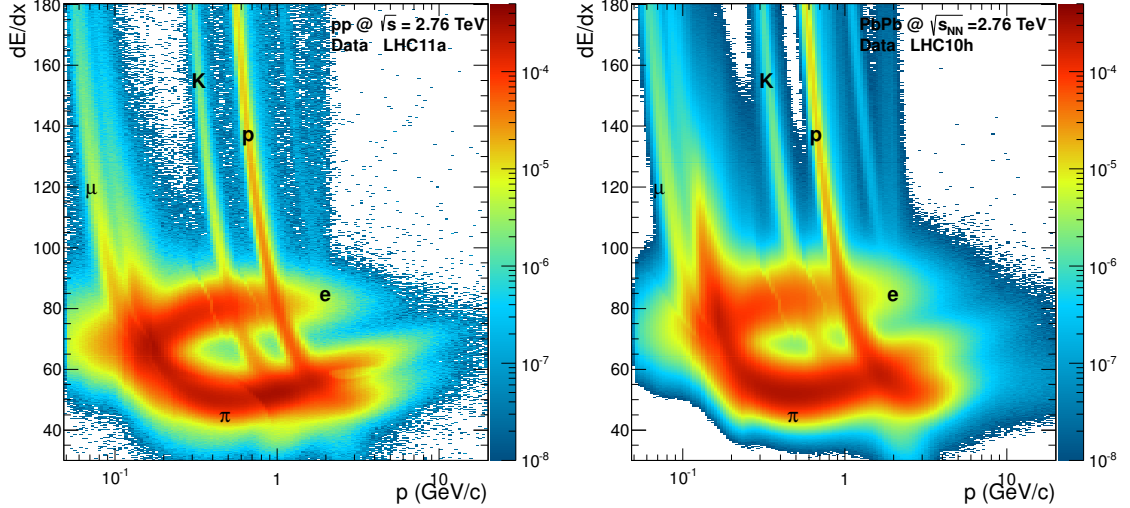
Figure 4.6.: dE/dx distribution in the TPC as a function of momentum for all secondary tracks, normalized to the number of events, after the basic track and V0 selection cuts for minimum bias pp (left) and Pb–Pb collisions (right).
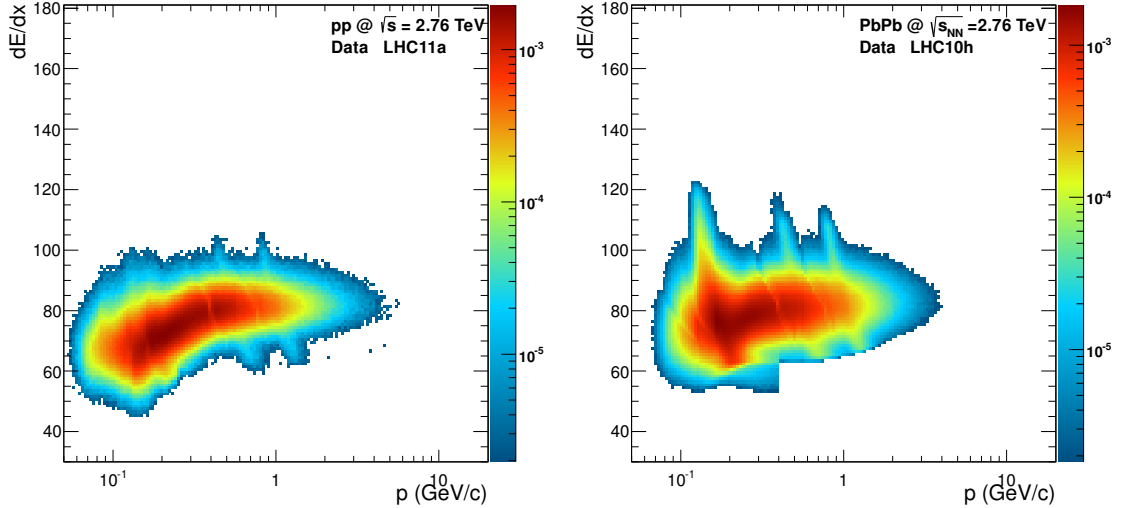

Figure 4.7.: dE/dx distribution for positrons for pp (left) and central (0-5%) Pb–Pb collisions (right) after all electron and photon selection cuts.

track sample in pp (Pb–Pb) collisions. Tightening this cut to the values mentioned in Table 4.6 leads to larger rejection factors for pions, while the electrons are kept as only a minimal fraction is contained in excluded regions.

In order to further remove the pions, which start to merge with the electrons above $p \approx 4$ GeV/c, as it can be seen in Figure 4.6 , we use a pion rejection cut based on the distance in terms of $n\sigma_\pi$ to the expected pion energy loss hypothesis (pion-line) in the TPC. This cut can be varied for two different momentum ranges in order to keep all tracks at high momenta. The standard cut for the pp analysis removes all tracks between 0.25 GeV/c < p < 3.5 GeV/c which have a $n\sigma_\pi \leq 2$, everything which is further away than 2 σ_π above the pion line is kept. For tracks with a momentum higher than 3.5 GeV/c we exclude everything which is below 0.5 σ_π above the pion line.

Figure 4.6 shows the dE/dx distribution for secondary tracks normalized to the respective number of events for pp and Pb–Pb collisions with only the tracks cuts applied. Therefore, the pions, protons and kaons still dominate the secondary track sample. However, compared to the distribution for primary tracks (Figure 3.5) the enhancement of electrons in the secondary track sample
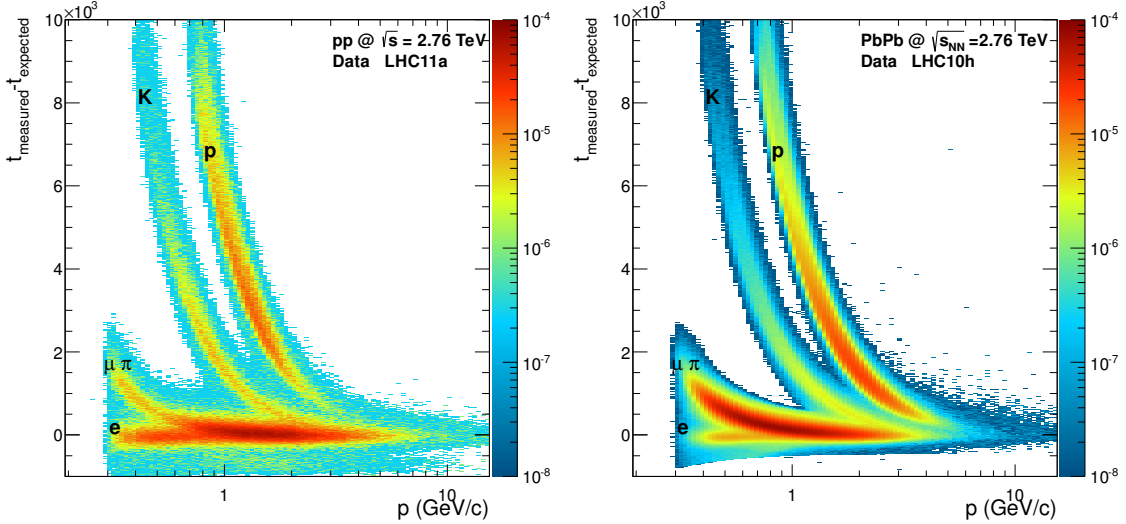
49

Figure 4.8.: Distribution of the TOF time difference for all electron candidates, after a $5\sigma_e$ cut in the TPC, versus momentum for pp (left) and Pb–Pb collisions (right).
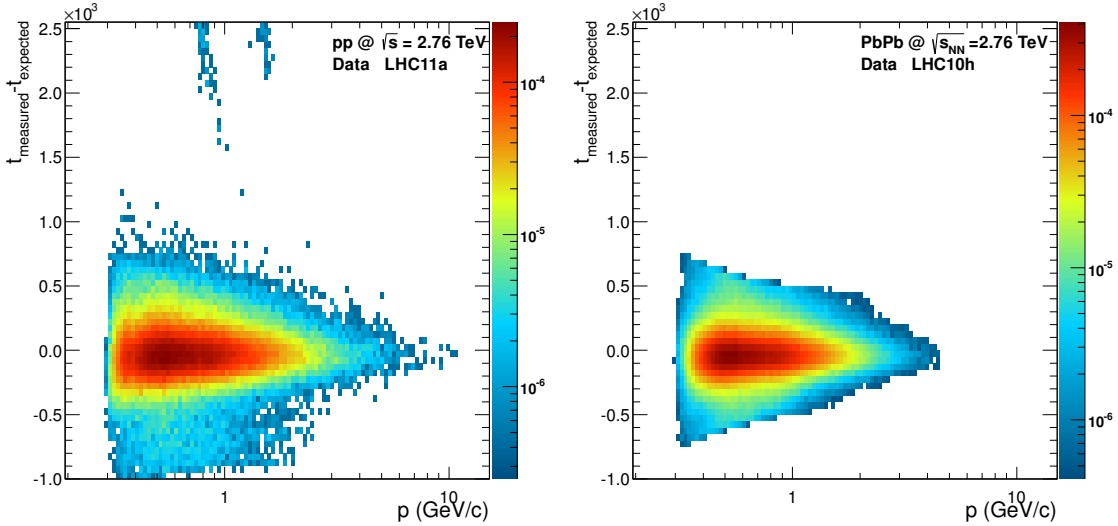

Figure 4.9.: Distribution of the TOF time difference for all electron candidates from photon candidates, after all PID and photon selection cuts, versus momentum for pp (left) and Pb–Pb collisions (right)r. While for the *pp* data sample no cut on the TOF $n\sigma$ around the electron line was applied, a $5\sigma_e$ inclusion was used for the Pb–Pb data sample.

is clearly visible. While the statistics in pp and Pb–Pb is quite different the resolutions of the dE/dx distributions for the different particles seems to be compatible. The dE/dx distribution for positrons coming from the final photon candidates for pp and central (0-5%) Pb–Pb collisions, can be seen in Figure 4.7. This plot shows the combined effects of all electron PID cuts and the photon cuts, which will be described in the next section. Moreover, it shows that there is still a fraction of pions, protons and kaons left, which is larger in central Pb–Pb collisions than in pp collisions, thus causing a larger combinatorial background in Pb–Pb collisions. The sharp edges at $p = 0.25$ GeV/c and $p = 3.5$ GeV/c (pp data) are caused by the rejection of pions below 2σ above the theoretical Bethe-Bloch curve for pions.

For Pb–Pb collisions in addition to the TPC dE/dx cuts a 5σ inclusion around the electron hypothesis in the TOF is used to further remove the background. However, only $3-5\%$ of the secondary tracks originating in our photon candidates reach the TOF. Therefore, we only use this cut if the track could be matched to a signal in the TOF detector, otherwise we only use the PID provided by the TPC. The distribution of the time difference measured in TOF for all secondary tracks

reaching the TOF and passing a $\pm 5\sigma_e$ cut in the TPC is shown in Figure 4.8 for both collision systems. From this plots it becomes obvious that part of the contamination, especially the protons and kaons, can be removed by a cut on the $n\sigma$ around the electron line in the TOF response. The distributions after all PID and photon cuts can be seen in Figure 4.9. For the pp sample no TOF cut was used as the background under the π^0 peak behaves well and including another PID detector might introduce additional systematic error sources.

4.2.3. Photon selection

Photon cuts	Material Budget	Meson Analysis pp	Meson Analysis Pb–Pb
χ^2_γ /ndf	< 20	< 30 (0.9, 7 TeV) < 20 (2.76 TeV)	< 20
q_{T}	< 0.02 GeV/c	< 1 GeV/c (0.9, 7 TeV) < 0.05 GeV/c (2.76 TeV)	< 0.05 GeV/c

Table 4.7.: Standard photon selection cuts for the different analysis.

After having selected mainly electrons as legs of the V^0s, the photon sample reaches a purity of approximately 80%. To improve the purity even further we can use additional constraints on the reconstructed photon mass and on the opening angle between the reconstructed photon momentum vector and the vector joining the collision vertex and the conversion point. As the photons are reconstructed using the AliRoot KFParticle package [175] we can impose these constraints in the construction of the photons and afterwards cut on the χ^2/ndf, thus cutting in the "quality" of the photon. However, it has to be verified, that the distribution can be reproduced with Monte Carlo simulations to avoid errors in the efficiency calculation due to this cut. The comparison between data and Monte Carlo can be seen in Figure 4.10 for pp and 0-5% central Pb–Pb collisions. The distribution is peaked at zero and the distribution can be reproduced by the Monte Carlo simulation within reasonable errors. To remove fake photon candidates we use a minimum opening angle cut of 5 mrad.

The remaining K^0_S, Λ and $\overline{\Lambda}$ can be removed from the sample using a cut in $q_{\mathrm{T}} = p \times \sin\theta_{\mathrm{mother\text{-}daughter}}$ of the Armenteros-Podolanski plot [176]. The Armenteros-Podolanski plot shows the projection
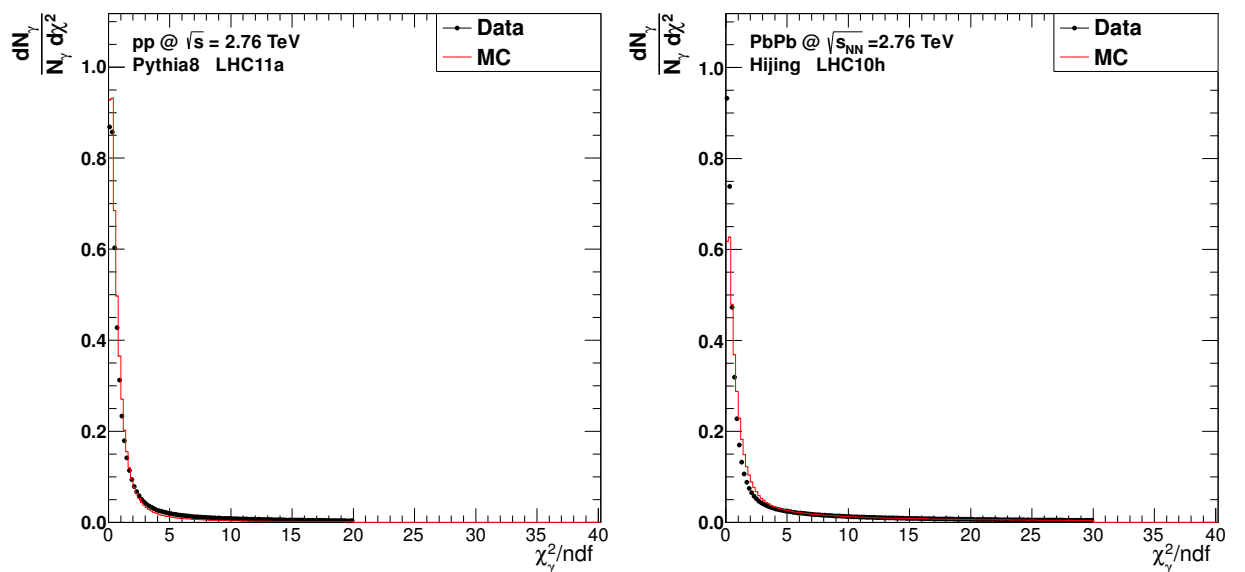

Figure 4.10.: Comparison of the distribution of the χ^2/ndf of the photon candidates in data and Monte Carlo for pp (left) and central Pb–Pb collisions (right).
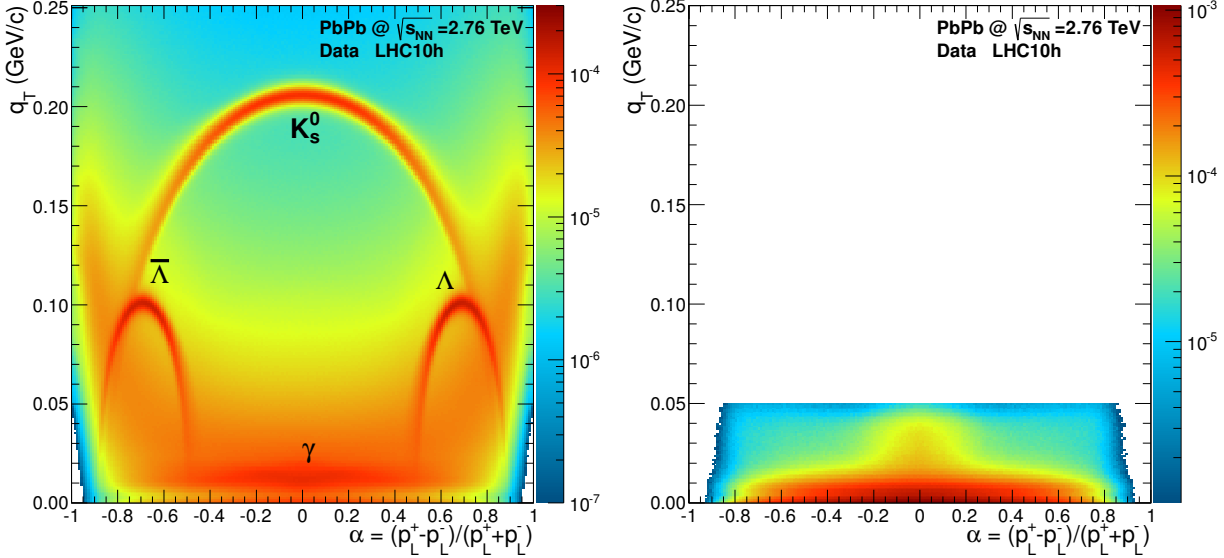
Figure 4.11.: Armenteros-Podolanski-Plot of all V0 candidates after the basic track and V0 cuts, mentioned in Section 4.2.1 , for the Pb–Pb minimum bias events (left). On the right the remaining photon candidates after all cuts are shown in the same representation for the 0-5% central Pb–Pb collisions.

of the momentum of the daughter particle with respect to the mother particle in the transverse direction (q_T) versus the longitudinal momentum asymmetry ($\alpha = (p_L^+ - p_L^-)/(p_L^+ + p_L^-)$). As the daughter particles of the photon fly, in the laboratory frame, in the same direction as the photon within a very small opening angle, the q_T of the real photons is close to zero. Moreover, the distribution is symmetric in α as the decay products have the same mass. For heavier particles the opening angle is larger and, therefore, the q_T is larger. Cutting in the q_T distribution thus allows to separate photons from the remaining contamination of K_S^0, Λ and $\overline{\Lambda}$. Figure 4.11 (left) shows the Armenteros-Podolanski-Plot for all V0 candidates after the basic track cuts, which have been mentioned in Section 4.2.1 for minimum bias Pb–Pb collisions. Four different distribution are clearly visible: the symmetric distributions of the photons with a q_T close to 0 GeV/c and the K_s^0's with a q_T ranging from $0.1 - 0.23$ GeV/c. Moreover, the asymmetric distributions representing the Λ and $\overline{\Lambda}$ can be identified around $\alpha = \pm 0.7$. The asymmetry in α for Λ and $\overline{\Lambda}$ is caused by the mass difference of the decay products. The right plot of Figure 4.11 shows the distribution after all electron PID and photon cuts, the sharp line at 0.5 GeV/c is caused by the q_T cut itself. It can be seen, that only very few Λ and $\overline{\Lambda}$ survive our cuts below the sharp q_T cut, leading to a high purity photon sample.

The purity (ϵ_{pur}) of the remaining photon candidates surviving the meson cuts in pp and Pb–Pb collisions is shown in the left plot of Figure 4.12. The purity is defined as the fraction of reconstructed true photons (verified with Monte Carlo information) to all reconstructed photon candidates $\epsilon_{pur} = \frac{N_{reco,\ true}^\gamma}{N_{reco}^\gamma}$. For Pb–Pb collisions the purity at low transverse momentum decreases from $\sim 99\%$ to 83% ($p_T = 0.2$ GeV/c) with increasing centrality. This change at low momentum can be attributed to the increasing multiplicity especially at low momentum, leading to a larger combinatorial background if the photon selection cuts stay the same for all centralities. At high p_T the decrease of purity versus centrality is seen as well, however the range is smaller. The black points represent the purity in pp collisions. Although the cuts are not as tight as in Pb–Pb collisions the purity at low momenta is similar to the purity in mid central Pb–Pb collision. At high transverse momenta on the other hand it drops significantly as the rejection of pions via the TPC dE/dx is relaxed and therefore the contamination with hadrons is larger. For the material budget analysis the purity (right plot of Figure 4.12) is close to the purity measured for peripheral Pb–Pb collisions.

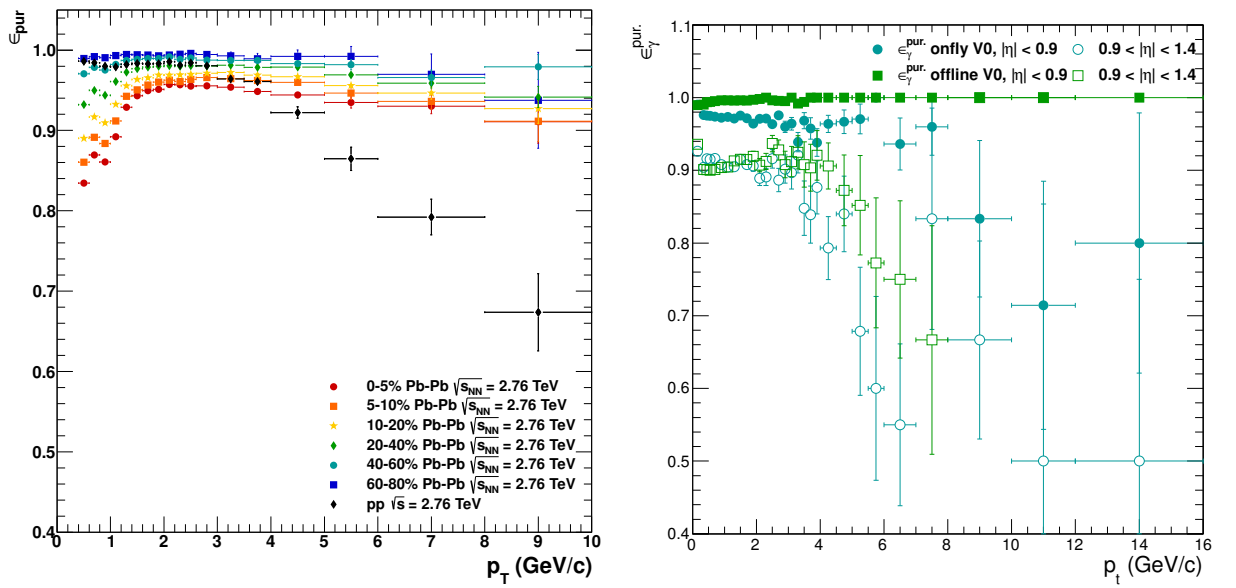**Figure 4.12.:** Purity of the photon candidates surviving all cuts for the meson analysis for pp and Pb–Pb collisions (left) and for the material cuts for pp collisions (right). The right plot shows the purity for the two different V0-finders, On-The-Fly (blue) and Offline (green), in addition the two different η regions are shown, $|\eta| < 0.9$ (full symbols) and $0.9 < |\eta| < 1.4$ (open symbols).

5. Material Budget

This chapter will be mainly dedicated to the systematic error estimate of the material budget in ALICE up to the middle of the TPC ($R < 180$ cm) with the PCM. It provides a cross check of the real detector geometry and the chemical composition of the material compared to the implemented ones in the simulation. The first section will be devoted to the method, which has already been explained in detail in [119], while the second section will focus on the obtained resolution. Afterwards, the current estimate on the systematic error of the material budget will be presented. Furthermore, a second method to check the implementation of the detector geometry will be presented in this chapter based on secondary hadronic interactions.

5.1. Photon Conversions

5.1.1. The Method

The ALICE detector system was designed to keep the material budget in the central acceptance to a minimum, while having at the same time very good vertex resolution to be able to reconstruct secondary vertices from hyperons, as well as from D and B mesons. Moreover, the geometry and chemical composition influence the charged particle tracking and reconstruction, the amount of produced secondaries, the energy loss corrections, the photon conversion probability and many other quantities. Therefore, the implementation of the detectors in AliRoot needs to be as accurate as possible. However, this implementation does not only affect the Monte Carlo simulations but the reconstruction as well, as the geometry and energy-loss correction, provided by GEANT3 [133] from the geometry implemented in AliRoot, are used in the track reconstruction.

The main process exploited in this analysis, as described in Section 2.3, are photon conversions (pair productions). This process is sensitive to the material (quantity, geometry and chemical composition) in which the photons convert. The main contributors to the material budget within the fiducial acceptance ($|\eta| < 0.9$) up to $R_{\mathrm{conv}} < 180$ cm are the beam pipe, the 6 layers of the ITS detector, the TPC vessels and part of the TPC drift gas. A summary of the detailed locations of the individual parts is given in Table 5.1. In this analysis, photons can be reconstructed up to $|\eta| < 1.4$, as they need to point to the primary vertex but still need to be reconstructed in the TPC with a sufficient track length. In the η region ($0.9 < |\eta| < 1.4$) mainly support and service structures of the ITS and TPC can be found. Only the SPD and TPC can provide track points in this region, thus the resolution of the conversion points is worse than for the central acceptance. The details on the coverage (η, φ) of the individual detectors can be found in Table 3.1. The material distribution in units of radiation length X_0 as a function of pseudo rapidity is presented in Figure 5.1.

In this analysis we compare the amount of reconstructed converted photons in data and Monte Carlo simulation and extract from this the systematic error of the material budget. The photons observed in our detector ($N_\gamma^{\mathrm{observed}}$) are composed of the following sources.

$$N_\gamma^{\mathrm{produced}} = N_\gamma^{\pi^0} + N_\gamma^{\eta} + N_\gamma^{\omega} + N_\gamma^{\eta'} + N_\gamma^{\phi} + N_\gamma^{\mathrm{direct}} + N_\gamma^{\mathrm{add}}. \tag{5.1}$$

The additional sources which are not mentioned explicitly (N_γ^{add}) contribute less than 1 ‰ to the total amount of photons. In the Monte Carlo simulation only primary photons or photons which

Name	R	R bin	R range (cm)	X (% X_0)
Beam pipe	2.98	00	[0.0,3.5[	0.226
SPD1	3.9	01	[3.5,5.75[	1.14
SPD2	7.6	02	[5.75,9.5[	1.14
Thermal shield/support	9.0	03	[9.5,13.0[	0.52
SDD1	15.0	04	[13.0,21.0[	1.13
Thermal shield	21.0-23.1	04/05		0.25
SDD2	23.9	05	[21.0,27.5[	1.26
Thermal shield	25-35	06	[27.5,35.0[	0.53
SSD1	38	07	[35.0,42.0[	0.83
SSD2	43	08	[42.0,55.0[	0.86
Thermal Shield	59.0-59.5	09	[55.0,72.0[	0.53
Air	0-60.65	09		0.08
TPC inner containment vessel	60.65	09		1.0
CO_2 volume	60-78.8	09/10		0.085
TPC inner field cage vessel	78.8	10	[72.0,79.5[	0.401
TPC rods +Ne:CO_2:N_2	80	11	[79.5,90.0[	1.4
Ne:CO_2:N_2 (R<180 cm)	78.8-180	12	[90.0,180.0[	0.607

Table 5.1.: Summary of the location of the different detectors and their corresponding material budget as implemented in the AliRoot simulation for straight tracks perpendiculary to the detector surface. (tracks within the fiducial acceptance ($|\eta| < 0.9$). Definition of the bins used in radial direction in order to check the material description between data and Monte Carlo simulation.
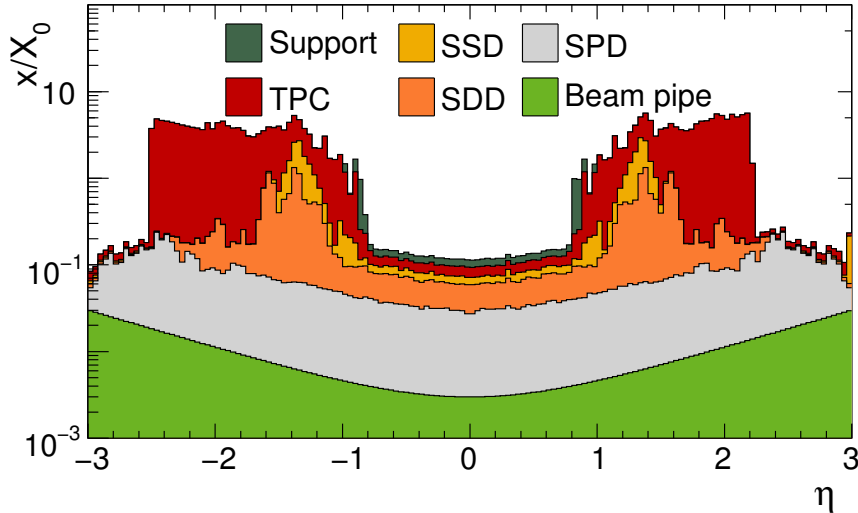

Figure 5.1.: Material distribution (in radiation length X_0) of the ALICE central tracking region as implemented in the simulation, averaged over the azimuthal angle [159]. Contributions of individual sub-detectors include services and support structures.

have a primary particle as mother (e.g. π^0, η, η', ω, ϕ), are considered in the spectrum. A detailed description of the selected photons in the Monte Carlo simulation and the additional conditions, which need to be met for the converted photons can be found in [119]. The number of observed photons can be related to the material budget by

$$N_\gamma^{\text{observed}} = N_\gamma^{\text{produced}} \cdot P_{\text{conv}} \cdot \epsilon_\gamma^{\text{rec}}, \tag{5.2}$$

where P_{conv} is the conversion probability and $\epsilon_\gamma^{\text{rec}}$ the photon reconstruction efficiency. The conversion probability is related to the material budget by Equation 2.20. Due to the fact that the
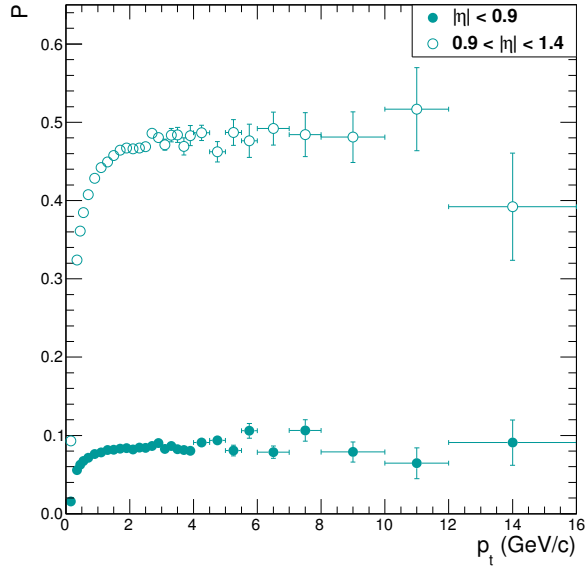
Figure 5.2.: Conversion probability for different regions in η.

reconstruction efficiency enters in the $N_\gamma^{\text{observed}}$, we have to ensure that the Monte Carlo simulation reproduces the data as close as possible. Therefore, applying too tight cuts in order to increase the purity of the photon sample can lead to larger discrepancies in the material. From Equation 5.2, one concludes that in the analysis one cannot distinguish between discrepancies in the reconstruction efficiency and material budget itself. To estimate the radiation length, which our photons traverse, we calculate the conversion probability as defined in Equation 2.21, in addition. Figure 5.2 shows the conversion probability versus transverse momentum for two different η regions. Fitting the plateau above a transverse momentum of approximately 2 GeV/c allows to extract the effective radiation length X/X_0 using Equation 2.20. For the central acceptance ($|\eta| < 0.9$) this yields an effective radiation length of $X/X_0 = 0.1114$, while for the larger η ($0.9 < |\eta| < 1.4$) the average effective radiation length is $X/X_0 = 0.8041$.

The total charged-particle multiplicity measured in data [177] is not reproduced by the simulations which are used in this analysis, as we have already seen in Figure 4.1. Thus, the total number of photons, which are produced initially, is different as well. To remove this uncertainty in our comparison we scale all distributions by the number of events (N_{evt} from Table 4.2) and the mean number of charged particles reconstructed in the corresponding η window in the TPC, passing the same event selection cuts.

The PCM method allows to perform a γ-ray tomography of the inner detectors (ITS and TPC) with sufficient precision to separate the different detector layers and even small structures within the individual detectors. The full two dimensional view of the γ-ray tomography measured in pp collisions at $\sqrt{s} = 7$ TeV in two different planes , XY and ZR, can be seen in Figure 5.3 and Figure 5.4, respectively. These plots reflect the sensitivity of this method, as even the detectors closest to the beam pipe can be separated from each other. Moreover, in particular in Figure 5.3, a lot of details in the individual layers of the ITS and TPC are visible.

5.1.2. Resolution of the Conversion Point

Although the two dimensional plots already show the enormous accuracy of the conversion analysis, this section will be dedicated to quantifying this observation. Therefore, the spatial resolution of the conversion point is estimated based on the Monte Carlo simulations.

Hereby each particle is stored at least twice, once with the real track properties propagated through the detector with GEANT and the second time with the reconstructed track properties, which are
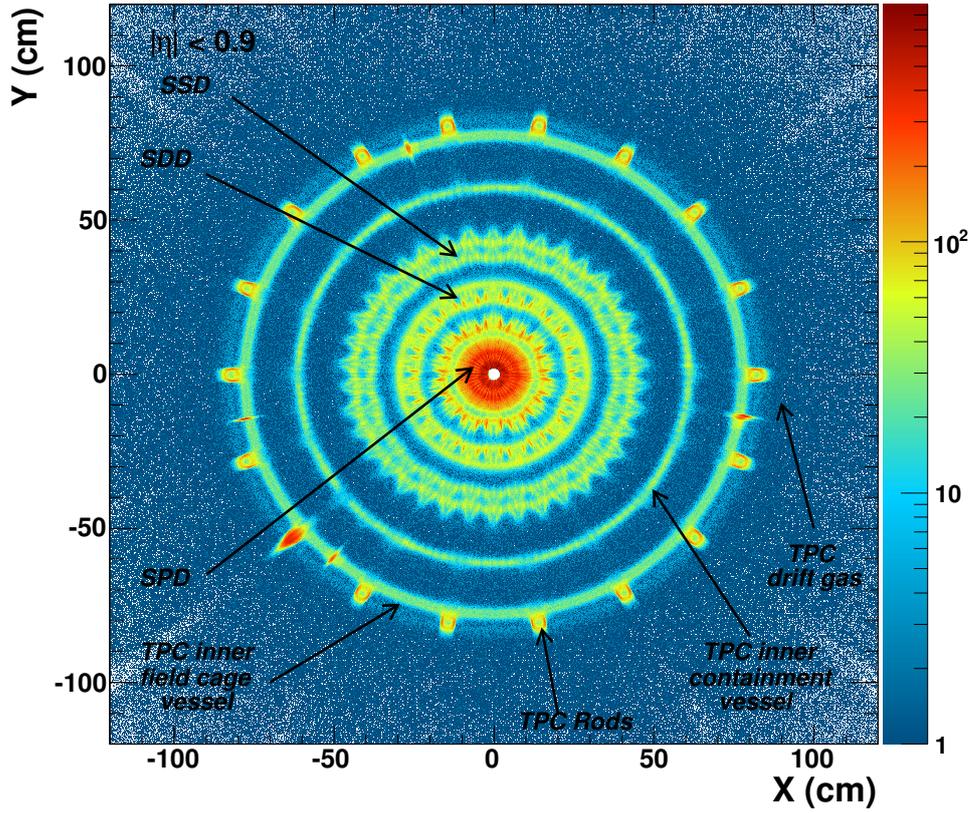
Figure 5.3.: Distribution of the conversion points in the XY-plane for the fiducial acceptance $|\eta| < 0.9$ measured for pp collisions at $\sqrt{s} = 7$ TeV. The detector geometry of the inner detectors is clearly visible as well as their φ distribution.
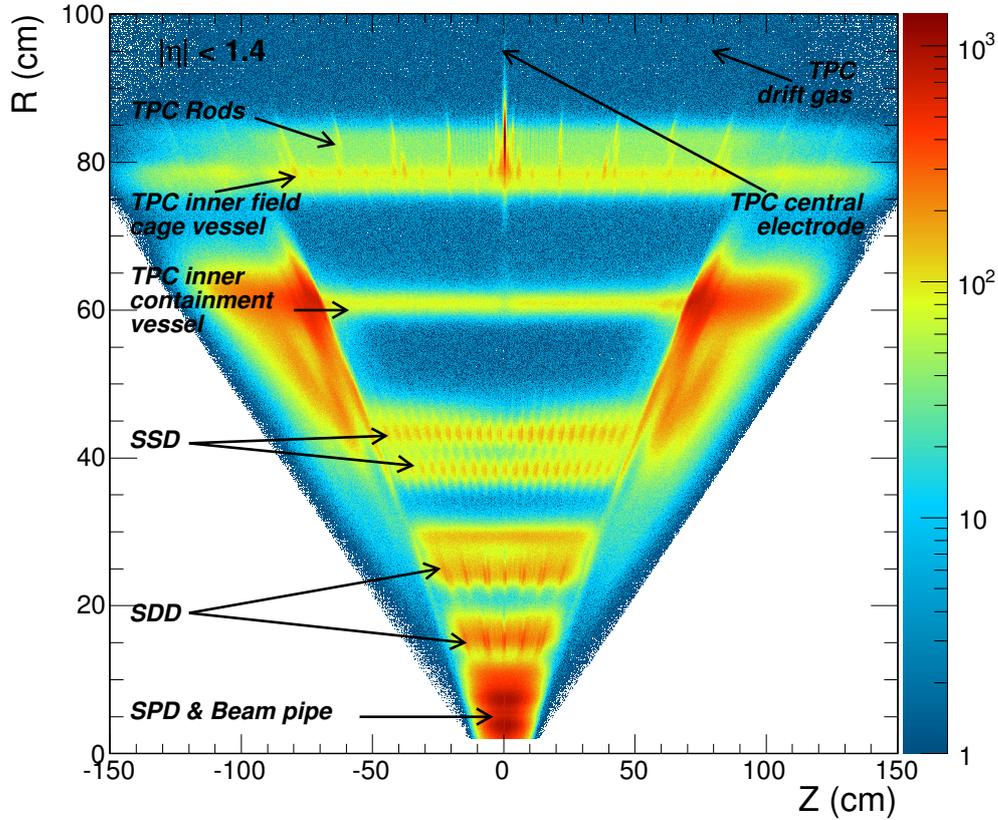
Figure 5.4.: Distribution of the conversion point in the ZR-plane for the full pseudo-rapidity range covered by the photon conversions measured for pp collisions at $\sqrt{s} = 7$ TeV. In the fiducial area the structures of the different detectors can be nicely separated, while for larger η due to missing space-point for the tracks the resolution gets worse and the structures are blurred out.

reconstructed under the same conditions as real data. Both tracks can be linked by their unique identification number. Therefore, we can compare the real parameter set with the reconstructed parameters to obtain the resolution in each parameter. To extract the resolution σ and a possible offset μ we subtract for each quantity the Monte Carlo truth from the reconstructed parameter.

$$\mathrm{d}X = X_{\mathrm{rec}} - X_{\mathrm{MC}} \qquad (X = R, Z, \Phi) \tag{5.3}$$

This distribution should be a Gaussian distribution centered, at approximately 0 for each parameter except p_{T}, as the deviation from the mean should be statistically distributed. The distribution of the transverse momenta can have a tail on the positive side due to energy loss via Bremsstrahlung. A Gauss function is defined as:

$$f(x) = \frac{1}{\sqrt{2\pi}\sigma} \exp\left(-\frac{1}{2}\left(\frac{x-\mu}{\sigma}\right)^2 \right), \tag{5.4}$$

where μ is the mean (or peak position) of the distribution, which is identified with a mean shift in the corresponding coordinate, and σ is the standard deviation, which we identify with the resolution in this coordinate. In order to avoid influences from a second Gaussian distribution, which can be attributed to multiple scattering at very low momenta and which has a much larger width, we restrict the fit range to $\pm 2\sigma$ around the mean μ. This is implemented with a recursive fit, which either stops because the width of the fit does not change anymore within a given precision ($\approx 0.05\%$) or because the fit did not converge within 100 iterations. The fitting routine tries to minimize the χ^2 of the fit.

As the material distribution is not homogeneous in R, Z and η the projections in these coordinates are optimized to have approximately the same integral in all bins, thus the binning in R, Z and η is not homogeneous. Figure 5.5 and Figure 5.6 show the mean shift μ in the conversion coordinate and the resolution in the individual coordinates versus the relevant spatial coordinates (R, Z, φ). The first row in both plots reflects the mean shift μ and the resolution, respectively, in φ (red points) given in μrad versus the position in R, Z and φ. The second row in both plots shows the the mean or resolution for R (blue points) and Z (green points) in cm, respectively. The mean shift in φ is smaller than ± 0.1 μrad and thus we can identify missing pieces with a very high precision in φ. The mean shift in R and Z is smaller than ± 0.2 cm in the regions where we have material, thus misplaced objects can be found on this level of precision. The mean resolution in φ is better than 3 μrad, while the resolution in R and Z is approximately 1.3 cm and 0.8 cm, respectively.

The first column of Figure 5.5 shows the mean shift in R, Z and φ versus R, while the first column of Figure 5.6 shows the resolution in the corresponding coordinates versus R. The mean shift and resolution in R versus R shows that the resolution is best shortly before or in a sensitive detector layer, while it is worst directly behind a sensitive detector layer. The same can be seen for the other resolution parameters versus R, however, the dependence is less visible. The resolution versus Z is shown in the second column of Figure 5.6. The resolutions in R and Z show opposite behavior versus Z as the resolution in R gets worse the more material the photons have to traverse, while the resolution in Z gets worse going further outwards in η. Therefore, the R resolution is worst for $Z = 0$, while the Z resolution is the best at $Z=0$. The resolution parameters versus φ all show the same behavior, reflecting the segmentation of the readout of the TPC in 18 sectors in φ. The resolution gets worse for the φ regions between two readout sectors.

The resolution plots for larger η ($0.9 < |\eta| < 1.4$) are shown in Figure 5.7 and Figure 5.8. In this η region the resolution is worse as we have no sensitive detector material between the TPC and the SPD, thus the extrapolation error of the tracking are larger and the resolution is worse. Nevertheless the mean shift in φ is only of the order of ± 0.5 μrad and the shift in R and Z is less than 3.5 cm in all regions in R, Z, and φ. The mean resolution in φ is of the order of 4 μrad, while the R and Z resolution are better than 7 cm in the region, where there is no sensitive detector
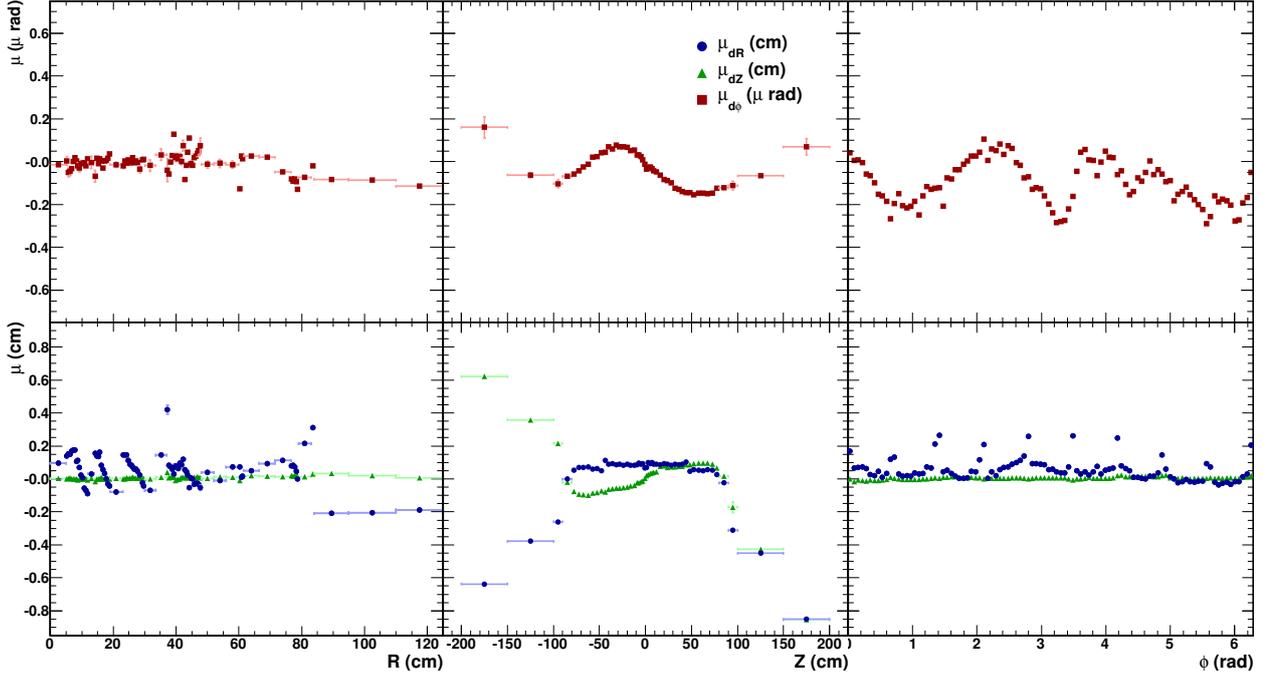
Figure 5.5.: Mean shift of the reconstructed φ (top), R and Z (bottom) coordinates versus R (left), Z (middle) and φ (right) for $|\eta| < 0.9$. The shifts are calculated fitting a Gaussian distribution to the $\mathrm{d}X = X_{\mathrm{rec}} - X_{\mathrm{MC}}$ ($X = R, Z, \Phi$), identifying the μ of the Gaussian distribution with the mean shift in the corresponding coordinate.

Figure 5.6.: Resolution of the reconstructed coordinates, φ (top), R and Z (bottom), of the conversion point versus R (left), Z (middle) and φ (right) for $|\eta| < 0.9$. The resolutions are calculated fitting a Gaussian distribution to the $\mathrm{d}X = X_{\mathrm{rec}} - X_{\mathrm{MC}}$ ($X = R, Z, \Phi$), identifying the σ of the Gaussian distribution with the resolution in the corresponding coordinate.
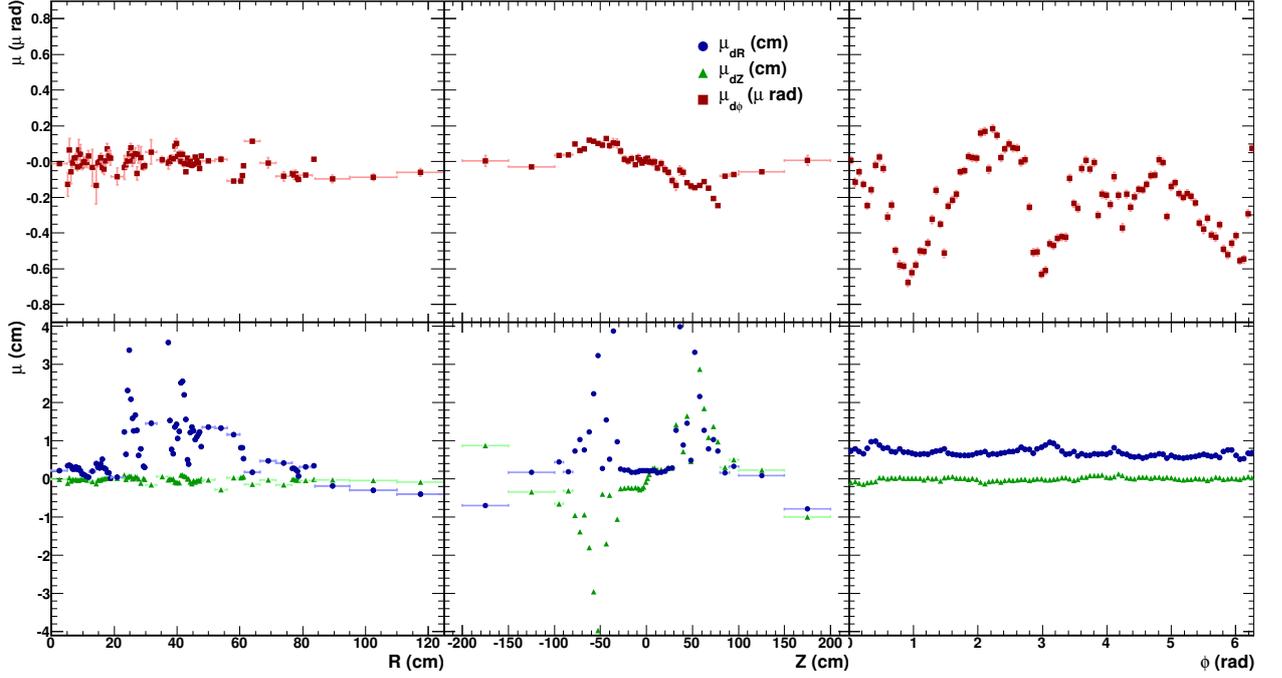
Figure 5.7.: Mean shift of the reconstructed φ (top), R and Z (bottom) coordinates versus R (left), Z (middle) and φ (right) for $0.9 < |\eta| < 1.4$. The shifts are calculated fitting a Gaussian distribution to the $dX = X_{\mathrm{rec}} - X_{\mathrm{MC}}$ ($X = R, Z, \Phi$), identifying the μ of the Gaussian distribution with the mean shift in the corresponding coordinate.
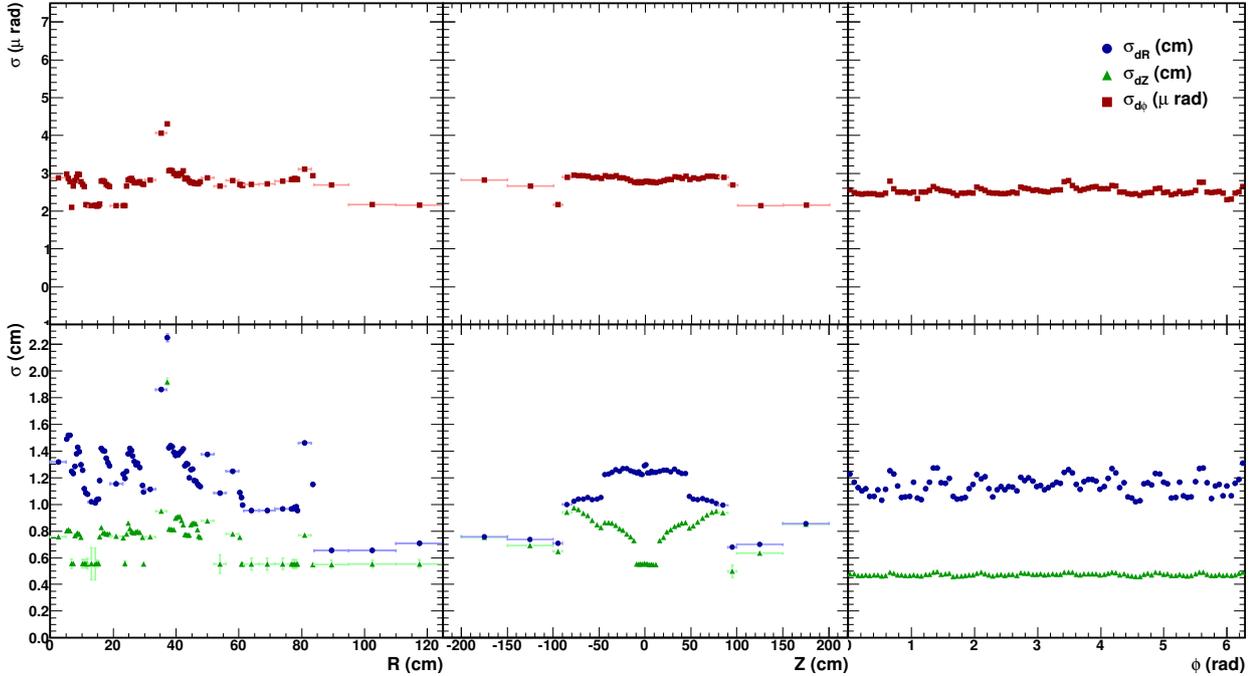

Figure 5.8.: Resolution of the reconstructed coordinates, φ (top), R and Z (bottom), of the conversion point versus R (left), Z (middle) and φ (right) for $0.9 < |\eta| < 1.4$. The resolutions are calculated fitting a Gaussian distribution to the $dX = X_{\mathrm{rec}} - X_{\mathrm{MC}}$ ($X = R, Z, \Phi$), identifying the σ of the Gaussian distribution with the resolution in the corresponding coordinate.
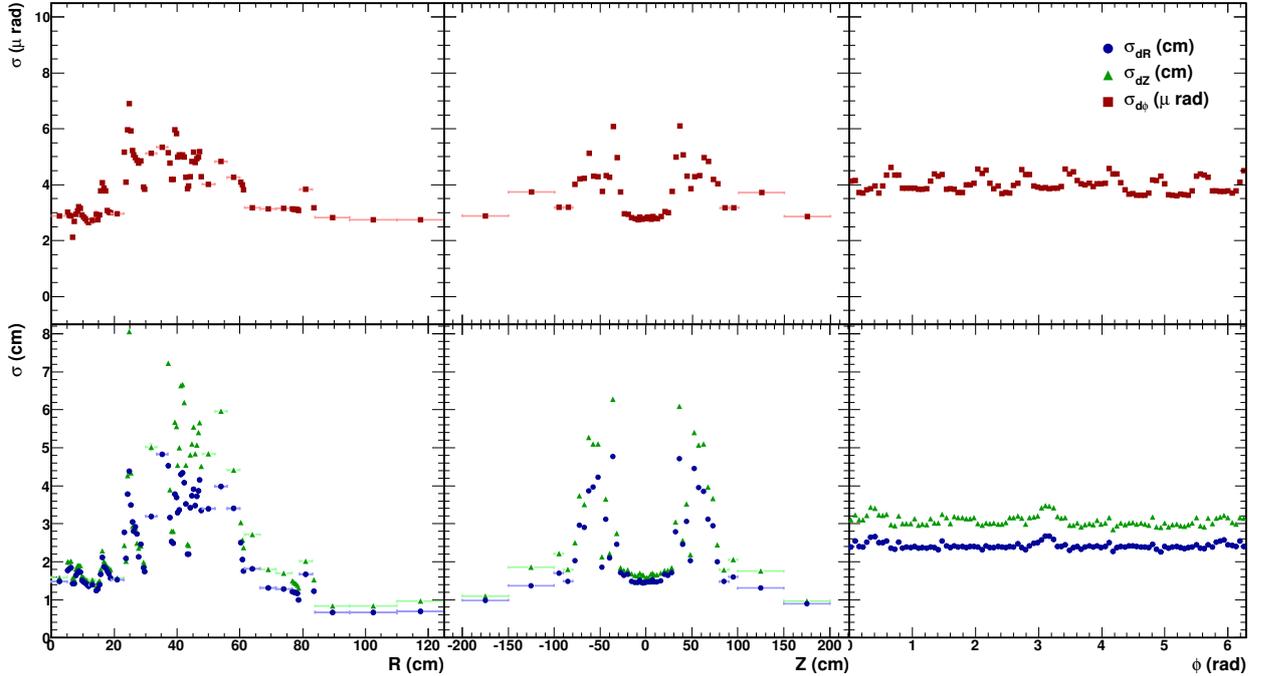
61

material and better than 2 cm, where the electron tracks can be constrained by additional track points.

In the future we will try to estimate the resolution based on data, as the method explained here relies on the correct modeling of the tracking and V^0 resolution in the simulation. For the data driven method we plan to select distinct pieces, like the central electrode, which have a very small width in reality and very little material around them to calculate the resolution. For each coordinate these pieces have to be chosen carefully, as they have to have a small width in the respective coordinate, should be surround by a much smaller amount of material and furthermore should be of uniform material. Good candidates for this material pieces for the resolution in R are the beam pipe and the TPC inner containment vessel. Furthermore, we need to disentangle the actual width of the material from the conversion point resolution.

5.1.3. Calculation of the Systematic Error

For the calculation of the systematic error of the material budget the R distributions of the converted photon in data ($\sqrt{s} = 7$ TeV) and two different Monte Carlo generators are compared. The same could be done for the Z, η or φ distribution. Choosing the R distribution, however, allows to estimate in addition the systematic error of the material budget up to a certain detector layer, which is needed for analyses in which the material error would mainly influence the secondary production.

The R distribution for the two different η slices is shown in Figure 5.9 for the full data sample recorded in 2010 at $\sqrt{s} = 7$ TeV and the merged Monte Carlo simulations generated with Pythia 6 tune Perugia 0. In addition to the reconstructed photons in data (black points) and in Monte Carlo simulation (red line) the individual contribution from true primary (secondary) photons are shown in yellow (green) indicating the purity of the sample. Moreover, the physics background originating in π^0 and η Dalitz decays (blue dashed area), the combinatorial background originating from hadronic decays (black shaded area) and from random combinatorics (brown shaded area) is displayed. For the fiducial η region ($|\eta| < 0.9$) the contamination is very low and the agreement betweend data and Monte Carlo simulation is very good. Going further outwards in η the contamination increases to up to 2-3%. Furthermore, the agreement gets worse as the implementation of the detectors in this region is not yet optimal. The same conclusion can be draw from the Z distribution, which is displayed in Figure 5.10 for the same η regions. The sharp cut in the right plot around 0 is caused by the line cut to exclude the fiducial region. For the larger η it becomes obvious that we are missing structures which are close to the TPC inner containment vessel and probably correspond to the thermal shield between the ITS and TPC, which was not implemented in the simulations used for the estimate on the material budget, yet. In this area there is still room for improvement and large efforts are undertaken to implement the missing pieces in all regions. However, this is a really challenging task as not all material pieces which were build, i.e. cables trees, are properly documented and thus hard to implement. The comparison of the number of photons in data and Monte Carlo simulations versus η can be seen in Figure 5.11. The comparison shows, that the data and simulation agree within 2-5% for central η, while the differ by a large amount at larger η. Furthermore, the onset of the additional contamination from true combinatorial background can be seen around $\eta = \pm 0.8$, in this region the resolution of the photons gets worse and thus the purity decreases. However, this contribution still stays below 2-3%.

The systematic error is calculated for the full R range ($0 < R < 180$ cm) by calculating the difference of the integral of the R distribution, which is normalized by the number of events and the mean number of charged particles, between data and Monte Carlo.

$$d_\gamma = \left(\frac{N_\gamma^{\mathrm{rec}}}{N_{\mathrm{ch}}} \right)_{\mathrm{data}} - \left(\frac{N_\gamma^{\mathrm{rec}}}{N_{\mathrm{ch}}} \right)_{\mathrm{MC}} \qquad (5.5)$$

Figure 5.9.: R distribution of the reconstructed conversion points (black) for $|\eta| < 0.9$ (left) and $0.9 < |\eta| < 1.4$ (right) compared to Monte Carlo simulations done with Pythia 6 tune Perugia 0 (red). The distribution for true primary (secondary) converted photons is shown in yellow (green), while the physics contamination from true π^0 and η Dalitz decays is shown in blue dashed. The true random combinatorial background is shown in brown, while the hadronic background (contamination from e.g. K_s^0, Λ, $\overline{\Lambda}$) is shown in black.
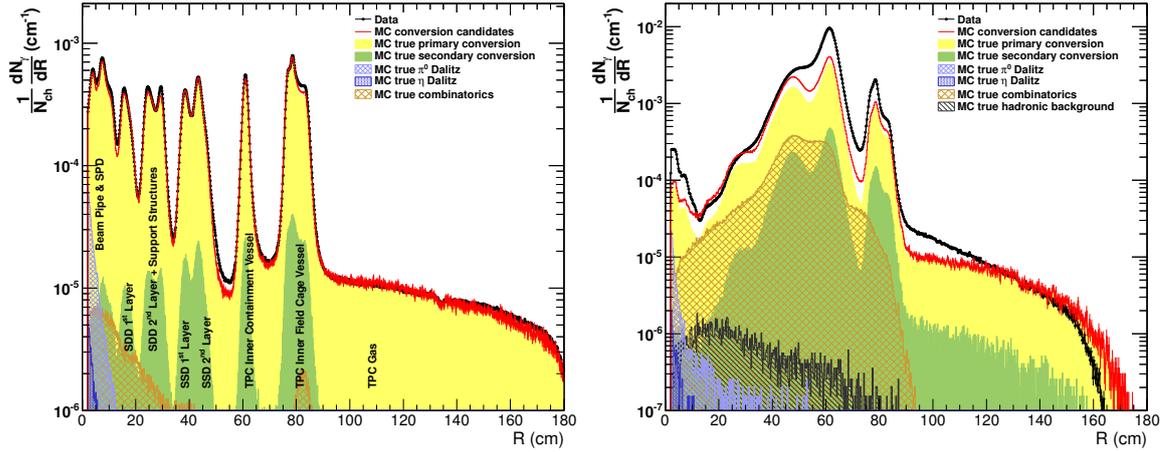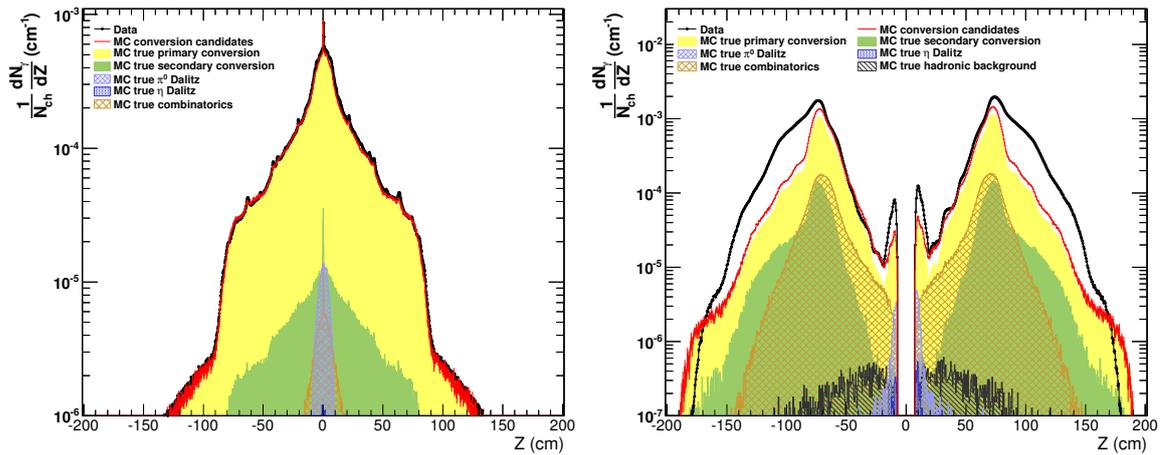

Figure 5.10.: Z distribution of the reconstructed conversion points (black) for $|\eta| < 0.9$ (left) and $0.9 < |\eta| < 1.4$ (right) compared to Monte Carlo simulations done with Pythia 6 tune Perugia 0 (red). The distribution for true primary (secondary) converted photons is shown in yellow (green), while the physics contamination from true π^0 and η Dalitz decays is shown in blue dashed. The true random combinatorial background is shown in brown, while the hadronic background (contamination from e.g. K_s^0, Λ, $\overline{\Lambda}$) is shown in black.

In order to estimate the systematic error up to smaller R, the R distribution can be divided into 13 different regions (bins) in R with the ranges given in the fourth column of Table 5.1.

In order to determine the systematic error of the material budget we vary the V0-finder, the Monte Carlo generator and the p_T range of the selected photons. The variation of the Monte Carlo generators, allows to estimate the systematic error contribution due to the variation of the total number of produced photons. The contribution from the reconstruction efficiency on the other hand can be addressed by varying the V^0 finder from the On-the-Fly V^0 finder to the Offline V^0 finder. The restriction of the p_T range to 1 GeV/c < p_T < 3 GeV/c allows to estimate the systematic error due to the different shape of the p_T distributions of the produced photons in the simulation and in the data. The mean deviation (d_γ^{abs}) of the data from the Monte Carlo simulations is calculated by averaging the result obtained with the On-the-Fly V^0 finder for the
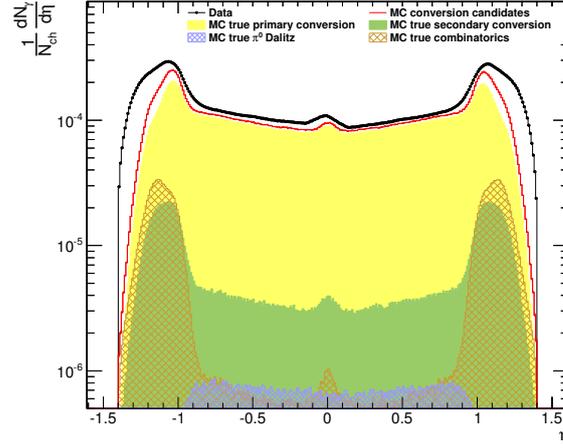
Figure 5.11.: η distribution of the reconstructed conversion points (black) for $|\eta| < 1.4$ compared to Monte Carlo simulations done with Pythia 6 tune Perugia 0 (red). The distribution for true primary (secondary) converted photons is shown in yellow (green), while the physics contamination from true π^0 and η Dalitz decays is shown in blue dashed. The true random combinatorial background is shown in brown, while the hadronic background (contamination from e.g. K_s^0, Λ, $\overline{\Lambda}$) is shown in black.

two Monte Carlo simulations.

$$d_\gamma^{\mathrm{abs}} = \frac{d_\gamma^{\mathrm{Phojet,\ On\text{-}the\text{-}Fly}} + d_\gamma^{\mathrm{Pythia,\ On\text{-}the\text{-}Fly}}}{2} \tag{5.6}$$

$$\Delta d_\gamma^{\mathrm{Gen}} = \left| d_\gamma^{\mathrm{Phojet,\ On\text{-}the\text{-}Fly,\ all}\ p_{\mathrm{T}}} - d_\gamma^{\mathrm{Pythia,\ On\text{-}the\text{-}Fly,\ all}\ p_{\mathrm{T}}} \right| / \sqrt{2} \tag{5.7}$$

$$\Delta d_\gamma^{\mathrm{V0\text{-}finder}} = \left| d_\gamma^{\mathrm{Phojet,\ On\text{-}the\text{-}Fly,\ all}\ p_{\mathrm{T}}} - d_\gamma^{\mathrm{Phojet,\ Offline,\ all}\ p_{\mathrm{T}}} \right| / \sqrt{2} \tag{5.8}$$

$$\Delta d_\gamma^{p_{\mathrm{T}}} = \left| d_\gamma^{\mathrm{Phojet,\ On\text{-}the\text{-}Fly,\ all}\ p_{\mathrm{T}}} - d_\gamma^{\mathrm{Phojet,\ On\text{-}the\text{-}Fly,\ mid}\ p_{\mathrm{T}}} \right| / \sqrt{12} \tag{5.9}$$

The variations which are done for the systematic error evaluation are close to maximum deviations thus would need to be divided by $\sqrt{12}$. But for the first two contribution ($\Delta d_\gamma^{\mathrm{Gen}}$, $\Delta d_\gamma^{\mathrm{V0\text{-}finder}}$) the errors would then be too small, thus we remain conservative and divide these error sources only by $\sqrt{2}$. The combination of the systematic error sources is done as follows.

$$\Delta d_\gamma^{\mathrm{abs}} = \sqrt{\left(\Delta d_\gamma^{\mathrm{Gen}}\right)^2 + \left(\Delta d_\gamma^{\mathrm{V0\text{-}finder}}\right)^2 + \left(\Delta d_\gamma^{p_{\mathrm{T}}}\right)^2} \tag{5.10}$$

$$\Delta_{\mathrm{Mat}} = d_\gamma^{\mathrm{abs}} + \Delta d_\gamma^{\mathrm{abs}} \tag{5.11}$$

A lower limit on the uncertainty of the material budget is currently given by the difference in the quantity $N_\gamma^{\mathrm{prod}} \times P_\gamma^{\mathrm{conv}}/N_{\mathrm{ch}}$ in Pythia 6 Perugia 0 and Phojet, which is 2.3%.
Theoretically the systematic error of the material budget needs to be calculated for each data sample and the corresponding Monte Carlo samples, as the implementation of the material budget improved since the first simulations. Thus, the Monte Carlo simulations used to obtain the results of this thesis can be divided into three samples according to the software version which was used

Generator LHC10[b,c]	V0-finder	full p_{T} Error [%]	mid p_{T} Error [%]	Generator LHC10[d,e,h]	V0-finder	full p_{T} Error [%]	mid p_{T} Error [%]
Phojet	Onfly	2.57	5.58	Phojet	Onfly	3.69	9.14
	Offline	1.56	2.06		Offline	3.49	7.69
Pythia	Onfly	-0.90	-8.48	Pythia	Onfly	0.33	-5.37
	Offline	-2.19	-11.07		Offline	-0.05	-6.31

Table 5.2.: Error calculation for different particle generators (Phojet / Pythia), two V0-finders (Onfly/ Offline) and p_{T}-ranges for the photon (full p_{T} and intermediate p_{T} ($1.0 - 3.0$ GeV/c). The differences are always Data - MC in % of MC.

value	LHC10[b,c]	LHC10[d,e,h]
d_γ^{abs}	0.83%	2.01%
$\Delta d_\gamma^{\text{Gen}}$	2.45%	2.37%
$\Delta d_\gamma^{\text{V0-finder}}$	0.71%	0.14%
$\Delta d_\gamma^{p_{\text{T}}}$	0.87%	1.57%
Δ_{Mat}	3.53%	4.86%

Table 5.3.: Final systematic error estimate of the material budget for the different samples.

for the reconstruction or simulation. The first sample combines the periods LHC10b and LHC10c and their corresponding Monte Carlo simulations, while the second sample consists of the periods LHC10d, LHC10e and LHC10h with the dedicated Monte Carlo samples. For the third set, period LHC11a, the reconstruction and Monte Carlo simulation was done very recently and thus the implementation of the material budget should be the best for this sample. However, the Monte Carlo simulation was done with an incorrect primary vertex distribution in Z and thus cannot be used for estimating the systematic error of the material budget. Therefore, the values will only be given for the first two samples. The individual results for these two sets are given in Table 5.2. The final systematic uncertainty on the material budget is then shown in Table 5.3.

The systematic error of the material budget got slightly worse for the later sample (LHC10[e,d,h]) due to the changes in the reconstruction which affect the two V^0 finders and the two p_{T} ranges differently. If we want to obtain the final systematic error of the material budget for the 7 TeV data sample we need to weight the systematic error according to the statistics in the two different data samples (LHC10[b,c] and LHC10[d,e]). This leads to a final systematic error of the material budget for the 7 TeV data sample of 4.5%. Since the data sample recorded at $\sqrt{s} = 0.9$ TeV was reconstructed with the same software as used for the periods LHC10[d,e,h], the systematic error on the material budget is taken from this sample, the same accounts for the Pb–Pb data sample. For the 2.76 TeV data sample the implementation of the material should be better again than for the LHC10d and e data samples, thus we take the same systematic error as we have obtained for the full 7 TeV data sample.

5.2. Secondary Hadronic Interactions

In this section a second method to test the implemented detector geometry is described, it was inspired by [178,179]. It uses secondary vertices due to hadronic interactions of the primary collision products to probe the material and it is further referred to as Secondary Hadronic Interaction Method (SHIM). As this technique relies on the proper implementation of the hadronic cross sections in GEANT3, which is not the case at low momentum, it cannot yet yield quantitative results. However, it can provide information whether pieces are completely missing or misplaced in the geometry implementation at large pseudo-rapidities ($|\eta| > 1.4$), where the conversion method cannot be used anymore, as the photon originating in the primary vertex cannot be reconstructed in the TPC. Nevertheless these regions need to be inspected in order to estimate the error on the material budget to obtain the accuracy of the correction factors for the forward detectors like PMD, FMD and VZERO, which mainly have the ITS services in front of them.

5.2.1. Secondary Track Selection

The method is based on the reconstruction of secondary vertices from material interactions, thus the first step in this analysis is to select secondary tracks. In order to have a good track quality

we select tracks which have a minimum dE/dx signal of 40, at least 50 clusters in the TPC and at least 70% of the theoretically produced clusters in the TPC. Moreover, the tracks have to be TPC tracks with no kink topologies. To remove badly reconstructed tracks we reject tracks which have impact parameters larger than 250 cm in d_0^{xy} and 300 cm in d_0^z. Moreover, we need to discard the primary tracks thus we only accept tracks which fulfill the following conditions:

$$d_0^{xy} \geq 1.5 \text{ cm} \tag{5.12}$$

$$d_0^z \geq 1.5 \text{ cm} \tag{5.13}$$

$$\sqrt{\frac{(d_0^{xy})^2}{cov_{xy}}} \geq 8 \text{ cm}, \tag{5.14}$$

where cov_{xy} is the first diagonal element of the covariance matrix, which was calculated during the tracking. Moreover, low momentum tracks are removed from the sample by rejecting tracks which produce a loop in the detector. In addition to the criteria mentioned, the tracks are forbidden to be part of an identified γ, K_s^0, Λ or $\overline{\Lambda}$. Therefore, we compute for all track pairs the invariant mass, taking into account for each track three different mass hypotheses (m_e, m_π, m_p). We reject the individual tracks, if the absolute difference of the calculated invariant mass and the mass hypothesis for the corresponding particle (γ, K_s^0, Λ or $\overline{\Lambda}$) is smaller than 0.06 MeV/c^2.

5.2.2. Secondary Vertex Reconstruction and Selection

All remaining secondary track candidates are then paired to secondary vertices using the AliRoot KFParticle package [175]. The algorithm assumes that both tracks originate from a single point, modifies the track parameters, if necessary, and calculates the vertex position which can be expressed by (X_{sec}, Y_{sec}, Z_{sec}) or (R_{sec}, Z_{sec}, ϕ_{sec}). The differences between the measured track parameters and the recalculated ones determine the χ^2 of the secondary vertex. Only vertices with $R_{\text{sec}} < 250$ cm and $Z_{\text{sec}} < 300$ cm are accepted. Moreover, the χ^2 per degrees of freedom of the vertex has to be better than 3. To further reduce the number of random combinatorics the 3-dimensional error $\Delta_{3D} = \sqrt{\Delta_x^2 + \Delta_x^2 + \Delta_z^2/10}$ is calculated and constrained to be better than 2 cm[1]. Furthermore, the 3-dimensional error multiplied with χ needs to meet this condition. The precision in the XY-plane on the other hand is better than the precision in three dimensions, thus we require the 2-dimensional error ($\Delta_{2D} = \sqrt{\Delta_x^2 + \Delta_x^2}$) to be better than 1 cm to reduce the combinatorics even further. Additionally, the individual tracks of which the secondary vertex consists are not allowed to have ITS clusters assigned to the track below the radial coordinate of the secondary vertex.

After having found an initial set of secondary vertices, we try to increase the accuracy of the secondary vertices by looking for additional tracks which might originate from the same vertex. Therefore, the two tracks which are already assigned to the vertex are excluded from the secondary track sample and all other tracks are propagated to the secondary vertex. If the 3-dimesional DCA of a track to the secondary vertex (d_{3D}^{sec}) is smaller than 1 cm and and the following conditions are met

$$d_{xy}^{\text{sec}} \leq 6 \cdot \sqrt{\left(\sigma_Y^{\text{track}}\right)^2 + \left(\Delta_Y^{\text{sec. vtx}}\right)^2 + 0.1 \text{ cm}^2} \tag{5.15}$$

$$d_z^{\text{sec}} \leq 6 \cdot \sqrt{\left(\sigma_Z^{\text{track}}\right)^2 + \left(\Delta_Z^{\text{sec. vtx}}\right)^2 + 0.5 \text{ cm}^2}, \tag{5.16}$$

where d_{xy}^{sec} and d_z^{sec} are the DCA of the track to the vertex in the respective coordinates, the track is considered to belong to the secondary vertex. Moreover, no ITS cluster can be assigned to the

---

[1]The errors Δ_x, Δ_y and Δ_z are the calculated errors of the secondary vertex position in the corresponding coordinates.
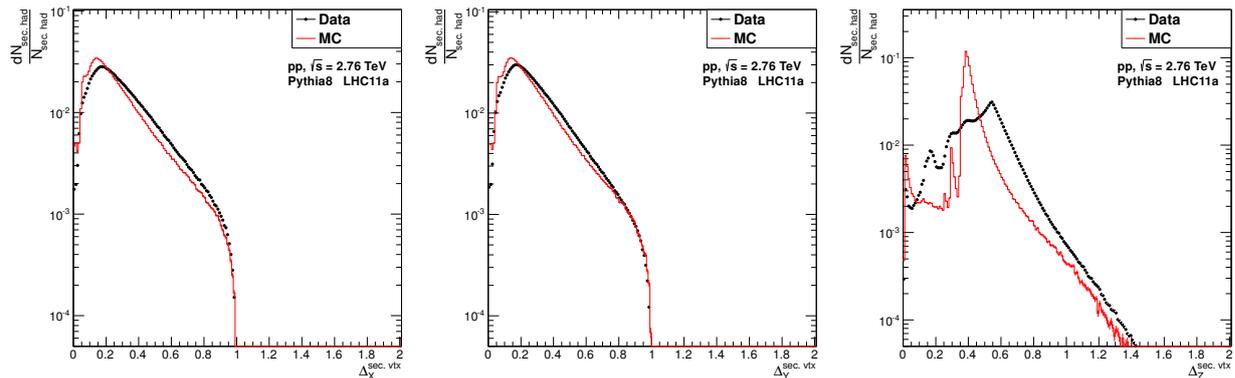
Figure 5.12.: Error estimates on the coordinates of the secondary hadronic vertices in X_{sec} (left), Y_{sec} (middle) and Z_{sec} (right) for data (black dots) and the Pythia 8 Monte Carlo simulation (red histogram) in pp collisions at $\sqrt{s} = 2.76$ TeV. Each distribution is normalized to its integral to enable the comparison for samples with different statistics.

track below the radial distance of the secondary vertex.

Due to the fact that this algorithm allows every track to be used in several vertices, we need to resolve this and ensure that all track-vertex associations are unique. Therefore, we perform an iterative process checking for each secondary vertex whether it has a track in common with a different vertex. The common track is then removed from the vertex with the worst χ^2 and it is checked whether the vertex nevertheless fulfills the selection criteria mentioned above. If it does not meet the criteria anymore it is discarded. This process continues until no close vertices or multiple-assigned tracks are left anymore.

In order improve the resolution of the secondary vertices no initial track p_T cut is applied, however, it is ensured that at least 2 tracks with a transverse momentum larger than 0.1 GeV/c are contained in a secondary vertex. After applying all these conditions the initial sample of secondary hadronic vertices is reduced by at least 80%. However, some of the fake vertices close to the primary vertex still survive. Therefore, we do not accept any secondary vertex below a radial distance of 2 cm to the center of the detector.

To estimate how good the different quantities are reproduced by the Monte Carlo simulation we look at the comparison of the relevant parameters after all cuts. Figure 5.12 displays the comparison of data and Monte Carlo simulation with respect to the error estimates of the secondary vertex coordinates, X_{sec} (left), Y_{sec} (middle) and Z_{sec} (right). Each distribution is normalized to the integral of the distribution in order to compare the shape for different statistics in Monte Carlo and data. While the distribution in data and Monte Carlo simulation look similar for the error estimate in X_{sec} and Y_{sec}, the error estimate on the Z_{sec} shows a completely different behavior. The reason for the discrepancy might be that the matching between ITS and TPC is not yet fully modeled in the Monte Carlo simulations as the matching windows and thus the error calculation for each track is still slightly different for the Z coordinate. Due to the differences of the error estimate of the Z coordinate between data and Monte Carlo simulation the distributions of the 3-dimensional error estimate do not agree well. The 2-dimensional error on the other hand can be mapped quite well by the Monte Carlo simulation. In addition to the error estimates on the secondary vertex we need to compare the distribution of the χ^2/N_{dof} for data and Monte Carlo simulations as the cut is very strict. Figure 5.13 (left) thus shows the comparison for data and Pythia 8 at $\sqrt{s} = 2.76$ TeV. Both distributions are nicely peaked at 0, however, the distribution from data appears to be a little wider than the Monte Carlo distribution. If we want to increase the precision of the secondary hadronic vertices, by requiring a minimum number of tracks originating in the vertex, it is necessary to correctly simulate the relative amount of vertices with a larger number of tracks originating from the secondary vertex to the two track case. Unfortunately, the Monte Carlo simulation does not reproduce this quantity very well with the current cuts, as it can
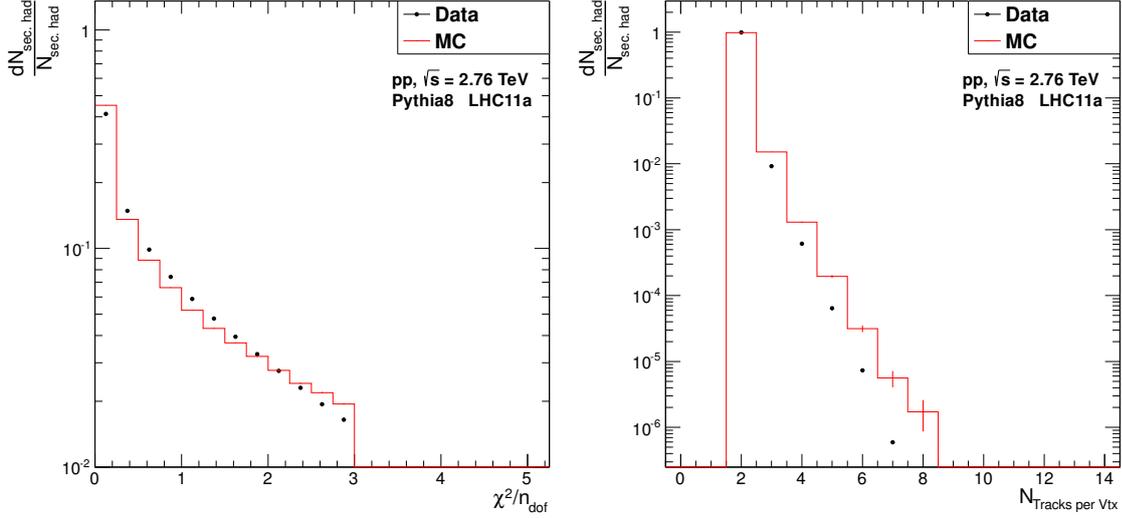
Figure 5.13.: Comparison of the distribution of the χ^2/N_{dof} for the secondary vertices obtained from the extrapolation of the tracks to the secondary vertex (left) and the number of tracks per secondary vertex (right) for Monte Carlo simulation (Pythia 8) and the data in pp collisions at $\sqrt{s} = 2.76$ TeV. Each distribution is normalized to its integral to enable the comparison regardless of the statistics in each data sample.

be seen in Figure 5.13 (right).

5.2.3. Qualitative Comparison of Data and Monte Carlo

From all the comparisons concerning the quality of the secondary vertices and the understanding of the different cuts using Monte Carlo simulation, it can be concluded that the SHIM currently cannot be used for quantitative estimates on the error of the material budget. Nevertheless, this method can provide a detailed view of the detector, making it possible to identify large pieces which are missing completely in the simulation or which are not there in the data but simulated in the Monte Carlo.

The two dimensional distribution of the secondary hadronic vertices in the ZR-plane is shown in Figure 5.14 for pp collisions and in Figure 5.15 for Pythia 8 simulations at $\sqrt{s} = 2.76$ TeV, respectively. The distributions are normalized to the number of events in the corresponding sample. Comparing both distributions the Monte Carlo simulation seems to have more secondary interaction in certain regions (e.g. the beam pipe). This reflects the mismatch of the Monte Carlo simulation and the data concerning the multiplicity of primary particles, which was already observed for the photon conversions. For the secondary hadronic interaction, however, this is not so easy to correct for, as the larger amount of primary particles in data implies that there will be more secondary interactions, leading to more secondary particles which can interact in the outer layers of the detector. Therefore, the relative amount of secondary hadronic vertices in data at larger radii is larger than in the simulation. On the other hand the resolution seems to be slightly overestimated in the Monte Carlo simulation, leading to sharper edges, in particular, at larger η in the Monte Carlo simulation than seen in the data. Moreover, it seems that close to the TPC inner containment vessel ($R \approx 60$ cm) a large piece of material is missing in the geometry implemented as the outer parts ($|Z| > 60$ cm) seem to be much thicker in data than in Monte Carlo simulation. On the contrary at $R \approx 5$ cm and $Z = \pm 12 - 18$ cm there seems to be a large piece of material in the Monte Carlo simulation, which is not seen in data at all.

Figure 5.16 shows the two dimensional distribution of the secondary hadronic vertices in the XY-plane for pp collisions at $\sqrt{s} = 2.76$ TeV for $|\eta| < 0.9$. If we compare this distribution to the
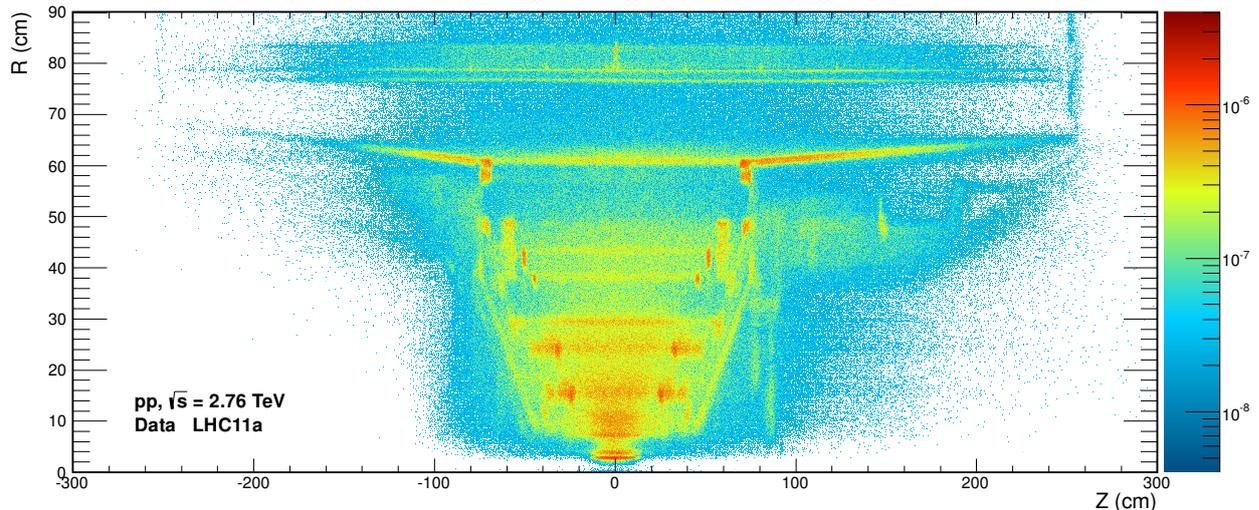
Figure 5.14.: Distribution of the secondary hadronic vertices normalized to the number of events in the ZR-plane for the full pseudo-rapidity range accessible by the SHIM measured in data for pp collisions at $\sqrt{s} = 2.76$ TeV.
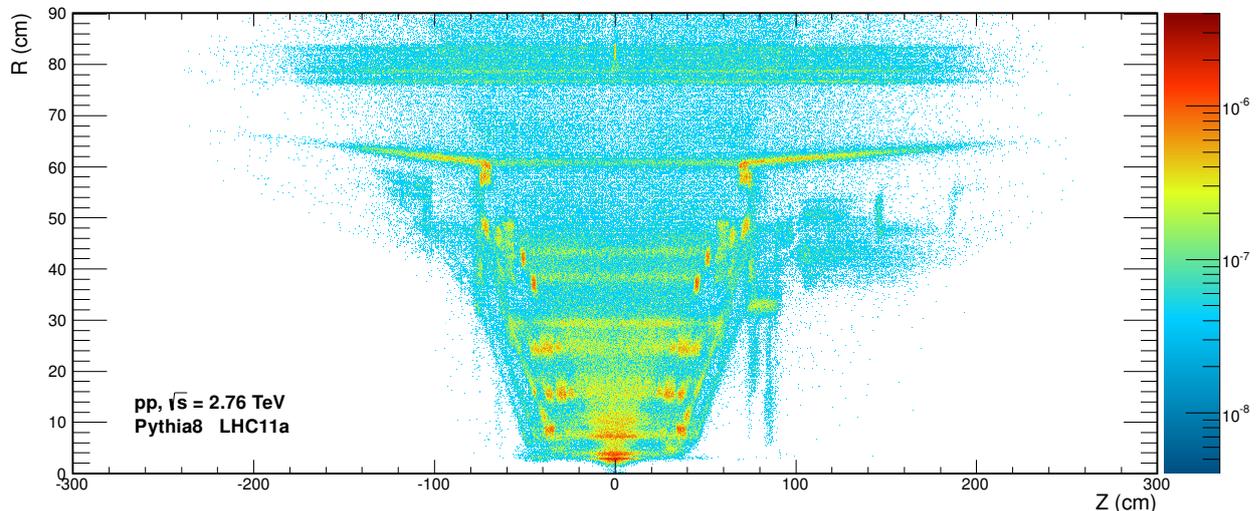

Figure 5.15.: Distribution of the secondary hadronic vertices normalized to the number of events in the ZR-plane for the full pseudo-rapidity range accessible by the SHIM reconstructed in Pythia 8 simulations for pp collisions at $\sqrt{s} = 2.76$ TeV.

same plot for photon conversions (Figure 5.3), it becomes obvious that the resolution for hadronic interaction close to the TPC is even better than for photon conversions. For instance even the high voltage cables in the TPC rod ($X \approx 62$ cm, $Y \approx 52$ cm) can be identified. Furthermore, the segmentation in the TPC inner field cage vessel can be seen as two rings. The resolution between the SPD and TPC on the other hand is much better for photon conversions than for hadronic interactions, probably due to the problems in the correct simulation of the track matching between ITS and TPC. If we come closer to the beam pipe the hadronic interaction have a much better resolution again, as it can be seen in Figure 5.17. For secondary hadronic interaction we can nicely separate the beam pipe ($R \approx 3$ cm) and the inner layer of the SPD with the 20 ladders of the inner ring. In addition, the next layer of the SPD ($R \approx 7$ cm) is visible as well, although it seems to be blurred and much less details can be seen than for the different ladders. The thermal shield and the first layer of the Silicon Drift Detector (SDD), which should be located at $R \approx 9$ cm and $R \approx 15$ cm, respectively, cannot be seen clearly anymore. In this region the conversions on the other hand already have a very good resolution in R (1.0-1.4 cm), thus the structures can be nicely separated with conversions.
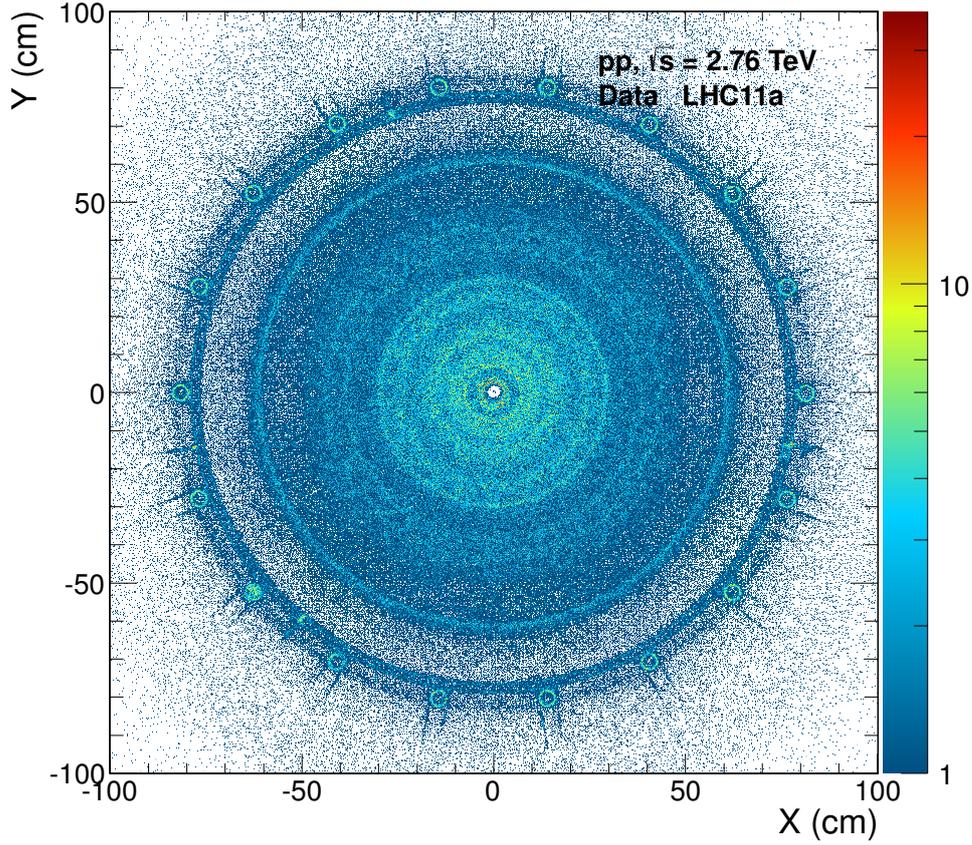
69

Figure 5.16.: Distribution of the secondary hadronic vertices in the *XY*-plane for the $\eta < 0.9$ measured in data for pp collisions at $\sqrt{s} = 2.76$ TeV.
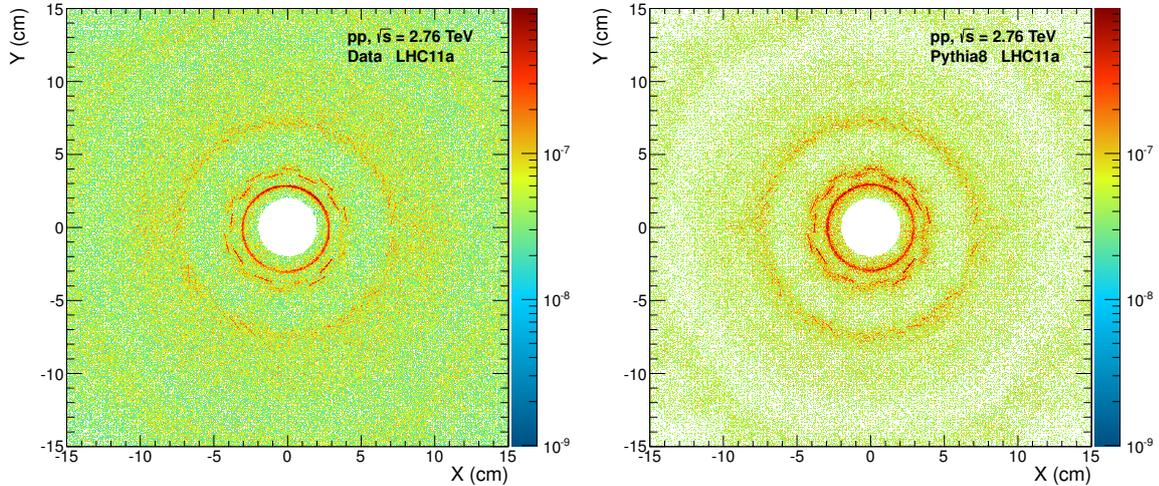
Figure 5.17.: Enlarged view of the distribution of the secondary hadronic vertices in the *XY*-plane for the $\eta < 0.9$ measured in data (left) and Pythia 8 (right) for pp collisions at $\sqrt{s} = 2.76$ TeV. Each distribution is normalized to the total number of events in the corresponding data sample.

In summary the SHIM is a good method to identify material pieces which are outside of the fiducial acceptance ($|\eta| > 0.9$), however, it has not yet reached the maturity of the photon conversion method and thus cannot give a systematic error estimate on the material budget. Moreover, the method needs to be studied further to understand the efficiency and vertex finding. Probably changes in the Monte Carlo simulations are needed to reproduce the measured data in the central acceptance.

6. Neutral Meson Analysis

This chapter is dedicated to the neutral meson analysis in pp collisions at $\sqrt{s} = 0.9$, 2.76 and 7 TeV as well as Pb–Pb collisions at $\sqrt{s_{\mathrm{NN}}} = 2.76$ TeV. The analyses have been carried out within the Photon Conversion Group [180].

The pp analysis was already described in detail in the [174, 181] and the 7 TeV π^0 and η meson transverse momentum spectra as well as the 900 GeV π^0 transverse momentum spectra have been published recently [182]. The contribution to the published analysis was the calculation of the systematic errors according to the method described in this thesis. As the spectra for pp collisions at $\sqrt{s} = 7$ TeV and 900 GeV were already discussed in detail in [174, 181], this thesis will be focusing on the presentation of the pp data sample at $\sqrt{s} = 2.76$ TeV, for which the spectra were solely obtained during this thesis.

A preliminary result for the Pb–Pb spectra in larger centrality bins was already obtained in [126]. During the course of this thesis the spectra were further improved regarding the finer centrality binning and the systematic error evaluation. Moreover, the results were combined with the π^0 transverse momentum spectra which were obtained by reconstructing the photons in PHOS via their energy deposit in the calorimeter cells.[1] Furthermore, a detailed investigation of the Monte Carlo simulation samples used for the corrections was part of this thesis.

As the analysis in pp and Pb–Pb collisions are based on the same analysis software package [183], the first section will be dedicated to the analysis method itself. Thus the reconstruction of the neutral mesons, the corrections for the measured spectra and the systematic error evaluation will be explained. Afterwards, the results on the neutral pion and eta meson in pp collisions at the three different energies will be combined with the available PHOS spectra [184]. Moreover, the results will be compared to theory calculations [127, 185]. The next section will be dedicated to the results on the π^0 meson in Pb–Pb collisions at $\sqrt{s_{\mathrm{NN}}} = 2.76$ TeV and the comparison to other measurement of charged [186] and neutral pions [187]. Last but not least, the nuclear modification factor (R_{AA}) of the neutral pion will be discussed and compared to the R_{AA} of charged particles [95], charged pions [186] and results from different energies [109, 188, 189] and theory calculations [190–194].

6.1. Neutral Meson Reconstruction

The photon candidates which have been extracted from the V^0 sample, according to Section 4.2, are combined into pairs. However, pairs which share a track or which have an opening angle smaller than 5 mrad are excluded from the sample. For each pair the invariant mass is calculated, which is given by

$$M_{\gamma\gamma} = \sqrt{2E_{\gamma_1}E_{\gamma_2}(1 - \cos\theta_{12})}, \tag{6.1}$$

where $E_{\gamma_{1,2}}$ represent the energies of the two photons and θ_{12} is the opening angle between them in the laboratory frame. The π^0 and η mesons are reconstructed as excess yield, visible at their

---

[1]The π^0 (η) meson reconstruction via the energy deposit of their decay photons in PHOS, is in the following referred to as the PHOS analysis and the resulting transverse momentum spectra are referred to as PHOS spectrum. Moreover, the spectra measured via the Photon Conversion Method (PCM) are referred to as PCM spectra or results
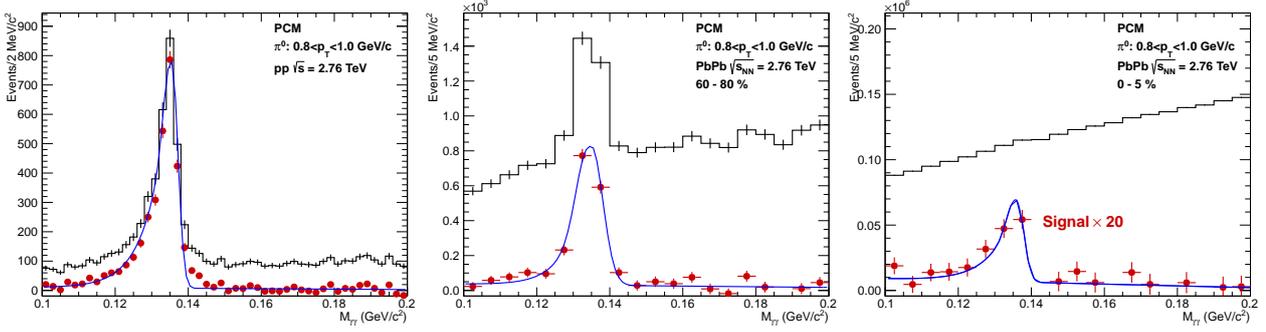
Figure 6.1.: Invariant-mass distribution of reconstructed photon pairs $M_{\gamma\gamma}$ around the neutral pion mass (0.135 GeV/c^2) in selected p_T slices in pp collisions at $\sqrt{s} = 2.76$ TeV (left) and in peripheral (middle) and central (right) Pb–Pb collisions at $\sqrt{s_{NN}} = 2.76$ TeV. The black histogram and the red bullets show the data before and after background subtraction, respectively. The blue curve is a fit to the invariant mass spectrum after background subtraction.

Figure 6.2.: Invariant-mass distribution of reconstructed photon pairs $M_{\gamma\gamma}$ around the mass of the η meson (0.548 GeV/c^2) in selected p_T slices in pp collisions at $\sqrt{s} = 2.76$ TeV (left) and in peripheral (middle) and central (right) Pb–Pb collisions at $\sqrt{s_{NN}} = 2.76$ TeV. The black histogram and the red bullets show the data before and after background subtraction, respectively. The blue curve is a fit to the invariant mass spectrum after background subtraction.
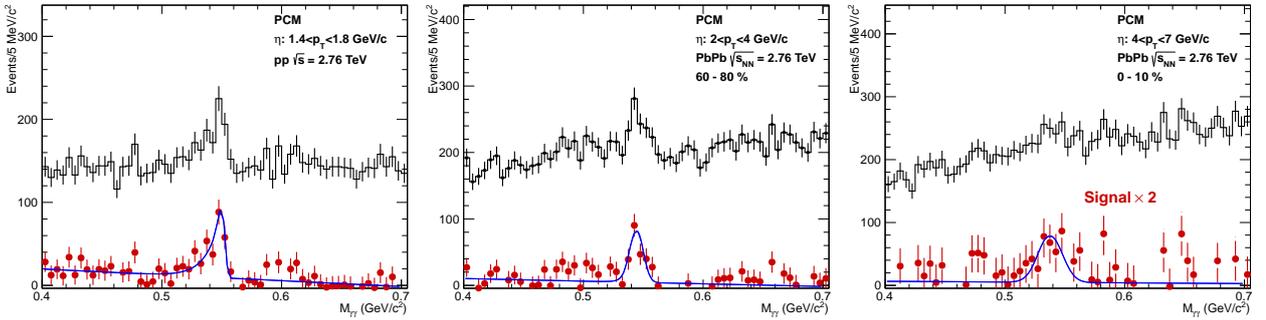
respective rest mass, 0.135 GeV/c^2 for the π^0 meson and 0.548 GeV/c^2 for the η meson. Figure 6.1 and Figure 6.2 show the two photon invariant mass distribution (black) close to the rest mass of the π^0 or η meson, respectively, for pp collisions at $\sqrt{s} = 2.76$ TeV (left) as well as peripheral (middle) and central (right) Pb–Pb collisions at $\sqrt{s_{NN}} = 2.76$ TeV. A clear peak at the mass position of the π^0 meson is visible on top of a combinatorial background. This background gets larger for increasing multiplicity in the event until the peak cannot be seen by eye anymore in central Pb–Pb collisions. While for the π^0 meson the significance is rather large except in most central collisions the η meson can be barely distinguished from the fluctuations in the background. Thus the extraction of the η meson is much harder, moreover it has a larger width and is therefore even harder to extract. The background under the peaks should be purely of combinatorial nature and can therefore be calculated with different techniques.

Event Mixing method
The event mixing method destroys the correlations of the photon pairs by combining photons from different events. However, it was found that the shape of the combinatorial background depends on the multiplicity in the event, the primary vertex position in Z and the transverse momentum. Thus the photons were divided into bins regarding the multiplicity in the event (5 bins) and the Z-Vertex position (7 bins), with the limits chosen such that each class has similar statistics. The mixing is then done only among the photons which belong to the same bin in multiplicity and the Z-vertex position. Therefore, the photons are stored in a first-in-first-out (FIFO) buffer with a maximum of 80 (50) photons in pp (Pb–Pb) collisions and all photons from the current event are mixed with the photons in the respective pool.

Class	Bin	pp	Pb–Pb
V^0 multiplicity (photon candidates)	1	2	2
	2	3	3 - 10
	3	4	11 - 30
	4	5	31 - 50
	5	≥ 5	≥ 50
Charged particle multiplicity	1	0 - 8	0 - 199
	2	9 - 16	200 - 499
	3	17 - 27	500 - 999
	4	28 - 41	1000 - 1499
	5	41 - 200	1499 - 4999
Z-vertex coordinate	1	-50.00 - -3.38	-50.00 - -3.38
	2	-3.38 - -1.61	-3.38 - -1.61
	3	-1.61 - -0.23	-1.61 - -0.23
	4	-0.23 - 1.07	-0.23 - 1.07
	5	1.07 - 2.45	1.07 - 2.45
	6	2.45 - 4.25	2.45 - 4.25
	7	4.25 - 50.00	4.25 - 50.00

Table 6.1.: Class definition for event mixing classes.

Afterwards, the photons from the current event are added to the respective pool. Moreover, two different multiplicity definitions were tested, one based on the number of charged particle tracks in the acceptance and the other based on the number of photon candidates in the event. Both approaches showed similar results as discussed in detail in [174, 181]. The definition of the different multiplicity and Z-vertex classes for pp and Pb–Pb can be found in Table 6.1.

Rotation method
Another possibility for the background calculation is the rotation of one photon of the pair in φ by a random value in the range $]\pi - \frac{\pi}{9}, \pi + \frac{\pi}{9}[$ and the subsequent recalculation of the invariant mass. This procedure keeps the event topology but destroys the correlations in the event. It has to be repeated several times to gain statistics.

Extensive studies showed [174, 181] that the mixed event method reproduces the background shape over the full transverse momentum range, if the background is normalized to the data close to the respective peak. The rotation method on the other hand cannot reproduce the spectral shape at high transverse momenta that well. Moreover, the mixed event method based on the V^0 multiplicity describes the data slightly better than the one based on the charged track multiplicity. At low momenta on the other hand all three methods are equal. For the data presented in this thesis the mixed event technique with bins in V^0 multiplicity will be used as the default method. The differences to the other two methods will be used as a source of a systematic error.

Due to the limited acceptance of the detectors in the central barrel of ALICE ($|\eta| < 0.9$) the rapidity of the meson has been restricted to $y < 0.9$ (0.8) for pp (Pb–Pb) collisions. Moreover, to enhance the signal a cut on the energy asymmetry ($\alpha = |E_{\gamma_1} - E_{\gamma_2}|/(E_{\gamma_1} + E_{\gamma_2})$) of the two photons of 0.6 (0.8) is applied in central (peripheral) Pb–Pb collisions. Furthermore, a cut on the minimum radial distance of the conversion point from the center of the detector is applied for each photon at $R_{\mathrm{conv}} > 5$ cm in order to reduce the contribution from the π^0 and η Dalitz decays ($\pi^0(\eta) \to \gamma\gamma^* \to e^+e^-e^+e^-$). This decay channel can contribute to the $\gamma\gamma$ decay channel if the e^+e^- originating in the virtual photon is reconstructed as real photon. The branching ratio for the π^0 and η Dalitz decay is much smaller, $(1.174 \pm 0.035)\%$ and $(7.0 \pm 0.7) \times 10^{-3}\%$ respectively, than for the two photon decay channels, which is for the π^0 meson $(98.823 \pm 0.034)\%$ and for the η meson $(39.31 \pm 0.20)\%$. However, the efficiency is higher thus the statistics is similar. As it can be seen in Figure 5.9 most of the reconstructed Dalitz pairs have a conversion radius smaller than
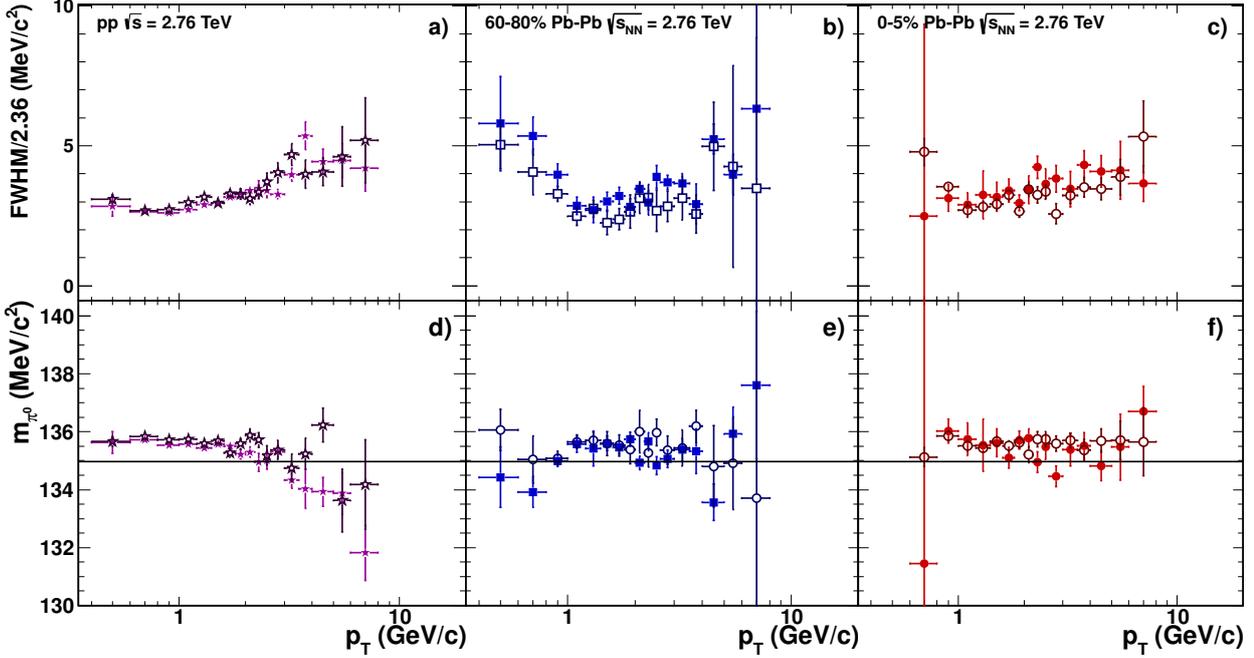
Figure 6.3.: Reconstructed mass resolution (a-c) and mass (d-f) for the π^0 meson as function of transverse momentum for pp collisions at $\sqrt{s}$ = 2.76 TeV (a,d) as well as 60-80% (b,e) and 0-5% central Pb–Pb collisions (c,f). The parameters are extracted using the fit described in Equation 6.3. The simulated data is represented by the open symbols, while the real data are shown with filled symbols. Moreover, the nominal mass position according to [130] is indicated by the black line. The resolution is given as the full width at half maximum (FWHM) divided by 2.36 in order to show the corresponding width of the peak in terms of σ of a pure Gaussian distribution.

5-10 cm, thus the cut on the radial distance ($R_{\mathrm{conv}} > 5$ cm) removes most of the Dalitz pairs from the invariant mass distribution of the $\gamma\gamma$ channel.

6.1.1. Signal Extraction

For the signal extraction we calculate the invariant mass distributions of the recorded photon pairs (combined signal and background) and the mixed event (rotation) background in different p_{T} slices, according to the binning in transverse momentum of the final meson spectra. The background distribution is then normalized to the combined signal and background distribution, taking into account the different weights of the Z-vertex and multiplicity classes. This normalization can be done either on the left or on the right side of the peak, but it has to be as close to the peak as possible without entering in the distribution of the signal. Afterwards, the normalized background is subtracted from the combined signal and background distribution and the remaining signal is fitted with a Gaussian function combined with an exponential low-energy tail on the left side to account for electron bremsstrahlung. Moreover, a linear part is added to this function to calculate the remaining combinatorial background under the peak, in case the calculated combinatorial background does not fully describe the background shape under the signal.

$$y = A \cdot \left(G(M_{\gamma\gamma}) + \exp\left(\frac{M_{\gamma\gamma} - M_{\pi^0(\eta)}}{\lambda}\right)(1 - G(M_{\gamma\gamma}))\theta(M_{\gamma\gamma} - M_{\pi^0,\eta}) \right) + B + C \cdot M_{\gamma\gamma} \quad (6.2)$$

$$, \text{ with } G = \exp\left(-0.5\left(\frac{M_{\gamma\gamma} - M_{\pi^0,\eta}}{\sigma_{M_{\gamma\gamma}}}\right)^2\right) \quad (6.3)$$

Here G is a Gaussian function with the width σ, the amplitude A and the mean position $M_{\pi^0(\eta)}$, which can be identified with the reconstructed mass position of the corresponding meson. The
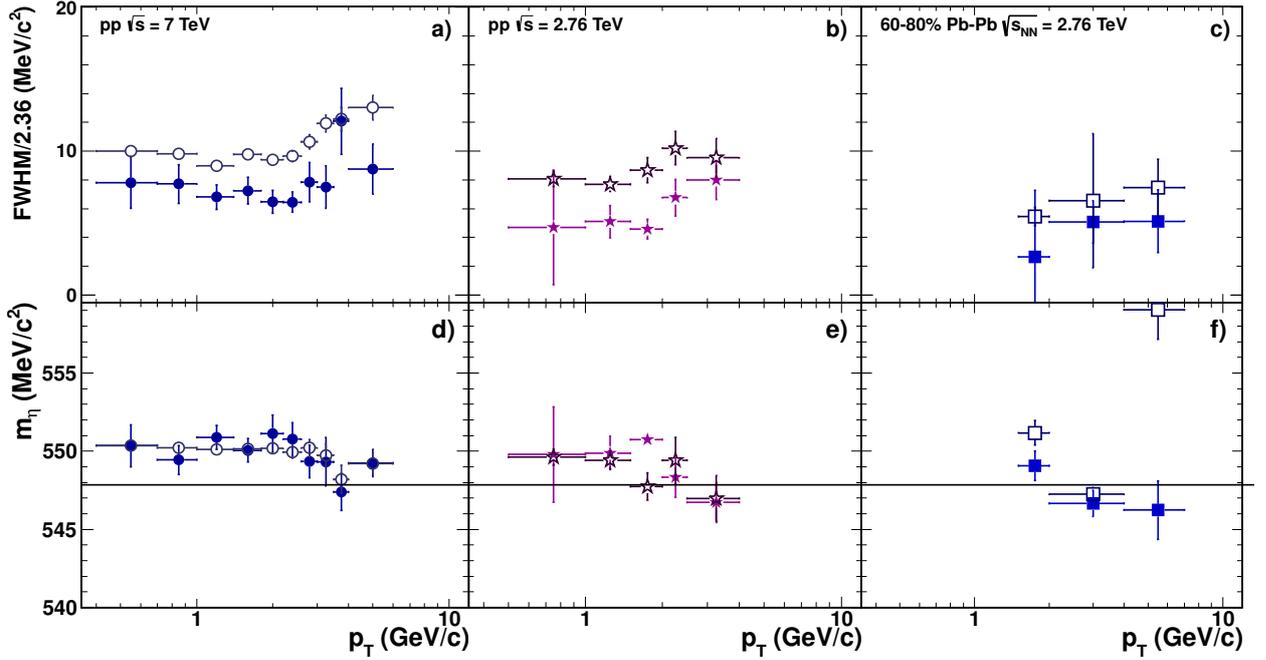
Figure 6.4.: Reconstructed mass resolution (a-c) and mass (d-f) for the η meson as function of transverse momentum for pp collisions at $\sqrt{s} = 7$ TeV (a,d) and 2.76 TeV (b,e) as well as 60-80% Pb–Pb collisions (c,f). The parameters are extracted using the fit described in Equation 6.3. The simulated data is represented by the open symbols, while the real data are shown with filled symbols. Moreover, the nominal mass position according to [130] is indicated by the black line. The resolution is given as the full width at half maximum (FWHM) divided by 2.36 in order to show the corresponding width of the peak in terms of σ of a pure Gaussian distribution.

parameter λ represents the inverse slope of the exponential function. The contribution of the exponential function above $M_{\pi^0(\eta)}$ is switched off by the Heavyside function $\theta(M_{\gamma\gamma} - M_{\pi^0,\eta})$. B and C are the parameters of the linear function. In Figure 6.1 and Figure 6.2 the red dots represent the invariant mass distribution after subtraction, the fit given in Equation 6.3 is shown as blue line. The remaining background under the π^0 meson peak in most of the p_T slices is very small and thus the correction is as well. For the η meson on the other hand this correction becomes important as the background does not describe the data well within this invariant mass region. The invariant mass distributions for the π^0 and η meson in all p_T slices can be found in Appendix B for pp collisions at $\sqrt{s} = 2.76$ TeV and Pb–Pb collisions at $\sqrt{s_{NN}} = 2.76$ TeV. For pp collisions at $\sqrt{s} = 0.9$ TeV and 7 TeV these distributions have been shown in [174]. From the fits to the individual invariant mass peaks in p_T slices the reconstructed mass position ($M_{\pi^0(\eta)}$) and the FWHM can be extracted, the results for simulated and recorded data are shown in Figure 6.3 and Figure 6.4 for the π^0 and η meson, respectively. These plots show that the reconstructed mass in the simulations and the real data agrees within the errors for the π^0 and η meson regardless of the collision system. However, a shift of 0.5 (2) MeV/c^2 can be seen compared to the nominal rest mass of the π^0 (η) meson, which is indicated by the black line in the panels (d-f). In the simulation a slightly better resolution (FWHM/2.36) is observed for the neutral pion in Pb–Pb collisions. While the resolution of the η meson peak is underestimated in pp and Pb–Pb collisions. Thus the integration windows for the yield extraction were chosen such, that these discrepancies do not affect the final result.

In order to extract the meson yield the subtracted invariant-mass distribution is integrated in a mass range around the fitted meson mass $M_{\pi^0(\eta)}$ and the remaining background is subtracted using the integral of the linear part of Equation 6.3. The standard integration range for π^0 meson is (M_{π^0} - 0.035 GeV/c^2, M_{π^0} + 0.010 GeV/c^2), while for the η the integration is performed in the interval (M_η - 0.047 GeV/c^2, M_η + 0.023 GeV/c^2), taking into account the larger reconstructed

width of the η meson. The integration window is asymmetric to incorporate most of the tail on the left hand side of the peak, which originates in electron Bremsstrahlung.

$$N_{\text{raw}}^{\pi^0} = \int\limits_{M_{\pi^0}-0.035\ \text{GeV}/c^2}^{M_{\pi^0}+0.010\ \text{GeV}/c^2} (N^{\gamma\gamma} - N^{\text{comb. BG}})dM_{\gamma\gamma} - \int\limits_{M_{\pi^0}-0.035\ \text{GeV}/c^2}^{M_{\pi^0}+0.010\ \text{GeV}/c^2} (B + C \cdot M_{\gamma\gamma})dM_{\gamma\gamma} \qquad (6.4)$$

The resulting raw yields for the π^0 and η meson for pp collisions at the three different energies and for Pb–Pb collisions for different centralities are shown in Figure 6.5 and Figure 6.6, respectively. Each spectrum is normalized by the bin width in p_{T} and the corresponding number of events given in Table 4.2 or Table 4.4. For pp collisions the transverse momentum reach is limited by the statistics in the corresponding sample, thus the momentum reach decreases going to lower energies for which only small samples were collected. For Pb–Pb collisions the momentum reach for the π^0 meson measurement is determined by a combination of significance of the signal (low momentum) and statistics (high momentum), thus for the final spectrum we restrict our measurement in p_{T} to 0.6 - 8.0 GeV/c for 0-10% and to 0.4 - 8.0 GeV/c for 10-80% Pb–Pb collisions. The number of π^0 mesons per event in Pb–Pb scales with the multiplicity per event, therefore the largest raw yields are measured in central collisions. For the η meson the yield extraction is much more difficult in Pb–Pb collisions as we would need large statistics to have a smooth background, thus the error bars are much larger and we need to have much wider slices in p_{T}.

6.1.2. Meson Spectra Corrections

After having obtained the raw yield of the mesons several corrections need to be applied. At first the contribution from secondary π^0 mesons from weak decay or hadronic interactions in the detector material need to be removed from the reconstructed raw neutral pions yield. Afterwards, corrections for the geometrical acceptance and reconstruction efficiency are applied. During the last step we will correct the spectra for the finite bin width in transverse momentum.

Correction for secondary neutral pions

In order to extract exclusively the primary neutral pions the contributions from secondary π^0 mesons from weak decays or hadronic interactions need to be removed from the raw yield of the π^0 meson. This correction has been evaluated using the same Monte Carlo simulations, which have been used for efficiency and acceptance calculations. The decay $K_s^0 \to \pi^0\pi^0$ with a branching ratio of BR = 30.7% represents the largest source of the secondary neutral pions. Figure 6.7 shows the fraction of all secondary pions (r_{all}, black) or secondary pions from K_s^0 decays ($r_{K_s^0}$, blue) to the all reconstructed pions in pp collisions at 7 TeV. These distributions have been obtained using all Monte Carlo simulations for pp at $\sqrt{s}$ = 7 TeV regardless of the generator. As the statistics in the simulations for pp at $\sqrt{s}$ = 2.76 TeV and Pb–Pb collisions at $\sqrt{s_{\text{NN}}}$ = 2.76 TeV is not sufficient to directly extract the fractions with errors smaller than the actual correction, the fraction in 7 TeV were fitted with the following function

$$f(x) = \frac{a}{x^b}, \quad \text{where} \quad a = (3.034 \pm 0.048) \cdot 10^{-2}, b = 0.809 \pm 0.031 \text{ for all secondary } \pi^0$$

$$a = (2.665 \pm 0.045) \cdot 10^{-2}, b = 0.706 \pm 0.032 \text{ for secondary } \pi^0 \text{ from } K_s^0$$

and then binned like the raw spectrum. A comparison of the fits and the fractions directly obtained from the corresponding simulations showed that they agree within the statistical errors for these two samples (pp $\sqrt{s}$ = 2.76 TeV, Pb–Pb $\sqrt{s_{\text{NN}}}$ = 2.76 TeV). The total contribution at high p_{T}
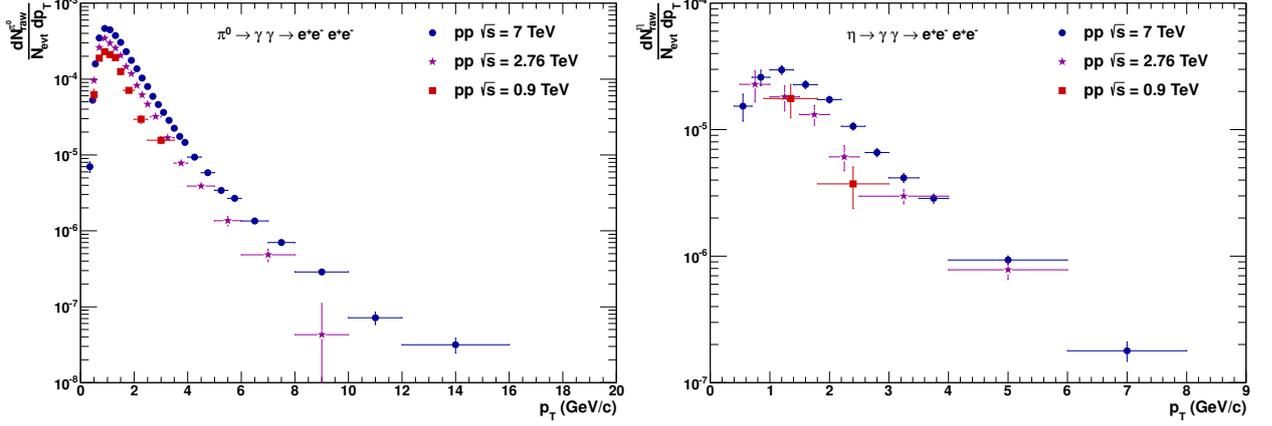
Figure 6.5.: Raw yield of the π^0 (left) and η (right) meson in pp collisions at $\sqrt{s} = 0.9$ (red), 2.76 (magenta) and 7 TeV (blue) as function of the transverse momentum. The yield is normalized to the number of events N_{evt}, according to Table 4.2 and the spectra are divided by the bin width in p_{T}.
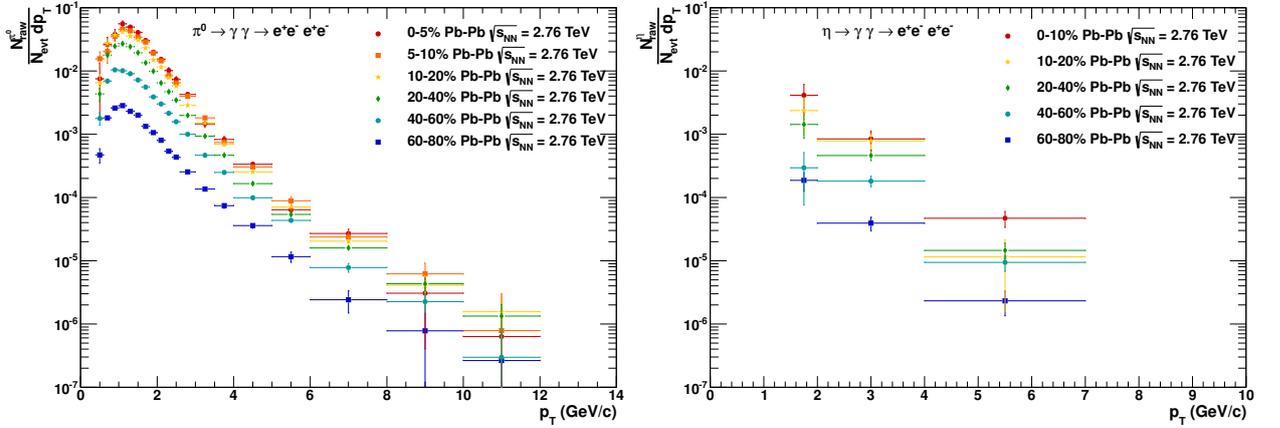

Figure 6.6.: Raw yield of the π^0 (left) and η (right) meson in Pb–Pb collisions at $\sqrt{s} = 2.76$ TeV. The yield is normalized to the number of events N_{evt}, according to Table 4.4 and the spectra are divided by the bin width in p_{T}.

($p_{\mathrm{T}} > 2$ GeV/c) is of the order of 1%, while it grows up to 7% at low transverse momentum. For the correction the p_{T} dependent r_{all} is multiplied with the measured raw yield and this estimated raw yield from secondary π^0 mesons is subtracted from the measured raw yield.

However, it has been discovered that the Monte Carlo simulations used for the corrections (Pythia, Phojet, Hijing) cannot reproduce the measured differential yields for kaons. They underestimate the yield in pp collisions at $\sqrt{s} = 900$ GeV by approximately 40% [195] and by about 25 % at $\sqrt{s} = 7$ Tev [196,197]. For pp collisions at $\sqrt{s} = 2.76$ TeV no final kaon spectrum is available yet, therefore the mismatch has been calculated to be 31% assuming a linear dependence between $\sqrt{s} = 900$ GeV and 7 TeV. In Pb–Pb collisions on the other hand the K_s^0 yield in Hijing is too large compared the measured spectra [197]. The ratio of generated over reconstructed K_s^0 has been measured to be 1.27 for 60-80% and 1.37 for 0-5% Pb–Pb collisions [198].[2] Thus to correct for the mismatch between measured and simulated data the raw yield from secondary π^0 mesons from K_0^s ($r_{K_s^0} \times$ measured π^0 raw yield) is scaled by the fraction needed to match the measured data and then subtracted for pp collisions or added for Pb–Pb collisions to the measured raw yield.

---

[2]For the other centrality classes a linear interpolation is done to derive the correction factor.
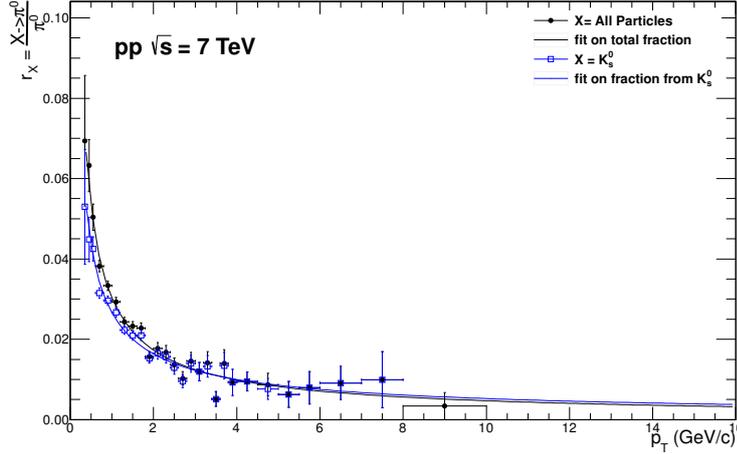
Figure 6.7.: Ratio r_X of reconstructed secondary π^0 mesons from K_s^0 mesons (blue squares) or all secondary π^0 mesons (black dots) to reconstructed neutral pions. The blue and black line represent the fit to the corresponding fractions with $f(x) = \frac{a}{x^b}$.

Acceptance and Efficiency Correction

After the correction for secondary neutral pions the remaining primary raw yield of the π^0 meson needs to be corrected for detector acceptance and reconstruction efficiency. Both quantities are calculated using all available Monte Carlo simulations for the respective collision systems and center-of-mass energies, regardless of the generator.

The geometrical acceptance $A_{\pi^0(\eta)}$ is defined as the ratio of π^0 (η) mesons within $|y| < 0.8$ for pp and $|y| < 0.7$ for Pb–Pb collisions, whose daughter particles are within the fiducial acceptance ($|\eta| < 0.9$), over all π^0 (η) mesons generated in the same rapidity window.

$$A_{\pi^0(\eta)} = \frac{N_{\pi^0(\eta),|y|<y_{\max}} \text{ with the daughter particles within } |\eta_\gamma| < 0.9}{N_{\pi^0(\eta),|y|<y_{\max}}} \tag{6.5}$$

Figure 6.8 shows the resulting geometrical acceptance for π^0 (left) and η (right) mesons for all collision system, energies and centralities. As the mass of the η meson is larger than the mass of the π^0 meson the opening angle between the daughter particles is wider and thus the acceptance rises slower to unity than for the π^0 meson. The difference between the distributions in Pb–Pb and pp collisions can be attributed to the different rapidity intervals. As expected no discrepancy between the different energies in pp collisions or within different centrality classes is seen.

In order to estimate the reconstruction efficiency the same analysis as in real data has been performed on simulated data. However, each photon is verified using the Monte Carlo information and it has been checked that they originate from the same particle (π^0 or η meson). Thus the contribution from Dalitz decays is rejected. Moreover, only primary particles are taken into account. The resulting reconstruction efficiency $\epsilon_{\text{reco}, \pi^0(\eta)}$ is shown in Figure 6.9 for the π^0 and η meson at the different energies. For the Pb–Pb sample the Monte Carlo statistics is not sufficient to extract a stable efficiency at high transverse momentum ($p_{\text{T}} > 4$ GeV/c), therefore the efficiencies in Pb–Pb are fitted above 1.2 GeV/c using

$$f(p_T) = 1 - a\exp(b\,p_{\text{T}}) + c \tag{6.6}$$

as a fit function. The fit is then sampled again in the same p_{T} slices as the raw yield to correctly extract the statistical errors of the efficiency. The efficiencies shown in Figure 6.9 for the different centralities in Pb–Pb collisions are obtained following this procedure, the unmodified efficiencies can be found in Appendix B. A detailed description of the calculation of the efficiencies for the
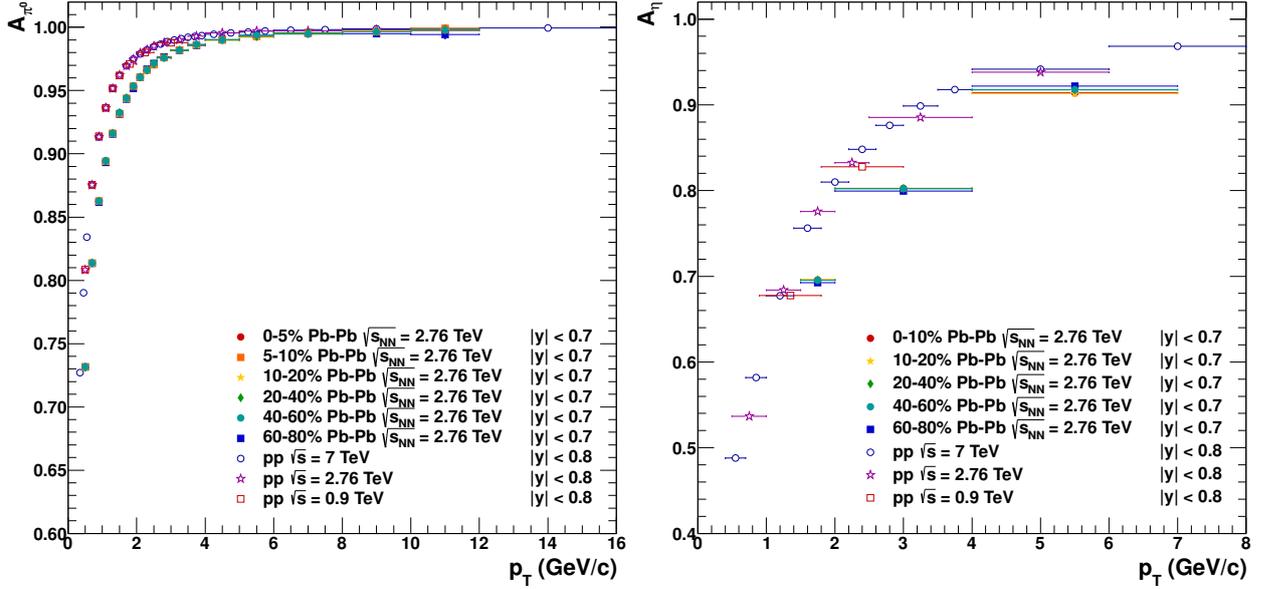
Figure 6.8.: Geometrical acceptance of the π^0 (left) and η (right) meson in pp collisions at $\sqrt{s} = 0.9, 2.76$ and 7 TeV, as well as Pb–Pb collisions in all centrality bins considered in this analysis.

data sample measured at $\sqrt{s} = 7$ TeV can be found in [174].

The shape of the reconstruction efficiency is determined by the shape of the conversion probability and the photon reconstruction efficiency. As both photons have to convert within the acceptance and the individual electrons and positrons need to reach the TPC the π^0 (η) meson reconstruction efficiencies rises slowly until it reaches a plateau above a transverse momentum of 4 GeV/c. The photon conversion probability ($\approx 8\%$) and reconstruction efficiency ($\approx 67\%$ for pp at $\sqrt{s} = 7$ TeV) enter quadratically in the meson reconstruction efficiency, giving for pp collisions a maximum reconstruction efficiency of about 0.34% for the mesons. This value is not reached in the simulation, most likely due to the asymmetric energy distribution of the decay photons. While the efficiencies for the π^0 (η) meson agree for $\sqrt{s} = 0.9$ and 7 TeV, the efficiencies for pp collisions at $\sqrt{s} = 2.76$ TeV are approximately 10% lower. This can be attributed to the missing clusters in the SDD (Section 4.1.1). The decrease in efficiencies going from peripheral to central collisions is caused by the smaller single particle reconstruction efficiency due to the larger multiplicity in central Pb–Pb events and by the tighter α cut for central collisions. While for the primary particle tracking this effect is of the order of 5%, the neutral pion efficiency is reduced by about 20% as the discrepancy enters for all four electron tracks. Similar effects can be observed for the η meson reconstruction efficiencies. However, the statistical errors on the efficiencies are rather large and a fit cannot be performed due to a lack of transverse momentum bins. Thus the precision on the final result for the η meson is currently limited by the Monte Carlo statistics.

Correction for Finite Bin Width

The neutral meson spectra are binned in the transverse momentum and the bin width of these transverse momentum slice increases for higher p_T. The underlying spectrum, however, is steeply falling with increasing transverse momentum. Thus the yield measured in a p_T interval does not correspond to the yield measured at the center of the p_T bin. Therefore, the true p_T value for the yield measured in the interval needs to be determined [199]. This can be done with two different approaches either shifting the data point horizontally in p_T such, that it corresponds to the true p_T for a given yield or by shifting the data point vertically to the true yield for the p_T at the bin center. Both methods depend on the same underlying model assumptions. For the spectra the points are
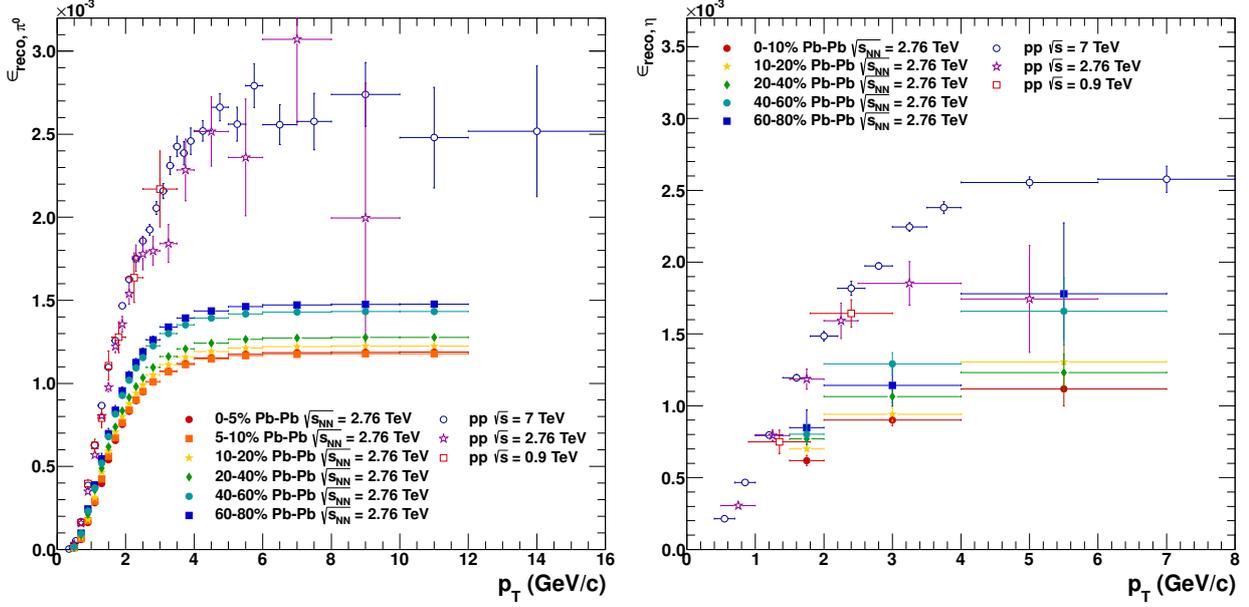
Figure 6.9.: Reconstruction efficiency for π^0 (left) and η (right) mesons in pp collisions at $\sqrt{s} = 0.9$, 2.76 and 7 TeV as well as for Pb–Pb collisions at $\sqrt{s_{NN}} = 2.76$ TeV. For the neutral pion efficiency in Pb–Pb collisions the efficiencies obtained from the Monte Carlo simulations were fitted using Equation 6.6 above 1.2 GeV/c. The original efficiencies can be found in Figure B.1.

shifted in the p_T direction while for the R_{AA} calculation they are shifted in the y-direction. The shifting in the vertical direction for the R_{AA} has been chosen, due to the fact that the spectra in pp and Pb–Pb have different shapes and thus for the same binning the points would shift by a different amount in the p_T direction, making it harder to correctly calculate the R_{AA}. For pp collisions the spectra have been shifted assuming the Tsallis function [200] as an approximation of the underlying spectrum.

$$\frac{\mathrm{d}^2 N}{\mathrm{d}y\mathrm{d}p_T} = \frac{(n_{\mathrm{Tsallis}} - 1)(n_{\mathrm{Tsallis}} - 2)}{n_{\mathrm{Tsallis}}T[n_{\mathrm{Tsallis}}T + m(n_{\mathrm{Tsallis}} - 2)]} \times A \times p_T \times \left(1 + \frac{m_T - m}{n_{\mathrm{Tsallis}}T}\right)^{-n_{\mathrm{Tsallis}}}. \tag{6.7}$$

The parameters m and $m_T = \sqrt{m^2 + p_T^2}$ correspond to the particle mass and the transverse mass, while A, T and n_{Tsallis} are the free parameters of the fit function. In Pb–Pb collisions on the other hand a combined fit of the Tsallis function and a power law function has been assumed as underlying distribution for 0-60% central events, while a pure Tsallis fit was used for the peripheral events. The power law function is given by

$$\frac{\mathrm{d}^2 N}{\mathrm{d}y\mathrm{d}p_T} = C \times p_T \times \left(\frac{1}{p_T}\right)^{n_{\mathrm{pow}}}, \tag{6.8}$$

where C and n_{pow} are the free parameters of the function. The exact point where the Tsallis fit and the power law are matched is left as a free parameter. However, it has to be somewhere between 2 and 6 GeV/c depending on the centrality. In order to be able to combine different measurements in ALICE this bin width correction is only applied to the combined spectrum off all available measurements. Moreover, this allows to constrain the fit even more as each individual measurement covers a slightly different transverse momentum region, resulting in smaller correction factors at high p_T. The amount of this correction depends on the width of the bin in transverse momentum and on the steepness of the spectrum in this momentum interval. The larger the bin and the steeper the spectrum in this interval the larger the correction which needs to be applied. For the neutral pion measurement this correction ranges from 1-4% up to 8 GeV/c afterwards the corrections can be of the order of 10-15% depending on the size of the bin (i.e. 2 GeV/c).

6.1.3. Systematic Error Evaluation

In order to estimate the systematic error for the π^0 and η meson in pp and Pb–Pb collision, each cut which has been performed to select the tracks, electrons, photons and mesons is varied. These variations are chosen such that either the underlying Gaussian distribution is sampled (i.e variation of the pion rejection cut) or that maximum deviations can be accessed (i.e. variation of the single track momentum cut). To calculate the contribution of every cut variation only one cut is varied at a time and the differences in the fully corrected spectra are calculated bin by bin in p_T.

$$\Delta(p_\mathrm{T}) \;=\; \left(\frac{\mathrm{d}^2N}{\mathrm{d}y\mathrm{d}p_\mathrm{T}}\right)_{\mathrm{modified}}(p_\mathrm{T}) - \left(\frac{\mathrm{d}^2N}{\mathrm{d}y\mathrm{d}p_\mathrm{T}}\right)_{\mathrm{standard}}(p_\mathrm{T}) \tag{6.9}$$

$$\sigma_\Delta(p_\mathrm{T}) \;=\; \sqrt{\left|\sigma^2_{\left(\frac{\mathrm{d}^2N}{\mathrm{d}_y\mathrm{d}p_\mathrm{T}}\right)_{\mathrm{modified}}}(p_\mathrm{T}) - \sigma^2_{\left(\frac{\mathrm{d}^2N}{\mathrm{d}_y\mathrm{d}p_\mathrm{T}}\right)_{\mathrm{standard}}}(p_\mathrm{T})\right|} \tag{6.10}$$

The statistical error for each fully corrected spectrum is given by $\sigma_A(p_\mathrm{T})$. As some of these variations can be of statistical nature it was checked whether the deviation was significant ($\Delta(p_\mathrm{T})/\sigma_\Delta(p_\mathrm{T}) > 0.9$), where the error ($\sigma_\Delta(p_\mathrm{T})$) on $\Delta(p_\mathrm{T})$ has been calculated using Equation 6.10, assuming that the errors among the subsets are correlated.

All errors within one cut variation are calculated bin by bin as maximum negative or positive deviation from the standard cut and then the average of the maximum deviations in both directions is taken as the systematic error for this particular cut variation in the corresponding p_T bin. However, as only significant deviations contribute to the error estimate unphysical fluctuations might appear. Thus, if a systematic error for one p_T bin is 0, it is checked whether the neighboring bins show larger contributions. If this is the case the systematic uncertainty is smoothed by taking the average of the neighboring bins. In order to avoid an overestimation of the systematic error close to the edges of the spectrum due to lack statistics the p_T bins closer to the center of the measured spectrum get larger weights (80%) compared to the edges (20%).

The detailed variation, except the yield extraction, considered for the analyses in pp collisions at $\sqrt{s} = 2.76$ TeV and Pb–Pb collisions at $\sqrt{s_{\mathrm{NN}}} = 2.76$ TeV can be found in Table 6.2 and Table 6.3, respectively. The table for pp collisions at $\sqrt{s} = 0.9$ and 7 TeV is shown in Appendix B. Slightly different variations for the pp data collected at 7 TeV and 2.76 TeV have been chosen due to different detector conditions. All individual systematic errors from the different cut variations are divided by $\sqrt{2}$ and then added quadratically for each p_T bin. Afterwards, the p_T independent systematic error from the material budget is added quadratically as well.

The different systematic error sources can be summarized in five categories:

Material Budget
The systematic error on the material budget, which has been described in detail in Section 5.1, represents the largest contribution to the total systematic error with 9.00% for pp collisions and 9.72% for Pb–Pb collisions, as the error has to be counted for both photons. Due to the fact that the systematic error has been calculated using the differences between the two V^0 finders as well as different Monte Carlo generators, these sources are not included separately in the meson systematic error. Additionally, the systematic error of the material budget is based on the R distribution of the photon candidates and thus no variations of the R cut will be included for the meson systematics to avoid double counting in the systematic error.

Signal Extraction
This category combines the cut variation concerning the background, the energy asymmetry α of the two photons as well as the actual signal extraction error. The later is estimated varying the integration window for the signal extraction as well as the range for the normalization of the background. Table 6.4 shows the detailed values of these variations for the π^0 and η

Quantity	Standard	Cut variation 1	Cut variation 2	Cut variation 3	Cut variation 4
dE/dx e-line					
$\sigma_{\mathrm{d}E/\mathrm{d}x,e}$	$-4 < \sigma < 5$	$-5 < \sigma < 5$	$-3 < \sigma < 5$		
dE/dx π-line					
π rej. low p					
$\sigma_{\mathrm{d}E/\mathrm{d}x,\pi}$	< 2	< 2	< 2	< 0	< 2
π rej. high p					
$\sigma_{\mathrm{d}E/\mathrm{d}x,\pi}$	< 0.5	< 1	< -10	< -10	< -0.5
$p_{\min,\,\pi\ \mathrm{rej}}$	0.25 GeV/c	0.25 GeV/c	0.3 GeV/c	0.5 GeV/c	0.4 GeV/c
$p_{\max,\,\pi\ \mathrm{rej}}$	3.5 GeV/c	3.5 GeV/c	3.5 GeV/c	100 GeV/c	3 GeV/c
single $p_{\mathbf{T}}$ $e^{\pm}$	> 0.05 GeV/c	> 0.075 GeV/c	> 0.1 GeV/c		
χ^2 γ	< 20	< 30	< 15	< 50	
min TPC clust./ find. clust.	> 0.6	> 0	> 0.35		
$q_{\mathbf{T,max}}$	< 0.05 GeV/c	< 0.03 GeV/c	< 0.07 GeV/c		
α **meson**	< 1	< 0.7			
Background Method	Mixed event (track mult)	Mixed event (V0 mult)			
N_{γ} mixing	60	100	50		

Table 6.2.: Variations for the systematic error evaluation in pp collisions at $\sqrt{s} = 2.76$ TeV. The column with the title "Standard" reflects the standard cut for each cut respectively, while the columns titled with "Cut variation" show the variations, which were done for the respective cut (row). Only one cut is varied at a time to estimate the systematic error.

Quantity	Standard	Cut variation 1	Cut variation 2	Cut variation 3	Cut variation 4
dE/dx e-line					
$\sigma_{\mathrm{d}E/\mathrm{d}x,e}$	$-3 < \sigma < 5$	$-4 < \sigma < 5$	$-2.5 < \sigma < 4$		
dE/dx π-line					
π rej. low p	< 3	< 3	< 2	< 2.5	< 3.5
$\sigma_{\mathrm{d}E/\mathrm{d}x,\pi}$					
π rej. high p	< -10	< -10	> -10	> -10	> -10
$\sigma_{\mathrm{d}E/\mathrm{d}x,\pi}$					
$p_{\min,\,\pi\ \mathrm{rej}}$	0.4 GeV/c	0.3 GeV/c	0.3 GeV/c	0.4 GeV/c	0.4 GeV/c
$p_{\max,\,\pi\ \mathrm{rej}}$	100 GeV/c	5 GeV/c	5 GeV/c	100 GeV/c	100 GeV/c
σ_e **TOF**	$-5 < \sigma_e < 5$	$-3 < \sigma_e < 5$	$-2 < \sigma_e < 3$		
single $p_{\mathbf{T}}$ $e^{\pm}$	> 0.05 GeV/c	> 0.075 GeV/c	> 0.1 GeV/c		
χ^2 γ	< 30	< 50	< 20		
min TPC clust./ find. clust.	> 0.6	> 0.7	> 0.35		
$q_{\mathbf{T,max}}$	< 0.05 GeV/c	< 0.03 GeV/c	< 0.07 GeV/c		
α **meson** $<$	0-40%: 0.6 40-80% 0.8	0.65 0.75	0.7 0.85		
Background N_{γ} mixing	50	20	5		

Table 6.3.: Variations for the systematic error evaluation in Pb–Pb collisions. The column with the title "Standard" reflects the standard cut for each cut respectively, while the columns titled with "Cut variation" show the variations, which were done for the respective cut (row). Only one cut is varied at a time to estimate the systematic error.

	π^0	η
Normalization window		
Right side (standard)	(0.17, 0.3) GeV/c^2	(0.58, 0.8) GeV/c^2
Left side (standard)	(0.05, 0.08) GeV/c^2	(0.35, 0.48) GeV/c^2
Integration range		
standard	$M_{\pi^0} - 0.035,\ M_{\pi^0} + 0.010)$ GeV/c^2	$M_\eta - 0.047,\ M_\eta + 0.023)$ GeV/c^2
narrow	$M_{\pi^0} - 0.015,\ M_{\pi^0} + 0.005)$ GeV/c^2	$M_\eta - 0.032,\ M_\eta + 0.013)$ GeV/c^2
wide	$M_{\pi^0} - 0.055,\ M_{\pi^0} + 0.025)$ GeV/c^2	$M_\eta - 0.067,\ M_\eta + 0.033)$ GeV/c^2

Table 6.4.: Variations of the integration and normalization windows for the estimate of the systematic error from the signal extraction.

mesons. The yield extraction error is one of the largest systematic error sources, contributing between 3-5% to the total systematic error for the neutral pions and 10-15% to the error on the η. For Pb–Pb collisions the error for the neutral pions is of the same order, while it increases for the η to up to 30 % as the signal extraction is much more difficult in Pb–Pb collisions.

For the systematic error of the background two variations are taken into account for pp at $\sqrt{s} = 2.76$ TeV and Pb–Pb collisions: the variation of the number of photons in the buffer and the background calculations based on the mixed event method with different multiplicity estimators. For the data recorded at $\sqrt{s} = 0.9$ and 7 TeV all three different background calculation methods are considered.

Track Reconstruction

This category summarizes all systematic error sources related to the secondary track sample, thus it combines the systematic errors from the variation of the TPC cluster over findable cluster cut and the minimum transverse momentum cut. This systematic error contributes mainly at low momentum, where the tracks are not that well defined. The contribution to the systematic error for the π^0 meson spectrum is of the order of $2 - 5\%$ in the medium p_{T} region ($1 - 5$ GeV/c). For the η meson on the other hand this error is of the order of $5 - 10\%$.

Electron PID

All cut variations which are related to electron identification or pion rejection are combined in the electron PID systematic error. Thus, the variations of the σ cuts on the TPC dE/dx as well as possible TOF cuts. This cut variation is the largest contribution to the systematic error for Pb–Pb collisions after the material budget error. For pp collisions it contributes approximate $2 - 3\%$ to the total systematic error.

Photon Reconstruction

The systematic error assigned to the photon reconstruction combines the error from the q_{T} cut as well as the χ^2 photon cut. In pp collisions it is of the order of $2 - 3\%$ ($4 - 10\%$) for the π^0 (η) meson like the systematic error from the electron PID and the track reconstruction. For Pb–Pb collisions on the other hand it is of the order of $4 - 7\%$ for the π^0 and $10 - 20$ % for the η meson.

The final systematic errors for pp collisions at $\sqrt{s} = 2.76$ TeV for the π^0 (left) and η meson (right) are visualized in Figure 6.10, the detailed tables can be found in the Appendix B, as well as the errors for 900 GeV and 7 TeV. For peripheral and central Pb–Pb collisions the systematic errors for both mesons are shown in Figure 6.11 and Figure 6.12, respectively. For the remaining centrality classes the plots and tables can be found in the Appendix B. The systematic errors on the neutral pion spectrum are dominated by the material error, regardless of the collision system. In the regions, where the signal extraction is stable and enough statistics is available the total errors are of the order of 10-14%. Moreover, it can be seen that all other systematic error sources, except

the material, are approximately of the same order. For the η meson the errors are considerably larger, $\sim$ 15-20% in pp at $\sqrt{s} = 2.76$ TeV and $\sim$ 40% for Pb–Pb collisions. This can be attributed to the difficult signal extraction which is the dominating error for all collision systems.
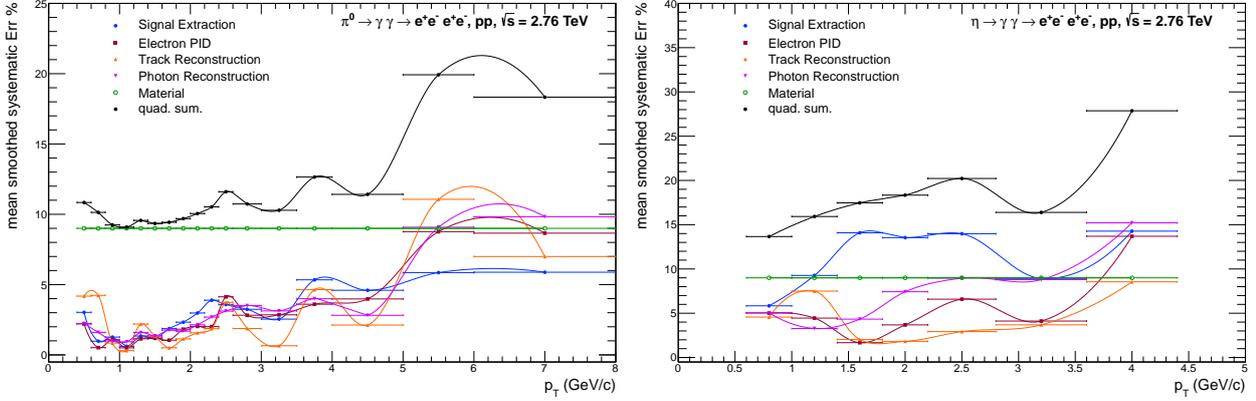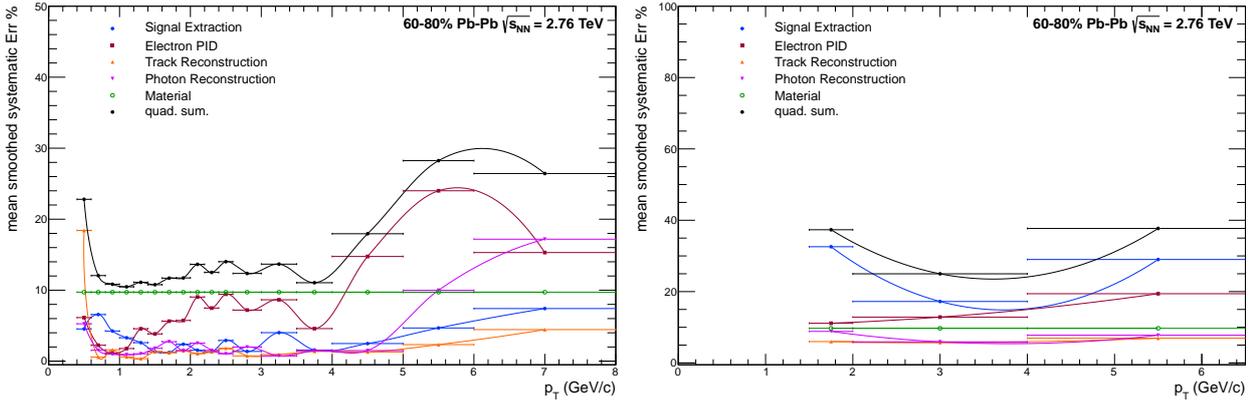

Figure 6.10.: Visualization of the systematic errors for pp collisions at $\sqrt{s} = 2.76$ TeV. The colored points represent the individual error sources, while the black points represent the final systematic error for the π^0 (left) and η (right) meson spectra.
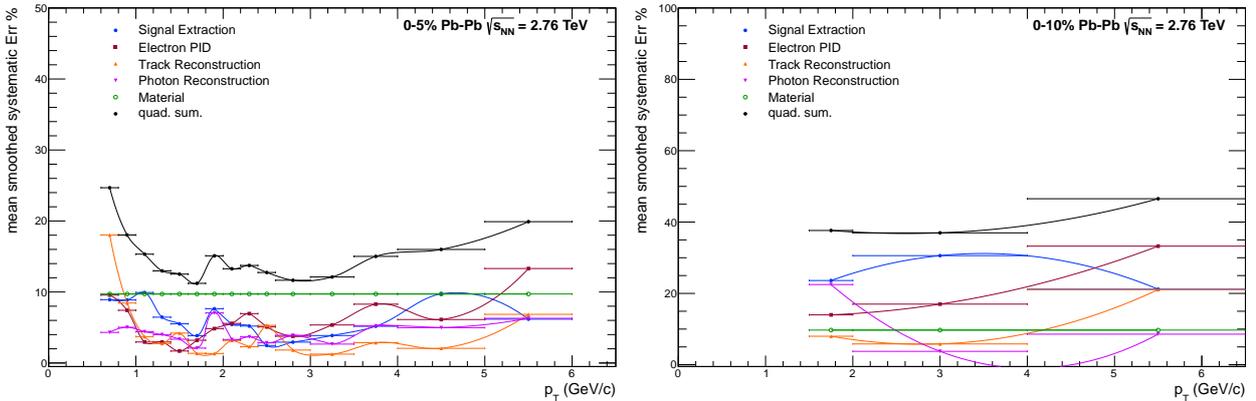

Figure 6.11.: Visualization of the systematic errors for 60-80% Pb–Pb collisions at $\sqrt{s_{NN}} = 2.76$ TeV. The colored points represent the individual error sources, while the black points represent the final systematic error for the π^0 (left) and η (right) meson spectra.

Figure 6.12.: Visualization of the systematic errors for the π^0 (left) and η (right) meson for 0-5%(0-10%) Pb–Pb collisions at $\sqrt{s_{NN}} = 2.76$ TeV. The colored points represent the individual error sources, while the black points represent the final systematic error of the spectra.

6.2. π^0 and η Meson Cross Sections in pp Collisions at the LHC

After having corrected the raw yield of the π^0 meson, for the secondary π^0 meson contamination, the differential invariant cross section can be calculated using the geometrical acceptance and reconstruction efficiency, described in Section 6.1.2.

$$E\frac{\mathrm{d}^3\sigma}{\mathrm{d}p^3} = \frac{1}{2\pi}\frac{\sigma_{\mathrm{MB_{OR}}}}{N_{\mathrm{evt.}}}\frac{1}{p_T}\frac{1}{\epsilon_{\mathrm{reco,}\ \pi^0(\eta)}}\frac{1}{A_{\pi^0(\eta)}}\frac{1}{\mathrm{BR}}\frac{N^{\pi^0(\eta)}}{\Delta y \Delta p_{\mathrm{T}}} \tag{6.11}$$

Here $N_{\mathrm{evt.}}$ is the number of events for normalization, shown in Table 4.2, $\sigma_{\mathrm{MB_{OR}}}$ the cross section for the $\mathrm{MB_{OR}}$ trigger (Table 4.1), BR the branching ratio of the decay $\pi^0(\eta) \to \gamma\gamma$ and $N^{\pi^0(\eta)}$ the reconstructed raw yield for the π^0 or η meson within the rapidity range [-0.8,0.8] and the transverse momentum bin Δp_{T}. The p_{T} is the corrected p_{T} obtained from the shift in the x direction.

6.2.1. Comparison and Combination of PCM and PHOS Results

In order to arrive to the final transverse-momentum spectra the combined spectrum is calculated as a weighted average of the results obtained with the Photon Conversion Method (PCM) and the measurement of neutral pions via the energy deposit of their decay photons in PHOS [184], using the statistical and systematic errors of the individual analysis as weights [130]. This is done for all measurements, where both analysis have a result. The invariant cross section of the η at $\sqrt{s} = 0.9$ and 2.76 TeV is solely based on the PCM measurement. The combination of the two measurements allows to cover a larger p_{T} range, as well as the precision increases, as both measurement have no systematic uncertainties in common. For pp collisions at $\sqrt{s} = 7$ TeV the PCM measurement for the π^0 meson reaches from 0.3 GeV/c to 12 GeV/c in transverse momentum, while the PHOS spectrum covers the p_{T} range 0.8 to 25 GeV/c. At high transverse momenta both analysis are limited by the statistics in the data. Thus the p_{T} reach for the data sample recorded at $\sqrt{s} = 2.76\ (0.9)$ TeV decreases to 8 (3.5) GeV/c for the PCM analysis and 12 (7) GeV/c for the PHOS analysis. Furthermore, their resolution shows opposite trends as it can be seen in Figure 6.14.
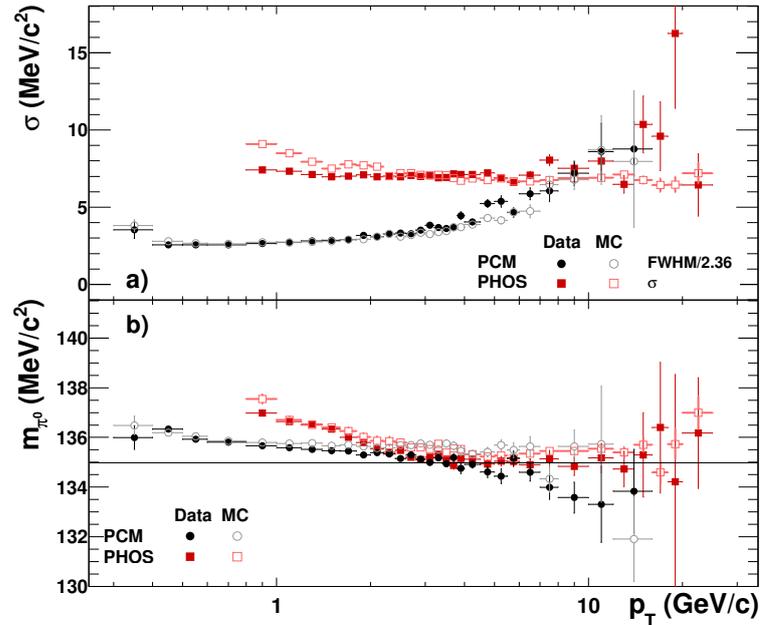

Figure 6.13.: Reconstructed π^0 meson invariant mass resolution (a) and peak position (b) as a function of p_{T} in pp collisions at $\sqrt{s} = 7$ TeV. Both measurements are compared to the corresponding analysis in Monte Carlo simulations and the nominal π^0 mass is indicated by the horizontal black line in (b).
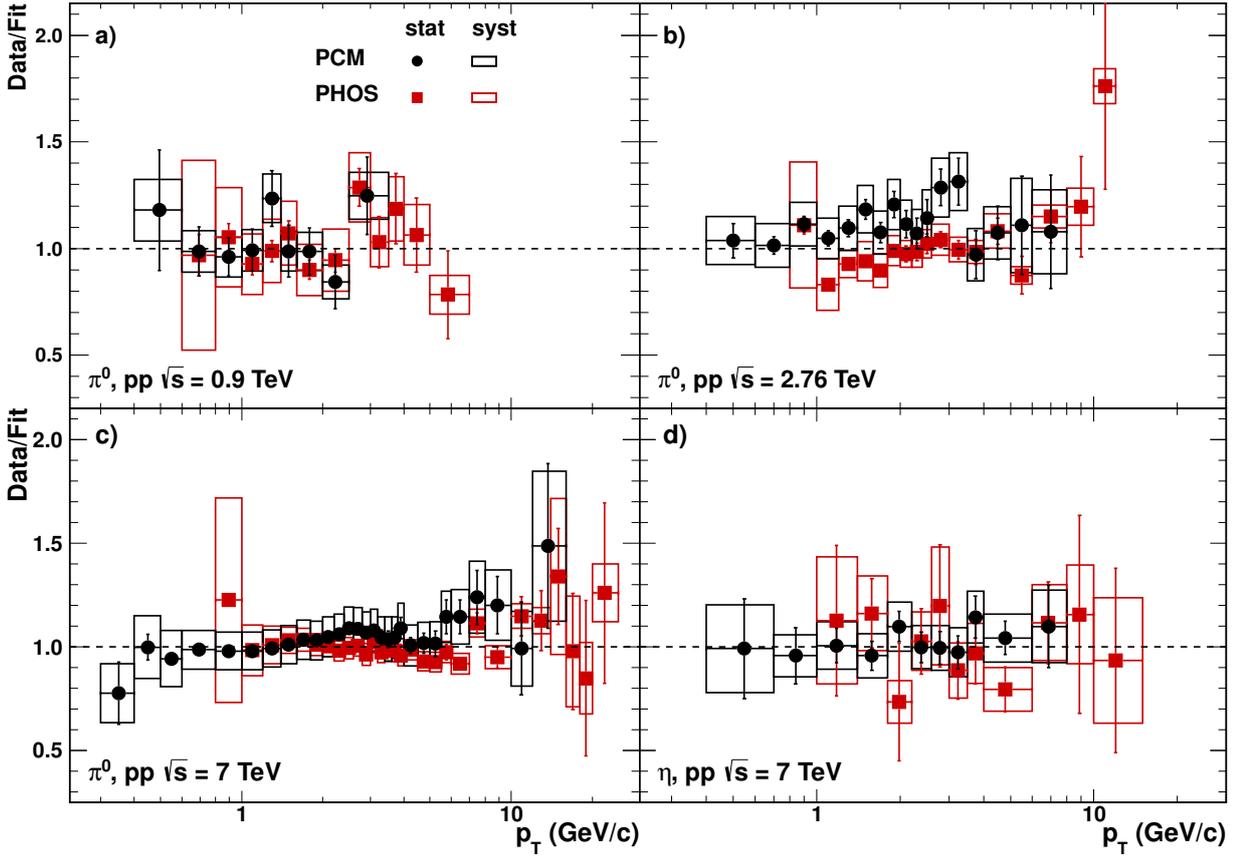
Figure 6.14.: Ratio of the two independent π^0 meson measurements in pp collisions at $\sqrt{s} = 0.9$, 2.76 and 7 TeV (a-c) to the fit of the combined normalized invariant production cross section at the corresponding energies. Moreover, the comparison for the η meson at $\sqrt{s} = 7$ TeV (d) is shown.

While the invariant mass resolution of the PCM method deteriorates with increasing momentum, the resolution in the calorimeter improves. At low momentum ($p_\mathrm{T} < 2$ GeV/c) on the other hand the fitted mass position obtained with the Photon Conversion Method method is closer to the nominal mass and is nearly ideally matched by the simulated mass resolution and position. Thus at low p_T the precision of the conversion method is larger and the spectra can be measured down to 0.3 GeV/c.

The combined spectra are fitted with a Tsallis function (Equation 6.7) and the fit on the combined spectrum is compared to the individual measurements to quantify the agreement of the two methods. The resulting comparisons for the π^0 meson at the three center-of-mass energies and the η meson at $\sqrt{s} = 7$ TeV can be seen in Figure 6.14. The measured spectra in PCM and PHOS agree well within the systematic errors in the region where both measurement have enough significance and statistics ($p_\mathrm{T} \sim 1 - 5$ GeV/c), whereas they start to deviate at high p_T. In this region on the other hand the PCM resolution deteriorates and the statistical error is large, thus at high p_T ($p_\mathrm{T} > 5 - 6$ GeV/c) the PHOS measurement dominates the combined spectrum.

The final parameters of the Tsallis fits are shown in Table 6.5. The parameter A can be identified with the integral of this function over p_T from 0 to $\sqrt{s}/2$ and thus can be treated as an estimate of the total yield at $y = 0$ per inelastic pp collision. The errors of the cross sections are not included in the error estimate of A. As expected the total yield increases with increasing center-of-mass energy for the π^0 and for the η meson between 2.76 TeV and 7 TeV. For the η at $\sqrt{s} = 0.9$ TeV only two p_T points could be measured, which does not allow to draw conclusions from a fit with 3 free parameters. The parameter n_Tsallis on the other hand can be identified with the parameter n_pow from a pure power law function (Equation 6.8). Therefore, this parameter reflects the steepness of the spectrum. From the fits to the π^0 meson spectrum it can be seen that n_Tsallis decreases

Meson	$\sqrt{s}$ (TeV)	A	T (MeV/c^2)	n_{Tsallis}
π^0	7	2.45 ± 0.16	137.6 ± 4.2	6.87 ± 0.08
	2.76	2.18 ± 0.24	125.7 ± 7.3	7.01 ± 0.17
	0.9	1.53 ± 0.30	132.2 ± 14.9	7.84 ± 0.52
η	7	0.21 ± 0.03	229.3 ± 20.6	6.99 ± 0.47
	2.76	0.17 ± 0.05	217.5 ± 31.5	7.01

Table 6.5.: Fit parameters of the Tsallis parameterization (Equation 6.7) to the combined invariant production yield of π^0 and η mesons for inelastic events.

with increasing energy, which can be interpreted as a spectrum which becomes flatter for larger center-of-mass energies. For the fit on the η spectra at lower energies not enough points have been measured to leave all parameters free, therefore the parameter n has been fixed to the result from the neutral pions, as n_{Tsallis} should be a species in dependent parameter. The parameter T seems to be a species dependent parameter as well, as the results for the π^0 meson at the three different energies are compatible with $T \approx 130 - 132$ MeV/c, while this parameter for the η meson seems to be close to $210 - 230$ MeV/c.

6.2.2. Comparison to Theory

The combined π^0 and η differential invariant cross sections in pp collisions at $\sqrt{s} = 0.9$, 2.76 and 7 TeV have been compared to NLO pQCD calculations [127]. These calculations were obtained using CTEQ6M5 PDF's as parton distribution functions and DSS [201] fragmentation functions for the π^0 meson. For the η the AESSS [202] fragmentation functions have been used. The uncertainties of the theoretical predictions are estimated by varying the factorization, fragmentation and renormalization scale from $\mu = p_{\text{T}}$ to $\mu = 0.5\ p_{\text{T}}$ and $\mu = 2\ p_{\text{T}}$. Moreover, a different set of calculations based on the CTEQ5M PDF's and BKK [203] fragmentation functions has been included in the comparison for the π^0 in pp collisions at $\sqrt{s} = 0.9$ and 7 TeV. The calculations have been done using the INCNLO code [185].

The spectra for the π^0 meson can be seen in the left plot of Figure 6.15 together with the NLO pQCD calculation (dashed/dotted lines) and the fit (solid line) to the measured data. In order to compare data and theory, both have been divided by the fit result. This ratios are displayed in the right plot of Figure 6.15 for the three different center of mass energies. A similar procedure has been applied to the η spectra, however the fit does not reproduce the data as well as for the π^0. Figure 6.16 shows the measured invariant η cross section together with NLO pQCD calculations on the left hand side, while the right hand side depicts the ratio of the data (calculations) to the fit.

The data measured at $\sqrt{s} = 0.9$ TeV are in agreement with the theory corresponding to a μ of p_{T} or $2p_{\text{T}}$ for both mesons. For the measurement at $\sqrt{s} = 2.76$ TeV a deviation of $\approx 10\%$ can be seen for the neutral pion from the theoretical curve with $\mu = 2p_{\text{T}}$ for $p_{\text{T}} > 3$ GeV/c, all other curves are even further away from the measured data. This statement cannot be confirmed by the η measurement at the same center-of-mass energy. However, the error bars for the η are much larger. For the measurement at the highest collision energy $\sqrt{s} = 7$ TeV both measured spectra are more than $\approx 40\%$ below the NLO pQCD calculations with $\mu = 2p_{\text{T}}$ taking the fragmentation functions and PDF's which described well the data at lower center-of-mass energies. Only the calculations done with the BKK fragmentation functions and $\mu = 2p_{\text{T}}$ can reproduce the measured data between 2 and 8 GeV/c. However, at high transverse momenta they start do disagree as well. In the past a trend has been observed that larger collision energies require larger μ values, thus it should be tested, whether the calculations for $\mu = 4p_{\text{T}}$ would agree with the data, to confirm the observations from [204]. While the individual spectra cannot be fully reproduced by
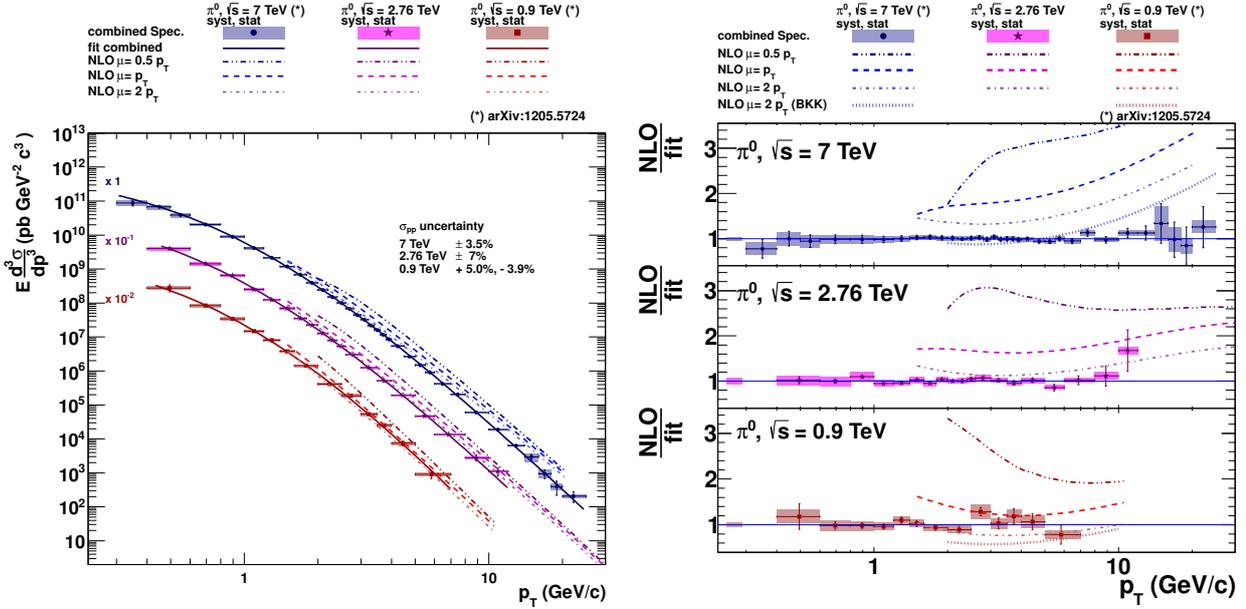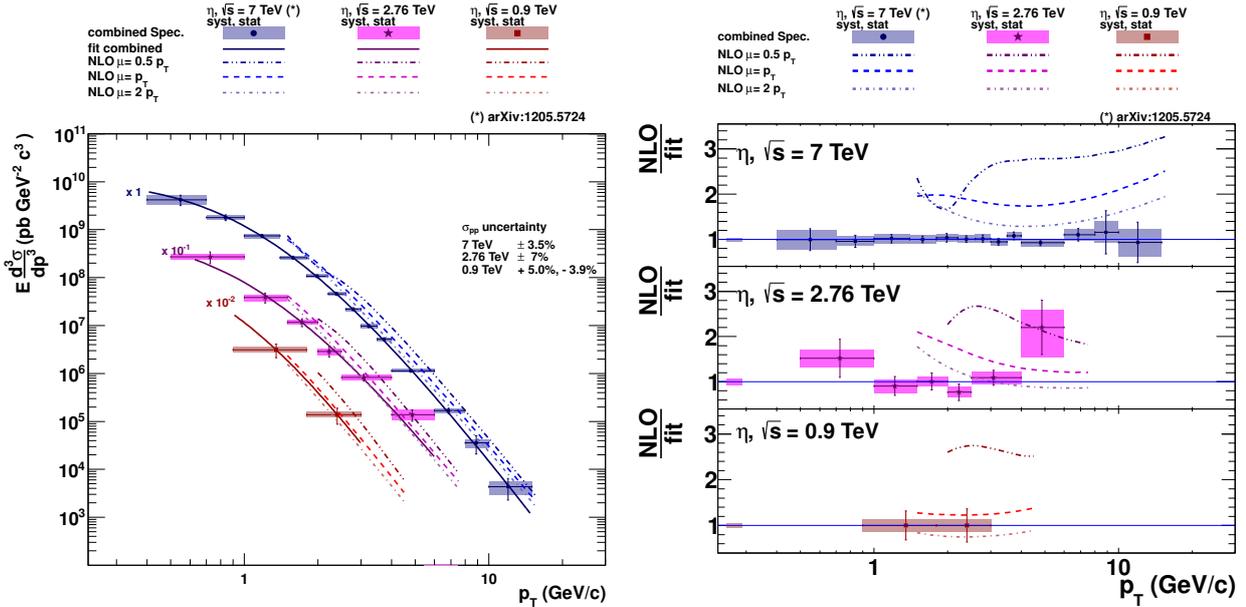
Figure 6.15.: Differential invariant cross section of the π^0 meson production (left) in pp at $\sqrt{s} = 0.9$ (red squares), 2.76 TeV (purple stars) and 7 TeV (blue dots). The shaded boxes indicate the systematic error, while the error bars show the statistical error. The solid lines represent the Tsallis fit the the combined spectrum. Ratio of the data and next to leading order calculation using CTEQ6M5 PDF and the DSS (BKK) fragmentation functions for three scales $\mu = 0.5p_{\mathrm{T}}$, p_{T} and $2p_{\mathrm{T}}$ (right).

Figure 6.16.: Differential invariant cross section of the η meson production (left) in pp at $\sqrt{s} = 0.9$ (red squares), 2.76 TeV (purple stars) and 7 TeV (blue dots). The shaded boxes indicate the systematic error, while the error bars show the statistical error. The solid lines represent the Tsallis fit the the combined spectrum. Ratio of the data and next to leading order calculation using CTEQ6M5 PDF and the AES fragmentation functions for three scales $\mu = 0.5\,p_{\mathrm{T}}$, p_{T} and $2p_{\mathrm{T}}$ (right).

the theoretical calculations the ratio of η/π^0 can be reproduced nicely, as it can be seen in the left plot of Figure 6.17.

6.2.3. η/π^0 ratio

The η/π^0 ratio gives insights into the particle production mechanisms. In this ratio the uncertainties for the cross section cancels. Moreover, for the individual measurements with PCM and
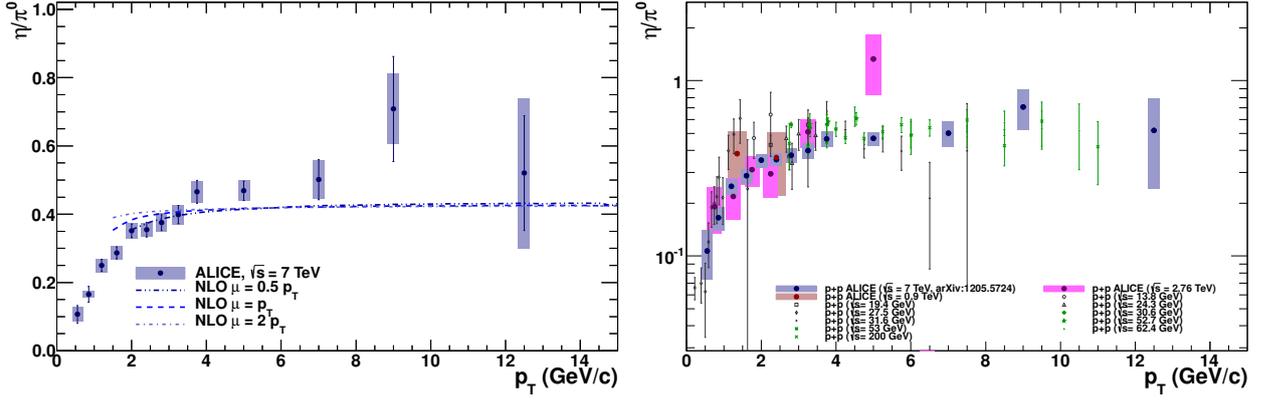
Figure 6.17.: Left: Measured η/π^0 ratio at $\sqrt{s} = 7$ TeV as a function of transverse momentum compared to theory [127]. Right: Measured η/π^0 ratio at $\sqrt{s} = 0.9$ (red), 2.76 (purple) and 7 TeV (blue) as a function of transverse momentum and previous measurements a lower energies [205]. While the boxes in the left plot reflect the systematic uncertainties and the error bars show the statistical error, the boxes in the right plot indicate the quadratically summed statistical and systematic error as the error bars for the lower energy data.

PHOS several systematic errors cancel (i.e. the material error for PCM), as they would affect both spectra in the same way. For the result at $\sqrt{s} = 7$ TeV, first the η/π^0 ratio has been built from the spectra of the individual measurement in PCM and PHOS and then the combined ratio has been calculated as a weighted average of both measurements. The right plot of Figure 6.17 shows the measured η/π^0 ratio for pp collisions at $\sqrt{s} = 0.9$ (red), 2.76 (purple) and 7 (blue) TeV together with measurements at lower energies [205]. The results for $\sqrt{s} = 7$ TeV show the characteristic behavior of the η/π^0, the ratio increases with transverse momentum until it flattens above a p_T of ≈ 3.5 GeV/c. A similar behavior can be seen for the η/π^0 ratio at $\sqrt{s} = 2.76$ TeV, however the points above 4 GeV/c have large statistical and systematic error bars. For the data sample collected at $\sqrt{s} = 900$ GeV only two points for the η could be extracted and the systematic error are huge. Nevertheless, the η/π^0 ratio is in agreement with the data measured at higher energies. The comparison to the data measured at lower energies shows good agreement over the full transverse momentum range. The displayed low energy data have been measured in pp collisions at different center-of-mass energies ranging from $\sqrt{s} = 13.8$ GeV to 200 GeV. However, only the data at $\sqrt{s} = 30.6, 52.7, 53, 63.4$ and 200 GeV (green points) have been measured in collider experiments. This shows that the measurements presented in this thesis are the first which cover the low and high momentum part of the ratio for a collider experiment, while the other collider data only cover the high momentum region starting at $p_T = 2.5$ GeV/c. This is only possible due to the reconstruction of the π^0 and η mesons down to very low p_T with the Photon Conversion Method, reflecting the impact of this method for precision low transverse momentum measurements.

6.3. Neutral Pions and Eta Mesons in Pb–Pb Collisions

For Pb–Pb collisions the differential invariant yield for each centrality class is calculated using Equation 6.12

$$E\frac{\mathrm{d}^3N}{dp^3} = \frac{\mathrm{d}^3N}{p_{\mathrm{T}}\mathrm{d}p_{\mathrm{T}}\mathrm{d}y\mathrm{d}\varphi} = \frac{1}{2\pi}\frac{1}{p_{\mathrm{T}}}\frac{\mathrm{d}^2N}{\mathrm{d}y\mathrm{d}p_{\mathrm{T}}} = \frac{1}{2\pi}\frac{1}{N_{\mathrm{evt.}}}\frac{1}{p_T}\frac{1}{\epsilon_{\mathrm{reco,}~\pi^0(\eta)}}\frac{1}{A_{\pi^0(\eta)}}\frac{1}{\mathrm{BR}}\frac{N^{\pi^0(\eta)}}{\Delta y\Delta p_{\mathrm{T}}}. \quad (6.12)$$

Here $N_{\mathrm{evt.}}$ corresponds to the number of events in the different centrality classes, as shown in Table 4.4, $\epsilon_{\mathrm{reco,}~\pi^0(\eta)}$ is the reconstruction efficiency and $A_{\pi^0(\eta)}$ is the acceptance for each meson in the respective centrality class, as defined in Section 6.1.2. The remaining variables are the same as in Equation 6.11 for the invariant cross section.

6.3.1. Neutral Pion Transverse Momentum Spectra in Pb–Pb

In Pb–Pb collisions the π^0 can be reconstructed with the Photon Conversion Method in a p_{T} range from 0.6 (0.4) to 8 GeV/c for $0-10\%$ ($10-80\%$) Pb–Pb collisions with a systematic errors of the order of $10-15\%$ in the mid p_{T} region ($p_{\mathrm{T}} \approx 1-6$ GeV/c). In order to extend the momentum reach and to decrease the errors the PCM result is combined with the measurement of the neutral pions using the PHOS detector [187]. In the momentum region where both spectra overlap the weighted average is taken as for pp collisions, while for low momenta ($p_{\mathrm{T}} < 1$ GeV/c) only PCM is taken and at high momentum ($p_{\mathrm{T}} > 8$ GeV/c) only PHOS points are taken into account for the combined spectrum.

The combined differential invariant yield for different centrality classes can be seen in Figure 6.18, together with pp reference spectrum at $\sqrt{s} = 2.76$ TeV. In order to quantify the agreement between the two measurements and to shift the measured points to the correct position in the wide momentum bins the combined spectra have been fitted with a combination of a power law (Equation 6.8) at high momentum and a Tsallis function (Equation 6.7) at low momentum. For 60-80% a pure Tsallis function was used. The results for all centralities can be seen in Table 6.6. Afterwards, the individual spectra are compared to the fit. The pp reference spectrum has been fitted with a power law and a Tsallis function. The results of the Tsallis fit for pp collisions are displayed in Table 6.5, the power law fit showed an n_{pow} of 6.03 ± 0.12.

The comparison of the individual measurements in PHOS and PCM to the combined fit is shown in Figure 6.19 for all six centrality classes. Unfortunately, the fit in the first four centrality classes cannot describe the spectrum in the full momentum range and tends to underestimate the spectra for the 2-3 lowest momentum bins, thus the first points all seem to be a little bit too high compared to the fit. While the spectra in PHOS and PCM agree in all centrality classes above

Centrality	A	n_{Tsallis}	T (MeV/c^2)	$p_{T,\mathrm{bound}}$	n_{pow}
$0-5\%$	106.04 ± 21.49	20.4 ± 3.5	211.6 ± 19.3	3.98 ± 0.22	7.12 ± 0.26
$5-10\%$	131.20 ± 22.38	14.7 ± 1.2	177.7 ± 12.0	4.50 ± 0.20	6.81 ± 0.21
$0-10\%$	102.38 ± 33.28	20.2 ± 3.8	210.0 ± 17.9	3.72 ± 0.20	7.41 ± 0.15
$10-20\%$	109.83 ± 18.43	13.9 ± 1.2	170.2 ± 12.6	4.20 ± 0.22	7.00 ± 0.17
$20-40\%$	66.25 ± 9.76	15.2 ± 1.6	173.9 ± 12.2	3.00 ± 0.71	7.41 ± 0.08
$40-60\%$	31.92 ± 10.65	10.7 ± 0.5	137.9 ± 8.1	4.20 ± 0.21	7.12 ± 0.13
$60-80\%$	34.83 ± 3.87	7.8 ± 0.3	148.7 ± 8.5	$-$	$-$

Table 6.6.: Fit parameters of the Tsallis parameterization (Equation 6.7) combined with a power law function (Equation 6.8) at high momentum to the combined invariant production yield of π^0 in Pb–Pb collisions at $\sqrt{s_{\mathrm{NN}}} = 2.76$ TeV for different centralities. The peripheral bin was fitted with a pure Tsallis function.
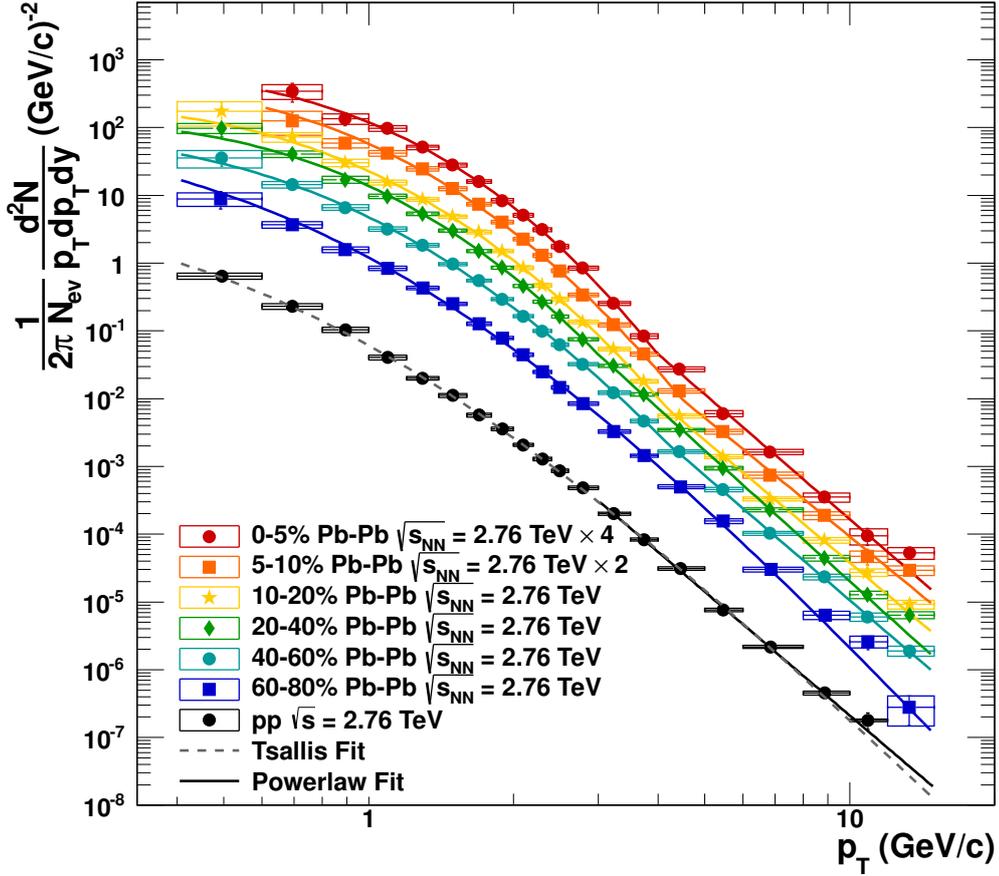
Figure 6.18.: π^0 meson differential invariant yield for different centrality classes in Pb–Pb collisions at $\sqrt{s_{\mathrm{NN}}} = 2.76$ TeV and for pp collisions at $\sqrt{s} = 2.76$ TeV. The pp result was fitted with a pure power law (solid black line, Equation 6.8) and a Tsallis function (dashed gray line, Equation 6.7). For Pb–Pb collisions the spectra have been fitted with a combination of a power law at high momentum and a Tsallis function at low momentum. The resulting fit for each centrality is displayed in the corresponding color.

$p_{\mathrm{T}} = 3$ GeV/c, a clear disagreement for the central classes can be seen below $p_{\mathrm{T}} = 3$ GeV/c. For peripheral Pb–Pb collisions the agreement between PCM and PHOS is better than 10 % and thus well within the systematic and statistical uncertainties. However, the signal extraction in central events $(0 - 40\%)$ is challenging for both analyses, while the PCM measurement suffers from the loss of efficiency in the tracking and larger combinatorial background, the occupancy in PHOS leads to severe shower overlap for the photons. Thus only the core energy in the cluster in PHOS can be used for energy estimate of the photon and the remaining energy needs to be corrected for using Monte Carlo simulations. These corrections can be very large at low momentum, therefore the PHOS analysis will be revisited with respect to their systematic uncertainties and correction factors for low momentum neutral pions in central Pb–Pb collisions.

Moreover, the comparison to the charged pion spectra at low [57] and high momenta [186], which is shown in Figure 6.20, lead to the conclusion that the efficiencies and corrections for the PHOS measurement at low transverse momentum in central Pb–Pb collisions are not fully understood and need to be revisited. The low momentum charged pion measurement relies on the particle identification in the ITS, TPC and TOF. For the high momentum charged pions the fraction of pions in the relativistic rise of the TPC has been calculated in different p_{T} slices, using a multiple Gaussian fit of the $\mathrm{d}E/\mathrm{d}x$ distribution. These fractions have then been multiplied with unidentified charged hadron measurement to arrive to the final charged pion spectra. The comparison of the PCM measurement (blue and black points) to the two charged pion measurements shows that they agree with unity within the systematic and statistical uncertainties. However, for the peripheral
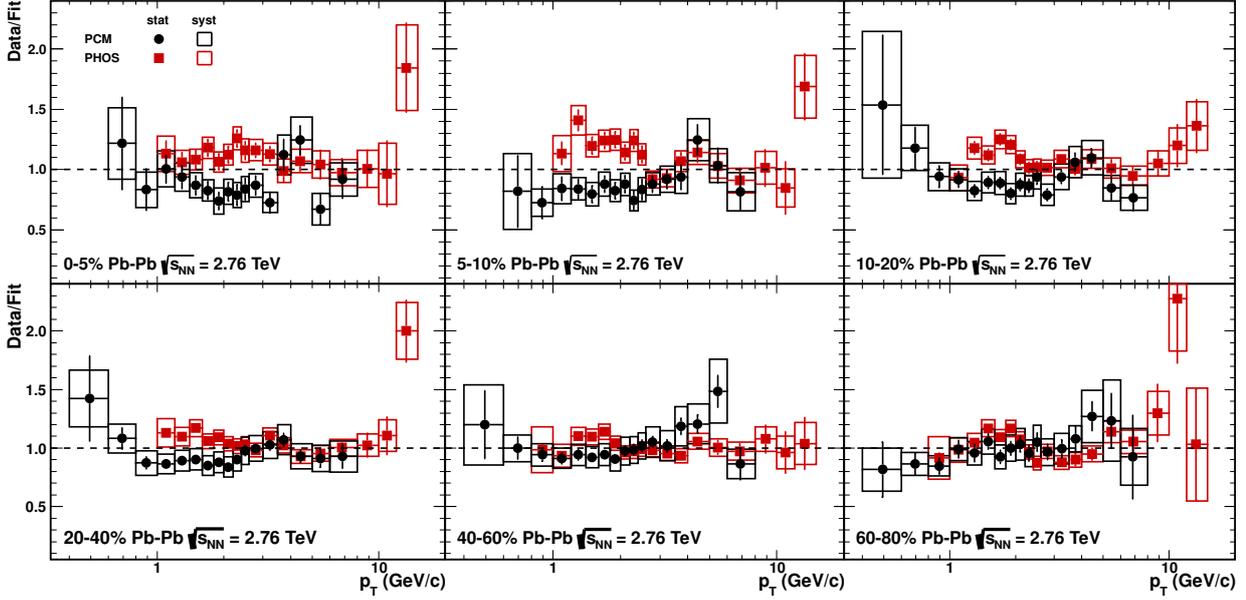
Figure 6.19.: Ratio of the fully corrected π^0 spectra in Pb–Pb collisions at $\sqrt{s_{NN}} = 2.76$ TeV in six centrality bins measured with the PHOS and PCM methods to the fits to the combined result in each bin. The vertical lines represent the statistical errors, while the boxes indicate the individual systematic errors, the error of the fit it not included in the errors.
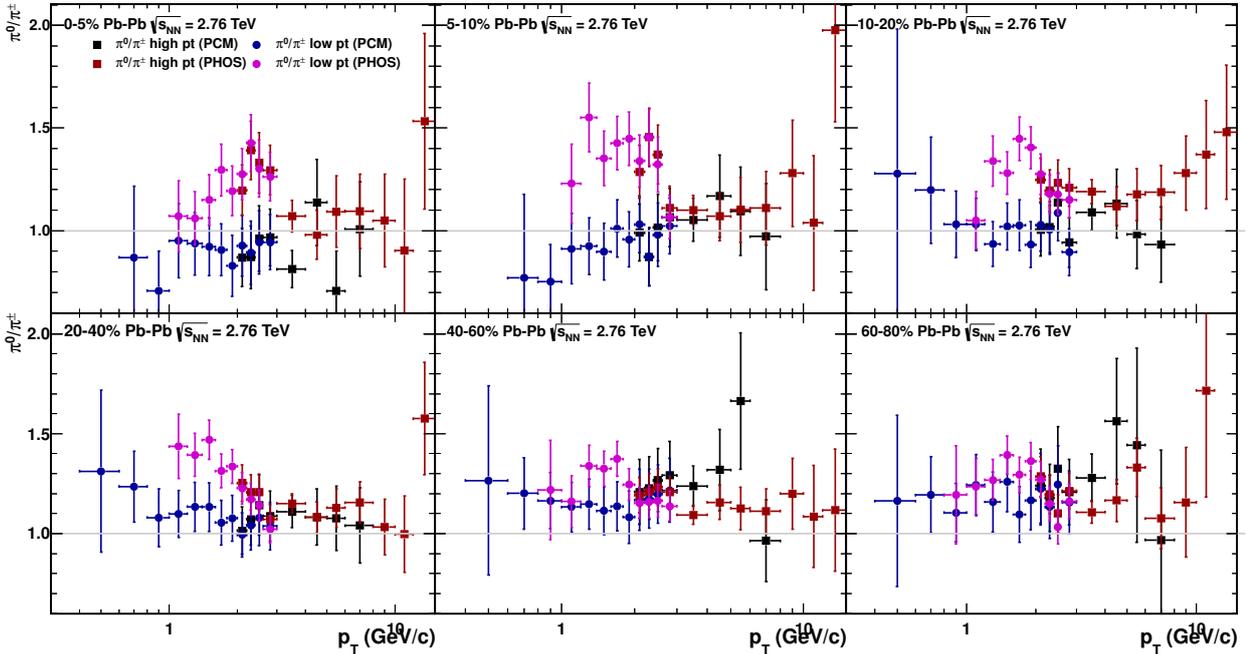

Figure 6.20.: Comparison of the individual measurements of the neutral pion to the low momentum charged pions measured via a combined ITS, TPC and TOF analysis [57] and the high momentum charged pions measured via the particle fractions in the relativistic rise of the dE/dx of the TPC [186]. The error bars reflect the quadratically summed systematic and statistical uncertainties of the measurements. The measurements of the charged pions have been averaged between the two charges to be able to directly compare the π^0 and $\pi^{\pm}$ measurements.
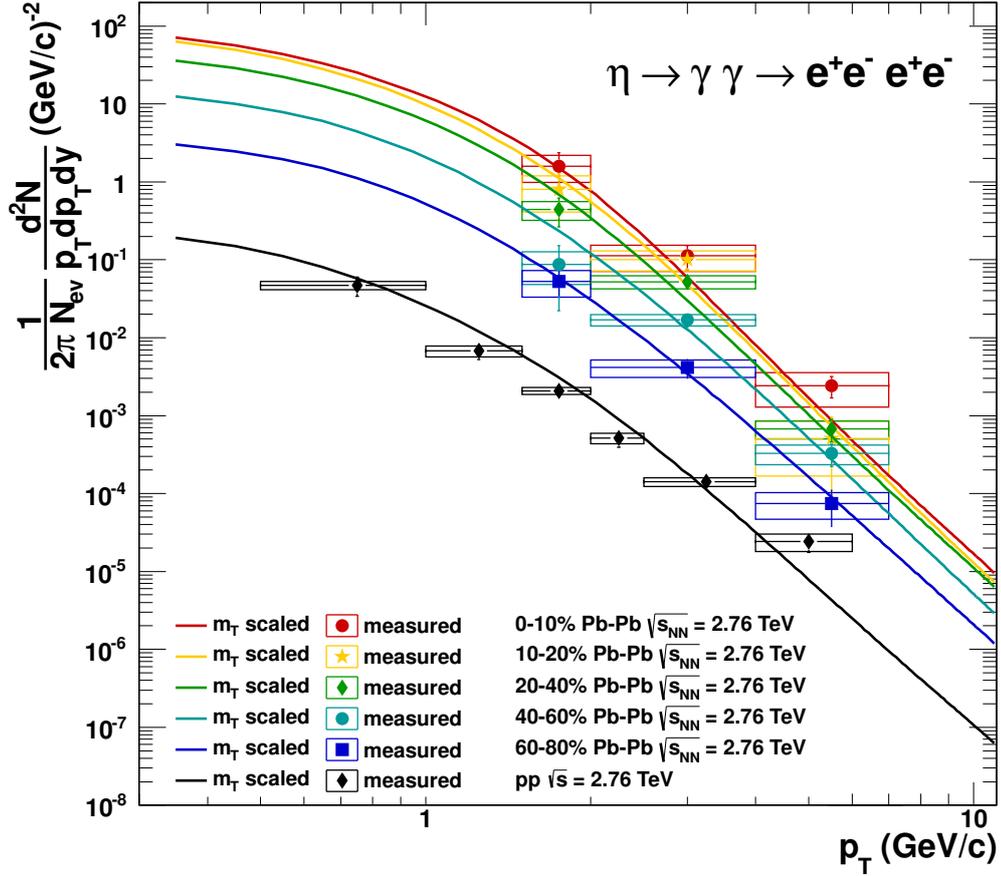
Figure 6.21.: η differential invariant yield for different centrality classes in Pb–Pb collisions at $\sqrt{s_{NN}} = 2.76$ TeV and for pp collisions at $\sqrt{s} = 2.76$ TeV. The spectra expected from m_T scaling of the neutral pions are shown as colored lines for the respective centrality classes and collision systems. For the spectra in Pb–Pb collisions no bin width correction (Section 6.1.2) has been applied.

classes the neutral pions seem to have a $\approx 10\%$ higher yield than the charged pions, which is independent of p_T. For central collisions this cannot be stated without doubt due to larger statistical and systematic errors. Small discrepancies ($\approx 2-3\%$) can be expected at low momentum due to iso-spin violating decays. Moreover, some of the systematic errors, like the systematics due to the error of the material budget ($\sim 10\%$), are p_T and centrality independent and would therefore shift the full spectrum in one direction. Thus it can be concluded that the PCM measurement is in agreement with the charged pion measurements. For the spectra measured with PHOS at high transverse momentum (> 3 GeV/c) similar conclusions can be drawn, below $p_T = 3$ GeV/c the discrepancy stays significant for $0-40\%$ Pb–Pb collisions.

6.3.2. Eta Transverse Momentum Spectra in Pb–Pb

This section is dedicated to the first measurement of the η meson in Pb–Pb collisions at $\sqrt{s_{NN}} = 2.76$ TeV for five centrality classes. The invariant yield of the η meson together with the expected spectra from m_T scaling of the π^0 meson in the same centrality class are shown in Figure 6.21. Moreover, the pp reference measurement at $\sqrt{s} = 2.76$ TeV is shown together with the expected spectrum from m_T scaling.

The m_T scaling phenomenology was found by the WA80 collaboration [206]. They reported a similarity of the η and π^0 spectrum up to a constant factor when expressed as a function of transverse mass. In [122] this method is extended to a broader set of different mesons. An excellent

agreement was found in most cases. For the calculation of the η yields presented in Figure 6.21 the measured π^0 yields are fitted with the function:

$$P(p_{\mathrm{T}})_{\pi^0} = A \cdot p_{\mathrm{T}}^{-(B+C/(p_{\mathrm{T}}^D+E))}. \tag{6.13}$$

It is found to describe the π^0 meson yields in all centrality bins over the full range of measured p_{T} equally well. The m_{T} scaling is performed in a cocktail calculation. A similar calculation is used for the direct photon analysis based on the measurement of the presented neutral meson yields. It is used for the determination of the background ratio $\gamma^{\mathrm{decay}}/\pi^0$. In the cocktail calculation a π^0 meson spectrum, following the fit, is generated. From it a π^0 meson transverse mass spectrum is deduced. The η meson transverse momentum spectrum is then obtained via the formula:

$$E\frac{\mathrm{d}^3 N}{\mathrm{d}p^3} = C_m \cdot P_\pi \left(\sqrt{p_{\mathrm{T}}^2 + m_\eta^2 - m_{\pi^0}^2} \right). \tag{6.14}$$

The factor C_m represents the relative normalization of the η-m_{T} spectrum to the neutral π^0-m_{T} spectrum and must be obtained from experimental results. For the comparison presented here the values are taken from [122].

A precise measurement of a transverse-momentum spectrum of the η meson in Pb–Pb collisions allows to test the m_{T} scaling hypothesis and thus reduce the uncertainties on the decay photon cocktail for the direct photon measurement. The Pb–Pb spectra shown in Figure 6.21 are in good agreement with the expected spectra from m_{T} scaling, in particular as the points are not yet shown at the correct position in p_{T} due to a lack of constraints for the fit. For pp collisions, however, the m_{T} scaled spectrum does not seem to follow the measured point, here the bin width correction has already been applied. A similar observation at low momentum has been made for the measurement at 7 TeV, thus it is even more important to measure the η meson with high precision in Pb–Pb collisions.

The measurement presented in this thesis is based on the Pb–Pb data sample collected in 2010, therefore not yet the full available statistics has been used. Including the data collected at the end of 2011 will probably allow to measure the spectrum in finer p_{T} bins while staying with the same centrality classes. Moreover, due to the large statistical and systematic errors in the pp and Pb–Pb measurement no nuclear suppression factor (R_{AA}) has been calculated for the η meson, yet.

6.3.3. Neutral Pion Suppression Factor R_{AA}

In order to obtain the nuclear suppression in Pb–Pb collisions the invariant yield in the different centrality classes is scaled by the mean number of binary collisions $\langle N_{\mathrm{coll}} \rangle$ in the respective centrality bin (Table 4.3). As already explained in Section 2.2.2 the nuclear suppression factor gives insight into the suppression of particle production at high p_{T}, it is calculated following the formula given in Equation 2.11.

The systematic uncertainties for the R_{AA} are composed of the individual uncertainties in the pp measurement and Pb–Pb measurement, as well as the uncertainties on the mean number of collisions and the cross section in pp collisions. While the latter are p_{T} independent and common for all measurements in ALICE, the first two can be p_{T} dependent. Some of those could cancel each other, if they would affect the measurements in the same way. One of these uncertainties is the systematic uncertainty on the material budget, as it would shift both spectra in the same direction, which cancels in the ratio. Thus the systematic errors of the R_{AA} can be smaller than the systematic errors of the individual measurements in Pb–Pb and pp collisions.

Consequently the combined neutral meson R_{AA} has been calculated based on the individual R_{AA} measurements in PCM and PHOS. Nevertheless, the bin width correction has been applied based on the fit to the combined spectrum to reduce the uncertainties originating in the shifting procedure. As the pp reference shows large statistical fluctuations above 8 GeV/c in transverse
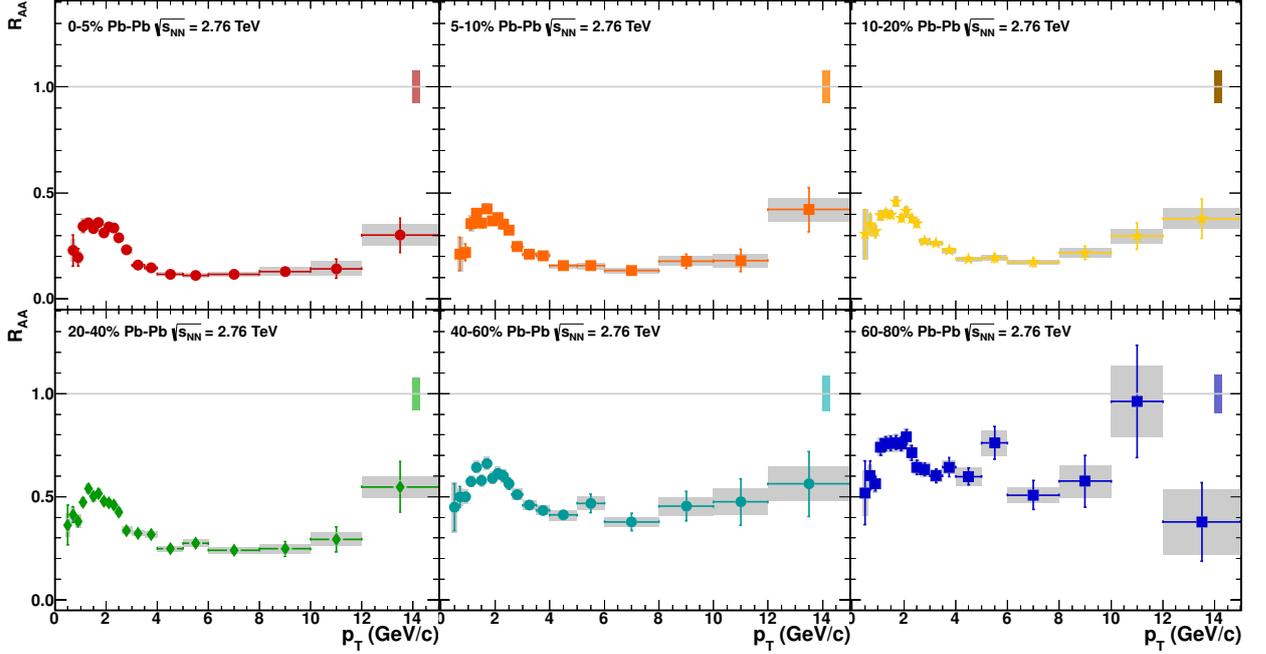
Figure 6.22.: Combined nuclear modification factor, R_{AA}, from individual measurements using PHOS and PCM in Pb–Pb collisions at $\sqrt{s_{NN}} = 2.76$ TeV for six centrality classes, 0-5 %, 5-10 %, 10-20%, 20-40%, 40-60% and 60-80%. Vertical lines represent the statistical error while the boxes reflect the systematic uncertainty. The boxes around unity reflect the uncertainties of the average nuclear overlap function (T_{AA}) and the normalization uncertainty in the pp added in quadrature.

momentum, thus above 8 GeV/c the Tsallis fit to the combined spectrum is used as reference for the high p_T point. The uncertainty of the fit is included in the highest momentum R_{AA} points using the error estimate from the covariance matrix of the fit. While the systematic uncertainties for the spectra are of the same order in the PCM and PHOS measurement, the systematic uncertainty on the R_{AA} at low momentum is significantly lower for the PCM result compared to PHOS result. Thus the R_{AA} at low p_T is dominated by the R_{AA} measured with PCM, while at high momenta on the other hand PHOS measurement dominates the combined R_{AA}.

Figure 6.22 shows the neutral pion R_{AA} in six centrality classes reaching from 0-5% central events to 60-80% Pb–Pb collisions. A clear suppression for all centrality bins is visible. For the 0-5% most central events this suppression reaches nearly a factor 10 ($R_{AA} \approx 0.11$ for the p_T bins between 4 and 8 GeV/c. Even in peripheral collisions at high p_T an R_{AA} of ≈ 0.6 is measured corresponding to a suppression of nearly a factor 2.

Comparison to Theory

The neutral pion R_{AA} can be compared to various theory calculations. One of these model is the WHDG model [190, 191], which includes inelastic and elastic scattering in the quark-gluon plasma as well as path length fluctuations. In this model the R_{AA} can be calculated with:

$$R_{AA} = \left\langle \int d\epsilon (1-\epsilon)^{n(p_T)} \cdot P(\epsilon) \right\rangle_{\text{geom}} , \qquad (6.15)$$

where $P(\epsilon)$ is the probability distribution for the energy loss ϵ and $n(p_T)$ represents the steepness of underlying p_T distribution as a function of p_T. After having fixed the parton flavor, the energy (E), the path length (L) and α_s the only remaining free parameter is the density of the medium, which is assumed to be proportional to the number of participating nucleons from the Glauber model. The
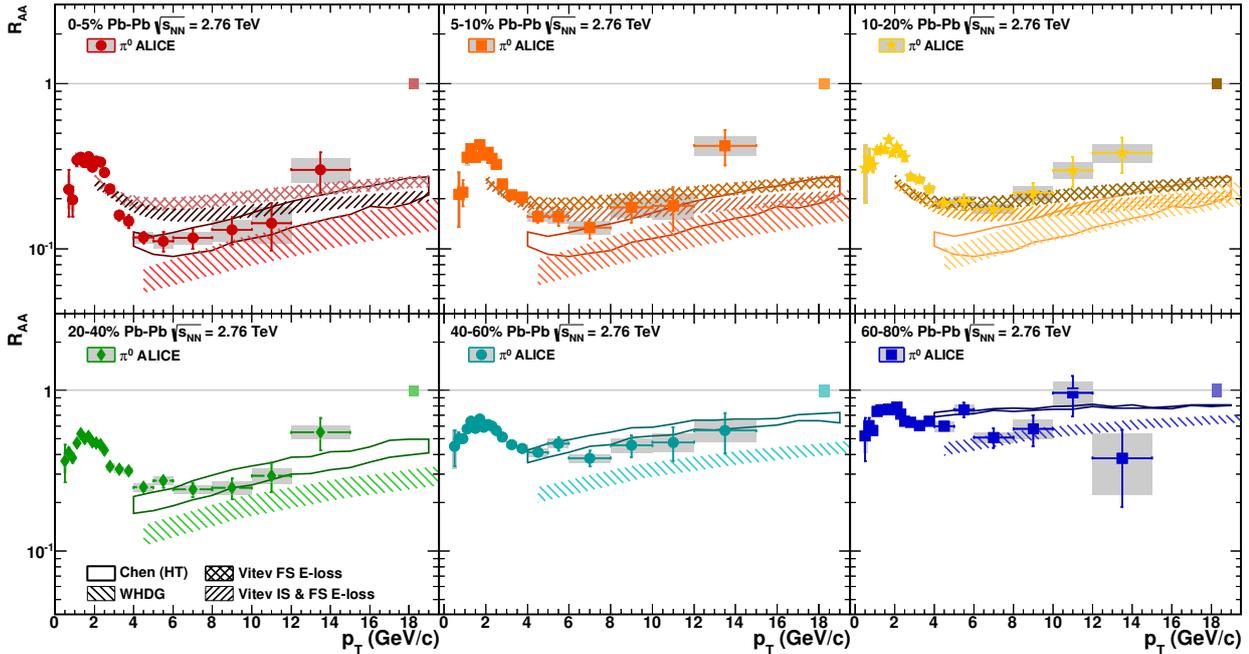
Figure 6.23.: Comparison of the measured R_{AA} to predictions from the WHDG model [190, 191] and the higher-twist calculations by Chen et al. [192]. For the first three centrality classes only the WHDG model predictions are available for each centrality bin, thus the comparison has been done to the higher-twist calculations in the 0-20% central events. Moreover, these three centrality classes are compared to the calculations by I. Vitev et al. with and without initial state (IS) parton energy loss in addition to final state (FS) energy loss for the 0-20% most events [193, 194].

hard parton-parton scatterings on the other hand are proportional to the number of binary nucleon-nucleon collisions. In order to consider all path length the mean over the geometry is calculated ($\langle \ \rangle_{\mathrm{geom}}$). The parameters of the model were constrained by the neutral pion R_{AA} measurement at RHIC and the predictions for the π^0 in Pb–Pb collisions were obtained by translating the measured charged-particle multiplicity in Pb–Pb collisions at $\sqrt{s_{NN}} = 2.76$ TeV into an initial energy density of the medium. The comparison of the model to the measured data for all six centrality classes is presented in Figure 6.23. It can be seen that the model overestimates the suppression in nearly all centrality classes except for the most peripheral Pb–Pb collisions. However, in this centrality bin the error bars of the measurement are quite large and thus no final conclusion can be drawn. While the total suppression factor is too low the p_T dependence seems to be reproduced by the model in the selected p_T range.

In the calculations by Chen et al. [192] the energy loss and the effective fragmentation functions are calculated within a higher-twist approach (HT) [207, 208], in which the high p_T parton loses energy via multiple scattering and induced gluon bremsstrahlung. The characteristic parameter for the energy loss in the medium is the jet transport parameter $\hat{q}$ [209]. Moreover, the space time evolution of the medium is described with a 3+1 dimensional ideal hydrodynamical calculation. In order to predict the neutral pion R_{AA} at LHC energies the measured $dN_{ch}/d\eta$ is translated into an initial parton density as input for the hydrodynamical calculations. Figure 6.23 shows that these calculations describe the centrality and transverse momentum dependence from $20 - 80\%$ Pb–Pb collisions. For the three most central bins no calculation were available in the same centrality binning, therefore all three centrality classes measured in data are compared to the 0-20% central class for the calculations. While the 0-20% calculation nearly perfectly describes the 0-5% central events measured in data, it overestimates the suppression in the two remaining centralities.

For the remaining two models by I. Vitev et al. [193, 194] two variations are considered illustrating how the π^0 R_{AA} is affected by the initial state effects. While the first calculation contains only final state parton energy loss in the created fireball, the second calculation takes into account the
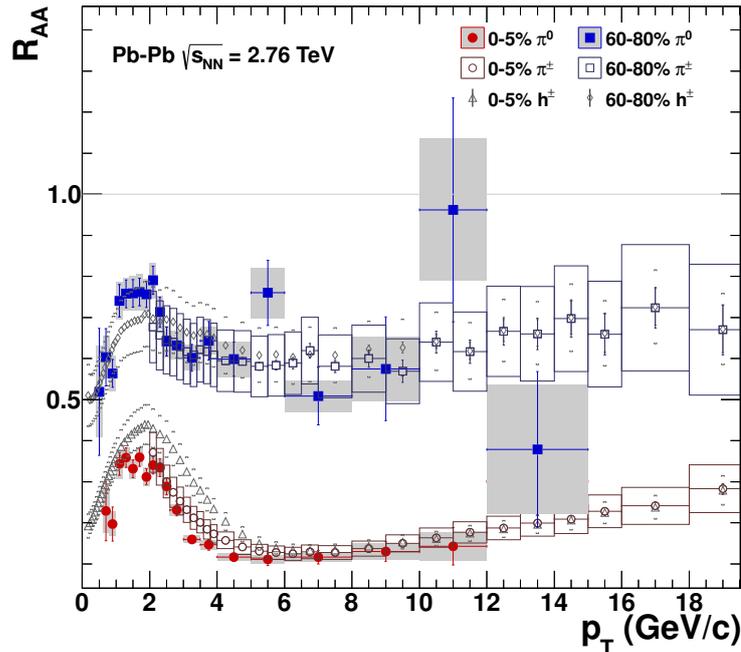
Figure 6.24.: Comparison of the neutral pion R_{AA} in most central (0-5%) and peripheral (60-80%) Pb–Pb collisions to the measurement for unidentified charged hadrons [95] and for charged pions [186] in the same centrality classes.

energy loss of the incoming parton (initial-state energy loss) as well. Furthermore, the broadening of the transverse momenta of the incoming partons in the cold nuclear matter is taken into account ("Cronin effect"). These calculations were only available for 0-20% central Pb–Pb collisions. They are compared to the measured results in the three smaller centrality classes 0-5%, 5-10% and 10-20% Pb–Pb collisions. As it can be seen in Figure 6.23 the inclusion of the initial state radiation lowers the predictions of this model above $p_T = 5$ GeV/c. While the calculations underestimate the suppression in the measured data for the most central 0-5%, they start to match for the 5-10% and 10-20% central events. Therefore, the calculations in the correct binning might describe these bins nearly perfectly, while a small discrepancy will stay for the most central event class.

Comparison to Other Particle Species

In this section the measured neutral pion R_{AA} in central (0-5%) and peripheral (60-80%) will be compared to the unidentified charged hadron [95] and to the charged pion R_{AA} [186]. The comparison can be seen in Figure 6.24. The R_{AA} for charged pions is only available in the high momentum region, as the pp reference has not yet been measured for the low momentum analysis in ITS,TPC and TOF. It can be seen that the charged and neutral pion R_{AA} agree for peripheral collisions and central collisions between 2 and 12 GeV/c, although some of the bins are at the edge of the systematic errors, which are indicated as boxes for the individual measurements. Compared to the charged hadron R_{AA}, the very low momentum points agree well within the errors. In the intermediate momentum (1.5 − 6 GeV/c) region, however, both charged and neutral pions differ from the inclusive charged hadron measurement, as expected due to the contribution from kaons and protons, which are less suppressed in this transverse momentum region. At high momenta all three measurements agree within the errors again, which points to a similar suppression of pions, kaons and protons at high momenta.
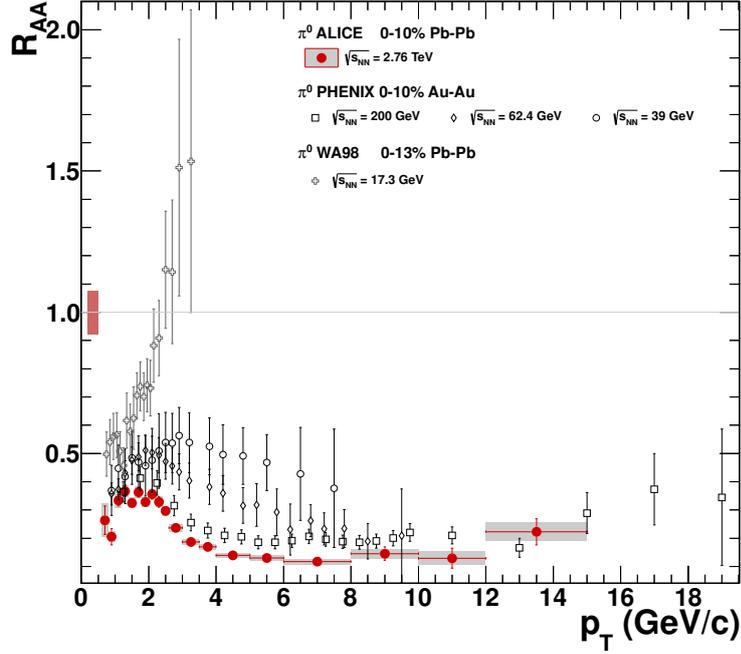
Figure 6.25.: Comparison of the combined nuclear modification factor measured for 0-10% central Pb–Pb collisions at $\sqrt{s_{NN}} = 2.76$ TeV to the R_{AA} measurements for the neutral pion at lower center-of-mass energies. The results for Au–Au collisions at $\sqrt{s_{NN}} = 39$, 63.4 [188] and 200 GeV [109] were obtained by the PHENIX collaboration and the result from the CERN SPS in Pb–Pb collision at $\sqrt{s_{NN}} = 17.3$ GeV was measured by the WA98 collaboration [189]. The vertical lines for the measurements at lower energies show the combined systematic and statistical error, however the common scale uncertainty of the 10-15% is not included in the errors. For the results obtained in this thesis the boxes indicate the systematic errors, while the vertical lines show the statistical errors. The box around unity reflects the uncertainty of the average nuclear overlap function (T_{AA}) and the normalization uncertainty in the pp added in quadrature.

Comparison of the Neutral Pion Nuclear Suppression Factor at Different $\sqrt{s_{NN}}$

Finally, the result on the neutral pion R_{AA} in 0-10% Pb–Pb collisions at $\sqrt{s_{NN}} = 2.76$ TeV is compared to results at lower center-of-mass energies in the same centrality class. Therefore the neutral pion R_{AA} had been calculated in this centrality class in addition to the already presented centrality bins. Figure 6.25 shows the neutral pions R_{AA} for 0-10 % central Pb–Pb collisions compared to the π^0 R_{AA} seen in Au–Au collisions at $\sqrt{s_{NN}} = 39$, 62.4 [188] and 200 GeV [109]. Moreover, the result from Pb–Pb collisions at $\sqrt{s_{NN}} = 17.3$ GeV in the WA98 experiment at SPS [189] is included in the comparison. It can be seen that the neutral pion suppression at low momentum ($p_T < 2$ GeV/c) is similar at all center-of-mass energies, while it increases with increasing $\sqrt{s_{NN}}$ for the larger momenta. This indicates that the decrease of R_{AA} resulting from the higher initial energy densities created at larger center-of-mass energies dominates over the increase of the R_{AA} expected from the flattening of the parton p_T spectra. Moreover, the shapes of the $R_{AA}(p_T)$ in central Pb–Pb collision at $\sqrt{s_{NN}} = 2.76$ TeV and Au–Au collisions at $\sqrt{s_{NN}} = 200$ GeV appear to be similar. Last but not least the maximum of the R_{AA} at low momentum seems to shift to lower transverse momenta with increasing $\sqrt{s_{NN}}$.

7. Summary and Outlook

In this thesis a measurement of the π^0 and η meson invariant cross section versus transverse momentum for pp collisions at $\sqrt{s} = 0.9$, 2.76 and 7 TeV has been presented. Additionally, the first measurement of the invariant yield of neutral pions and eta mesons in several centrality classes for Pb–Pb collisions at $\sqrt{s_{\mathrm{NN}}} = 2.76$ TeV has been shown. Furthermore, the neutral pion nuclear suppression factor (R_{AA}) has been calculated in six centrality bins. The data samples for $\sqrt{s} = 0.9$ TeV and $\sqrt{s} = 7$ TeV as well as the heavy-ion data sample were collected by ALICE during the data taking period in 2010. The pp reference for the nuclear suppression factor in pp collisions at $\sqrt{s} = 2.76$ TeV has been obtained from the data taken in March of 2011.

Both mesons are measured in the two photon decay channel by reconstructing the photons, which converted in the detector material, via the reconstruction of e^+ and e^- tracks in the Inner Tracking System and the Time Projection Chamber of ALICE. Afterwards the detected photons are combined into pairs. The combinatorial background, calculated via the mixed event technique, is subtracted from the invariant mass distribution and the remaining signal distribution is fitted with a Gaussian distribution modified with a exponential tail to account for electron Bremsstrahlung. It has been shown that the achieved mass resolution of the neutral pion is about $3 - 4$ MeV/c^2 up to a transverse momentum of 4 GeV/c^2 for all collision systems. For the eta meson the achieved mass resolution ranges between $5 - 10$ MeV/c^2 depending on the transverse momentum. The invariant yield of the π^0 and η meson has been determined by integrating the remaining signal distribution in the invariant mass window $[M_{\pi^0} - 0.035$ GeV/c^2, $M_{\pi^0} + 0.010$ GeV/$c^2]$ and $[M_\eta - 0.047$ GeV/c^2, $M_\eta + 0.023$ GeV/$c^2]$, respectively. To subtract the remaining combinatorial background a linear fit has been included in the signal fit and the integral under this linear function has been subtracted.

In order to estimate the systematic error of the measured spectra resulting from the material budget as implemented in the ALICE simulations, a detailed study has been performed using the converted photons to perform a γ-ray tomography of the detector. The study shows that the systematic error of the material budget in the fiducial acceptance ($|\eta| < 0.9$) is 4.5% for the data samples measured at $\sqrt{s} = 0.9$, 2.76 and 7 TeV, while for the Pb–Pb sample a slightly larger error of 4.86% has been assigned, due to changes in the detector implementation in the simulations. Furthermore, a second method to qualitatively measure the real material distribution in ALICE has been presented, which is based on the reconstruction of secondary hadronic vertices. This method extends the pseudo-rapidity coverage of the photon conversion method beyond $|\eta| < 1.4$ as the individual tracks do not need to point to the primary vertex to reconstruct a secondary hadronic vertex. However, the method has not yet reached the same maturity as the photon conversion method and thus cannot provide quantitative numbers yet.

Furthermore, extensive systematic error studies for the neutral pion and eta measurement have been presented to access the systematic errors, which are related to tracking, particle identification, photon reconstruction and signal extraction. The total systematic error for the neutral pion spectra ranges from $9 - 12\%$ for the pp measurements and from $12 - 15\%$ for 0-5% central Pb–Pb collisions. For the η meson the total systematic error is of the order of $15 - 20\%$ in pp collisions at $\sqrt{s} = 2.76$ TeV and $30 - 50\%$ for 0-10% central Pb–Pb collisions at $\sqrt{s_{\mathrm{NN}}} = 2.76$ TeV.

Additionally, in the ALICE detector system the production of neutral pions and eta mesons can

be studied using the photons reconstructed via the energy deposit in the calorimeters. Thus, to obtain a common measurement of the invariant cross section in pp and the invariant yield in Pb–Pb collision the final spectra measured with the photon conversion method have been combined with the measurements carried out using the Photon Spectrometer (PHOS) by calculating the weighted average of both measurements.

The combined π^0 and η meson transverse momentum spectra in pp collisions at $\sqrt{s} = 0.9$, 2.76 and 7 TeV have been compared to NLO pQCD calculations. The presented calculations using CTEQ6M5 PDF and DSS FF, which were able to describe the data measured at RHIC and Fermilab, reproduce the data at $\sqrt{s} = 0.9$ TeV for the π^0 and η meson, but fail to describe the higher energy data.

For Pb–Pb collisions the η meson transverse momentum spectra are compared to the expected spectra from m_{T} scaling of the neutral pion measurement in the same centrality class. Within the fairly large systematic errors the data seem to confirm the m_{T} scaling hypothesis. In pp collisions at $\sqrt{s} = 2.76$ TeV indications exist that m_{T} scaling cannot reproduce the measured data.

Finally the nuclear suppression factor of neutral pions in the different centrality classes has been compared to theory calculations and previous measurements at different center-of-mass energies. The comparison to the calculations showed that none of the calculations is able to describe simultaneously the p_{T} and centrality dependence seen in the data. From the comparison to the lower energy data it can be deduced that the suppression is stronger for higher energies, but the shape of the suppression factor seems to stay the same going from Au–Au collisions at $\sqrt{s_{\mathrm{NN}}} = 200$ GeV to Pb–Pb collisions at $\sqrt{s_{\mathrm{NN}}} = 2.76$ TeV. Additionally the neutral pion nuclear suppression factor and the transverse momentum spectra have been compared to the charged pion results. Within the errors both measurements agree and R_{AA} at high-p_{T} seems to follow the charged hadron R_{AA}.

In order to decrease the statistical error of the measurements presented in this thesis the data collected in 2011 can be included. Moreover, it will be interesting to see whether the discrepancy between the theory calculations in pp collisions grows even further with increasing energy. Thus it will be interesting to see the results from the data taken in 2012 at $\sqrt{s} = 8$ TeV. Additionally, a variety of electron or photon triggered data, based on EMCal, PHOS or TRD, has been collected in 2011 and 2012, which should increase the momentum reach of the photon conversion method as well as the reach of the calorimeters.

Last but not least, further efforts are undertaken to improve the material budget description in the simulation for the ITS and TPC, as this is the main systematic error for the photon conversion method and more precise measurements are needed in order to extract the direct photon signal at low-momentum in Pb–Pb collisions with smaller systematic uncertainties.

A. Acronyms and Technical Terms

ACORDE   ALICE cosmic ray detector

AGS   Alternating Gradient Synchrotron

ALICE   A Large Ion Collider Experiment

AOD   Analysis Object Data

ATLAS   A Toroidal LHC Apparatus

BNL   Brockhaven National Laboratory

CERN   European Organization for Nuclear Research

CMS   Compact Muon Solenoid experiment

CTP   Central Trigger Processor

DAQ   Data Acquisition

DCA   distance of closest approach

DPM   Dual Parton Model

EMCal   Electromagnetic Calorimeter

ESD   Event Summary Data

FEE   Front End Electronics

FMD   Forward Multiplicity Detector

FPGA   Field Programmable Gate Array

FWHM   full width at half maximum

GEANT   Geometry and Tracking Software

GTU   Global Tracking Unit

HLT   High Level Trigger

HMPID   High Momentum Particle Identification Detector

INEL   Inelastic

ITS   Inner Tracking System

L1   level-1

L3   High Energy Physics Experiment at LEP

LEP   Large Electron Positron Collider

LHA   Les Houches Accord

LHC   Large Hadron Collider

LHCb	LHC beauty experiment
LHEF	Les Houches Event Files
LO	Leading Order
LTU	Local Trigger Unit
LQCD	Lattice QCD
MRPC	Multigap Resistive Plate Chamber
MWPC	multi-wire-proportional chamber
NSD	Non Single Diffractive Events
NLO	Next-to-Leading Order
NNLO	Next-to-Next-to Leading Order
PDF	Parton distribution function
PHOS	Photon Spectrometer
RICH	Ring Imaging Cherenkov detector
PCM	Photon Conversion Method
PDF	parton density functions
PHENIX	Pioneering High Energy Nuclear Interactions eXperiment
PID	particle identification
PMD	Photon Multiplicity Detector
pQCD	perturbative QCD
QCD	Quantum Chromodynamics
QED	Quantum Electrodynamics
QFT	Quantum Field Theory
QGP	Quark-Gluon Plasma
RHIC	Relativistic Heavy Ion Collider
SDD	Silicon Drift Detector
SHIM	Secondary Hadronic Interaction Method
SM	Standard Model
SPD	Silicon Pixel Detector
SPS	Super Proton Synchrotron
SSD	Silicon Strip Detector
TZERO	Timing and Trigger detector at ALICE
TOF	Time-Of-Flight detector
TPC	Time Projection Chamber
TR	transition radiation

TRD	Transition Radiation Detector
TRG	Trigger System
V^0	Unknown Particle
VZERO	V0 detector
ZDC	Zero Degree Calorimeter
ZEM	Zero Degree Electromagnetic Calorimeter
ZN	Zero Degree Neutron Calorimeter
ZP	Zero Degree Proton Calorimeter

B. Additional Neutral Meson Plots

B.1. Neutral Meson Efficiency
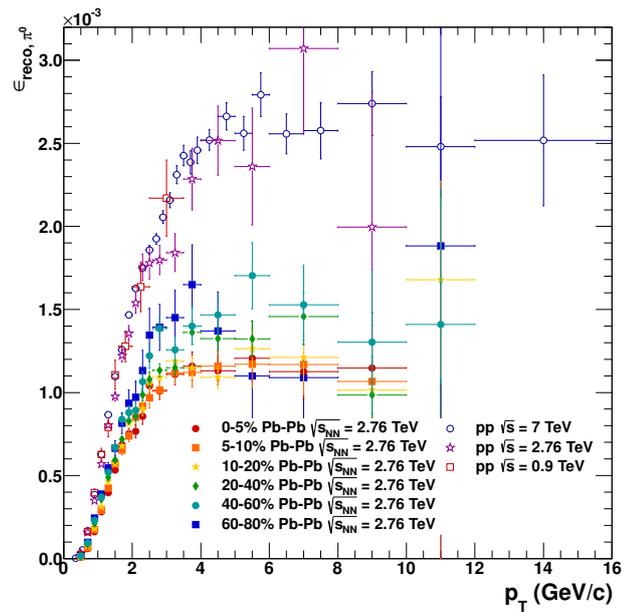
Figure B.1.: Neutral pion reconstruction efficiency obtained from Monte Carlo simulations for pp collisions at $\sqrt{s} = 0.9$, 2.76 and 7 TeV as well as Pb–Pb collisions in different centrality bins.

B.2. π^0 and η in pp Collisions

B.2.1. Invariant Mass Distributions pp at $\sqrt{s}$ = 2.76 TeV

B.2.2. Systematic Errors

Quantity	Standard	Cut variation 1	Cut variation 2	Cut variation 3	Cut variation 4
dE/dx e-line					
$\sigma_{\mathrm{d}E/\mathrm{d}x,e}$	$-4 < \sigma < 5$	$-5 < \sigma < 5$			
dE/dx π-line					
π rej. low p					
$\sigma_{\mathrm{d}E/\mathrm{d}x,\pi}$	< 2	< 2	< 2	< 0	< 2
π rej. high p					
$\sigma_{\mathrm{d}E/\mathrm{d}x,\pi}$	< 0.5	< 1	< -10	< -10	< -10
$p_{\mathrm{min},\,\pi\,\mathrm{rej}}$	0.25 GeV/c	0.25 GeV/c	0.3 GeV/c	0.5 GeV/c	0.4 GeV/c
$p_{\mathrm{max},\,\pi\,\mathrm{rej}}$	3.5 GeV/c	3.5 GeV/c	3.5 GeV/c	100 GeV/c	3 GeV/c
single p_t $e^\pm >$	0.05 GeV/c	0.075 GeV/c	0.1 GeV/c	0.125 GeV/c	
χ^2 $\gamma <$	30	20	15	100	
min TPC clust./ find. clust.	0.35,	0	0.6		
α **meson $<$**	1	0.7			
Background	Mixed event (track mult)	Mixed event (V0 mult)	Rotation		

Table B.1.: Variations for the systematic error evaluation in pp collisions at $\sqrt{s} = 0.9$ and 7 TeV. The column with the title "Standard" reflects the standard cut for each cut respectively, while the columns titled with "Cut variation" show the variations, which were done for the respective cut (row). Only one cut is varied at a time to estimate the systematic error.
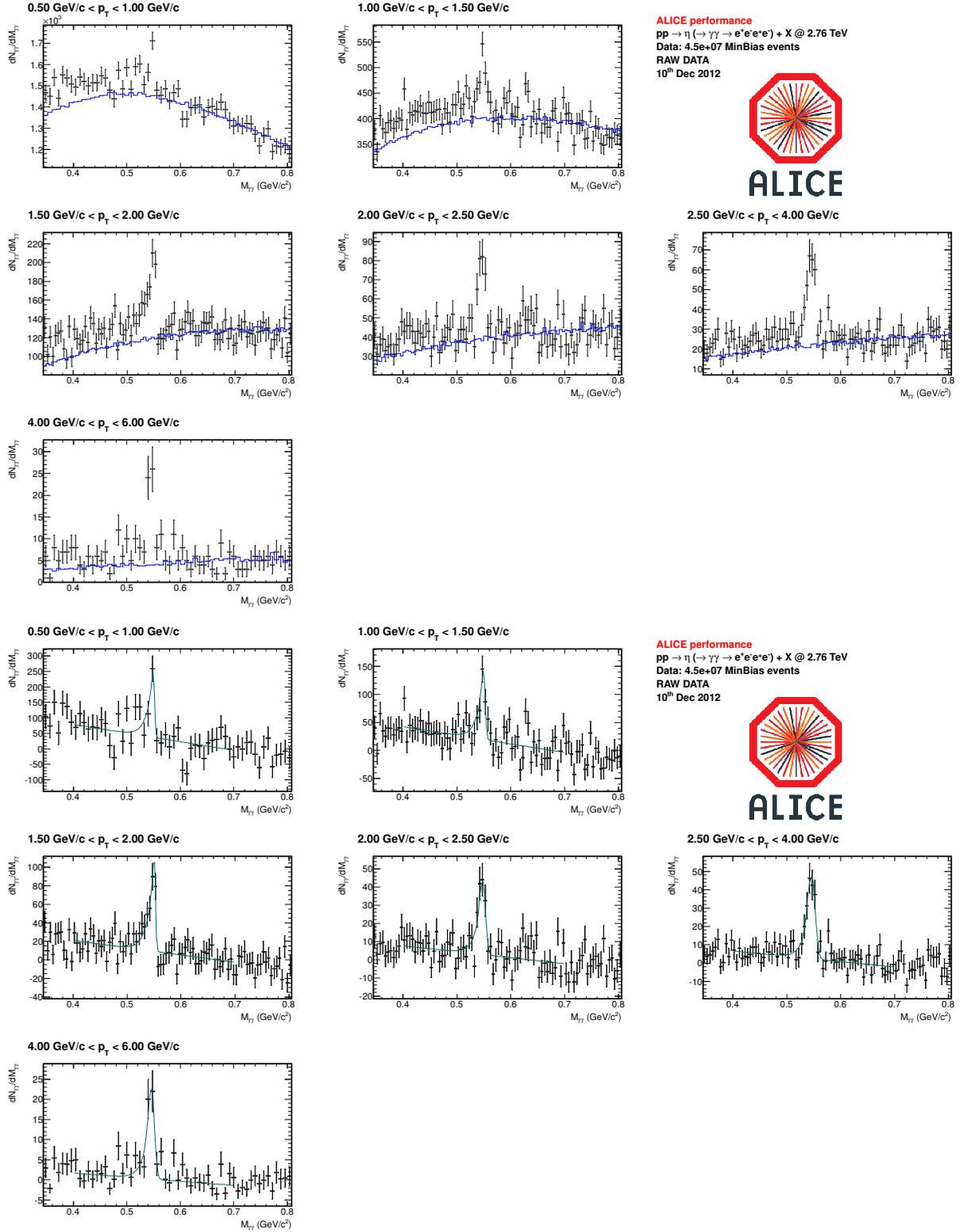
Figure B.2.: Invariant-mass distribution of reconstructed photon pairs $M_{\gamma\gamma}$ around the eta meson mass in p_{T} slices in pp collisions at $\sqrt{s} = 2.76$ TeV before (upper plot) and after subtraction (lower plot). The black histograms in the upper plot show the combined signal and background distribution and the blue histograms show the calculated and normalized mixed event background. After the subtraction the invariant mass distributions are fitted with Equation 6.3, which is shown in green in the lower plot.
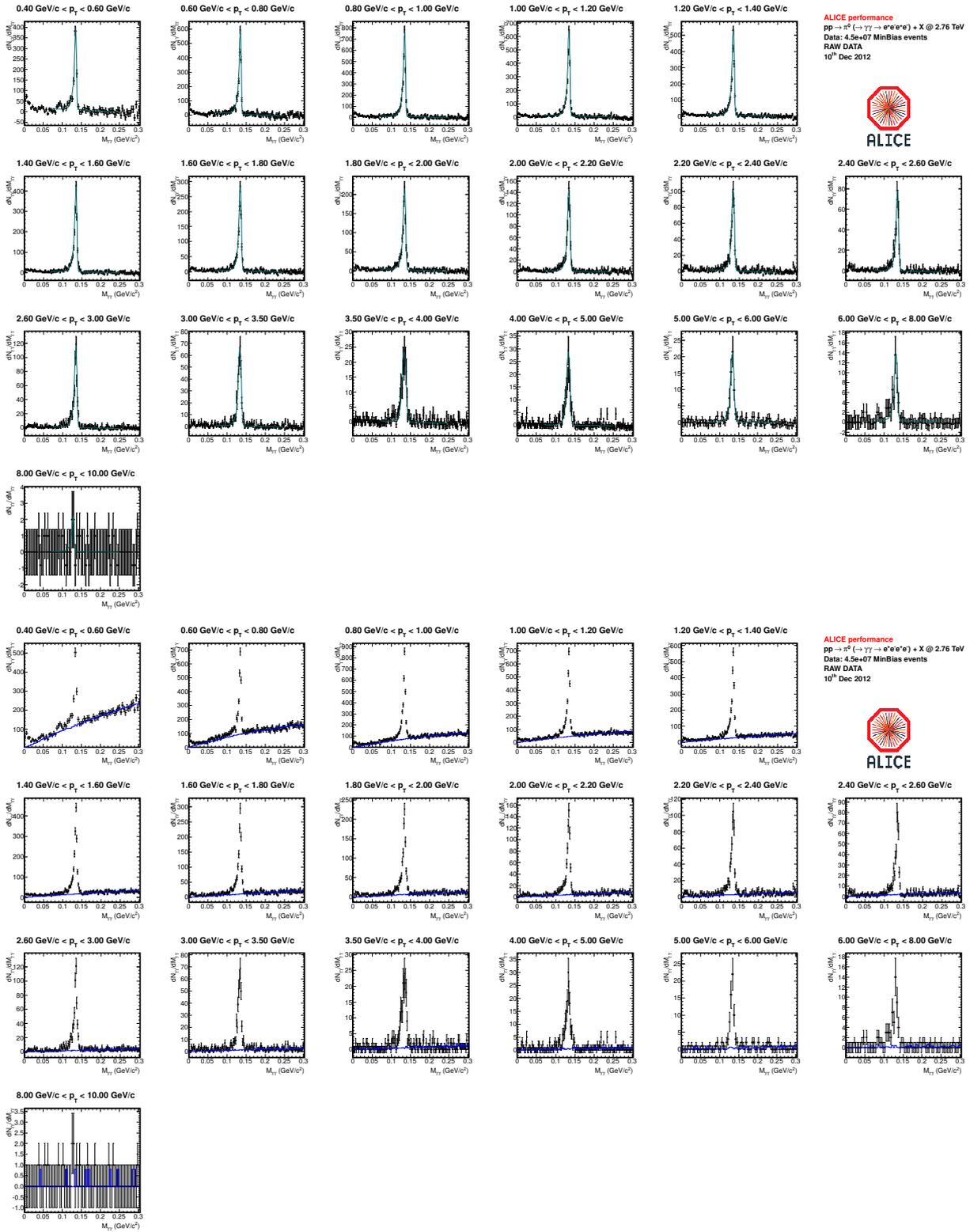
Figure B.3.: Invariant-mass distribution of reconstructed photon pairs $M_{\gamma\gamma}$ around the neutral pion mass in p_{T} slices in pp collisions at $\sqrt{s} = 2.76$ TeV before (upper plot) and after subtraction (lower plot). The black histograms in the upper plot show the combined signal and background distribution and the blue histograms show the calculated and normalized mixed event background. After the subtraction the invariant mass distributions are fitted with Equation 6.3, which is shown in green in the lower plot.
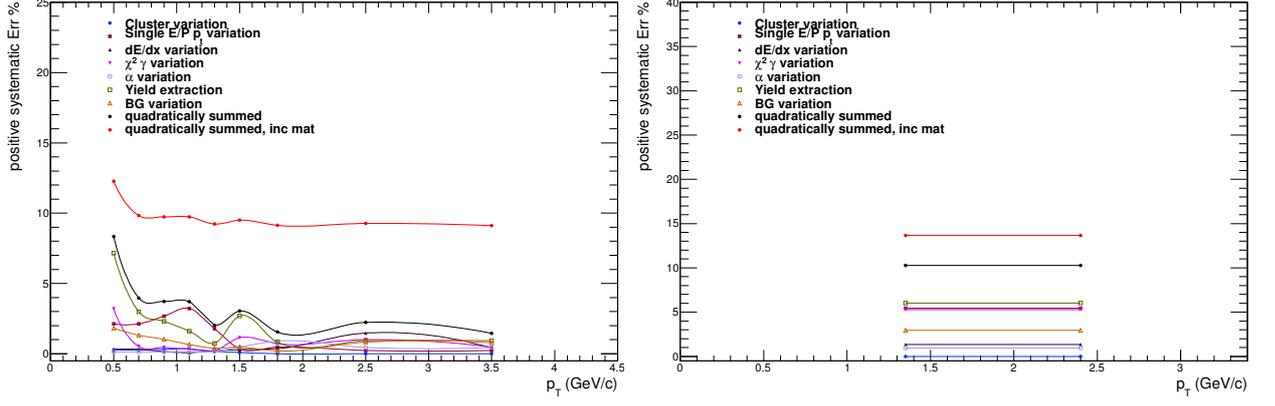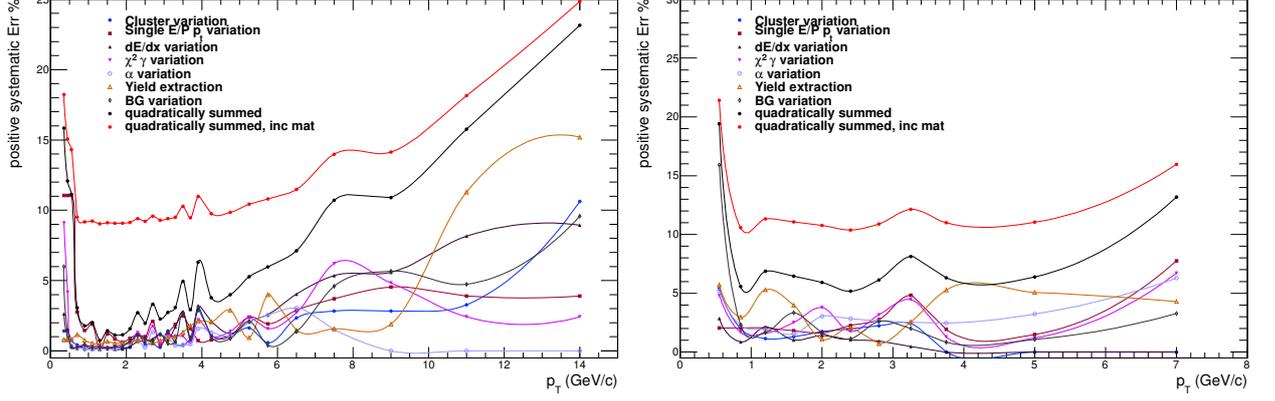
Figure B.4.: Visualization of the systematic errors for pp collisions at $\sqrt{s} = 7$ TeV. The colored points represent the individual error sources, while the red points represent the final systematic error for the π^0 (left) and η (right) meson spectra.

p_{T} (GeV/c)	Yield extraction (%)	PID e^+, e^- (%)	$\chi^2\gamma$ (%)	Reco. Eff. (%)	Material (%)	Total (%)
1.35	2.94	1.35	5.29	5.52	9.72	12.79
2.40	2.94	1.35	5.29	5.52	9.72	12.79

Figure B.5.: Detailed systematic error estimates for η meson measurement in pp at $\sqrt{s} = 0.9$ TeV.

p_{T} (GeV/c)	Yield extraction (%)	PID e^+, e^- (%)	$\chi^2\gamma$ (%)	Reco. Eff. (%)	Material (%)	Total (%)
0.50	1.82	0.32	3.19	2.15	9.72	10.62
0.70	1.32	0.32	0.52	2.15	9.72	10.06
0.90	1.03	0.16	0.44	2.70	9.72	10.15
1.10	0.65	0.08	0.33	3.25	9.72	10.28
1.30	0.40	0.22	0.23	1.81	9.72	9.90
1.50	0.47	0.30	1.14	0.60	9.72	9.82
1.80	0.20	0.37	0.70	1.02	9.72	9.81
2.50	0.83	1.47	1.01	0.51	9.72	9.93
3.50	0.78	0.40	0.47	0.51	9.72	9.78

Figure B.6.: Detailed systematic error estimates for π^0 meson measurement in pp at $\sqrt{s} = 0.9$ TeV.

p_T (GeV/c)	Material (%)	Yield extraction (%)	PID e^+, e^- (%)	γ rec. (%)	Track. rec. (%)	Total (%)
0.75	9.00	4.24	4.38	4.85	4.36	12.68
1.25	9.00	9.86	2.71	5.21	6.74	16.06
1.75	9.00	3.99	1.47	2.29	1.34	10.30
2.25	9.00	10.64	3.01	5.15	2.90	15.43
3.25	9.00	7.03	3.97	3.11	3.21	12.89
5.00	9.00	15.14	13.81	8.78	7.49	25.18

Figure B.7.: Detailed systematic error estimates for η meson measurement in pp at $\sqrt{s} = 2.76$ TeV.

p_T (GeV/c)	Material (%)	Yield extraction (%)	PID e^+, e^- (%)	γ rec. (%)	Track. rec. (%)	Total (%)
0.50	9.00	3.02	2.20	2.23	4.18	10.84
0.70	9.00	0.98	0.52	1.60	4.23	10.13
0.90	9.00	1.27	1.08	0.99	0.84	9.24
1.10	9.00	0.61	0.50	0.93	0.31	9.09
1.30	9.00	1.34	1.14	1.59	2.19	9.56
1.50	9.00	1.17	1.20	1.35	1.33	9.35
1.70	9.00	1.87	1.05	1.77	0.50	9.43
1.90	9.00	2.32	1.83	1.69	1.14	9.69
2.10	9.00	2.98	2.03	2.14	1.57	10.05
2.30	9.00	3.88	2.01	2.69	1.86	10.53
2.50	9.00	3.58	4.13	3.11	3.74	11.60
2.80	9.00	3.24	2.82	3.51	1.87	10.74
3.25	9.00	2.54	2.85	3.13	0.65	10.29
3.75	9.00	5.34	3.60	4.00	4.64	12.65
4.50	9.00	4.60	3.98	2.81	2.12	11.42
5.50	9.00	5.85	8.76	9.08	11.07	19.92
7.00	9.00	5.88	8.66	9.82	7.00	18.33

Figure B.8.: Detailed systematic error estimates for π^0 meson measurement in 0-10% Pb–Pb at $\sqrt{s_{\mathrm{NN}}} = 2.76$ TeV.

Figure B.9.: Visualization of the systematic errors for pp collisions at $\sqrt{s} = 7$ TeV. The colored points represent the individual error sources, while the red points represent the final systematic error for the π^0 (left) and η (right) meson spectra.

p_{T} (GeV/c)	Yield extraction (%)	PID e^+, e^- (%)	$\chi^2\gamma$ (%)	Reco. Eff. (%)	Material (%)	Total (%)
0.55	16.90	2.86	4.81	7.76	9.00	21.40
0.85	3.76	0.87	1.67	3.66	9.00	10.59
1.20	5.56	2.12	1.58	3.03	9.00	11.32
1.60	5.18	1.03	2.51	2.70	9.00	11.07
2.00	1.96	1.40	3.78	3.86	9.00	10.77
2.40	2.34	1.06	1.75	4.13	9.00	10.38
2.80	2.70	0.92	3.16	4.41	9.00	10.89
3.25	3.24	0.46	4.45	5.97	9.00	12.13
3.75	5.33	0.00	1.28	3.12	9.00	10.99
5.00	5.18	0.00	1.20	3.56	9.00	11.04
7.00	5.39	0.00	6.71	9.98	9.00	15.96

Figure B.10.: Detailed systematic error estimates for η meson measurement in pp at $\sqrt{s} = 7$ TeV.

p_{T} (GeV/c)	Yield extraction (%)	PID e^+, e^- (%)	$\chi^2\gamma$ (%)	Reco. Eff. (%)	Material (%)	Total (%)
0.35	6.05	2.63	9.09	11.18	9.00	18.22
0.45	1.69	0.95	4.18	11.18	9.00	15.07
0.55	0.86	0.33	0.24	11.10	9.00	14.32
0.70	1.18	0.18	0.35	2.79	9.00	9.51
0.90	0.88	0.31	0.37	1.47	9.00	9.17
1.10	0.59	0.12	0.29	1.91	9.00	9.23
1.30	0.55	0.14	0.38	0.26	9.00	9.03
1.50	0.69	0.27	0.21	1.22	9.00	9.11
1.70	0.61	0.08	0.34	0.89	9.00	9.07
1.90	0.68	0.14	0.46	0.80	9.00	9.07
2.10	0.90	0.31	0.59	1.10	9.00	9.14
2.30	1.34	0.68	1.29	1.84	9.00	9.40
2.50	1.20	0.69	0.78	1.13	9.00	9.21
2.70	0.89	0.85	1.74	2.53	9.00	9.59
2.90	1.38	1.20	0.51	1.25	9.00	9.28
3.10	1.09	0.80	1.05	2.13	9.00	9.40
3.30	1.22	1.71	1.05	1.99	9.00	9.51
3.50	3.02	2.79	1.03	2.55	9.00	10.27
3.70	2.01	0.73	0.59	1.92	9.00	9.47
3.90	3.79	3.04	2.21	3.35	9.00	10.99
4.25	2.28	2.09	1.08	1.90	9.00	9.76
4.75	3.02	1.22	1.38	1.84	9.00	9.85
5.25	2.30	2.06	2.36	3.56	9.00	10.43
5.75	4.01	2.58	1.58	3.24	9.00	10.81
6.50	2.00	4.04	2.71	4.80	9.00	11.48
7.50	4.85	5.35	6.21	4.90	9.00	13.99
9.00	5.98	5.58	4.83	5.35	9.00	14.14
11.00	12.25	8.16	2.42	5.10	9.00	18.15
14.00	17.95	8.95	2.42	11.33	9.00	24.85

Figure B.11.: Detailed systematic error estimates for π^0 meson measurement in pp at $\sqrt{s} = 7$ TeV.

B.2.3. Final Results

p_{T} (GeV/c)	Cross Section (pb GeV$^{-2}c^3$)	stat Err (pb GeV$^{-2}c^3$)	syst Err (pb GeV$^{-2}c^3$)
3.50E-01	8.86E+10	1.70E+10	1.61E+10
4.49E-01	6.74E+10	4.16E+09	1.02E+10
5.49E-01	3.87E+10	1.23E+09	5.53E+09
6.94E-01	2.06E+10	2.77E+08	1.95E+09
8.94E-01	8.90E+09	6.87E+07	8.00E+08
1.09E+00	4.17E+09	3.01E+07	3.09E+08
1.30E+00	2.15E+09	1.48E+07	1.38E+08
1.50E+00	1.19E+09	8.00E+06	6.00E+07
1.70E+00	6.78E+08	4.84E+06	3.14E+07
1.90E+00	3.94E+08	3.08E+06	1.81E+07
2.10E+00	2.41E+08	2.08E+06	1.09E+07
2.30E+00	1.50E+08	1.42E+06	6.57E+06
2.50E+00	9.97E+07	1.07E+06	4.49E+06
2.70E+00	6.72E+07	7.96E+05	3.05E+06
2.90E+00	4.44E+07	6.12E+05	2.08E+06
3.10E+00	3.25E+07	4.80E+05	1.46E+06
3.30E+00	2.20E+07	3.68E+05	9.92E+05
3.50E+00	1.60E+07	2.94E+05	7.71E+05
3.70E+00	1.17E+07	2.44E+05	5.27E+05
3.90E+00	8.54E+06	1.92E+05	4.05E+05
4.24E+00	5.38E+06	9.19E+04	2.36E+05
4.74E+00	2.68E+06	5.97E+04	1.20E+05
5.24E+00	1.47E+06	4.11E+04	6.80E+04
5.74E+00	9.08E+05	2.98E+04	4.37E+04
6.46E+00	4.20E+05	1.36E+04	2.09E+04
7.47E+00	2.06E+05	8.51E+03	1.14E+04
8.88E+00	6.00E+04	2.90E+03	3.31E+03
1.09E+01	1.89E+04	1.42E+03	1.01E+03
1.29E+01	6.36E+03	8.19E+02	3.51E+02
1.49E+01	2.96E+03	5.11E+02	8.30E+02
1.69E+01	9.48E+02	2.72E+02	2.58E+02
1.89E+01	3.94E+02	1.74E+02	8.00E+01
2.22E+01	2.05E+02	7.09E+01	2.27E+01

Table B.2.: Combined neutral pion results in pp collisions at $\sqrt{s} = 7$ TeV.

p_{T} (GeV/c)	Cross Section (pb GeV$^{-2}c^3$)	stat Err (pb GeV$^{-2}c^3$)	syst Err (pb GeV$^{-2}c^3$)
4.95E-01	3.98E+10	3.07E+09	4.32E+09
6.94E-01	1.42E+10	5.73E+08	1.44E+09
8.94E-01	6.42E+09	1.51E+08	5.72E+08
1.09E+00	2.50E+09	5.90E+07	1.96E+08
1.30E+00	1.24E+09	2.59E+07	6.90E+07
1.50E+00	6.90E+08	1.67E+07	4.70E+07
1.70E+00	3.53E+08	9.49E+06	2.28E+07
1.90E+00	2.22E+08	6.20E+06	1.27E+07
2.10E+00	1.29E+08	4.03E+06	6.97E+06
2.30E+00	8.00E+07	2.81E+06	4.71E+06
2.50E+00	5.33E+07	2.03E+06	3.06E+06
2.79E+00	3.00E+07	1.00E+06	1.75E+06
3.23E+00	1.24E+07	4.95E+05	6.24E+05
3.73E+00	5.13E+06	2.65E+05	2.66E+05
4.45E+00	1.93E+06	1.04E+05	1.18E+05
5.45E+00	4.70E+05	4.03E+04	2.79E+04
6.85E+00	1.34E+05	1.26E+04	7.40E+03
8.88E+00	2.80E+04	5.51E+03	2.05E+03
1.09E+01	1.11E+04	3.05E+03	5.17E+02

Table B.3.: Combined neutral pion results in pp collisions at $\sqrt{s} = 2.76$ TeV.

p_{T} (GeV/c)	Cross Section (pb GeV$^{-2}c^3$)	stat Err (pb GeV$^{-2}c^3$)	syst Err (pb GeV$^{-2}c^3$)
4.95E-01	2.78E+10	6.65E+09	3.41E+09
6.94E-01	8.46E+09	6.94E+08	1.02E+09
8.94E-01	3.40E+09	2.06E+08	3.38E+08
1.09E+00	1.47E+09	8.64E+07	1.29E+08
1.30E+00	8.01E+08	4.91E+07	6.91E+07
1.50E+00	3.80E+08	2.52E+07	3.24E+07
1.78E+00	1.43E+08	8.74E+06	1.16E+07
2.23E+00	4.12E+07	3.21E+06	3.77E+06
2.73E+00	1.85E+07	1.26E+06	2.35E+06
3.23E+00	5.38E+06	6.33E+05	6.03E+05
3.73E+00	2.53E+06	3.52E+05	3.23E+05
4.45E+00	7.41E+05	1.21E+05	9.87E+04
5.82E+00	9.13E+04	2.39E+04	1.05E+04

Table B.4.: Combined neutral pion results in pp collisions at $\sqrt{s} = 0.9$ TeV.

p_T (GeV/c)	Cross Section (pb GeV$^{-2}c^3$)	stat Err (pb GeV$^{-2}c^3$)	syst Err (pb GeV$^{-2}c^3$)
5.48E-01	4.22E+09	1.02E+09	9.02E+08
8.39E-01	1.80E+09	2.54E+08	1.90E+08
1.18E+00	7.41E+08	6.76E+07	7.21E+07
1.58E+00	2.61E+08	1.83E+07	2.31E+07
1.98E+00	1.08E+08	9.97E+06	8.50E+06
2.38E+00	4.59E+07	3.31E+06	3.70E+06
2.79E+00	2.20E+07	1.81E+06	2.08E+06
3.23E+00	9.72E+06	7.57E+05	9.02E+05
3.73E+00	5.20E+06	4.10E+05	4.55E+05
4.79E+00	1.13E+06	8.16E+04	9.56E+04
6.85E+00	1.67E+05	2.11E+04	1.91E+04
8.88E+00	3.58E+04	1.48E+04	7.33E+03
1.20E+01	4.35E+03	2.07E+03	1.41E+03

Table B.5.: Combined eta meson results in pp collisions at $\sqrt{s} = 7$ TeV.

p_T (GeV/c)	Cross Section (pb GeV$^{-2}c^3$)	stat Err (pb GeV$^{-2}c^3$)	syst Err (pb GeV$^{-2}c^3$)
7.25E-01	2.70E+09	7.53E+08	3.42E+08
1.22E+00	3.86E+08	8.91E+07	6.20E+07
1.72E+00	1.17E+08	2.17E+07	1.20E+07
2.23E+00	2.90E+07	6.89E+06	4.47E+06
3.08E+00	8.26E+06	1.27E+06	1.06E+06
4.86E+00	1.38E+06	3.73E+05	3.51E+05

Table B.6.: Final eta meson results in pp collisions at $\sqrt{s} = 2.76$ TeV.

p_T (GeV/c)	Cross Section (pb GeV$^{-2}c^3$)	stat Err (pb GeV$^{-2}c^3$)	syst Err (pb GeV$^{-2}c^3$)
1.35E+00	3.11E+08	9.77E+07	4.25E+07
2.40E+00	1.38E+07	5.05E+06	1.88E+06

Table B.7.: Final eta meson results in pp collisions at $\sqrt{s} = 0.9$ TeV.

B.3. π^0 **and** η **in Pb–Pb Collisions**

B.3.1. Invariant Mass Distributions

B.3.2. Systematic Errors

p_{T} (GeV/c)	Material (%)	Yield extraction (%)	PID e^+, e^- (%)	γ rec. (%)	Track. rec. (%)	Total (%)
0.70	9.72	8.92	9.57	4.30	18.04	24.69
0.90	9.72	8.87	7.42	5.03	8.45	18.03
1.10	9.72	9.92	2.96	4.40	3.72	15.33
1.30	9.72	6.45	2.96	3.99	2.75	12.98
1.50	9.72	5.52	1.69	3.35	4.21	12.52
1.70	9.72	3.85	3.20	2.10	1.36	11.22
1.90	9.72	7.65	4.84	7.05	1.33	15.10
2.10	9.72	5.43	5.57	3.31	3.18	13.27
2.30	9.72	5.20	6.95	3.68	2.30	13.74
2.50	9.72	2.46	5.09	2.84	5.29	12.75
2.80	9.72	2.93	3.77	3.90	1.82	11.65
3.25	9.72	3.87	5.36	2.66	1.25	12.12
3.75	9.72	5.17	8.28	5.23	2.87	15.02
4.50	9.72	9.74	6.12	4.98	2.06	15.99
5.50	9.72	6.17	13.30	6.30	6.85	19.90

Table B.8.: Detailed systematic error estimates for π^0 meson measurement in 0-5% Pb–Pb at $\sqrt{s_{\mathrm{NN}}} = 2.76$ TeV.
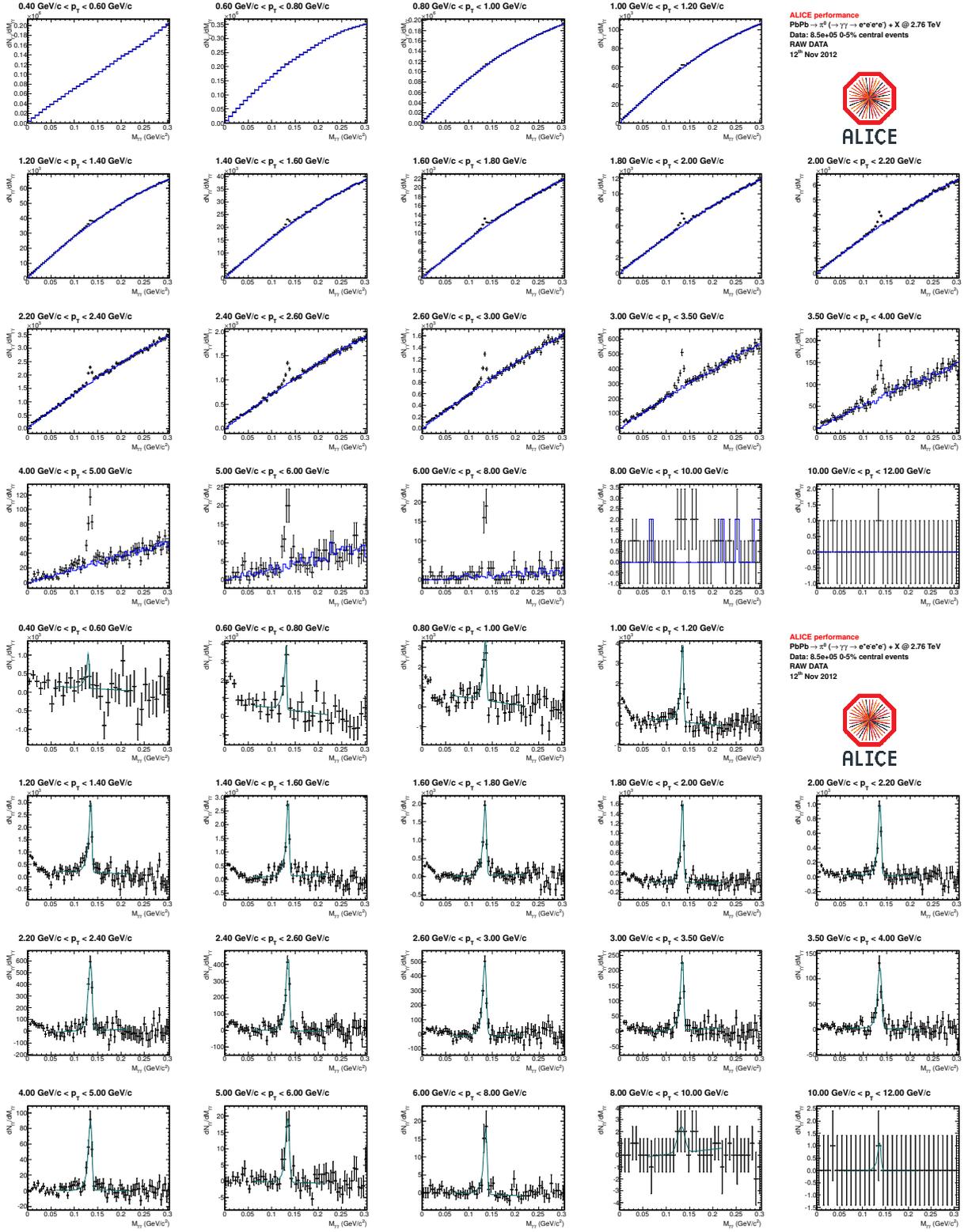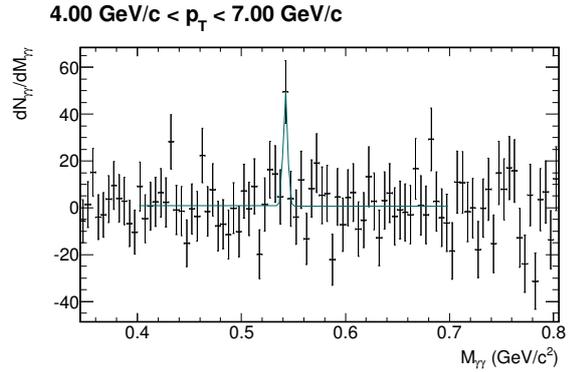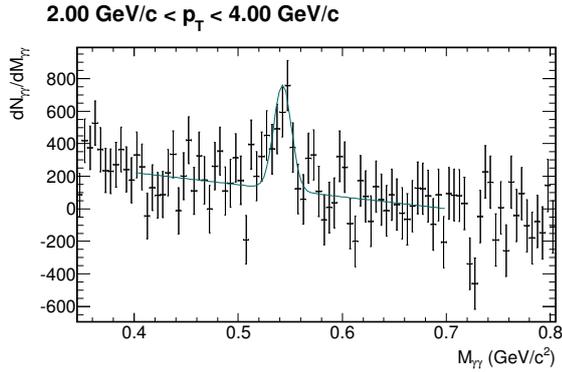
Figure B.12.: Invariant-mass distribution of reconstructed photon pairs $M_{\gamma\gamma}$ around the neutral pion mass in p_{T} slices in 0-5 % Pb–Pb collisions at $\sqrt{s_{\mathrm{NN}}} = 2.76$ TeV before (upper plot) and after subtraction (lower plot). The black histograms in the upper plot show the combined signal and background distribution and the blue histograms show the calculated and normalized mixed event background. After the subtraction the invariant mass distributions are fitted with Equation 6.3, which is shown in green in the lower plot.
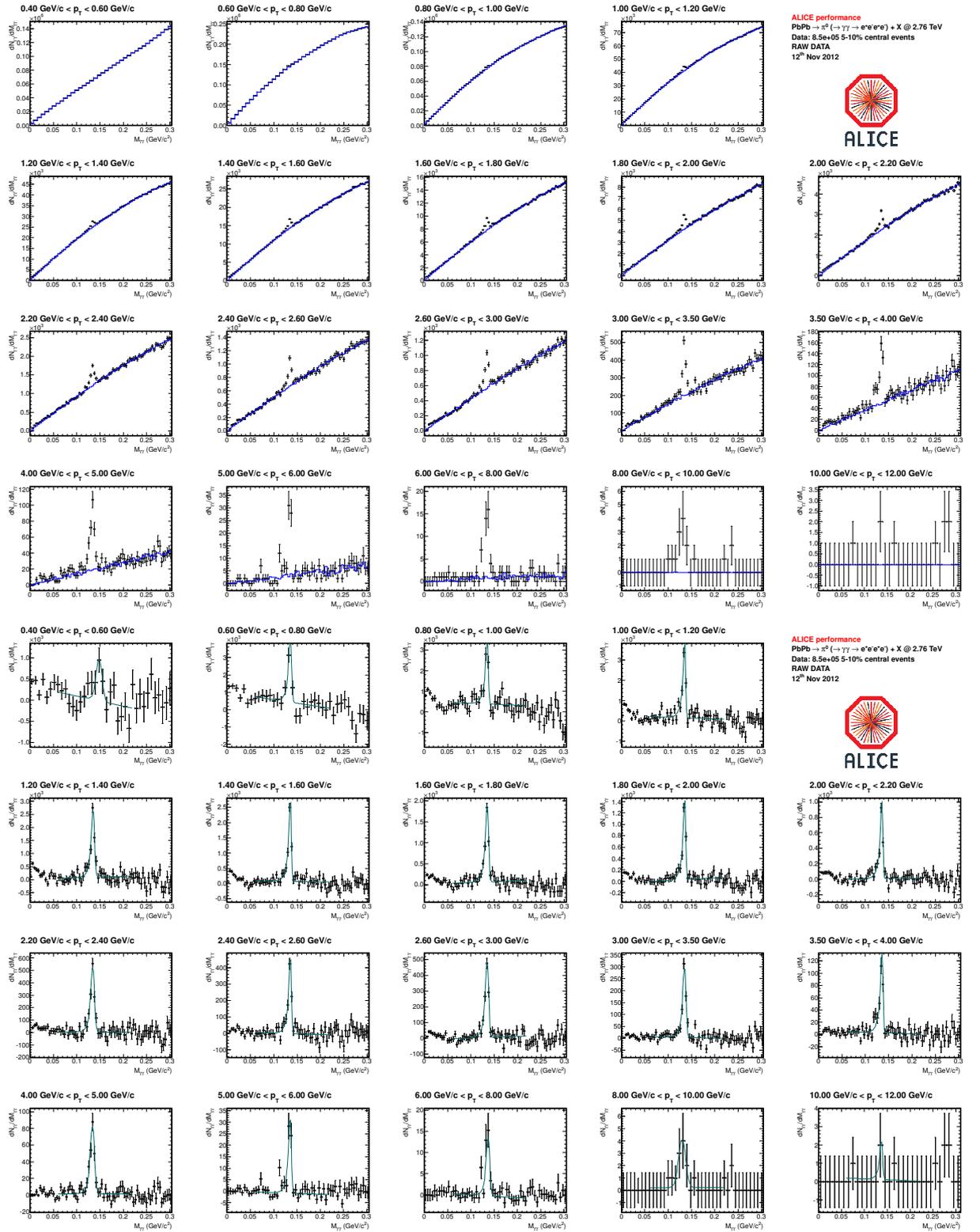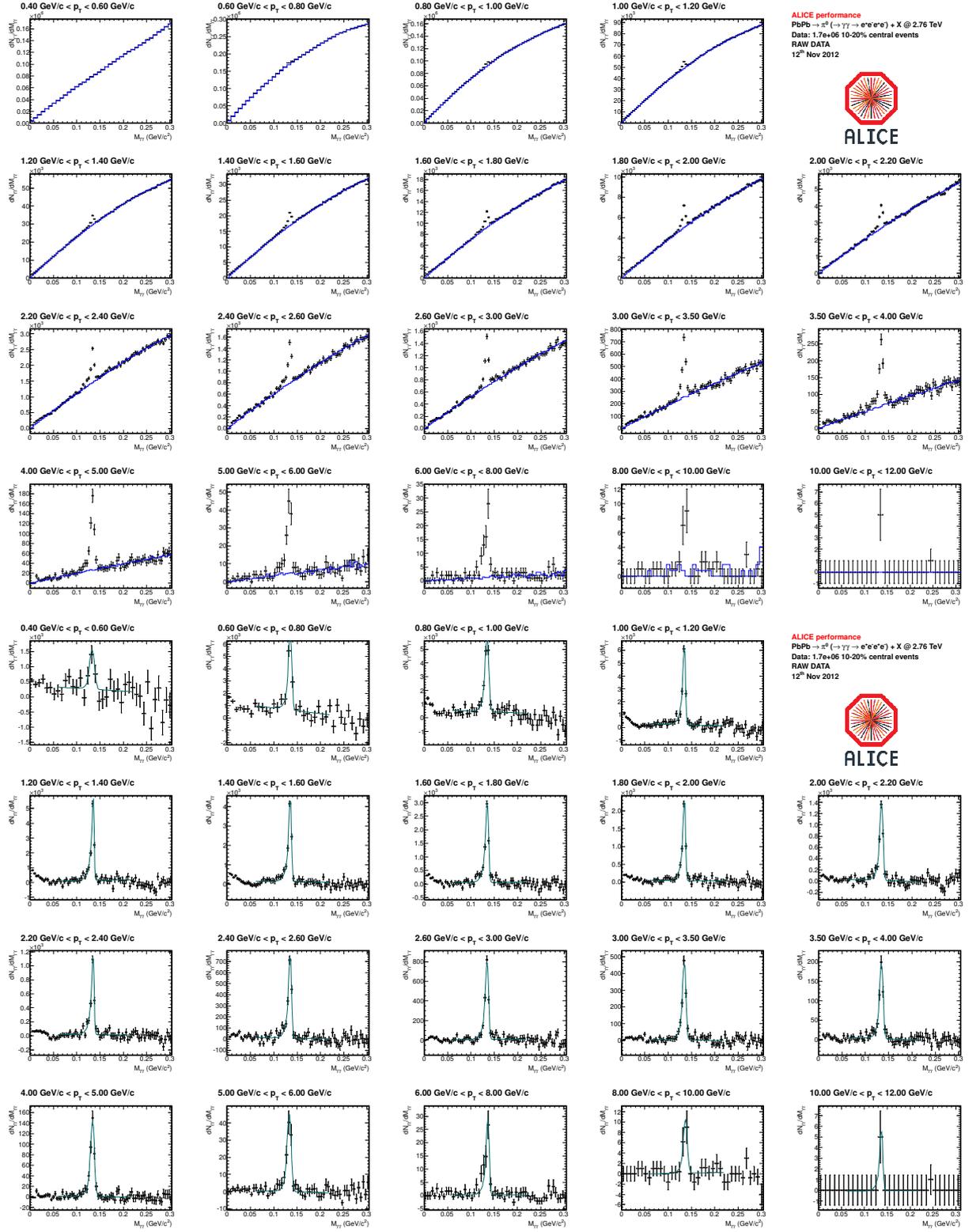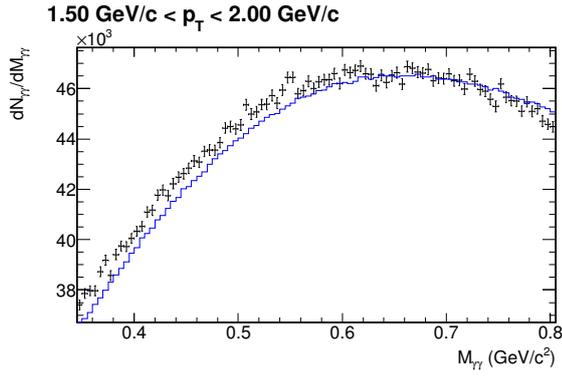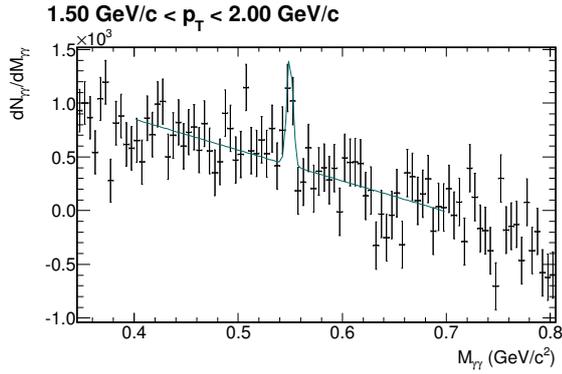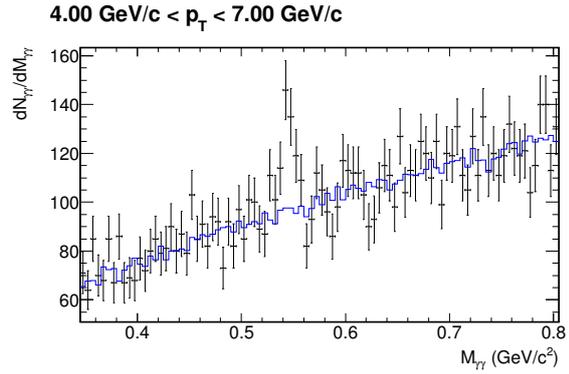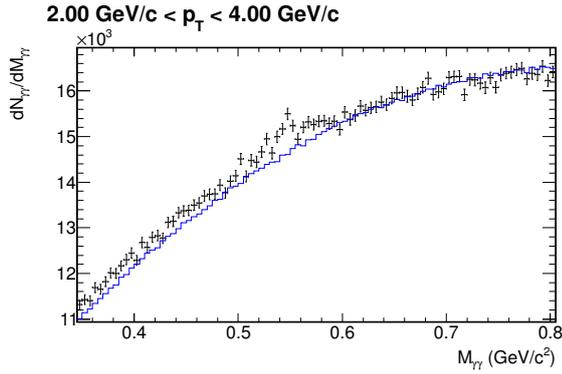
Figure B.13.: Invariant-mass distribution of reconstructed photon pairs $M_{\gamma\gamma}$ around the neutral pion mass in p_{T} slices in 5-10 %Pb–Pb collisions at $\sqrt{s_{\mathrm{NN}}} = 2.76$ TeV before (upper plot) and after subtraction (lower plot). The black histograms in the upper plot show the combined signal and background distribution and the blue histograms show the calculated and normalized mixed event background. After the subtraction the invariant mass distributions are fitted with Equation 6.3, which is shown in green in the lower plot.

Figure B.14.: Invariant-mass distribution of reconstructed photon pairs $M_{\gamma\gamma}$ around the eta meson mass in p_T slices in 0-10 Pb–Pb collisions at $\sqrt{s_{NN}} = 2.76$ TeV before (upper plot) and after subtraction (lower plot). The black histograms in the upper plot show the combined signal and background distribution and the blue histograms show the calculated and normalized mixed event background. After the subtraction the invariant mass distributions are fitted with Equation 6.3, which is shown in green in the lower plot.
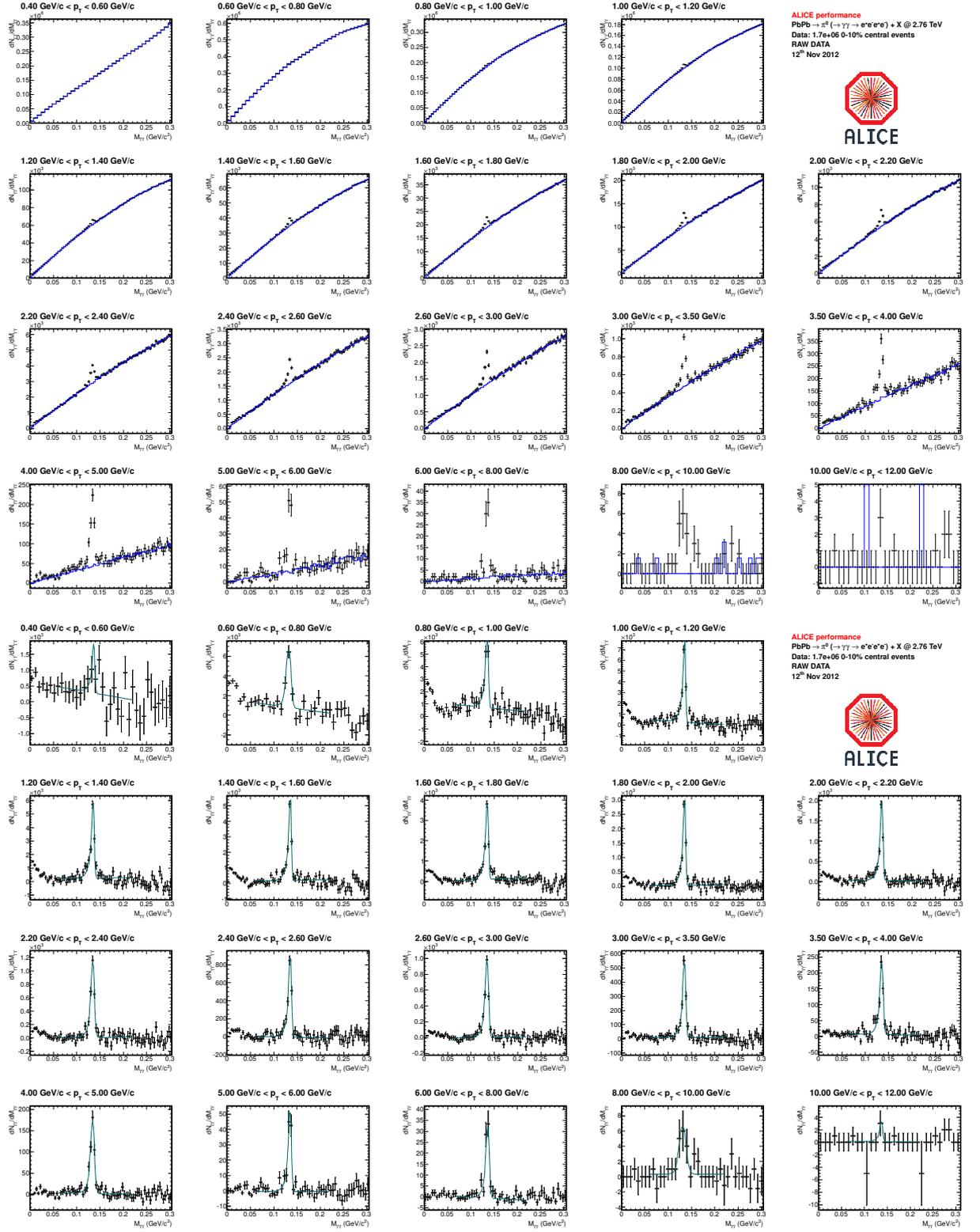
Figure B.15.: Invariant-mass distribution of reconstructed photon pairs $M_{\gamma\gamma}$ around the neutral pion mass in p_T slices in 0-10 % Pb–Pb collisions at $\sqrt{s_{NN}} = 2.76$ TeV before (upper plot) and after subtraction (lower plot). The black histograms in the upper plot show the combined signal and background distribution and the blue histograms show the calculated and normalized mixed event background. After the subtraction the invariant mass distributions are fitted with Equation 6.3, which is shown in green in the lower plot.
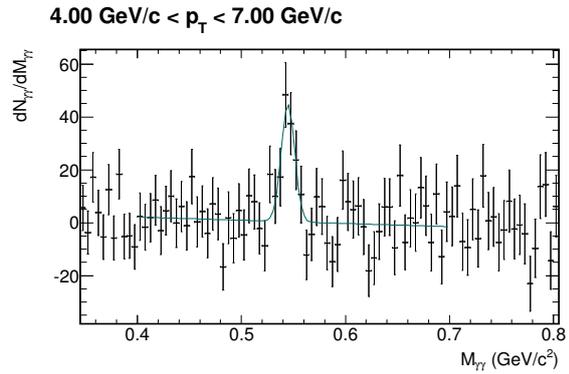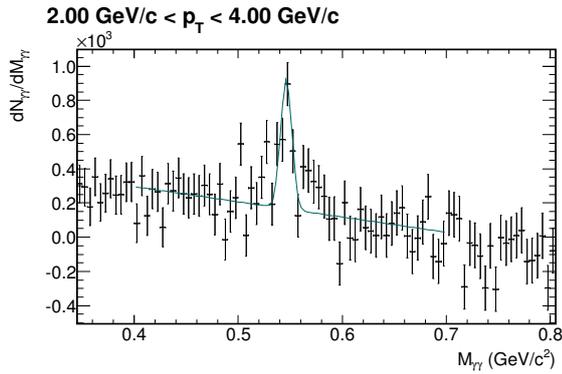
Figure B.16.: Invariant-mass distribution of reconstructed photon pairs $M_{\gamma\gamma}$ around the eta meson mass in p_T slices in 10-20 Pb–Pb collisions at $\sqrt{s_{NN}} = 2.76$ TeV before (upper plot) and after subtraction (lower plot). The black histograms in the upper plot show the combined signal and background distribution and the blue histograms show the calculated and normalized mixed event background. After the subtraction the invariant mass distributions are fitted with Equation 6.3, which is shown in green in the lower plot.
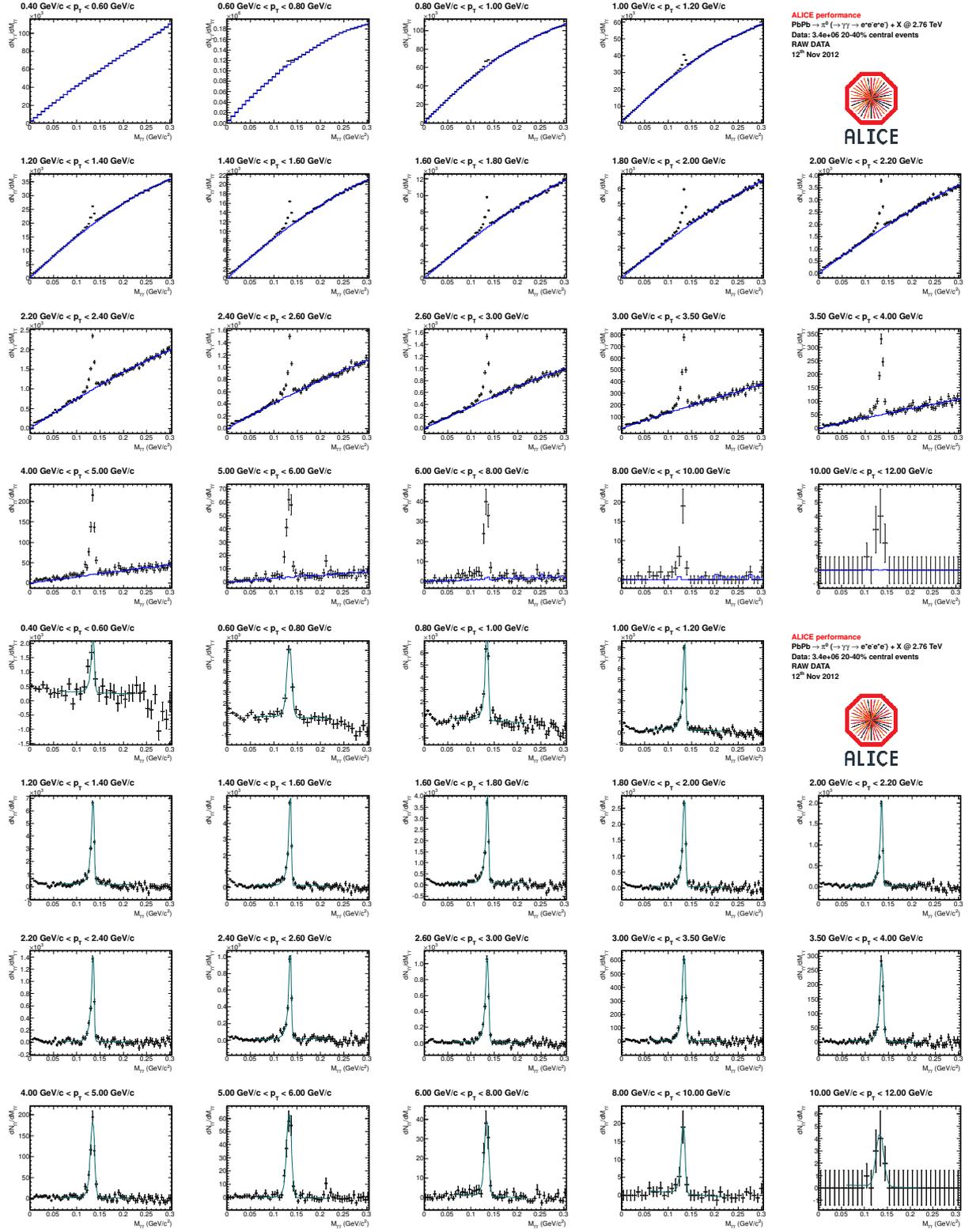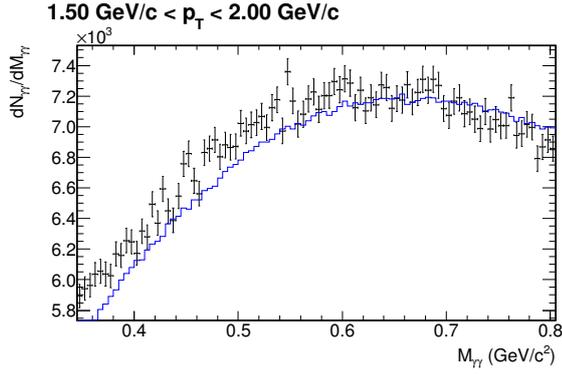
Figure B.17.: Invariant-mass distribution of reconstructed photon pairs $M_{\gamma\gamma}$ around the neutral pion mass in $p_{\rm T}$ slices in 10-20 % Pb–Pb collisions at $\sqrt{s_{\rm NN}} = 2.76$ TeV before (upper plot) and after subtraction (lower plot). The black histograms in the upper plot show the combined signal and background distribution and the blue histograms show the calculated and normalized mixed event background. After the subtraction the invariant mass distributions are fitted with Equation 6.3, which is shown in green in the lower plot.
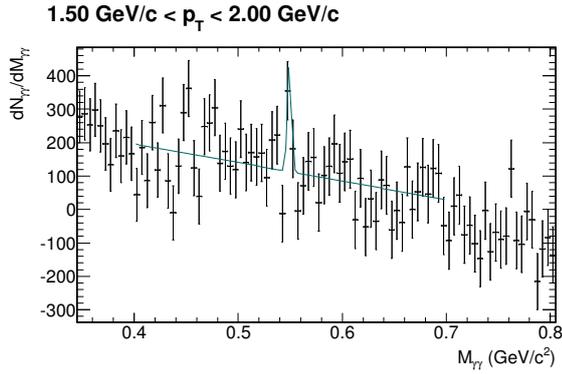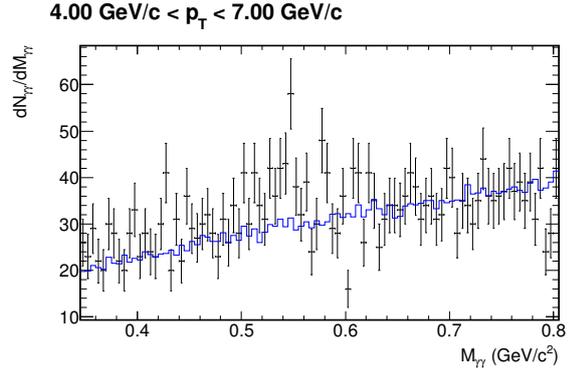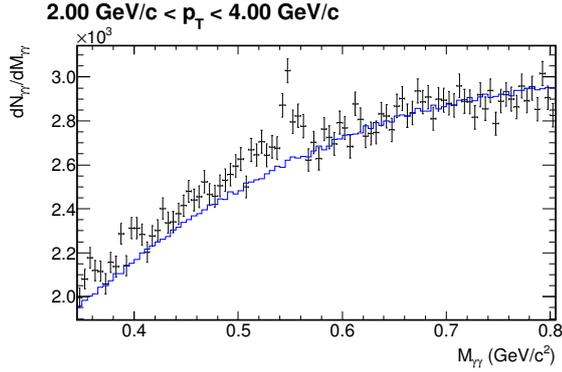
Figure B.18.: Invariant-mass distribution of reconstructed photon pairs $M_{\gamma\gamma}$ around the eta meson mass in p_{T} slices in 20-40 Pb–Pb collisions at $\sqrt{s_{\mathrm{NN}}} = 2.76$ TeV before (upper plot) and after subtraction (lower plot). The black histograms in the upper plot show the combined signal and background distribution and the blue histograms show the calculated and normalized mixed event background. After the subtraction the invariant mass distributions are fitted with Equation 6.3, which is shown in green in the lower plot.

Figure B.19.: Invariant-mass distribution of reconstructed photon pairs $M_{\gamma\gamma}$ around the neutral pion mass in p_{T} slices in 20-40 % Pb–Pb collisions at $\sqrt{s_{\mathrm{NN}}} = 2.76$ TeV before (upper plot) and after subtraction (lower plot). The black histograms in the upper plot show the combined signal and background distribution and the blue histograms show the calculated and normalized mixed event background. After the subtraction the invariant mass distributions are fitted with Equation 6.3, which is shown in green in the lower plot.
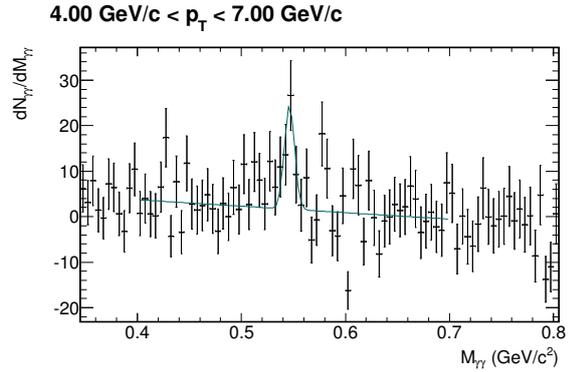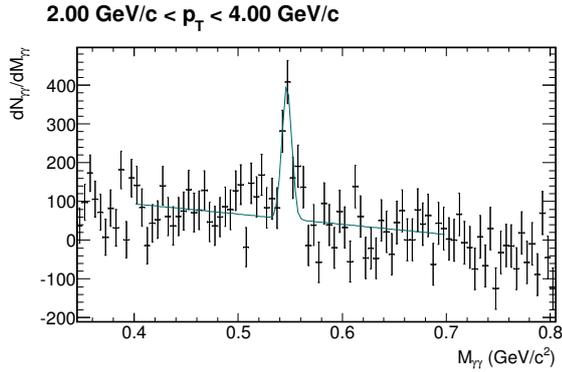
Figure B.20.: Invariant-mass distribution of reconstructed photon pairs $M_{\gamma\gamma}$ around the eta meson mass in p_{T} slices in 40-60 Pb–Pb collisions at $\sqrt{s_{\mathrm{NN}}} = 2.76$ TeV before (upper plot) and after subtraction (lower plot). The black histograms in the upper plot show the combined signal and background distribution and the blue histograms show the calculated and normalized mixed event background. After the subtraction the invariant mass distributions are fitted with Equation 6.3, which is shown in green in the lower plot.

Figure B.21.: Invariant-mass distribution of reconstructed photon pairs $M_{\gamma\gamma}$ around the neutral pion mass in p_{T} slices in 20-40 % Pb–Pb collisions at $\sqrt{s_{\mathrm{NN}}} = 2.76$ TeV before (upper plot) and after subtraction (lower plot). The black histograms in the upper plot show the combined signal and background distribution and the blue histograms show the calculated and normalized mixed event background. After the subtraction the invariant mass distributions are fitted with Equation 6.3, which is shown in green in the lower plot.
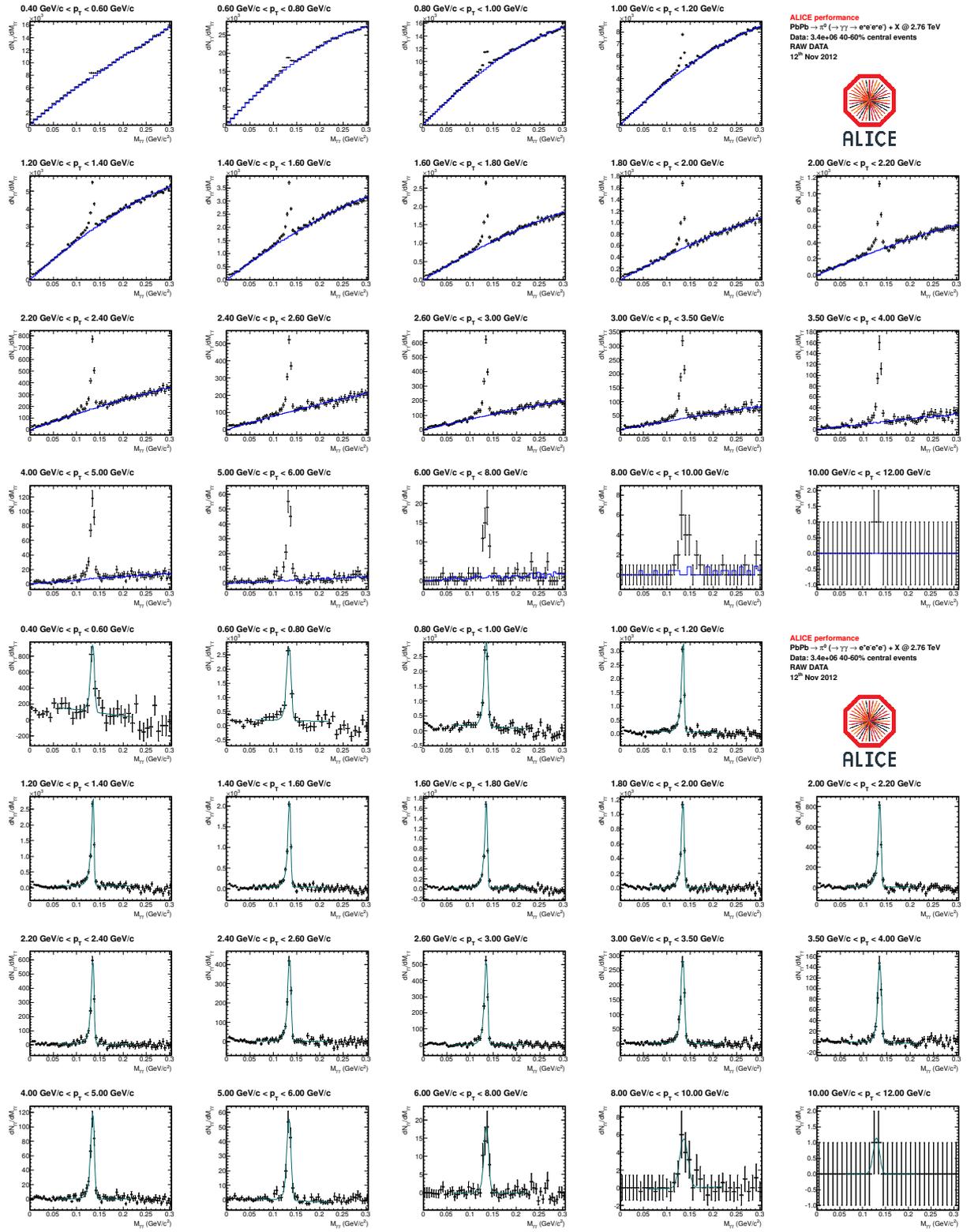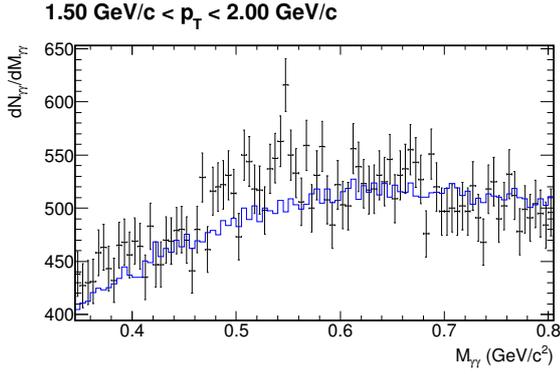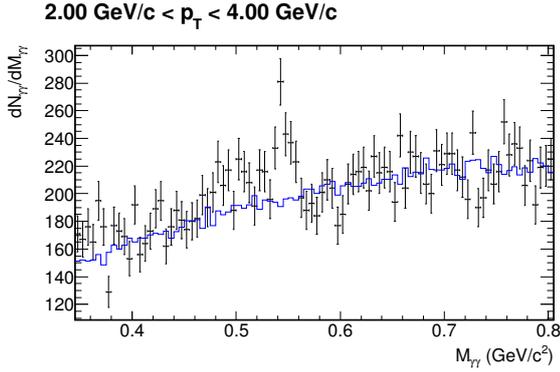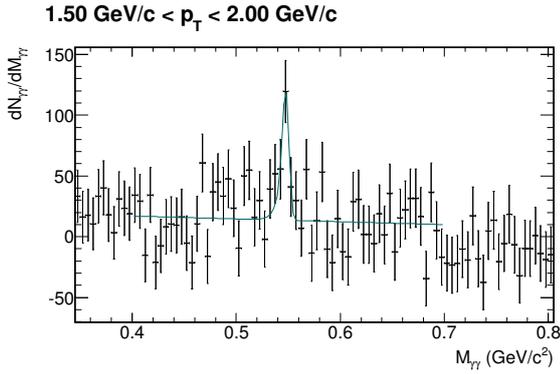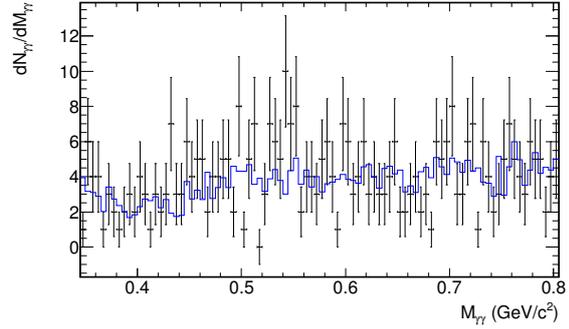
Figure B.22.: Invariant-mass distribution of reconstructed photon pairs $M_{\gamma\gamma}$ around the eta meson mass in p_T slices in 60-80 Pb–Pb collisions at $\sqrt{s_{NN}} = 2.76$ TeV before (upper plot) and after subtraction (lower plot). The black histograms in the upper plot show the combined signal and background distribution and the blue histograms show the calculated and normalized mixed event background. After the subtraction the invariant mass distributions are fitted with Equation 6.3, which is shown in green in the lower plot.
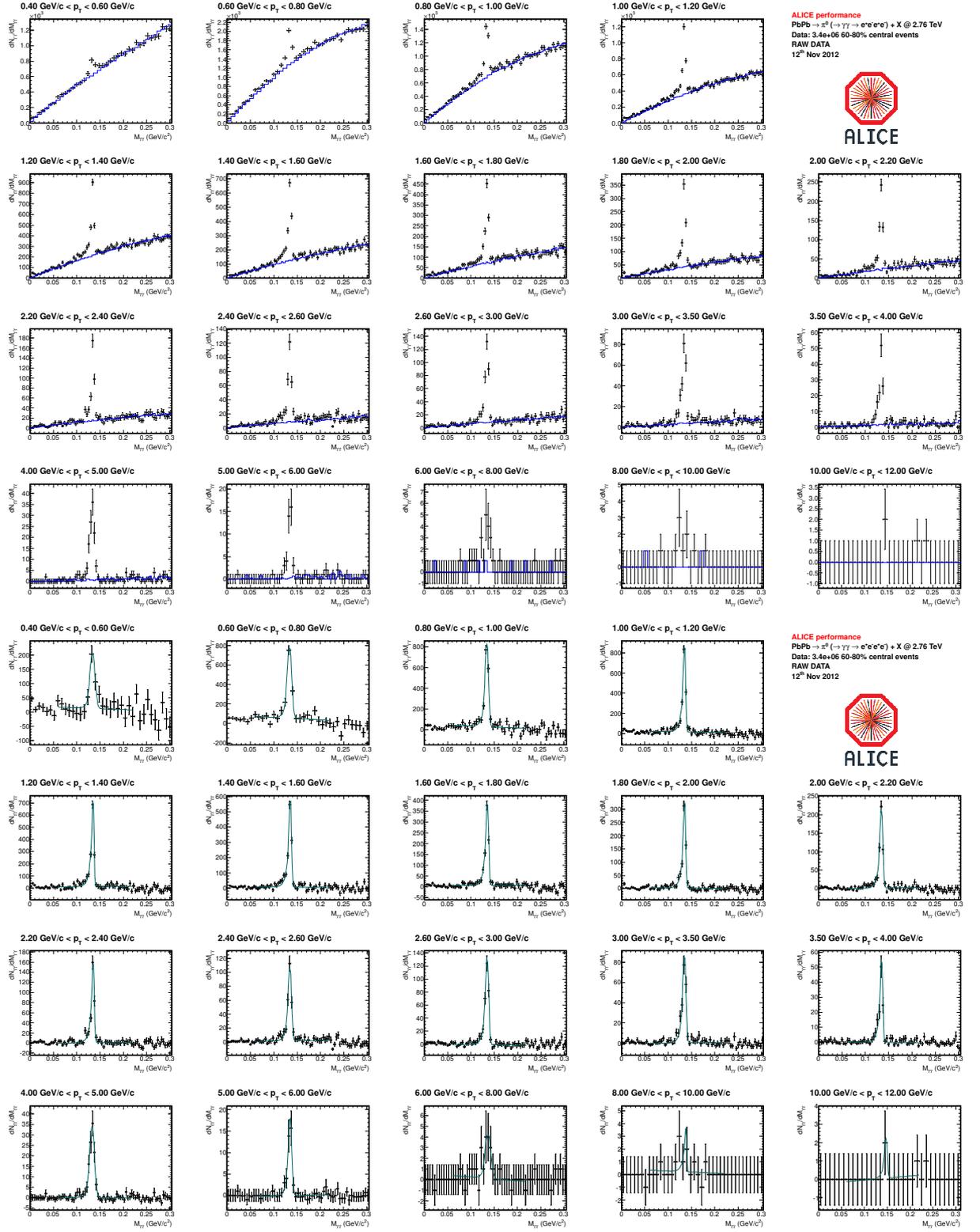
Figure B.23.: Invariant-mass distribution of reconstructed photon pairs $M_{\gamma\gamma}$ around the neutral pion mass in p_{T} slices in 60-80 % Pb–Pb collisions at $\sqrt{s_{\mathrm{NN}}} = 2.76$ TeV before (upper plot) and after subtraction (lower plot). The black histograms in the upper plot show the combined signal and background distribution and the blue histograms show the calculated and normalized mixed event background. After the subtraction the invariant mass distributions are fitted with Equation 6.3, which is shown in green in the lower plot.
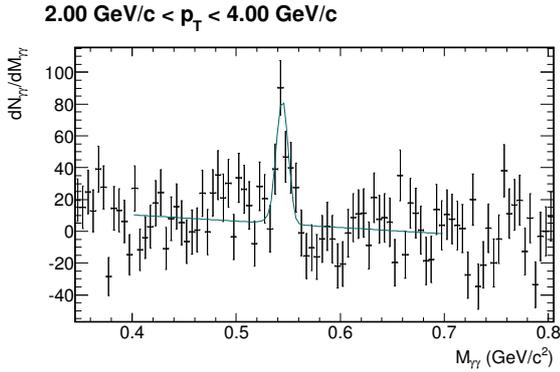
Figure B.24.: Visualization of the systematic errors for the π^0 meson for 5-10% Pb–Pb collisions at $\sqrt{s_{\mathrm{NN}}} = 2.76$ TeV. The colored points represent the individual error sources, while the black points represent the final systematic error of the spectra.

| p_{T} (GeV/c)	Material (%)	Yield extraction (%)	PID e^+, e^- (%)	γ rec. (%)	Track. rec. (%)	Total (%)
0.70	9.72	24.14	18.27	13.67	17.07	38.59
0.90	9.72	3.08	9.57	5.01	5.98	16.01
1.10	9.72	10.41	2.79	3.24	2.69	15.11
1.30	9.72	3.01	3.52	2.62	4.05	11.80
1.50	9.72	3.07	6.55	3.76	2.81	12.99
1.70	9.72	4.44	3.98	2.08	1.98	11.76
1.90	9.72	4.55	3.23	2.67	2.11	11.71
2.10	9.72	2.98	3.85	2.03	1.51	11.16
2.30	9.72	3.33	4.99	2.68	3.22	12.17
2.50	9.72	4.05	4.75	3.95	2.28	12.42
2.80	9.72	4.08	3.37	1.92	1.14	11.29
3.25	9.72	3.29	5.02	4.48	1.73	12.39
3.75	9.72	3.44	9.17	4.76	0.88	14.63
4.50	9.72	5.90	7.81	4.15	1.49	14.48
5.50	9.72	5.80	7.32	1.79	3.88	14.14

Figure B.25.: Detailed systematic error estimates for π^0 meson measurement in 5-10% Pb–Pb at $\sqrt{s_{\mathrm{NN}}} = 2.76$ TeV.
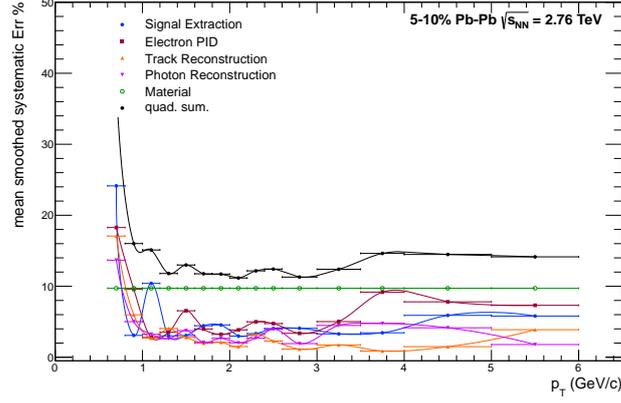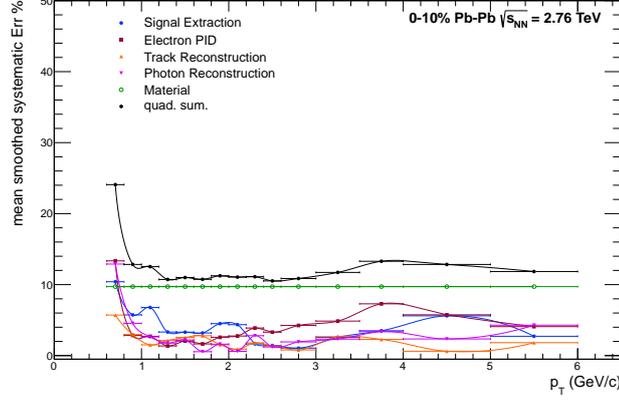
Figure B.26.: Visualization of the systematic errors for the π^0 meson for 0-10% Pb–Pb collisions at $\sqrt{s_{NN}} = 2.76$ TeV. The colored points represent the individual error sources, while the black points represent the final systematic error of the spectra.

p_T (GeV/c)	Material (%)	Yield extraction (%)	PID e^+, e^- (%)	γ rec. (%)	Track. rec. (%)	Total (%)
0.75	9.72	23.61	13.99	22.48	7.99	37.64
1.75	9.72	23.61	13.99	22.48	7.99	37.64
3.00	9.72	30.58	17.00	3.76	5.84	36.97

Figure B.27.: Detailed systematic error estimates for η meson measurement in 0-10% Pb–Pb at $\sqrt{s_{NN}} = 2.76$ TeV.

p_T (GeV/c)	Material (%)	Yield extraction (%)	PID e^+, e^- (%)	γ rec. (%)	Track. rec. (%)	Total (%)
0.70	9.72	10.41	13.35	12.90	5.71	24.08
0.90	9.72	5.73	2.85	4.54	2.97	12.84
1.10	9.72	6.78	2.72	2.64	1.52	12.53
1.30	9.72	3.32	1.36	1.76	2.14	10.73
1.50	9.72	3.31	2.05	2.20	2.56	11.00
1.70	9.72	3.19	1.65	0.55	2.80	10.75
1.90	9.72	4.50	2.58	1.62	1.55	11.24
2.10	9.72	4.36	2.76	0.60	0.91	11.06
2.30	9.72	1.65	3.89	2.81	1.79	11.11
2.50	9.72	1.43	3.30	1.22	1.37	10.53
2.80	9.72	1.06	4.25	1.93	0.80	10.86
3.25	9.72	2.57	4.86	2.33	2.67	11.72
3.75	9.72	3.50	7.30	3.38	2.28	13.29
4.50	9.72	5.61	5.75	2.35	0.62	12.84
5.50	9.72	2.73	4.09	4.29	1.82	11.85

Figure B.28.: Detailed systematic error estimates for π^0 meson measurement in 0-10% Pb–Pb at $\sqrt{s_{NN}} = 2.76$ TeV.
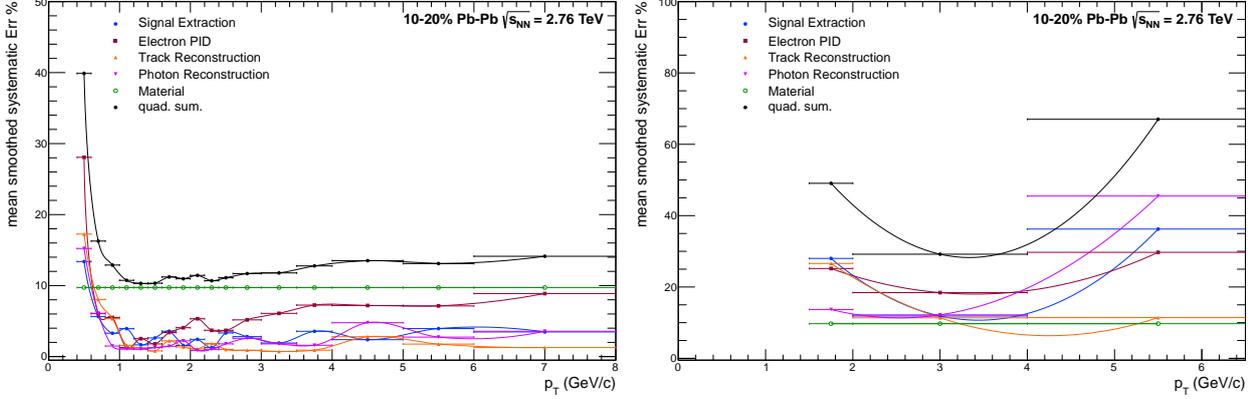
Figure B.29.: Visualization of the systematic errors for the π^0 (left) and η meson (rigth) for 10-20% Pb–Pb collisions at $\sqrt{s_{NN}} = 2.76$ TeV. The colored points represent the individual error sources, while the black points represent the final systematic error of the spectra.

p_T (GeV/c)	Material (%)	Yield extraction (%)	PID e^+, e^- (%)	γ rec. (%)	Track. rec. (%)	Total (%)
0.75	9.72	28.01	25.18	13.69	26.60	49.07
1.75	9.72	28.01	25.18	13.69	26.60	49.07
3.00	9.72	11.87	18.42	12.19	11.36	29.19

Figure B.30.: Detailed systematic error estimates for η meson measurement in 10-20% Pb–Pb at $\sqrt{s_{NN}} = 2.76$ TeV.

p_T (GeV/c)	Material (%)	Yield extraction (%)	PID e^+, e^- (%)	γ rec. (%)	Track. rec. (%)	Total (%)
0.50	9.72	13.38	28.07	15.22	17.26	39.89
0.70	9.72	5.65	6.05	6.09	8.04	16.27
0.90	9.72	3.29	5.50	1.48	5.34	12.89
1.10	9.72	3.94	1.28	1.09	1.58	10.74
1.30	9.72	1.66	2.52	1.05	1.25	10.31
1.50	9.72	2.63	1.78	1.26	0.80	10.33
1.70	9.72	3.57	3.40	1.46	2.22	11.22
1.90	9.72	1.56	4.07	2.22	1.36	10.97
2.10	9.72	2.43	5.33	0.87	1.09	11.43
2.30	9.72	1.26	3.70	1.02	1.84	10.69
2.50	9.72	3.33	3.69	1.79	1.00	11.11
2.80	9.72	2.81	5.17	2.58	0.90	11.69
3.25	9.72	1.91	6.08	1.79	0.73	11.78
3.75	9.72	3.56	7.25	1.59	0.91	12.77
4.50	9.72	2.38	7.19	4.77	2.80	13.51
5.50	9.72	3.94	7.14	2.74	1.76	13.10
7.00	9.72	3.47	8.88	3.57	1.27	14.13

Figure B.31.: Detailed systematic error estimates for π^0 meson measurement in 10-20% Pb–Pb at $\sqrt{s_{NN}} = 2.76$ TeV.
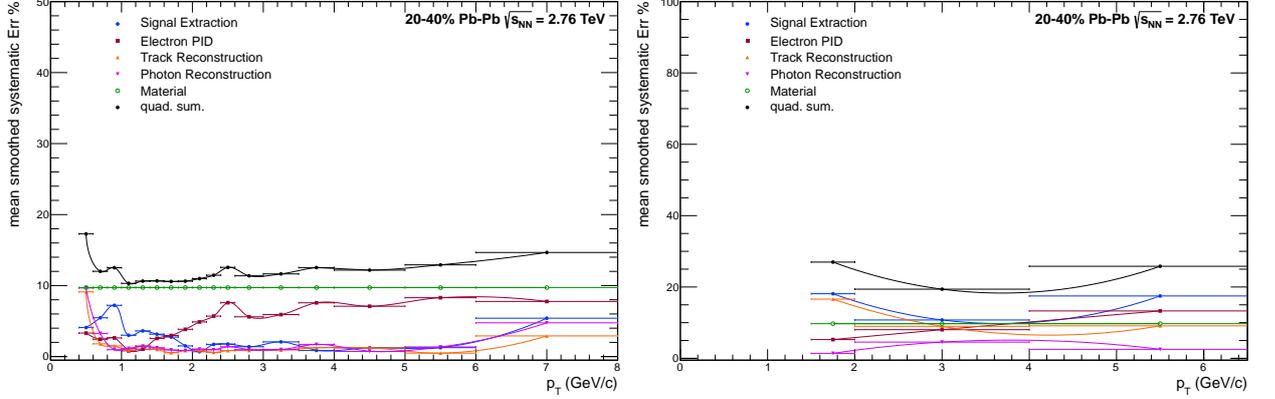
Figure B.32.: Visualization of the systematic errors for the π^0 (left) and η meson (rigth) for 20-40% Pb–Pb collisions at $\sqrt{s_{\mathrm{NN}}} = 2.76$ TeV. The colored points represent the individual error sources, while the black points represent the final systematic error of the spectra.

p_{T} (GeV/c)	Material (%)	Yield extraction (%)	PID e^+, e^- (%)	γ rec. (%)	Track. rec. (%)	Total (%)
0.75	9.72	18.11	5.27	1.40	16.61	26.98
1.75	9.72	18.11	5.27	1.40	16.61	26.98
3.00	9.72	10.76	8.03	4.55	8.98	19.39

Figure B.33.: Detailed systematic error estimates for η meson measurement in 20-40% Pb–Pb at $\sqrt{s_{\mathrm{NN}}} = 2.76$ TeV.

p_{T} (GeV/c)	Material (%)	Yield extraction (%)	PID e^+, e^- (%)	γ rec. (%)	Track. rec. (%)	Total (%)
0.50	9.72	4.09	3.31	9.67	9.12	17.28
0.70	9.72	5.47	2.44	3.26	1.80	12.01
0.90	9.72	7.21	2.63	0.97	1.50	12.52
1.10	9.72	3.01	0.81	1.16	0.92	10.31
1.30	9.72	3.62	1.05	1.46	1.49	10.63
1.50	9.72	3.16	2.56	1.24	1.01	10.66
1.70	9.72	2.75	2.96	0.93	0.54	10.58
1.90	9.72	1.50	3.84	0.85	0.85	10.63
2.10	9.72	0.68	4.88	1.06	0.83	10.98
2.30	9.72	1.72	5.70	0.96	0.59	11.45
2.50	9.72	1.77	7.59	1.38	0.84	0.56
2.80	9.72	1.39	5.60	0.97	0.86	11.38
3.25	9.72	2.07	5.91	1.00	0.94	11.64
3.75	9.72	0.87	7.57	1.72	1.25	12.53
4.50	9.72	1.24	7.09	0.73	1.23	12.18
5.50	9.72	1.26	8.29	1.36	0.48	12.92
7.00	9.72	5.41	7.76	4.75	2.91	14.66

Figure B.34.: Detailed systematic error estimates for π^0 meson measurement in 20-40% Pb–Pb at $\sqrt{s_{\mathrm{NN}}} = 2.76$ TeV.
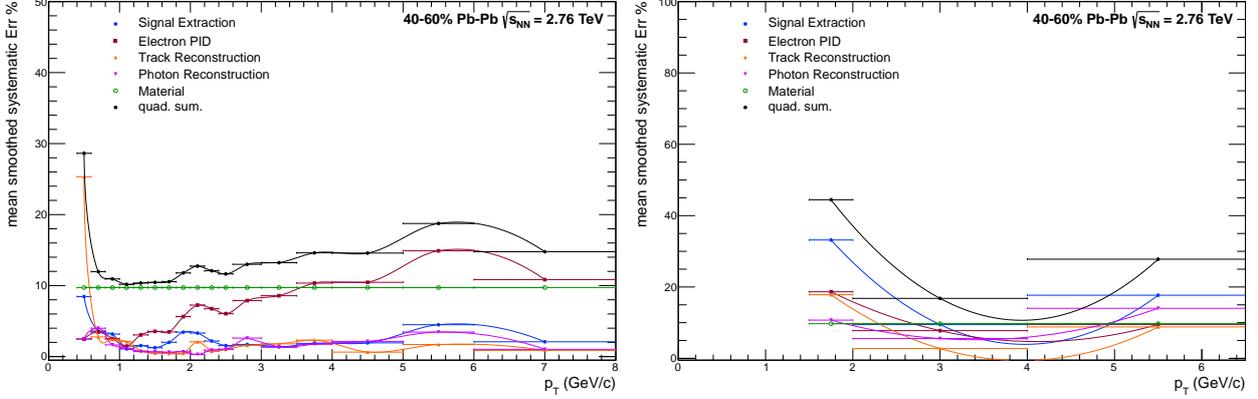
Figure B.35.: Visualization of the systematic errors for the π^0 (left) and η meson (rigth) for 40-60% Pb–Pb collisions at $\sqrt{s_{\mathrm{NN}}}$ = 2.76 TeV. The colored points represent the individual error sources, while the black points represent the final systematic error of the spectra.

p_{T} (GeV/c)	Material (%)	Yield extraction (%)	PID e^+, e^- (%)	γ rec. (%)	Track. rec. (%)	Total (%)
0.75	9.72	33.17	18.66	10.72	17.84	44.45
1.75	9.72	33.17	18.66	10.72	17.84	44.45
3.00	9.72	9.46	7.77	5.55	2.75	16.81

Figure B.36.: Detailed systematic error estimates for η meson measurement in 40-60% Pb–Pb at $\sqrt{s_{\mathrm{NN}}}$ = 2.76 TeV.

p_{T} (GeV/c)	Material (%)	Yield extraction (%)	PID e^+, e^- (%)	γ rec. (%)	Track. rec. (%)	Total (%)
0.50	9.72	8.45	2.47	2.48	25.33	28.63
0.70	9.72	3.62	3.46	4.00	2.77	11.97
0.90	9.72	3.17	2.54	1.65	2.43	10.94
1.10	9.72	1.07	1.47	1.15	2.11	10.18
1.30	9.72	1.55	3.05	0.71	0.81	10.36
1.50	9.72	1.25	3.55	0.67	0.50	10.46
1.70	9.72	2.01	3.48	0.61	0.44	10.55
1.90	9.72	3.44	5.64	0.68	0.46	11.78
2.10	9.72	3.31	7.25	0.30	2.09	12.75
2.30	9.72	2.19	6.74	0.92	0.75	12.09
2.50	9.72	1.55	6.05	1.04	1.02	11.64
2.80	9.72	1.71	7.88	2.60	1.58	12.99
3.25	9.72	1.38	8.57	1.32	1.79	13.22
3.75	9.72	1.86	10.35	1.74	2.32	14.61
4.50	9.72	1.93	10.46	2.14	0.63	14.58
5.50	9.72	4.49	14.90	3.45	1.70	18.75
7.00	9.72	2.09	10.84	1.02	0.87	14.77

Figure B.37.: Detailed systematic error estimates for π^0 meson measurement in 40-60% Pb–Pb at $\sqrt{s_{\mathrm{NN}}}$ = 2.76 TeV.

$p_{\rm T}$ (GeV/c)	Material (%)	Yield extraction (%)	PID e^+, e^- (%)	γ rec. (%)	Track. rec. (%)	Total (%)
0.75	9.72	32.58	11.13	8.85	5.99	37.34
1.75	9.72	32.58	11.13	8.85	5.99	37.34
3.00	9.72	17.23	12.85	5.92	5.72	24.99

Table B.9.: Detailed systematic error estimates for η meson measurement in 60-80% Pb–Pb at $\sqrt{s_{\rm NN}} = 2.76$ TeV.

$p_{\rm T}$ (GeV/c)	Material (%)	Yield extraction (%)	PID e^+, e^- (%)	γ rec. (%)	Track. rec. (%)	Total (%)
0.50	9.72	4.54	6.14	5.26	18.42	22.80
0.70	9.72	6.57	2.25	1.54	0.57	12.06
0.90	9.72	4.25	1.15	0.99	1.61	10.84
1.10	9.72	3.30	1.78	0.92	0.61	10.48
1.30	9.72	2.61	4.57	1.04	0.36	11.11
1.50	9.72	1.34	3.84	1.81	1.35	10.78
1.70	9.72	1.23	5.64	2.74	1.22	11.70
1.90	9.72	2.39	5.74	1.50	1.46	11.73
2.10	9.72	1.54	9.03	2.54	1.06	13.64
2.30	9.72	1.32	7.48v	1.34	12.50	
2.50	9.72	2.93	9.44	1.04	1.82	14.02
2.80	9.72	1.38	7.20	1.99	0.75	12.36
3.25	9.72	4.02	8.65	0.73	0.95	13.67
3.75	9.72	1.57	4.59	1.48	1.39	11.05
4.50	9.72	2.48	14.75	1.50	1.30	17.95
5.50	9.72	4.68	24.00	9.99	2.33	28.24
7.00	9.72	7.41	15.30	17.18	4.45	26.43

Table B.10.: Detailed systematic error estimates for π^0 meson measurement in 60-80% Pb–Pb at $\sqrt{s_{\rm NN}} = 2.76$ TeV.

B.3.3. Final results

p_T (GeV/c)	Inv. Yield (GeV$^{-2}c^2$)	stat Err (GeV$^{-2}c^2$)	syst Err (GeV$^{-2}c^2$)
6.94E-01	8.61E+01	2.71E+01	2.10E+01
8.93E-01	3.39E+01	6.98E+00	5.98E+00
1.09E+00	2.44E+01	1.77E+00	2.38E+00
1.29E+00	1.28E+01	7.76E-01	9.61E-01
1.49E+00	7.00E+00	3.88E-01	4.74E-01
1.69E+00	3.99E+00	2.02E-01	2.48E-01
1.89E+00	2.09E+00	1.11E-01	1.49E-01
2.09E+00	1.28E+00	6.51E-02	8.42E-02
2.30E+00	7.79E-01	4.07E-02	5.26E-02
2.50E+00	4.40E-01	2.52E-02	3.04E-02
2.78E+00	2.12E-01	9.85E-03	1.33E-02
3.23E+00	6.38E-02	3.63E-03	4.16E-03
3.73E+00	2.11E-02	1.50E-03	1.73E-03
4.42E+00	6.83E-03	4.14E-04	5.58E-04
5.44E+00	1.51E-03	1.49E-04	1.48E-04
6.82E+00	4.07E-04	4.02E-05	3.65E-05
8.86E+00	8.78E-05	1.33E-05	1.34E-05
1.09E+01	2.36E-05	6.67E-06	6.22E-06
1.33E+01	1.32E-05	2.68E-06	2.59E-06

Table B.11.: Combined neutral pion results in 0-5% Pb–Pb collisions at $\sqrt{s_\mathrm{NN}} = 2.76$ TeV.

p_T (GeV/c)	Inv. Yield (GeV$^{-2}c^2$)	stat Err (GeV$^{-2}c^2$)	syst Err (GeV$^{-2}c^2$)
6.94E-01	6.25E+01	2.26E+01	2.40E+01
8.93E-01	2.96E+01	5.34E+00	4.61E+00
1.09E+00	2.09E+01	1.45E+00	2.06E+00
1.29E+00	1.24E+01	6.73E-01	8.64E-01
1.49E+00	6.28E+00	3.11E-01	4.18E-01
1.69E+00	3.69E+00	1.66E-01	2.26E-01
1.89E+00	2.02E+00	9.21E-02	1.24E-01
2.09E+00	1.13E+00	5.38E-02	6.93E-02
2.30E+00	6.50E-01	3.39E-02	4.07E-02
2.50E+00	3.85E-01	2.08E-02	2.52E-02
2.78E+00	1.70E-01	7.96E-03	1.06E-02
3.23E+00	6.14E-02	2.97E-03	4.01E-03
3.73E+00	2.28E-02	1.31E-03	1.63E-03
4.42E+00	6.49E-03	3.69E-04	4.83E-04
5.44E+00	1.63E-03	1.35E-04	1.31E-04
6.82E+00	3.72E-04	3.61E-05	3.67E-05
8.86E+00	9.44E-05	1.43E-05	1.27E-05
1.09E+01	2.36E-05	6.02E-06	4.39E-06
1.33E+01	1.46E-05	2.40E-06	2.29E-06

Table B.12.: Combined neutral pion results in 5-10% Pb–Pb collisions at $\sqrt{s_\mathrm{NN}} = 2.76$ TeV.

p_{T} (GeV/c)	Inv. Yield (GeV$^{-2}c^2$)	stat Err (GeV$^{-2}c^2$)	syst Err (GeV$^{-2}c^2$)
6.94E-01	8.83E+01	1.65E+01	2.10E+01
8.93E-01	3.15E+01	4.29E+00	3.87E+00
1.09E+00	2.28E+01	1.20E+00	1.94E+00
1.29E+00	1.27E+01	5.31E-01	8.15E-01
1.49E+00	6.55E+00	2.51E-01	3.84E-01
1.69E+00	3.77E+00	1.30E-01	2.11E-01
1.89E+00	2.09E+00	7.21E-02	1.20E-01
2.09E+00	1.21E+00	4.22E-02	6.87E-02
2.30E+00	7.01E-01	2.65E-02	4.00E-02
2.50E+00	4.06E-01	1.64E-02	2.34E-02
2.78E+00	1.92E-01	6.33E-03	1.09E-02
3.23E+00	6.42E-02	2.32E-03	3.80E-03
3.73E+00	2.16E-02	1.00E-03	1.43E-03
4.42E+00	6.63E-03	2.79E-04	4.37E-04
5.44E+00	1.52E-03	1.01E-04	1.05E-04
6.82E+00	3.80E-04	2.60E-05	3.19E-05
8.86E+00	8.89E-05	1.10E-05	1.04E-05
1.09E+01	1.92E-05	4.44E-06	3.68E-06
1.33E+01	8.89E-06	8.89E-07	1.53E-06

Table B.13.: Combined neutral pion results in 0-10% Pb–Pb collisions at $\sqrt{s_{\mathrm{NN}}} = 2.76$ TeV.

p_{T} (GeV/c)	Inv. Yield (GeV$^{-2}c^2$)	stat Err (GeV$^{-2}c^2$)	syst Err (GeV$^{-2}c^2$)
4.95E-01	1.74E+02	6.53E+01	6.91E+01
6.94E-01	7.24E+01	1.05E+01	1.15E+01
8.93E-01	3.02E+01	2.84E+00	3.73E+00
1.09E+00	1.54E+01	7.08E-01	1.18E+00
1.29E+00	8.70E+00	3.26E-01	5.32E-01
1.49E+00	4.86E+00	1.59E-01	2.69E-01
1.69E+00	2.87E+00	8.34E-02	1.58E-01
1.89E+00	1.50E+00	4.65E-02	8.18E-02
2.09E+00	8.50E-01	2.74E-02	4.77E-02
2.30E+00	4.72E-01	1.66E-02	2.63E-02
2.50E+00	2.91E-01	1.08E-02	1.68E-02
2.78E+00	1.35E-01	4.26E-03	7.55E-03
3.23E+00	5.39E-02	1.61E-03	3.06E-03
3.73E+00	1.80E-02	7.22E-04	1.13E-03
4.42E+00	5.55E-03	2.09E-04	3.48E-04
5.44E+00	1.39E-03	8.35E-05	9.47E-05
6.82E+00	3.32E-04	2.23E-05	2.31E-05
8.86E+00	8.11E-05	8.06E-06	8.01E-06
1.09E+01	2.71E-05	3.97E-06	3.37E-06
1.33E+01	9.20E-06	1.51E-06	1.38E-06

Table B.14.: Combined neutral pion results in 10-20% Pb–Pb collisions at $\sqrt{s_{\mathrm{NN}}} = 2.76$ TeV.

p_{T} (GeV/c)	Inv. Yield (GeV$^{-2}c^2$)	stat Err (GeV$^{-2}c^2$)	syst Err (GeV$^{-2}c^2$)
4.95E-01	9.81E+01	2.49E+01	1.66E+01
6.94E-01	4.06E+01	3.39E+00	4.64E+00
8.94E-01	1.71E+01	1.01E+00	2.04E+00
1.09E+00	9.69E+00	2.75E-01	7.01E-01
1.29E+00	5.35E+00	1.22E-01	3.14E-01
1.49E+00	3.02E+00	5.77E-02	1.58E-01
1.69E+00	1.51E+00	2.95E-02	7.65E-02
1.90E+00	8.60E-01	1.65E-02	4.34E-02
2.10E+00	4.62E-01	9.74E-03	2.38E-02
2.30E+00	2.69E-01	6.11E-03	1.42E-02
2.50E+00	1.63E-01	3.84E-03	8.97E-03
2.78E+00	7.52E-02	1.53E-03	3.99E-03
3.23E+00	3.07E-02	6.52E-04	1.65E-03
3.73E+00	1.16E-02	3.03E-04	6.57E-04
4.43E+00	3.46E-03	9.50E-05	1.96E-04
5.44E+00	9.40E-04	3.85E-05	5.74E-05
6.82E+00	2.30E-04	1.10E-05	1.47E-05
8.86E+00	4.43E-05	4.23E-06	4.15E-06
1.09E+01	1.28E-05	1.89E-06	1.58E-06
1.33E+01	6.41E-06	8.52E-07	7.88E-07

Table B.15.: Combined neutral pion results in 20-40% Pb–Pb collisions at $\sqrt{s_{\mathrm{NN}}} = 2.76$ TeV.

p_{T} (GeV/c)	Inv. Yield (GeV$^{-2}c^2$)	stat Err (GeV$^{-2}c^2$)	syst Err (GeV$^{-2}c^2$)
4.95E-01	3.56E+01	8.57E+00	1.01E+01
6.94E-01	1.44E+01	1.34E+00	1.64E+00
8.94E-01	6.62E+00	2.58E-01	6.26E-01
1.09E+00	3.18E+00	9.77E-02	2.26E-01
1.29E+00	1.83E+00	4.49E-02	1.05E-01
1.49E+00	9.71E-01	2.06E-02	5.02E-02
1.69E+00	5.53E-01	1.10E-02	2.78E-02
1.90E+00	2.93E-01	6.07E-03	1.52E-02
2.10E+00	1.65E-01	3.62E-03	8.87E-03
2.30E+00	9.97E-02	2.38E-03	5.35E-03
2.50E+00	6.26E-02	1.63E-03	3.36E-03
2.78E+00	3.23E-02	6.58E-04	1.76E-03
3.23E+00	1.22E-02	2.93E-04	6.84E-04
3.73E+00	4.66E-03	1.44E-04	2.83E-04
4.43E+00	1.66E-03	5.01E-05	9.99E-05
5.44E+00	4.55E-04	2.10E-05	3.28E-05
6.82E+00	1.03E-04	6.52E-06	6.79E-06
8.86E+00	2.35E-05	2.58E-06	2.31E-06
1.09E+01	6.01E-06	1.12E-06	8.71E-07
1.33E+01	1.90E-06	4.07E-07	3.31E-07

Table B.16.: Combined neutral pion results in 40-60% Pb–Pb collisions at $\sqrt{s_{\mathrm{NN}}} = 2.76$ TeV.

p_{T} (GeV/c)	Inv. Yield (GeV$^{-2}c^2$)	stat Err (GeV$^{-2}c^2$)	syst Err (GeV$^{-2}c^2$)
4.93E-01	8.88E+00	2.55E+00	2.00E+00
6.93E-01	3.69E+00	3.99E-01	4.23E-01
8.94E-01	1.58E+00	8.12E-02	1.53E-01
1.09E+00	8.37E-01	3.30E-02	6.08E-02
1.30E+00	4.29E-01	1.46E-02	2.52E-02
1.50E+00	2.51E-01	6.94E-03	1.31E-02
1.70E+00	1.28E-01	3.54E-03	6.70E-03
1.90E+00	7.84E-02	2.14E-03	4.11E-03
2.10E+00	4.45E-02	1.29E-03	2.48E-03
2.30E+00	2.48E-02	8.61E-04	1.38E-03
2.50E+00	1.46E-02	5.62E-04	8.80E-04
2.79E+00	8.45E-03	2.72E-04	4.70E-04
3.23E+00	3.29E-03	1.21E-04	1.95E-04
3.74E+00	1.44E-03	7.31E-05	8.33E-05
4.45E+00	5.01E-04	2.29E-05	3.45E-05
5.46E+00	1.56E-04	9.92E-06	1.27E-05
6.87E+00	3.02E-05	3.23E-06	2.52E-06
8.90E+00	6.37E-06	1.20E-06	9.16E-07
1.09E+01	2.59E-06	6.29E-07	5.11E-07
1.33E+01	2.78E-07	1.29E-07	1.31E-07

Table B.17.: Combined neutral pion results in 60-80% Pb–Pb collisions at $\sqrt{s_{\mathrm{NN}}} = 2.76$ TeV.

Bibliography

[1] S. Glashow, "Partial Symmetries of Weak Interactions", *Nucl.Phys.* **22** (1961) 579–588.

[2] A. Salam, "Weak and Electromagnetic Interactions", *Conf.Proc.* **C680519** (1968) 367–377.

[3] A. Salam, "Fundamental Theory of Matter: A Survey of Results and Methods", in "Contemporary physics: Trieste Symposium: Proceedings of the International Symposium on Contemporary Physics organized by and held at the International Centre for Theoretical Physics, Trieste, from 7 to 28 June 1968", vol. 19, p. 3. International Atomic Energy Agency, 1969.

[4] S. Weinberg, "A Model of Leptons", *Phys.Rev.Lett.* **19** (1967) 1264–1266.

[5] "Wikipedia.org: Standard model".
http://en.wikipedia.org/wiki/Standard_Model

[6] T. Eichten, H. Faissner, F. Hasert, S. Kabe, W. Krenz, *et al.*, "Measurement of the neutrino - nucleon anti-neutrino - nucleon total cross-sections", *Phys.Lett.* **B46** (1973) 274–280.

[7] **E598 Collaboration**, J. Aubert *et al.*, "Experimental Observation of a Heavy Particle J", *Phys.Rev.Lett.* **33** (1974) 1404–1406.

[8] **SLAC-SP-017 Collaboration**, J. Augustin *et al.*, "Discovery of a Narrow Resonance in e$^+$ e$^-$ Annihilation", *Phys.Rev.Lett.* **33** (1974) 1406–1408.

[9] C. Rubbia, "Experimental Observation of the Intermediate Vector Bosons W$^+$, W$^-$, and Z^0", *Rev.Mod.Phys.* **57** (1985) 699–722.

[10] **CDF Collaboration**, F. Abe *et al.*, "Observation of top quark production in $\bar{p}p$ collisions", *Phys.Rev.Lett.* **74** (1995) 2626–2631, arXiv:hep-ex/9503002.

[11] **D0 Collaboration**, S. Abachi *et al.*, "Observation of the top quark", *Phys.Rev.Lett.* **74** (1995) 2632–2637, arXiv:hep-ex/9503003.

[12] **DONUT Collaboration**, K. Kodama *et al.*, "Observation of tau neutrino interactions", *Phys.Lett.* **B504** (2001) 218–224, arXiv:hep-ex/0012035.

[13] F. Englert and R. Brout, "Broken Symmetry and the Mass of Gauge Vector Mesons", *Phys.Rev.Lett.* **13** (1964) 321–323.

[14] P. W. Higgs, "Broken symmetries, massless particles and gauge fields", *Phys.Lett.* **12** (1964)a 132–133.

[15] P. W. Higgs, "Broken Symmetries and the Masses of Gauge Bosons", *Phys.Rev.Lett.* **13** (1964)b 508–509.

[16] G. Guralnik, C. Hagen, and T. Kibble, "Global Conservation Laws and Massless Particles", *Phys.Rev.Lett.* **13** (1964) 585–587.

[17] P. W. Higgs, "Spontaneous Symmetry Breakdown without Massless Bosons", *Phys.Rev.* **145** (1966) 1156–1163.

[18] T. Kibble, "Symmetry breaking in nonAbelian gauge theories", *Phys.Rev.* **155** (1967) 1554–1561.

[19] **ALEPH Collaboration, CDF Collaboration, D0 Collaboration, DELPHI Collaboration, L3 Collaboration, OPAL Collaboration, SLD Collaboration, LEP Electroweak Working Group, Tevatron Electroweak Working Group, SLD Electroweak and Heavy Flavour Groups**, "Precision Electroweak Measurements and Constraints on the Standard Model", `arXiv:1012.2367`.

[20] **LEP Working Group for Higgs boson searches, ALEPH Collaboration, DELPHI Collaboration, L3 Collaboration, OPAL Collaboration**, R. Barate *et al.*, "Search for the standard model Higgs boson at LEP", *Phys.Lett.* **B565** (2003) 61–75, `arXiv:hep-ex/0306033`.

[21] **CDF Collaboration**, T. Aaltonen *et al.*, "Measurement of Particle Production and Inclusive Differential Cross Sections in p anti-p Collisions at $\sqrt{s} = 1.96$ TeV", *Phys.Rev.* **D79** (2009) 112005, `arXiv:0904.1098`.

[22] **D0 Collaboration**, V. M. Abazov *et al.*, "Combined search for the standard model Higgs boson decaying to $b\bar{b}$ using the D0 Run II data set", *Phys.Rev.Lett.* **109** (2012) 121802, `arXiv:1207.6631`.

[23] **CDF Collaboration**, T. Aaltonen *et al.*, "Combined search for the standard model Higgs boson decaying to a bb pair using the full CDF data set", *Phys.Rev.Lett.* **109** (2012)a 111802, `arXiv:1207.1707`.

[24] **CDF Collaboration, D0 Collaboration**, T. Aaltonen *et al.*, "Evidence for a particle produced in association with weak bosons and decaying to a bottom-antibottom quark pair in Higgs boson searches at the Tevatron", *Phys.Rev.Lett.* **109** (2012)b 071804, `arXiv:1207.6436`.

[25] **ATLAS Collaboration**, G. Aad *et al.*, "Combined search for the Standard Model Higgs boson using up to 4.9 fb^{-1} of *pp* collision data at $\sqrt{s} = 7$ TeV with the ATLAS detector at the LHC", *Phys.Lett.* **B710** (2012)a 49–66, `arXiv:1202.1408`.

[26] **ATLAS Collaboration**, G. Aad *et al.*, "Observation of a new particle in the search for the Standard Model Higgs boson with the ATLAS detector at the LHC", *Phys.Lett.* **B716** (2012)b 1–29, `arXiv:1207.7214`.

[27] **CMS Collaboration**, S. Chatrchyan *et al.*, "Observation of a new boson at a mass of 125 GeV with the CMS experiment at the LHC", *Phys.Lett.* **B716** (2012) 30–61, `arXiv:1207.7235`.

[28] Y. Aoki, S. Borsanyi, S. Durr, Z. Fodor, S. D. Katz, *et al.*, "The QCD transition temperature: results with physical masses in the continuum limit II.", *JHEP* **0906** (2009) 088, `arXiv:0903.4155`.

[29] M. Cheng, N. H. Christ, S. Datta, J. van der Heide, C. Jung, *et al.*, "The Transition temperature in QCD", *Phys.Rev.* **D74** (2006) 054507, `arXiv:hep-lat/0608013`.

[30] F. Karsch, "Lattice QCD at high temperature and density", *Lect.Notes Phys.* **583** (2002) 209–249, `arXiv:hep-lat/0106019`.

[31] F. Karsch, E. Laermann, and A. Peikert, "Quark mass and flavor dependence of the QCD phase transition", *Nucl.Phys.* **B605** (2001) 579–599, `arXiv:hep-lat/0012023`.

[32] P. Braun-Munzinger and J. Stachel, "The quest for the quark–gluon plasma", *Nature* **448** (2007), no. 7151, 302–309.

[33] C. Wong, "Introduction to high-energy heavy-ion collisions", World Scientific Pub Co Inc, 1994.

[34] R. J. Fries and B. Müller, "Heavy ions at LHC: Theoretical issues", *Eur.Phys.J.* **C34** (2004) S279–S285, `arXiv:nucl-th/0307043`.

[35] M. L. Miller, K. Reygers, S. J. Sanders, and P. Steinberg, "Glauber modeling in high energy nuclear collisions", *Ann.Rev.Nucl.Part.Sci.* **57** (2007) 205–243, `arXiv:nucl-ex/0701025`.

[36] e. Sarkar, S., e. Satz, H., and e. Sinha, B., "The physics of the quark-gluon plasma", *Lect.Notes Phys.* **785** (2010) 1–369.

[37] B. Müller, J. Schukraft, and B. Wysłouch, "First results from pb+ pb collisions at the lhc", *Annual Review of Nuclear and Particle Science* **62** (2012), no. 1,.

[38] e. Armesto, N., e. Borghini, N., e. Jeon, S., e. Wiedemann, U.A., S. Abreu, *et al.*, "Heavy Ion Collisions at the LHC - Last Call for Predictions", *J.Phys.* **G35** (2008) 054001, `arXiv:0711.0974`.

[39] **ALICE Collaboration**, B. Abelev *et al.*, "Charged-particle multiplicity density at mid-rapidity in central Pb-Pb collisions at $\sqrt{s_{NN}} = 2.76$ TeV", *Phys.Rev.Lett.* **105** (2010) 252301, `arXiv:1011.3916`.

[40] **ATLAS Collaboration**, G. Aad *et al.*, "Measurement of the centrality dependence of the charged particle pseudorapidity distribution in lead-lead collisions at $\sqrt{s_{NN}} = 2.76$ TeV with the ATLAS detector", *Phys.Lett.* **B710** (2012) 363–382, `arXiv:1108.6027`.

[41] **CMS Collaboration**, S. Chatrchyan *et al.*, "Dependence on pseudorapidity and centrality of charged hadron production in PbPb collisions at a nucleon-nucleon centre-of-mass energy of 2.76 TeV", *JHEP* **1108** (2011) 141, `arXiv:1107.4800`.

[42] J. Bjorken, "Highly Relativistic Nucleus-Nucleus Collisions: The Central Rapidity Region", *Phys.Rev.* **D27** (1983) 140–151.

[43] **CMS Collaboration**, K. Krajczar, "Charged hadron multiplicity and transverse energy densities in Pb Pb collisions from CMS", *J.Phys.* **G38** (2011) 124041.

[44] B. Back, M. Baker, M. Ballintijn, D. Barton, B. Becker, *et al.*, "The PHOBOS perspective on discoveries at RHIC", *Nucl.Phys.* **A757** (2005) 28–101, `arXiv:nucl-ex/0410022`.

[45] **BRAHMS Collaboration**, I. Arsene *et al.*, "Quark gluon plasma and color glass condensate at RHIC? The Perspective from the BRAHMS experiment", *Nucl.Phys.* **A757** (2005) 1–27, `arXiv:nucl-ex/0410020`.

[46] **PHENIX Collaboration**, K. Adcox *et al.*, "Formation of dense partonic matter in relativistic nucleus-nucleus collisions at RHIC: Experimental evaluation by the PHENIX collaboration", *Nucl.Phys.* **A757** (2005) 184–283, `arXiv:nucl-ex/0410003`.

[47] **STAR Collaboration**, J. Adams *et al.*, "Experimental and theoretical challenges in the search for the quark gluon plasma: The STAR Collaboration's critical assessment of the evidence from RHIC collisions", *Nucl.Phys.* **A757** (2005) 102–183, `arXiv:nucl-ex/0501009`.

[48] P. Braun-Munzinger, K. Redlich, and J. Stachel, "Particle production in heavy ion collisions", `arXiv:nucl-th/0304013`.

[49] J. L. Albacete and A. Dumitru, "A model for gluon production in heavy-ion collisions at the LHC with rcBK unintegrated gluon densities", `arXiv:1011.5161`.

[50] F. Becattini, "An Introduction to the Statistical Hadronization Model", `arXiv:0901.3643`.

[51] C. Shen, U. Heinz, P. Huovinen, and H. Song, "Radial and elliptic flow in Pb+Pb collisions at the Large Hadron Collider from viscous hydrodynamic", *Phys.Rev.* **C84** (2011) 044903, `arXiv:1105.3226`.

[52] G. Kestin and U. W. Heinz, "Hydrodynamic radial and elliptic flow in heavy-ion collisions from AGS to LHC energies", *Eur.Phys.J.* **C61** (2009) 545–552, `arXiv:0806.4539`.

[53] S. A. Voloshin, A. M. Poskanzer, and R. Snellings, "Collective phenomena in non-central nuclear collisions", `arXiv:0809.2949`.

[54] R. Snellings, "Elliptic Flow: A Brief Review", *New J.Phys.* **13** (2011) 055008, `arXiv:1102.3010`.

[55] E. Schnedermann, J. Sollfrank, and U. W. Heinz, "Thermal phenomenology of hadrons from 200 A/GeV S+S collisions", *Phys.Rev.* **C48** (1993) 2462–2475, `arXiv:nucl-th/9307020`.

[56] M. Floris, "Identified particles in pp and Pb-Pb collisions at LHC energies with the ALICE detector", *J.Phys.* **G38** (2011) 124025, `arXiv:1108.3257`.

[57] **ALICE Collaboration**, B. Abelev *et al.*, "Pion, Kaon, and Proton Production in Central Pb–Pb Collisions at $\sqrt{s_{NN}} = 2.76$ TeV", `arXiv:1208.1974`.

[58] M. Bleicher, E. Zabrodin, C. Spieles, S. Bass, C. Ernst, *et al.*, "Relativistic hadron hadron collisions in the ultrarelativistic quantum molecular dynamics model", *J.Phys.* **G25** (1999) 1859–1896, `arXiv:hep-ph/9909407`.

[59] S. Bass, M. Belkacem, M. Bleicher, M. Brandstetter, L. Bravina, *et al.*, "Microscopic models for ultrarelativistic heavy ion collisions", *Prog.Part.Nucl.Phys.* **41** (1998) 255–369, `arXiv:nucl-th/9803035`.

[60] I. Kraus, J. Cleymans, H. Oeschler, and K. Redlich, "Particle production in p-p collisions and prediction for LHC energy", *Phys.Rev.* **C79** (2009) 014901, `arXiv:0808.0611`.

[61] A. Andronic, P. Braun-Munzinger, and J. Stachel, "Thermal hadron production in relativistic nuclear collisions: The Hadron mass spectrum, the horn, and the QCD phase transition", *Phys.Lett.* **B673** (2009) 142–145, `arXiv:0812.1186`.

[62] F. Becattini, P. Castorina, A. Milov, and H. Satz, "A Comparative analysis of statistical hadron production", *Eur.Phys.J.* **C66** (2010) 377–386, `arXiv:0911.3026`.

[63] J.-Y. Ollitrault, "Anisotropy as a signature of transverse collective flow", *Phys.Rev.* **D46** (1992) 229–245.

[64] S. Voloshin and Y. Zhang, "Flow study in relativistic nuclear collisions by Fourier expansion of Azimuthal particle distributions", *Z.Phys.* **C70** (1996) 665–672, `arXiv:hep-ph/9407282`.

[65] I. Selyuzhenkov, "Charged particle directed flow in Pb-Pb collisions at $\sqrt{s_{NN}} = 2.76$ TeV measured with ALICE at the LHC", *J.Phys.* **G38** (2011) 124167, `arXiv:1106.5425`.

[66] **ALICE Collaboration**, K. Aamodt *et al.*, "Elliptic flow of charged particles in Pb-Pb collisions at 2.76 TeV", *Phys.Rev.Lett.* **105** (2010) 252302, `arXiv:1011.3914`.

[67] **ALICE Collaboration**, K. Aamodt *et al.*, "Harmonic decomposition of two-particle angular correlations in Pb-Pb collisions at $\sqrt{s_{\mathrm{NN}}} = 2.76$ TeV", *Phys.Lett.* **B708** (2012) 249–264, `arXiv:1109.2501`.

[68] **ALICE Collaboration**, K. Aamodt *et al.*, "Higher harmonic anisotropic flow measurements of charged particles in Pb-Pb collisions at $\sqrt{(s_{(NN)})} = 2.76$ TeV", *Phys.Rev.Lett.* **107** (2011) 032301, `arXiv:1105.3865`.

[69] B. Müller and J. L. Nagle, "Results from the relativistic heavy ion collider", *Ann.Rev.Nucl.Part.Sci.* **56** (2006) 93–135, `arXiv:nucl-th/0602029`.

[70] **ALICE Collaboration**, M. Krzewicki, "Elliptic and triangular flow of identified particles at ALICE", *J.Phys.* **G38** (2011) 124047, `arXiv:1107.0080`.

[71] **ALICE Collaboration**, Z. Yin, "Multi-strange baryon elliptic flow in Pb-Pb collisions at $\sqrt{s_{NN}} = 2.76$ TeV measured with the ALICE detector", `arXiv:1202.0365`.

[72] U. Heinz, C. Shen, and H.-C. Song, "The viscosity of quark-gluon plasma at RHIC and the LHC", *AIP Conf.Proc.* **1441** (2012) 766–770, `arXiv:1108.5323`.

[73] Z. Conesa del Valle, "Heavy-flavor suppression and azimuthal anisotropy in pb–pb collisions at $\sqrt{s_{NN}} = 2.76$ tev with the alice detector", *to be published in Quark Matter procedings 2012*, 2012.

[74] W. Horowitz and M. Gyulassy, "Quenching and Tomography from RHIC to LHC", *J.Phys.* **G38** (2011) 124114, `arXiv:1107.2136`.

[75] W. Alberico, A. Beraudo, A. De Pace, A. Molinari, M. Monteno, *et al.*, "Heavy-flavour spectra in high energy nucleus-nucleus collisions", *Eur.Phys.J.* **C71** (2011) 1666, `arXiv:1101.6008`.

[76] P. Gossiaux, R. Bierkandt, and J. Aichelin, "Tomography of a quark gluon plasma at RHIC and LHC energies", *Phys.Rev.* **C79** (2009) 044906, `arXiv:0901.0946`.

[77] P. Gossiaux, J. Aichelin, T. Gousset, and V. Guiho, "Competition of Heavy Quark Radiative and Collisional Energy Loss in Deconfined Matter", *J.Phys.* **G37** (2010) 094019, `arXiv:1001.4166`.

[78] H. van Hees, V. Greco, and R. Rapp, "Heavy-quark probes of the quark-gluon plasma at RHIC", *Phys.Rev.* **C73** (2006) 034913, `arXiv:nucl-th/0508055`.

[79] O. Fochler, J. Uphoff, Z. Xu, and C. Greiner, "Jet quenching and elliptic flow at RHIC and LHC within a pQCD-based partonic transport model", *J.Phys.* **G38** (2011) 124152, `arXiv:1107.0130`.

[80] **CMS Collaboration**, S. Chatrchyan *et al.*, "Centrality dependence of dihadron correlations and azimuthal anisotropy harmonics in PbPb collisions at $\sqrt{s_{\mathrm{NN}}} = 2.76$ TeV", *Eur.Phys.J.* **C72** (2012) 2012, `arXiv:1201.3158`.

[81] J. Jia, "Measurement of elliptic and higher order flow from ATLAS experiment at the LHC", *J.Phys.* **G38** (2011) 124012, `arXiv:1107.1468`.

[82] **CMS collaboration**, W. Li, "Correlations and fluctuations measured by the CMS experiment in pp and PbPb", *J.Phys.* **G38** (2011) 124027, `arXiv:1107.2452`.

[83] **PHENIX Collaboration**, A. Adare *et al.*, "Measurements of Higher-Order Flow Harmonics in Au+Au Collisions at $\sqrt{s_{\mathrm{NN}}} = 200$ GeV", `arXiv:1105.3928`.

[84] **PHENIX Collaboration**, A. Adare *et al.*, "Measurements of Higher-Order Flow Harmonics in Au+Au Collisions at $\sqrt{s_{NN}} = 200$ GeV", *Phys.Rev.Lett.* **107** (2011)b 252301, `arXiv:1105.3928`.

[85] **STAR Collaboration**, P. Sorensen, "Higher Flow Harmonics in Heavy Ion Collisions from STAR", *J.Phys.* **G38** (2011) 124029, `arXiv:1110.0737`.

[86] S. Voloshin, "Anisotropic flow", *Nucl.Phys.* **A715** (2003) 379–388, `arXiv:nucl-ex/0210014`.

[87] R. J. Fries, B. Müller, C. Nonaka, and S. A. Bass, "Hadronization in heavy ion collisions: Recombination and fragmentation of partons", *Phys.Rev.Lett.* **90** (2003)a 202303, `arXiv:nucl-th/0301087`.

[88] R. J. Fries, B. Müller, C. Nonaka, and S. A. Bass, "Hadron production in heavy ion collisions: Fragmentation and recombination from a dense parton phase", *Phys.Rev.* **C68** (2003)b 044902, `arXiv:nucl-th/0306027`.

[89] V. Greco, C. Ko, and P. Levai, "Parton coalescence at RHIC", *Phys.Rev.* **C68** (2003) 034904, `arXiv:nucl-th/0305024`.

[90] **PHENIX Collaboration**, A. Adare *et al.*, "Scaling properties of azimuthal anisotropy in Au+Au and Cu+Cu collisions at $\sqrt{s_{\mathrm{NN}}} = 200$ GeV", *Phys.Rev.Lett.* **98** (2007) 162301, `arXiv:nucl-ex/0608033`.

[91] J. Cronin, H. J. Frisch, M. Shochet, J. Boymond, R. Mermod, *et al.*, "Production of Hadrons with Large Transverse Momentum at 200 GeV, 300 GeV, and 400 GeV", *Phys.Rev.* **D11** (1975) 3105.

[92] K. Eskola, H. Paukkunen, and C. Salgado, "EPS09: A New Generation of NLO and LO Nuclear Parton Distribution Functions", *JHEP* **0904** (2009) 065, `arXiv:0902.4154`.

[93] R. Baier, Y. L. Dokshitzer, A. H. Mueller, and D. Schiff, "Radiative energy loss of high-energy partons traversing an expanding QCD plasma", *Phys.Rev.* **C58** (1998) 1706–1713, `arXiv:hep-ph/9803473`.

[94] R. Baier, Y. L. Dokshitzer, S. Peigne, and D. Schiff, "Induced gluon radiation in a QCD medium", *Phys.Lett.* **B345** (1995) 277–286, `arXiv:hep-ph/9411409`.

[95] **ALICE Collaboration**, B. Abelev *et al.*, "Centrality Dependence of Charged Particle Production at Large Transverse Momentum in Pb–Pb Collisions at $\sqrt{s_{\mathrm{NN}}} = 2.76$ TeV", `arXiv:1208.2711`.

[96] **CMS Collaboration**, S. Chatrchyan *et al.*, "Study of high-p$_T$ charged particle suppression in PbPb compared to pp collisions at $\sqrt{s_{\mathrm{NN}}} =2.76$ TeV", *Eur.Phys.J.* **C72** (2012) 1945, `arXiv:1202.2554`.

[97] **ALICE Collaboration**, B. Abelev *et al.*, "Transverse Momentum Distribution and Nuclear Modification Factor of Charged Particles in p-Pb Collisions at $\sqrt{s_{NN}} = 5.02$ TeV", `arXiv:1210.4520`.

[98] **CMS Collaboration**, S. Chatrchyan *et al.*, "Measurement of isolated photon production in pp and PbPb collisions at $\sqrt{s_{\mathrm{NN}}} = 2.76$ TeV", *Phys.Lett.* **B710** (2012) 256–277, `arXiv:1201.3093`.

[99] **CMS Collaboration**, Y.-J. Lee, "Nuclear modification factors from the CMS experiment", *J.Phys.* **G38** (2011) 124015, `arXiv:1107.2131`.

[100] **CMS Collaboration**, S. Chatrchyan *et al.*, "Study of Z boson production in PbPb collisions at nucleon-nucleon centre of mass energy $\sqrt{s_{\mathrm{NN}}}= 2.76$ TeV", *Phys.Rev.Lett.* **106** (2011) 212301, `arXiv:1102.5435`.

[101] **CMS Collaboration**, S. Chatrchyan *et al.*, "Study of W boson production in PbPb and pp collisions at $\sqrt{s_{\mathrm{NN}}}$ = 2.76 TeV", *Phys.Lett.* **B715** (2012) 66–87, `arXiv:1205.6334`.

[102] P. Steinberg, "Recent Heavy Ion Results with the ATLAS Detector at the LHC", *J.Phys.* **G38** (2011) 124004, `arXiv:1107.2182`.

[103] A. Andronic, "The charm of hot matter - charmonium and open charm measurements in Pb-Pb collisions with ALICE at the LHC", International Workshop on Discovery Physics at the LHC, 3.-7. December 2012, unpublished.

[104] I. Vitev, "Jet tomography", *J.Phys.* **G30** (2004) S791–S800, `arXiv:hep-ph/0403089`.

[105] I. Vitev and M. Gyulassy, "High p_T tomography of d + Au and Au+Au at SPS, RHIC, and LHC", *Phys.Rev.Lett.* **89** (2002) 252301, `arXiv:hep-ph/0209161`.

[106] A. Dainese, C. Loizides, and G. Paic, "Leading-particle suppression and surface emission in nucleus-nucleus collisions", *Acta Phys.Hung.* **A27** (2006) 245–249, `arXiv:hep-ph/0511045`.

[107] T. Renk, H. Holopainen, R. Paatelainen, and K. J. Eskola, "Systematics of the charged-hadron p_T spectrum and the nuclear suppression factor in heavy-ion collisions from $\sqrt{s}$ = 200 GeV to $\sqrt{s}$ = 2.76 TeV", *Phys.Rev.* **C84** (2011) 014906, `arXiv:1103.5308`.

[108] **ALICE Collaboration**, K. Aamodt *et al.*, "Suppression of Charged Particle Production at Large Transverse Momentum in Central Pb–Pb Collisions at $\sqrt{s_{NN}}$ = 2.76 TeV", *Phys.Lett.* **B696** (2011) 30–39, `arXiv:1012.1004`.

[109] **PHENIX Collaboration**, A. Adare *et al.*, "Suppression pattern of neutral pions at high transverse momentum in Au+Au collisions at $\sqrt{s_{NN}}$ = 200 GeV and constraints on medium transport coefficients", *Phys. Rev. Lett.* **101** (2008) 232301, `arXiv:0801.4020`.

[110] **PHENIX Collaboration**, S. Adler *et al.*, "Centrality dependence of direct photon production in $\sqrt{s_{\mathrm{NN}}}$ = 200 GeV Au + Au collisions", *Phys.Rev.Lett.* **94** (2005) 232301, `arXiv:nucl-ex/0503003`.

[111] **PHENIX Collaboration**, T. Isobe, "Systematic study of high-p$_T$ direct photon production with the PHENIX experiment at RHIC", *J.Phys.G* **G34** (2007) S1015–1018, `arXiv:nucl-ex/0701040`.

[112] **ATLAS Collaboration**, G. Aad *et al.*, "Measurement of Z boson Production in Pb+Pb Collisions at $\sqrt{s_{NN}}$ = 2.76 TeV with the ATLAS Detector", `arXiv:1210.6486`.

[113] H. Appelshauser, "Particle Production at Large Transverse Momentum with ALICE", *J.Phys.* **G38** (2011) 124014, `arXiv:1110.0638`.

[114] A. Dainese, "Heavy-flavour production in Pb-Pb collisions at the LHC, measured with the ALICE detector", *J.Phys.* **G38** (2011) 124032, `arXiv:1106.4042`.

[115] A. Milov, "Centrality dependence of charged particle spectra and RCP in Pb+Pb collisions at $\sqrt{s_{NN}}$=2.76TeV with the ATLAS detector at the LHC", *J.Phys.* **G38** (2011) 124113, `arXiv:1107.0460`.

[116] J. M. Yang, "SUSY Dark Matter In Light Of CDMS/XENON Limits", *Int.J.Mod.Phys.* **D20** (2011) 1383–1388, `arXiv:1102.4942`.

[117] **CMS Collaboration**, S. Chatrchyan *et al.*, "Suppression of non-prompt J/psi, prompt J/psi, and Y(1S) in PbPb collisions at $\sqrt{s_{\mathrm{NN}}}$ = 2.76 TeV", *JHEP* **1205** (2012) 063, `arXiv:1201.5069`.

[118] Y. L. Dokshitzer, V. A. Khoze, and S. Troian, "On specific QCD properties of heavy quark fragmentation ('dead cone')", *J.Phys.* **G17** (1991) 1602–1604.

[119] F. Bock, "ALICE Capabilities for Studying Photon Physics with the Conversion Method at LHC Energies", bachelorthesis, University of Heidelberg, June 2010.

[120] S. Turbide, C. Gale, S. Jeon, and G. D. Moore, "Energy loss of leading hadrons and direct photon production in evolving quark-gluon plasma", *Phys.Rev.* **C72** (2005) 014906, `arXiv:hep-ph/0502248`.

[121] **WA98 Collaboration**, M. Aggarwal *et al.*, "Direct photon production in 158 A-GeV Pb^{208} + Pb^{208} collisions", *Phys.Rev.C*, 2000 `arXiv:nucl-ex/0006007`.

[122] P. Khandai, P. Shukla, and V. Singh, "Meson spectra and m_T scaling in $p + p$, d+Au, and Au + Au collisions at $\sqrt{s_{NN}} = 200$ GeV", *Phys.Rev.* **C84** (2011) 054904, `arXiv:1110.3929`.

[123] **STAR Collaboration**, B. Abelev *et al.*, "Inclusive π^0, η, and direct photon production at high transverse momentum in $p + p$ and d+Au collisions at $\sqrt{s_{NN}} = 200$ GeV", *Phys.Rev.* **C81** (2010) 064904, `arXiv:0912.3838`.

[124] M. Wilde, "Measurement of Direct Photons in pp and Pb-Pb Collisions with ALICE", `arXiv:1210.5958`.

[125] **ALICE Collaboration**, K. Reygers, "Production of Neutral Pions and Eta-mesons in pp Collisions Measured with ALICE", *J.Phys.* **G38** (2011) 124076, `arXiv:1106.5932`.

[126] R. Rusanov, "Measurement of neutral-pion production suppression in Pb–Pb collisions at $\sqrt{s_{NN}} = 2.76$ TeV with ALICE at the CERN LHC", November 2011.

[127] W. Vogelsang, "Private communication", 2010.

[128] **PHENIX Collaboration**, S. Adler *et al.*, "Centrality dependence of direct photon production in $\sqrt{s_{NN}} = 200$ GeV Au + Au collisions", *Phys.Rev.Lett.* **94** (2005) 232301, `arXiv:nucl-ex/0503003`.

[129] **PHENIX Collaboration**, A. Adare *et al.*, "Enhanced production of direct photons in Au+Au collisions at $\sqrt{s_{NN}} = 200$ GeV and implications for the initial temperature", *Phys.Rev.Lett.* **104** (2010) 132301, `arXiv:0804.4168`.

[130] **Particle Data Group**, K. Nakamura *et al.*, "Review of particle physics", *J.Phys.* **G37** (2010) 075021.

[131] D. Groom and S. Klein, "Passage of particles through matter", *The European Physical Journal C-Particles and Fields* **15** (2000), no. 1, 163–173.

[132] M. Sundaresan, "Handbook of particle physics", CRC, 2001.

[133] R. Brun, F. Bruyant, M. Maire, A. McPherson, and P. Zanarini, "GEANT3", 1987.

[134] e. Evans, L. and e. Bryant, P., "LHC Machine", *JINST* **3** (2008) S08001.

[135] "Lhc webpage", 2010.
`http://lhc.wb.cern.ch/lhc/`

[136] "Alice webpage".
`http://aliceinfo.cern.ch/`

[137] **ALICE Collaboration**, K. Aamodt *et al.*, "The ALICE experiment at the CERN LHC", *JINST* **3** (2008) S08002.

[138] **ALICE Collaboration**, G. Dellacasa *et al.*, "ALICE technical design report of the inner tracking system (ITS)", 1999.

[139] **ALICE Collaboration**, K. Aamodt *et al.*, "Alignment of the ALICE Inner Tracking System with cosmic-ray tracks", *JINST* **5** (2010) P03003, `arXiv:1001.0502`.

[140] **ALICE Collaboration**, G. Dellacasa *et al.*, "ALICE: Technical design report of the time projection chamber", 2000.

[141] J. Alme, Y. Andres, H. Appelshauser, S. Bablok, N. Bialas, *et al.*, "The ALICE TPC, a large 3-dimensional tracking device with fast readout for ultra-high multiplicity events", *Nucl.Instrum.Meth.* **A622** (2010) 316–367, `arXiv:1001.1950`.

[142] A. Kalweit, "Production of light flavor hadrons and anti-nuclei at the LHC", PhD thesis, Technische Universität Darmstadt, May 2012.

[143] **ALICE Collaboration**, "ALICE Transition-Radiation Detector (TRD): Technical Design Report", tech. rep., CERN/LHCC/2001–21, 2001.

[144] **ALICE Collaboration**, G. Dellacasa *et al.*, "ALICE technical design report of the time-of-flight system (TOF)", 2000.

[145] **ALICE Collaboration**, S. Beole *et al.*, "ALICE technical design report: Detector for high momentum PID", 1998.

[146] **ALICE Collaboration**, G. Dellacasa *et al.*, "ALICE technical design report of the photon spectrometer (PHOS)", 1999.

[147] G. Conesa, H. Delagrange, J. Diaz, M. Ippolitov, Y. Kharlov, *et al.*, "Performance of the ALICE photon spectrometer PHOS", *Nucl.Instrum.Meth.* **A537** (2005) 363–367.

[148] **ALICE Collaboration**, P. Cortese *et al.*, "ALICE electromagnetic calorimeter technical design report", 2008.

[149] **ALICE Collaboration**, "Aliroot".
http://svnweb.cern.ch/world/wsvn/AliRoot/

[150] "Root webpage".
http://root.cern.ch/

[151] T. Sjöstrand, S. Mrenna, and P. Z. Skands, "PYTHIA 6.4 Physics and Manual", *JHEP* **0605** (2006) 026, `arXiv:hep-ph/0603175`.

[152] T. Sjöstrand, "PYTHIA 8 Status Report", `arXiv:0809.0303`.

[153] T. Sjöstrand, S. Mrenna, and P. Z. Skands, "A Brief Introduction to PYTHIA 8.1", *Comput.Phys.Commun.* **178** (2008) 852–867, `arXiv:0710.3820`.

[154] R. Engel, "Phojet manual", *University of Siegen preprint*, 1995 95–05.

[155] X.-N. Wang and M. Gyulassy, "HIJING: A Monte Carlo model for multiple jet production in p p, p A and A A collisions", *Phys.Rev.* **D44** (1991) 3501–3516.

[156] Z.-W. Lin, C. M. Ko, B.-A. Li, B. Zhang, and S. Pal, "A Multi-phase transport model for relativistic heavy ion collisions", *Phys.Rev.* **C72** (2005) 064901, `arXiv:nucl-th/0411110`.

[157] **GEANT4**, S. Agostinelli *et al.*, "GEANT4: A Simulation toolkit", *Nucl.Instrum.Meth.* **A506** (2003) 250–303.

[158] A. Fasso, A. Ferrari, S. Roesler, P. Sala, F. Ballarini, *et al.*, "The Physics models of FLUKA: Status and recent developments", *eConf* **C0303241** (2003) MOMT005, `arXiv:hep-ph/0306267`.

[159] **ALICE Collaboration**, E. Alessandro, G *et al.*, "ALICE: Physics performance report, volume II", *J.Phys.* **G32** (2006) 1295–2040.

[160] R. Frühwirth, "Application of kalman filtering to track and vertex fitting", *Nuclear Instruments and Methods in Physics Research Section A: Accelerators, Spectrometers, Detectors and Associated Equipment* **262** (1987), no. 2–3, 444 – 450.

[161] S. van der Meer, "Calibration of the Effective Beam Height in the ISR", 1968.

[162] **ALICE Collaboration**, K. Oyama, "Cross section normalization in proton-proton collisions at $\sqrt{s} = 2.76$ TeV and 7 TeV, with ALICE at LHC", *J.Phys.* **G38** (2011) 124131, `arXiv:1107.0692`.

[163] **ALICE Collaboration**, B. Abelev *et al.*, "Measurement of inelastic, single- and double-diffraction cross sections in proton–proton collisions at the LHC with ALICE", *Eur. Phys. J. C*, 2012 `arXiv:1208.4968`.

[164] **UA5 Collaboration**, G. Alner *et al.*, "Scaling of Pseudorapidity Distributions at c.m. Energies Up to 0.9-TeV", *Z.Phys.* **C33** (1986) 1–6.

[165] R. Engel, J. Ranft, and S. Roesler, "Hard diffraction in hadron hadron interactions and in photoproduction", *Phys.Rev.* **D52** (1995) 1459–1468, `arXiv:hep-ph/9502319`.

[166] "The coordinated theoretical-experimental project on qcd". `http://www.phys.psu.edu/~cteq/`

[167] P. Collins, "An Introduction to Regge Theory and High-Energy Physics", Cambridge University Press, 1977.

[168] B. Andersson, S. Mohanty, and F. Söderberg, "Recent developments in the Lund model", `arXiv:hep-ph/0212122`.

[169] A. Capella, U. Sukhatme, C.-I. Tan, and J. Tran Thanh Van, "Dual parton model", *Phys.Rept.* **236** (1994) 225–329.

[170] R. K. Ellis, W. J. Stirling, and B. Webber, "QCD and collider physics", Cambridge University Press, 1996.

[171] **ALICE Collaboration**, K. Aamodt *et al.*, "Centrality dependence of the charged-particle multiplicity density at mid-rapidity in Pb-Pb collisions at $\sqrt{s_{\mathrm{NN}}} = 2.76$ TeV", *Phys.Rev.Lett.* **106** (2011) 032301, `arXiv:1012.1657`.

[172] B. Andersson, G. Gustafson, and B. Nilsson-Almqvist, "A Model for Low p(t) Hadronic Reactions, with Generalizations to Hadron - Nucleus and Nucleus-Nucleus Collisions", *Nucl.Phys.* **B281** (1987) 289.

[173] B. Nilsson-Almqvist and E. Stenlund, "Interactions Between Hadrons and Nuclei: The Lund Monte Carlo, Fritiof Version 1.6", *Comput.Phys.Commun.* **43** (1987) 387.

[174] K. Koch, "Measurement of π^0 and η mesons with photon conversions in alice in proton-proton collisions at $\sqrt{s} = 0.9, 2.76, 7$ tev", PhD thesis, University of Heidelberg, February 2012. `http://www.ub.uni-heidelberg.de/archiv/13113`

[175] S. Gorbunov and I. Kisel, "Alikf package".
http://alisoft.cern.ch/viewvc/branches/v4-18-Release/STEER/AliKFParticle.h

[176] J. Podolanski and R. Armenteros, "Analysis of v-events", *Phil. Mag.* **7** (1954).

[177] **ALICE Collaboration**, K. Aamodt *et al.*, "Charged-particle multiplicity measurement in proton-proton collisions at $\sqrt{s} = 7$ TeV with ALICE at LHC", *Eur.Phys.J.* **C68** (2010) 345–354, arXiv:1004.3514.

[178] **ATLAS Collaboration**, G. Aad *et al.*, "A study of the material in the ATLAS inner detector using secondary hadronic interactions", *JINST* **7** (2012) P01013, arXiv:1110.6191.

[179] M. Ivanov, "Private communication", 2011-2012.

[180] "Conversion group".
https://twiki.cern.ch/twiki/bin/viewauth/ALICE/PWGGA#Conversions

[181] K. Aamodt, "Photon, π^0 and η measurements in proton-proton collisions at $\sqrt{s} = 7$ tev with the alice tpc at the lhc", phd thesis, University of Oslo, 2011.

[182] **ALICE Collaboration**, B. Abelev *et al.*, "Neutral pion and η meson production in proton-proton collisions at $\sqrt{s} = 0.9$ TeV and $\sqrt{s} = 7$ TeV", *Phys.Lett.* **B717** (2012) 162–172, arXiv:1205.5724.

[183] A. Marín, F. Bock, M. Wilde, D. Lohner, K. Aamodt, and K. Koch, "ALICE Conversion Software".
http://svnweb.cern.ch/world/wsvn/AliRoot/trunk/PWGGA/GammaConv/

[184] Y. Kharlov, "Private communication", 2011-2012.

[185] P. Aurenche, M. Fontannaz, J. Guillet, B. A. Kniehl, and M. Werlen, "Large p_T inclusive π^0 cross-sections and next-to-leading-order QCD predictions", *Eur.Phys.J.* **C13** (2000) 347–355, arXiv:hep-ph/9910252.

[186] **ALICE Collaboration**, A. Ortiz Velasquez, "Production of pions, kaons and protons at high p_T in $\sqrt{s_{NN}} = 2.76$ TeV Pb-Pb collisions", arXiv:1210.6995.

[187] D. Peressounko, "Private communication", 2011-2012.

[188] **PHENIX Collaboration**, A. Adare *et al.*, "Evolution of π^0 suppression in Au+Au collisions from $\sqrt{s_{NN}} = 39$ to 200 GeV", *Phys.Rev.Lett.* **109** (2012) 152301, arXiv:1204.1526.

[189] **WA98 Collaboration**, M. M. Aggarwal *et al.*, "Suppression of High-p_T Neutral Pions in Central Pb+Pb Collisions at $\sqrt{s_{NN}} = 17.3$ GeV", *Phys.Rev.Lett.* **100** (2008) 242301, arXiv:0708.2630.

[190] W. A. Horowitz and M. Gyulassy, "The Surprising Transparency of the sQGP at LHC", *Nucl.Phys.* **A872** (2011) 265–285, arXiv:1104.4958.

[191] S. Wicks, W. A. Horowitz, M. Djordjevic, and M. Gyulassy, "Elastic, inelastic, and path length fluctuations in jet tomography", *Nucl.Phys.* **A784** (2007) 426–442, arXiv:nucl-th/0512076.

[192] X.-F. Chen, T. Hirano, E. Wang, X.-N. Wang, and H. Zhang, "Suppression of high p_T hadrons in $Pb + Pb$ Collisions at LHC", *Phys.Rev.* **C84** (2011) 034902, arXiv:1102.5614.

[193] R. Sharma, I. Vitev, and B.-W. Zhang, "Light-cone wave function approach to open heavy flavor dynamics in QCD matter", *Phys.Rev.* **C80** (2009) 054902, arXiv:0904.0032.

[194] R. B. Neufeld, I. Vitev, and B.-W. Zhang, "A possible determination of the quark radiation length in cold nuclear matter", *Phys.Lett.* **B704** (2011) 590–595, `arXiv:1010.3708`.

[195] **ALICE Collaboration**, K. Aamodt *et al.*, "Strange particle production in proton-proton collisions at $\sqrt{(s)} = 0.9$ TeV with ALICE at the LHC", *Eur.Phys.J.* **C71** (2011) 1594, `arXiv:1012.3257`.

[196] **CMS Collaboration**, V. Khachatryan *et al.*, "Strange Particle Production in pp Collisions at sqrt(s) = 0.9 and 7 TeV", *JHEP* **1105** (2011) 064, `arXiv:1102.4282`.

[197] **ALICE Collaboration**, D. Chinellato, "Strange and Multi-Strange Particle Production in ALICE", `arXiv:1211.7298`.

[198] S. Schuchmann, "Private communication", 2012.

[199] G. D. Lafferty and T. R. Wyatt, "Where to stick your data points: The treatment of measurements within wide bins", *Nucl.Instrum.Meth.* **A355** (1995) 541–547.

[200] C. Tsallis, "Possible Generalization of Boltzmann-Gibbs Statistics", *J.Statist.Phys.* **52** (1988) 479–487.

[201] D. de Florian, R. Sassot, and M. Stratmann, "Global analysis of fragmentation functions for pions and kaons and their uncertainties", *Phys.Rev.* **D75** (2007) 114010, `arXiv:hep-ph/0703242`.

[202] C. A. Aidala, F. Ellinghaus, R. Sassot, J. P. Seele, and M. Stratmann, "Global Analysis of Fragmentation Functions for Eta Mesons", *Phys.Rev.* **D83** (2011) 034002, `arXiv:1009.6145`.

[203] J. Binnewies, B. A. Kniehl, and G. Kramer, "Next-to-leading order fragmentation functions for pions and kaons", *Z.Phys.* **C65** (1995) 471–480, `arXiv:hep-ph/9407347`.

[204] R. Sassot, P. Zurita, and M. Stratmann, "Inclusive Hadron Production in the CERN-LHC Era", *Phys.Rev.* **D82** (2010) 074011, `arXiv:1008.0540`.

[205] **PHENIX Collaboration**, S. Adler *et al.*, "High transverse momentum η meson production in p^+p, d^+ Au and Au+Au collisions at $\sqrt{s_{\mathrm{NN}}} = 200$ GeV", *Phys.Rev.* **C75** (2007) 024909, `arXiv:nucl-ex/0611006`.

[206] **WA80 Collaboration**, R. Albrecht *et al.*, "Production of eta mesons in 200 A/GeV S + S and S + Au reactions", *Phys.Lett.* **B361** (1995) 14–20, `arXiv:hep-ex/9507009`.

[207] X.-F. Guo and X.-N. Wang, "Multiple scattering, parton energy loss and modified fragmentation functions in deeply inelastic e A scattering", *Phys.Rev.Lett.* **85** (2000) 3591–3594, `arXiv:hep-ph/0005044`.

[208] X.-N. Wang and X.-F. Guo, "Multiple parton scattering in nuclei: Parton energy loss", *Nucl.Phys.* **A696** (2001) 788–832, `arXiv:hep-ph/0102230`.

[209] J. Casalderrey-Solana and X.-N. Wang, "Energy dependence of jet transport parameter and parton saturation in quark-gluon plasma", *Phys.Rev.* **C77** (2008) 024902, `arXiv:0705.1352`.

Acknowledgements

Erklärung

Ich versichere, dass ich diese Arbeit selbständig verfasst habe und keine anderen als die angegebenen Quellen und Hilfsmittel benutzt habe.

Heidelberg, den 13. Dezember 2012   Unterschrift: . . . .

Friederike Bock